Thermodynamic regulation of the amyloid-like aggregation of the functional domains of TDP-43

by

Divya Patni

10BB16A26040

A thesis submitted to the

Academy of Scientific & Innovative Research

for the award of the degree of

DOCTOR OF PHILOSOPHY

in

SCIENCE

Under the supervision of
Dr. Santosh Kumar Jha

CSIR- National Chemical Laboratory, Pune

Academy of Scientific and Innovative Research

AcSIR Headquarters, CSIR-HRDC campus
Sector 19, Kamla Nehru Nagar,
Ghaziabad, U.P. – 201 002, India

April 2023

Certificate

This is to certify that the work incorporated in this Ph.D. thesis entitled, " *Thermodynamic regulation of the amyloid-like aggregation of the functional domains of TDP-43",* submitted by *Divya Patni* to the Academy of Scientific and Innovative Research (AcSIR) in fulfillment of the requirements for the award of the Degree of *Doctor of Philosophy in Science*, embodies original research work carried-out by the student. We, further certify that this work has not been submitted to any other University or Institution in part or full for the award of any degree or diploma. Research material(s) obtained from other source(s) and used in this research work has/have been duly acknowledged in the thesis. Image(s), illustration(s), figure(s), table(s) etc., used in the thesis from other source(s), have also been duly cited and acknowledged.

(Signature of Student)
Divya Patni
Date: 19/04/2023

(Signature of Supervisor)
Santosh Kumar Jha
Date: 19/04/2023

Statements of Academic Integrity

I, Divya Patni, a Ph.D. student of the Academy of Scientific and Innovative Research (AcSIR) with Registration No. 10BB16A26040 hereby undertake that, the thesis entitled "*Thermodynamic regulation of the amyloid-like aggregation of the functional domains of TDP-43"* has been prepared by me and that the document reports original work carried out by me and is free of any plagiarism in compliance with the UGC Regulations on *"Promotion of Academic Integrity and Prevention of Plagiarism in Higher Educational Institutions (2018)"* and the CSIR Guidelines for "*Ethics in Research and in Governance (2020)".*

Signature of the Student

Date: 19/04/2023

Place : Pune

It is hereby certified that the work done by the student, under my/our supervision, is plagiarism-free in accordance with the UGC Regulations on *"Promotion of Academic Integrity and Prevention of Plagiarism in Higher Educational Institutions (2018)"* and the CSIR Guidelines for "*Ethics in Research and in Governance (2020)".*

Signature of the Supervisor

Name: Santosh Kumar Jha

Date: 19/04/2023

Place: Pune

Acknowledgment

The work that I present in my thesis would not have been possible without the constant support and help of many people. I am happy to write a few lines about each of these fantastic people who have been my pillar of strength throughout my tenure!

I owe my deepest gratitude to my research advisor, Dr. Santosh Kumar Jha, who has constantly supported me throughout the tenure. I am incredibly grateful to him for being patient and motivating me after all the failed experiments. I have evolved into a better researcher under his guidance. He has taught me how to approach a scientific problem, infer results critically without being biased in different ways, and, most importantly, present those results to the audience. His optimistic attitude each morning drove me to carry out research even on days when I did not feel motivated enough to work. His saying, "Kehne se kya hoga karke dikhao" will always remain in my head. He has also set an excellent example of how a workplace should look. He has not only helped me in dealing with scientific issues but also acted as a counsellor during difficult times. I would not have asked for a better mentor. I have learned a lot from him and will try to implement those in my future research career.

I would extend my sincere gratitude to my doctoral advisory committee members, Dr. Durba Sengupta, Dr. Jeetnder Chugh, and Dr. N.P. Argade for their constructive feedback, guidance, and support throughout my Ph.D. tenure. Their questions motivated me and helped me gain a very different perspective about my research work.

I would also like to thank Dr. Anjali Jha for being so cheerful and motivating and guiding me through life from time to time. I would love to thank Anwesha for being my favorite person in Pune and bringing fun to the hectic days, and Avishkar for bringing so much cuteness.

Dr. Nirbhik, Dr. Prajna, and Dr. Meenakshi, thanks for being patient while discussing the scientific problems with me despite your hectic schedules. You people have set a perfect example of a happy workplace. I cannot thank you enough for being available for me even after graduating from the lab. My research has improved from your insights. Priya, cannot thank you enough for introducing me to this fantastic lab. I feel fortunate to have got Abhilasha, Sonal, Anjali, and Mona, who supported me tremendously during the final stages of my Ph.D.

I also acknowledge master's students, Minnu, Kavya, and Sanskruti, whom I got the opportunity to train. I am lucky enough to have met some amazing friends in Pune: Priya, Shruti, Vaishnavi, Debopriya, Dr. Parag, Dr. Debjyoti, Monika who all added joy.

I acknowledge CSIR for funding and the Academy of Scientific and Innovative Research (AcSIR) for enrolment of my Ph.D. at NCL. I am grateful to the Director and HODs of the Physical and material chemistry division for providing access to various instrument facilities at NCL. I sincerely thank the staff of the library, the student academic office, and all other administrative offices for their support and cooperation.

I owe my most enormous gratitude to my family, who kept me away from all the stress and let me pursue my dream freely. My grandfathers, who imbibed this scientific curiosity in me. My amazing grannies, who have been the audience and fans of my countless mock presentations. Your curious attitude towards my work makes me thrive for more. Mom, Dad, Saksham, I could not have done it without you. Thanks for being a great listener Saksham. Chacha, Chachi, mausi, mausaji, Mama, and Mami, thanks for cheering me up whenever I needed it. I am also indebted to my cousin Abhimanyu for providing me with a home-like experience in Pune. I feel grateful to have my mami, Mrs. Dipti Jain by my side at every lag of my Ph.D. She supported me both academically and non-academically. This list would be incomplete without mentioning my cousins. Thanks for being there.

Gaurav, as you say," We have grown together in life, in research" thanks for providing all those inaccessible research papers and being available for a pep talk at any time of the day. Kanika, no words can ever be enough to thank you. You, Gaurav, Subashree, and Sachin have lived my Ph.D. with me. You are not just my friends, you are my family.

My constant video calls with my gang in Jaipur: Neha, Abhinav, Mukund, Ruchita, Mrigank, Rupa, Arpita, Jayshree, and Prakhar, Silvi helped me sail through my Ph.D. Finally, you all can stop asking, " Arey teri Ph.D. kab khatam hogi, ghumne jana hai".

Disha, Asha, Gayatri, and Dr. Summi, you are the best roommates one could have ever asked for. Kanika and Disha, thanks for the impromptu trips.

Kalika, Pushkar, Dr. Aditi, and Dr. Vishal, I met you in the final year of my Ph.D. You were there for me each day, and somehow, you easily managed my anxiety attacks. Aditi and Vishal, your tips have been precious for me.

Divya Patni

List of Figures

Synopsis Report

Introduction

Dysregulation and aggregation of TAR DNA binding protein (TDP-43) under various cellular stresses is the key feature of TDP-43-associated proteinopathies.[1–3] The two most common neurodegenerative disorders associated with the TDP-43 include amyotrophic lateral sclerosis (ALS) and frontotemporal lobar degeneration (FTLD).[4] It has been depicted that 90% of the disease conditions arise as a result of various stresses experienced by the cells during their lifetime. In contrast, only 10% of the disease happens due to familial inheritance.[5] This suggests that environmental stress plays an important role in the aggregation of TDP-43. Different studies have studied the role of different domains of TDP-43 in aggregation.[6–9] RRM domains of TDP-43 have been shown to sense various stresses and undergo amyloid-like aggregation.[10–12] Since RRM domains are the primary functional domains of TDP-43, it is crucial to understand how alterations in this crucial structural and functional domain lead to aggregation. Moreover, recent solid-state NMR and X-ray studies on the aggregates of TDP-43 have highlighted the crucial role of RRM domains in the formation of the aggregates.[10,13] It thus becomes interesting to understand the thermodynamic and molecular basis behind the stress sensing by the RRM domains of TDP-43 (a.a. 97-261; called TDP-43^{tRRM} hereafter) and the concomitant formation of aggregates. Advancement in understanding the aggregation mechanism will translate into the deduction of new factors which help in its regulation. This knowledge could also be used to deduce therapeutic strategies which could be exploited to curb the aggregation.

Statement of problem

The presence of misfolded protein assemblies has been a hallmark across neurodegenerative diseases. One such set of disorders is TDP-43 proteinopathies. Lack of understanding of the thermodynamic and molecular basis behind protein aggregation involved in ineluctably fatal TDP-43 proteinopathies has been a daunting reality of biomedical research. This knowledge gap has proven a bane for the development of efficient inhibition strategies for these neurodegenerative disorders. Recent studies postulate the simultaneous involvement of different mechanisms for the disease onset under different stress conditions. The different mechanism forms different noxious species, which demands the development of inhibition strategies targeting

different aspects of aggregation. In this regard, a thorough and improved understanding of aggregation and its regulation is crucial for the development of effective drugs against TDP-43 proteinopathies.

Objectives

The following questions have been attempted in the present thesis:

1. How does TDP-43^{tRRM} sense starvation stress at the molecular level? How can it be regulated?
2. Are the folding and aggregation energy landscape coupled?
3. What is the thermodynamic basis behind the amyloid-like aggregation of TDP-43^{tRRM}?
4. How does the thermodynamic destabilization of TDP-43^{tRRM} drive their amyloid-like aggregation?
5. How does the natural ligand binding partner modulate the energy landscape of folding and aggregation?
6. What are the mechanistic pathways/strategies employed by the natural ligand-binding partner? What are the end products of their interaction with proteins?
7. Can natural ligands divert the flux to more native-like species instead of amyloid-like aggregates?

Methodology

The TDP-43^{tRRM} is shown to undergo aggregation under different stress conditions. However, the molecular and thermodynamic basis of stress sensing by the protein is not known. To study this, we exposed TDP-43^{tRRM} to low pH stress conditions. We have probed the structural and thermodynamical characteristics of TDP-43^{tRRM} under various pH conditions using a battery of spectroscopic tools like fluorescence spectroscopy and circular dichroism. We performed systematic mutations on TDP-43^{tRRM} and characterized the final conformations to identify the critical amino acid residue responsible for the aggregation trigger. We also studied the impact of ss$(TG)_6$ on the stability of TDP-43^{tRRM} under various pH conditions. Further, we employed microscopic techniques to study the coacervates formed under different concentrations of protein and ss(DNA) and tuned environmental conditions to study the interactions important for coacervation. This helped us understand the aggregation trigger and its regulation by employing

different factors like mutations and nucleic acid binding. We also understood that the TDP-43^{tRRM} could achieve different fates under different solution conditions.

Conclusions

The results of the working chapters are discussed as follows:

Chapter 2: In this chapter, using a range of spectroscopic probes, we demonstrated that TDP-43^{tRRM} senses the low pH stress and undergoes a pH-dependent transition from the native state to β-sheet rich form (β form). The β form has disrupted tertiary structure and is oligomeric in nature. ThT assay and TEM image suggested that the β form possesses an amyloid-like protofibrillar structure. The midpoint of transition had a pKa value of ~4.0, which suggested that the ionization (protonation) of a buried amino acid residue with a similar pKa value might be the gatekeeping factor in stress sensing. We systematically mutated three amino acids (D105, H166, and H256) with pKa values in the targeted range to neutral amino acids (D105A, H166Q, and H256Q) to inhibit the protonation of the residues. We observed that H166Q abolishes the aggregation of TDP-43^{tRRM} by forming a molten globule evident by the intact native-like secondary structure but broken tertiary structure under low pH stress conditions. Therefore the protonation-deprotonation switch of histidine 166 of the TDP-43^{tRRM} is coupled to aggregation.

Chapter 3: In this chapter, by employing thermodynamic stability measurements, we argue that TDP-43^{tRRM} experiences pH-dependent changes in its stability. It remains maximally stable in the pH range of 6.5-8.0, below which stability decreases becoming minimum at pH 5.0. Destabilization of the TDP-43^{tRRM} at pH 5.0 also disrupts its tertiary structure. The destabilization makes TDP-43^{tRRM} prone to aggregation, as evidenced by the increased misfolding to β form below pH 5.0. We investigated the effect of the ss(TG)$_6$ binding partner on the thermodynamic stability of TDP-43^{tRRM} and observed that binding to ss(TG)$_6$ stabilizes TDP-43^{tRRM} under all pH conditions tested. We further observed that the ss(TG)$_6$ binding does not allow TDP-43^{tRRM} to access the aggregation energy landscape under low pH stress and instead keeps the secondary and tertiary structure of the TDP-43^{tRRM} intact, thereby regulating its aggregation.

Chapter 4: In the final working chapter, we noticed that the ss(TG)$_6$ can direct the flux of TDP-43^{tRRM} to various states depending on its concentration. We observed ss(TG)$_6$-TDP-43^{tRRM} can undergo complex coacervation to protein-rich dense phase and soluble and monomeric light phase

under low pH stress conditions. In contrast, free TDP-43^{tRRM} undergoes aggregation to misfolded β form. The two phases were found to be in equilibrium with one another. The onset of coacervation depends on the concentration of the ss$(TG)_6$ and TDP-43^{tRRM}, as well as their ratio. Furthermore, the coacervates appeared spherical (1 μm – 5 μm) under the DIC microscope. FRAP analysis suggests that the dynamics of the coacervates are rigid as they fail to exchange the TDP-43^{tRRM} with the solution under the studied time range. We also observed that environmental conditions like temperature, pH, and salt could tune the equilibrium between the dense and the light phase. We observed that the hydrophobic and charge-charge interactions are crucial for the formation of coacervates, as evident upon tuning the environmental conditions. Nevertheless, we report an essential observation that competition exists between aggregation to β form and complex coacervation under low pH stress conditions. In the presence of its specific binding partner, TDP-43^{tRRM} senses pH stress and undergo coacervation, preventing its irreversible aggregation to β form. We suggest that the complex coacervation could be an adaptive strategy against starvation stress to direct the flux from misfolded states.

References

(1) Prasad, A.; Bharathi, V.; Sivalingam, V.; Girdhar, A.; Patel, B. K. Molecular Mechanisms of TDP-43 Misfolding and Pathology in Amyotrophic Lateral Sclerosis. *Front. Mol. Neurosci.* **2019**, *12*. https://doi.org/10.3389/fnmol.2019.00025.

(2) Neumann, M.; Sampathu, D. M.; Kwong, L. K.; Truax, A. C.; Micsenyi, M. C.; Chou, T. T.; Bruce, J.; Schuck, T.; Grossman, M.; Clark, C. M.; McCluskey, L. F.; Miller, B. L.; Masliah, E.; Mackenzie, I. R.; Feldman, H.; Feiden, W.; Kretzschmar, H. A.; Trojanowski, J. Q.; Lee, V. M.-Y. Ubiquitinated TDP-43 in Frontotemporal Lobar Degeneration and Amyotrophic Lateral Sclerosis. *Science* **2006**, *314* (5796), 130–133. https://doi.org/10.1126/science.1134108.

(3) Arai, T.; Hasegawa, M.; Akiyama, H.; Ikeda, K.; Nonaka, T.; Mori, H.; Mann, D.; Tsuchiya, K.; Yoshida, M.; Hashizume, Y.; Oda, T. TDP-43 is a Component of Ubiquitin-Positive Tau-Negative Inclusions in Frontotemporal Lobar Degeneration and Amyotrophic Lateral Sclerosis. *Biochem. Biophys. Res. Commun.* **2006**, *351* (3), 602–611. https://doi.org/10.1016/j.bbrc.2006.10.093.

(4) Zhang, L.; Chen, Y.; Liu, M.; Wang, Y.; Peng, G. TDP-43 and Limbic-Predominant Age-Related TDP-43 Encephalopathy. *Front. Aging Neurosci.* **2020**, *11*, 376. https://doi.org/10.3389/fnagi.2019.00376.

(5) Sun, Y.; Chakrabartty, A. Phase to Phase with TDP-43. *Biochemistry* **2017**, *56* (6), 809–823. https://doi.org/10.1021/acs.biochem.6b01088.

(6) Suzuki, H.; Lee, K.; Matsuoka, M. TDP-43-Induced Death is Associated with Altered Regulation of BIM and BCL-XL and Attenuated by Caspase-Mediated TDP-43 Cleavage. *J. Biol. Chem.* **2011**, *286* (15), 13171–13183. https://doi.org/10.1074/jbc.M110.197483.

(7) Johnson, B. S.; McCaffery, J. M.; Lindquist, S.; Gitler, A. D. A Yeast TDP-43 Proteinopathy Model: Exploring the Molecular Determinants of TDP-43 Aggregation and Cellular Toxicity. *Proc. Natl. Acad. Sci.* **2008**, *105* (17), 6439–6444. https://doi.org/10.1073/pnas.0802082105.

(8) Igaz, L. M.; Kwong, L. K.; Chen-Plotkin, A.; Winton, M. J.; Unger, T. L.; Xu, Y.; Neumann, M.; Trojanowski, J. Q.; Lee, V. M.-Y. Expression of TDP-43 C-Terminal Fragments in Vitro Recapitulates Pathological Features of TDP-43 Proteinopathies. *J. Biol. Chem.* **2009**, *284* (13), 8516–8524. https://doi.org/10.1074/jbc.M809462200.

(9) Zhang, Y.-J.; Xu, Y.-F.; Cook, C.; Gendron, T. F.; Roettges, P.; Link, C. D.; Lin, W.-L.; Tong, J.; Castanedes-Casey, M.; Ash, P.; Gass, J.; Rangachari, V.; Buratti, E.; Baralle, F.; Golde, T. E.; Dickson, D. W.; Petrucelli, L. Aberrant Cleavage of TDP-43 Enhances Aggregation and Cellular Toxicity. *Proc. Natl. Acad. Sci.* **2009**, *106* (18), 7607–7612. https://doi.org/10.1073/pnas.0900688106.

(10) Agrawal, S.; Kuo, P.-H.; Chu, L.-Y.; Golzarroshan, B.; Jain, M.; Yuan, H. S. RNA Recognition Motifs of Disease-Linked RNA-Binding Proteins Contribute to Amyloid Formation. *Sci. Rep.* **2019**, *9*, 6171. https://doi.org/10.1038/s41598-019-42367-8.

(11) Pillai, M.; Jha, S. K. The Folding and Aggregation Energy Landscapes of Tethered RRM Domains of Human TDP-43 are Coupled Via a Metastable Molten Globule-Like Oligomer. *Biochemistry* **2019**, *58* (6), 608–620. https://doi.org/10.1021/acs.biochem.8b01013.

(12) Zacco, E.; Martin, S. R.; Thorogate, R.; Pastore, A. The RNA-Recognition Motifs of TAR DNA-Binding Protein 43 May Play a Role in the Aberrant Self-Assembly of the Protein. *Front. Mol. Neurosci.* **2018**, *11*, 372. https://doi.org/10.3389/fnmol.2018.00372.

(13) Shenoy, J.; El Mammeri, N.; Dutour, A.; Berbon, M.; Saad, A.; Lends, A.; Morvan, E.; Grélard, A.; Lecomte, S.; Kauffmann, B.; Theillet, F.-X.; Habenstein, B.; Loquet, A. Structural Dissection of Amyloid Aggregates of TDP-43 and its C-Terminal Fragments TDP-35 and TDP-16. *FEBS J.* **2020**, *287* (12), 2449–2467. https://doi.org/10.1111/febs.15159.

Chapter 1

Molecular basis of TAR-DNA binding protein (TDP-43) misfolding in TDP-43 proteinopathies: An energy landscape perspective

1.1 Introduction

Dysregulation and aggregation of TAR DNA binding protein (TDP-43) is the critical feature of TDP-43-associated proteinopathies.[1–3] The most common proteinopathies comprise of amyotrophic lateral sclerosis (ALS) and frontotemporal lobar degeneration (FTLD).[4] ALS is a detrimental, progressive neurodegenerative disorder characterized by the loss of the upper and lower motor neurons, leading to muscle weakness.[5] 90% of cases of ALS occur spontaneously due to environmental factors.[6,7] FTLD is a common form of dementia characterized by personality, behavior, language, and emotional changes.[8–12] Similarly, different TDP-43 proteinopathies, including Parkinson's, Huntington's, and some forms of Alzheimer's disease, have different clinical manifestations. The difference in the clinical manifestation of these disorders could be assigned to the different morphologies of the assemblies and their characteristic distribution pattern throughout the central nervous system (CNS).[13–15] The different morphologies of TDP-43 suggest that the assembly formation depends on environmental conditions, which are different in the different brain and spinal cord regions. Despite the difference, a common link between the TDP-43 proteinopathies is the nuclear clearance and cytoplasmic accumulation of insoluble TDP-43-positive inclusions.[2,3,6,16–19] However, despite intense research, there is ambiguity about what triggers the mislocalization and aggregation of TDP-43 and how it could be regulated.

The majority of the studies have focussed on the role of the C-terminal region in the aggregation of TDP-43. 25-35 kDa fragments of C-terminal are eminent species in ALS-affected brains.[20,21] Recently, a cryo-EM study showed the presence of C-terminal fragments in the aggregates derived from ALS patients.[22] On the other hand, Shodai et al. claimed that the RNA recognition motifs (RRM) of TDP-43 play essential roles in the initial onset of aggregate formation under stress conditions.[23,24] In addition, X-ray and solid-state NMR studies on the aggregates of TDP-43 suggested the crucial role of RRMs in the formation of the aggregates.[25,26] Therefore, it suggests that different domains of TDP-43 are involved in pathomechanism and concomitant formation of the aggregates. These observations raise several important questions. Why is TDP-43 susceptible to stress conditions? How and why do the different domains of TDP-43 sense stress? What are the impacts of various stresses on the structure of TDP-43? What is the role of the different domains of TDP-43 in the aggregation? Do they respond differently to stress? What is the thermodynamic basis of the aggregation? What are its different accessible fates or

conformations under different stress conditions? How are folding and aggregation energy landscape coupled? Can we use the current insights to sculpt the energy landscape in diseased conditions to populate non-pathogenic conformers? As the majority of the disease cases occur due to environmental stress, it would be interesting to understand how the energy landscape of protein folding, misfolding, and function are interrelated and modulated by microenvironmental factors.

Dependence on environmental factors suggests that elucidating the link between these factors and aggregation is essential for a complete understanding of the protein aggregation process. Advancement in understanding different aggregation steps will reflect in the generation of efficient therapeutics. This review explains the role of TDP-43 in various TDP-43 proteinopathies. We discuss the protein folding and aggregation energy landscape, highlight their coupling, and employ our knowledge to discuss the thermodynamic basis of aggregation from an energy landscape perspective. We consolidate the insights that suggest modulation of the energy landscape of TDP-43 by environmental factors. Finally, we discuss various non-native conformers which could result in aggregation, followed by an extensive discussion on how the modulation of the folding energy landscape of protein could help treat protein-misfolding diseases by facilitating folding.

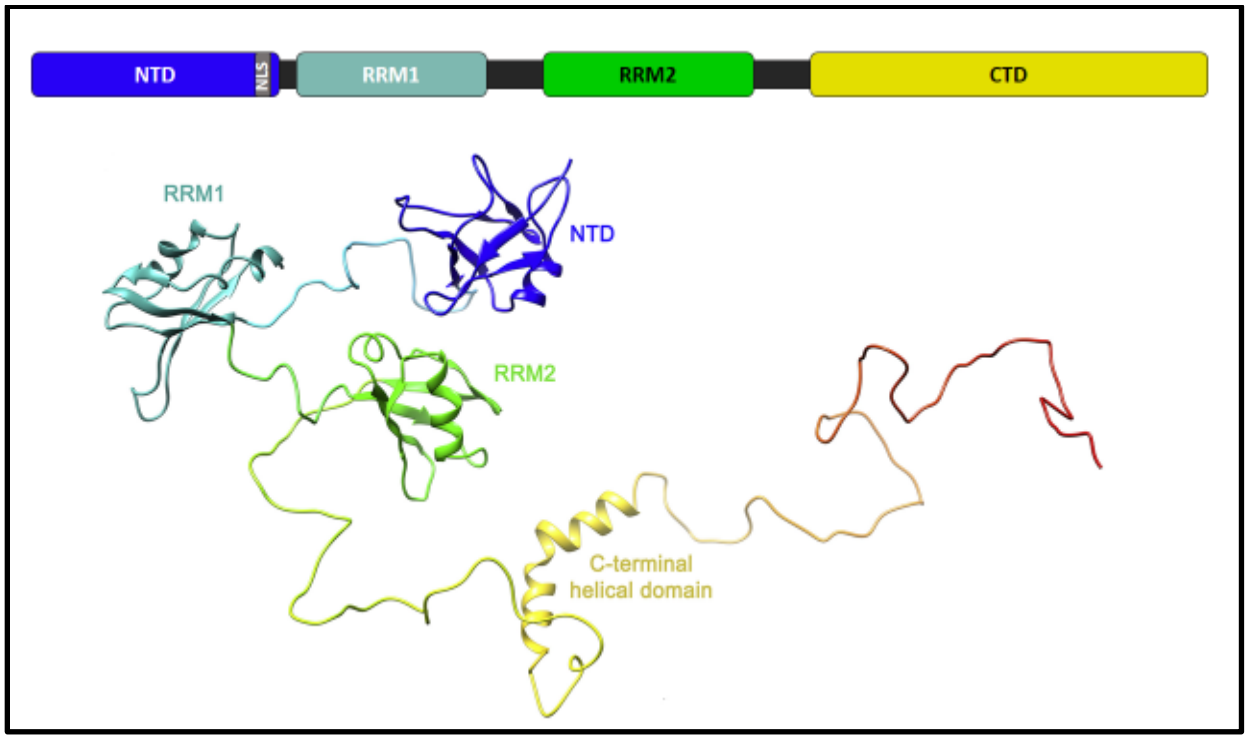

Figure 1.1 Model of full-length TDP-43 (FLTDP-43) after being refined from the SAXS data.[27] The model shows various domains of TDP-43, including NTD: N-terminal domain, tRRM: RRM1 and RRM2, CTD: C-terminal domain. The model represents the first low-resolution X-ray image of the FLTDP-43. The model has been adapted from reference no. 27.

1.2 TDP-43 structure and function

TAR DNA binding protein (TDP-43) was discovered as a repressor of the HIV-I gene expression in 1995 that binds to the transactive response element (TAR) DNA of the viral genome.[28] It is a ubiquitously expressed nucleic acid binding protein coded by the TARDBP gene (1p36.22) belonging to the hnRNP family of proteins.[29] TDP-43 is predominately present in the nucleus but often shuttles to the cytoplasm by active and passive processes to perform some of its functions, including mRNA stability and translation.[30] It consists of 414 amino acids divided among four domains (Figure 1.1). The N-terminal domain (NTD-1-102)[31] is involved in the formation of functional homodimers.[32] The nuclear localization sequence (NLS-82-98) present within the N-terminal domain is involved in the import of the TDP-43 back to the nucleus.[32] Two RNA recognition motifs, RRM1 (106–177) and RRM2 (192–259),[33] the primary functional domain of TDP-43, carry out essential functions related to mRNAs, like splicing, transcription,

and stability. The C-terminal domain (CTD-274–414) encompasses four different regions;[34] a Gly, Aromatic, Ser-rich region (274-317),[35] a hydrophobic region, prion-like glutamine/asparagine-rich (Q/N) region (341–366),[36] and a second glycine-rich region (366–414).[35] CTD is a site involved in protein-protein interactions with proteins such as UBQLN2 and FMRP.[37,38] TDP-43 is also associated with the mitochondria and is involved in the respiratory chain pathways.[39]

1.2.1 N-terminal domain

The NTD of TDP-43 is composed of a well-folded and a disordered region. The residues 1-77 fold to resemble CTD of Axin protein structurally, while the remaining residues 78-102 are chiefly disordered and bind to DNA oligos.[31] NTD facilitates dimer and higher-order oligomer formation.[32,40–42] Accumulating evidence suggests that the TDP-43 is natively dimeric or remains in a monomer-dimer equilibrium.[40,43] Along with association, the NTD is also involved in crucial functions such as splicing.[32] Removal of the first few residues of NTD annihilates the splicing and aggregation propensity of the TDP-43.[43] The NTD also contributes to phase separation. A single critical residue (S48) in NTD aids in the phase separation of TDP-43.[44,45] NTD is also reported to enhance the liquid-liquid phase separation of TDP-43.[46]

Interestingly, NTD is also involved in modulating the aggregation of TDP-43. The dimerization/oligomerization of TDP-43 abolishes the formation of cytoplasmic inclusion of the TDP-43.[32,47] Moreover, NTD harbors NLS, a positively charged region between NTD and RRM. Since NLS is involved in transferring TDP-43 back into the nucleus, any disruption in the NLS could lead to the accumulation of the TDP-43 in cytoplasm and trigger the formation of the cytoplasmic aggregates. For instance, the removal of NLS upon cleavage at the caspase cleavage site at Asp 89 could generate TDP-35 fragments capable of forming more cytoplasmic aggregates.[48] NLS can also be disrupted by initiation at an alternate site at residue 85.[49] These studies are supported by mice studies that have demonstrated that the expression of the ΔC-terminal TDP-43 impairs the concentration of notch1 mRNA and thereby induces age-dependent motor dysfunction.[50] The presented research highlights the dual role played by NTD in the functioning and pathology of TDP-43.

1.2.2 RNA recognition motifs

RRM is one of the most abundant domains present in eukaryotes.[51] These are the primary functional motifs of the protein and are involved in various functions involving RNA, for example, mRNA splicing, stability, and transport.[52] TDP-43 contains two RRMs separated by 14 amino acid long linkers.[33] They associate explicitly with the UG or TG-rich nucleic acids.[53–56] The RRMs of TDP-43 (TDP-43^{tRRM}) bind to RNA in a reverse manner to allow the linker region to participate more extensively with the nucleic acid.[33] RRM1 majorly binds to the nucleic acids, while tethering to RRM2 enhances the binding affinity.[56] Many nucleic acid-binding proteins are involved in neurodegenerative diseases,[57] suggesting a crucial role of the RRM in the aggregation of proteins. Several studies from our and other labs have now suggested the role of these domains in amyloid-like aggregation in stress-like conditions.[23,24,58–60] Also, the RRMs have been shown to determine the final architectural structure of the amyloid-like aggregates.[26] Two regions (166-173[24] and 246-255[23]) in the RRMs have been identified as critical aggregation players. These regions are sensitive to various modifications. These events are discussed later in the manuscript. Interestingly, RRM1 and RRM2 can also independently undergo aggregation, as depicted by MD simulations and in-vitro experiments.[25,61] Five disease-linked disease mutations have been identified in the RRM domain of TDP-43, which include P112H, D169G, K181E, N259S, and K263E.[62–66] These mutations trigger the aggregation cascade driven by various factors. Interestingly, the RRMs also contain caspase cleavage sites. The cleavage at these sites generates toxic fragments. For instance, the cleavage at Arg 208, Asp 219, and Asp 247 can generate CTF-25.[67,68]

In addition to being drivers of aggregation, TDP-43^{tRRM} can also regulate aggregation. Binding to its natural ligands has been shown to increase the solubility and hence decrease the aggregation of the TDP-43.[7,69]

1.2.2 C-terminal domain

The CTD of TDP-43 is required for it to function as a splicing inhibitor at some targets and act as a transcriptional insulator for the mouse sp-10 gene.[70–72] It is a highly disordered region rich in glycine residues.[35] It is also enriched in uncharged polar amino acids, mostly aspargine and glutamine (N/Q).[36] In this way, the CTD of TDP-43 resembles the prion-like domain of other proteins.[73] It is the most studied domain of TDP-43. One of the prime reasons is its known

aggregation-prone nature in-vitro,[74] yeast cells, and in cultured mammalian cells,[21,68,75] which is essential in the pathogenesis of various neurodegenerative diseases. CTD harbors the majority of the ALS-linked mutations and phosphorylation sites and is the prime constituent of the inclusion bodies.[76] As a reason, its presence in the inclusions is often considered the hallmark of neurodegeneration.[2,77,78] Various studies across the globe have highlighted the role of different regions in aggregation. Jiang et al. showed that residues 318-343 are crucial for aggregation.[79] In addition, the amino acids 311-360 of CTD can efficiently form amyloid fibrils, which can act as seeds for the aggregation of the soluble TDP-43.[80,81] Saini et al. suggested that two different peptides (311-320 and 346-355) of CTD are the core aggregation sequences.[82] The mutations (TDP-43^{M337V} and TDP-43^{A315T}) serve as cleavage sites for calcium-dependent calpain enzymes.[83] In addition to aggregation, CTD is also reported to undergo phase separation to liquid droplets,[84] which can function as hotspots for the initiation of self-assembly of protein molecules giving rise to solid amyloid-like aggregates.

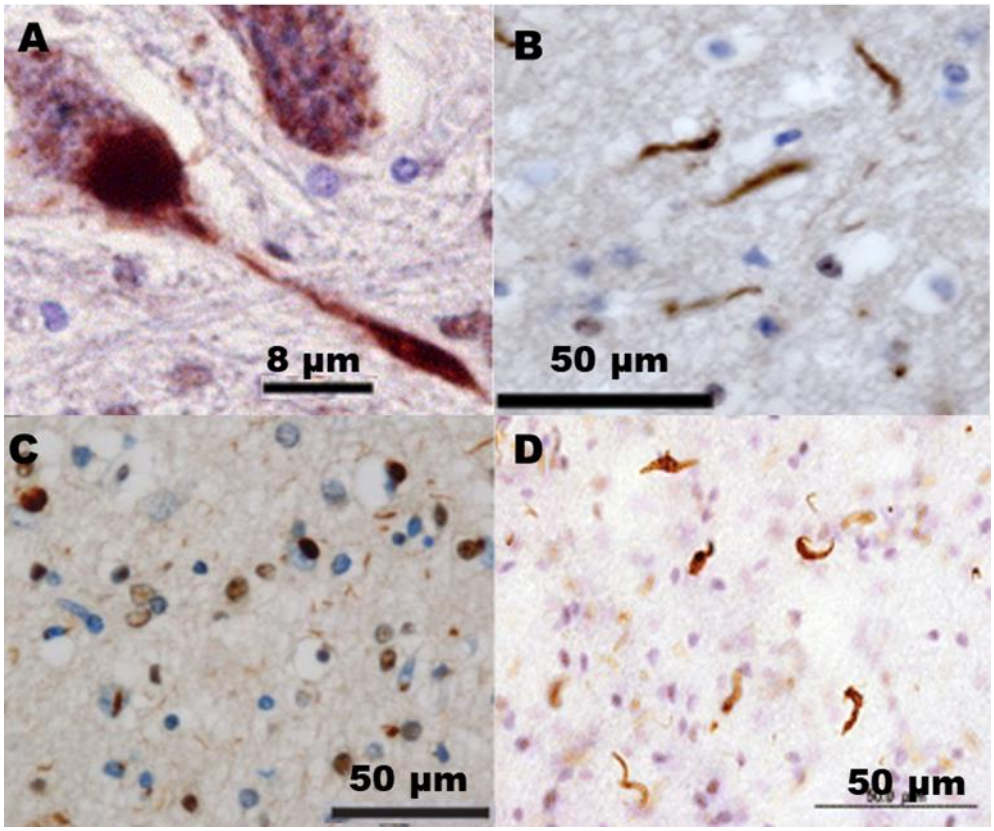

Figure 1.2 TDP-43 plaques in different proteinopathies. (A) TDP-43 in the anterior horn of the lumbar spinal cord of ALS patients.[3] (B) TDP-43 deposition in FTLD-TDP.[2] (C) TDP-43 positive

inclusions in the frontal cortex of Alzheimer's patient.[85] (D) coiled worm-like plaques of TDP-43 in the white matter of the frontal lobe in Guam parkinsonism–dementia complex brains.[17] The images have been adapted with permission, from reference no. 2,3,85, and 17, respectively.

1.3 TDP-43 in neurodegeneration

Two exciting discoveries related to TDP-43 triggered the era of research. Those findings include 1) the discovery that mutation of TARDBP can cause familial ALS and FTLD[76] and 2) the presence of TDP-43 as a major component of the ubiquitinated inclusion bodies present in the cortical neuron in FTD and motor neurons of the ALS cases.[2,3] After these exciting findings, the role of TDP-43 pathology has also been implicated in various other neurodegenerative diseases, including Parkinson's disease,[86] a subset of Alzheimer's disease,[16] Huntington's disease,[87] primary lateral sclerosis,[88] progressive muscular atrophy,[89] Guam Parkinson's dementia complex,[17,19] Parkinson's with and without dementia[18] and most recently, limbic-predominant age-related TDP-43 encephalopathy (LATE).[90] These diseases together are termed TDP-43 proteinopathies. Proteinopathies refers to a group of diseases caused by the accumulation of a specific protein. The protein accumulation occurs in the central nervous system (CNS) in neurodegenerative proteinopathies. The cell type and cellular localization of the accumulation differ in different diseases.[91] In TDP-43 proteinopathies, the deposition of the full-length or fragmented TDP-43 in the ubiquitinated and hyperphosphorylated inclusions in the neuronal cytoplasm is the marker of the transformation of the protein (Figure 1.2).[2,3]

1.3.1 Amyotrophic lateral sclerosis (ALS)

ALS is a progressive neurodegenerative disease caused by the degeneration of the upper and lower motor neurons.[92] The early symptoms include the weakening of the muscles. The muscle progressively weakens further, ultimately wasting away. The aggressive degeneration proves fatal, leading to paralysis, respiratory failure, and ultimately death within 2-5 years of disease onset.[93] Moreover, recent research has also demonstrated alterations in language, social cognition, and apathy as prominent symptoms of ALS.[94] Approximately 90% of ALS cases are sporadic, arising spontaneously with no familial history.

Interestingly, 97% of cases of ALS-affected brains showed the presence of the TDP-43 positive inclusions bodies (Figure 1.2A), making TDP-43 accumulation a prime hallmark of ALS.[6,95] Postmortem studies from the brain of ALS patients also showed the presence of smaller fragments of TDP-43 along with the FLTDP-43 in the detergent-resistant inclusions.[2,96] FLTDP-43 and its C-terminal fragments have been detected in the exosomes of patients suffering from ALS and FTLD.[97,98] Till date, more than 50 different mutations in TDP-43 have been reported as a cause behind ALS, most of which are located in the CTD.[63,74,99–102] Recent accumulating pieces of evidence have listed five disease-associated mutations in the TDP-43^{tRRM}.

1.3.2 Frontotemporal lobar degeneration (FTLD)

FTLD is one of the most common forms of dementia after Alzheimer's.[103] It is a progressive neurodegenerative disorder marked by changes in behavior or language. As the name suggests, the disease impacts the frontal and anterior temporal lobes of the brain.[104] It is caused due to the degeneration of the fork cells and von Economo neurons within the frontoinsular and anterior cingulate cortices.[105,106] Figure 1.2B shows the inclusions present in the FTLD-TDP. FTLD is characterized into three subtypes depending on the type of protein present in the inclusion bodies.[104] The three subtypes are FTLD-tau, FTLD-FUS, and FTLD-TDP-43.[107] TDP-43 positive inclusions are present in 50% of the FTLD cases.[108] FTLD-TDP-43 is further subdivided into four subtypes based on the type of TDP-43 positive structure and its distribution. Type A consists of crescentic or oval-shaped neuronal cytoplasmic inclusions (NCIs) and numerous short dystrophic neurites (DNs). Type B is characterized by the NCIs spread throughout the cortical layer and very few DNs. Type C is marked by the presence of elongated DNs and very few NCIs in the upper cortical layer, while Type D consists of numerous short DNs and frequent lentiform intranuclear inclusions (NIIs).[109] Recently, one more subtype has been included in the classification, Type E, which shows the presence of granulofilamentous nuclear inclusions and abundant grains.[110]

1.3.3 Parkinson's Disease

Parkinson's disease is also a neurodegenerative disease marked by the degeneration of the dopaminergic neurons in the substantia nigra. The degeneration of the neurons disrupts the dopamine level in the body.[111] The association of TDP-43 with Parkinson’s disease is coming to

light with the presence of TDP-43 in Parkinson's cases.[18] In addition, a mutation in the TARDBP gene (N267S) has been associated with Parkinson's disease.[112]

1.3.4 Huntington's Disease

Huntington's disease is a progressive neurodegenerative disease caused due to the expression of the extended polyglutamine tract in the huntingtin protein.[113] Huntington's disease is primarily caused due to the accumulation of the huntingtin protein in the medium spiny neurons of the striatum. TDP-43 is found to mislocalize to the cytoplasm in the superior frontal cortex of the HD brain.[114] Sampedro et al. demonstrated that the apathy was exacerbated in the presence of TDP-43 along with cortical thinning and microstructural degeneration.[115]

1.3.5 Alzheimer's Disease

Alzheimer's is a leading cause of dementia and is caused by the extracellular aggregates of the β-amyloid and intraneuronal tangles of the tau protein.[116] In addition to the plaques and tangles, TDP-43 aggregates have also been studied to contribute to Alzheimer's pathology (Figure 1.2C). Involvement of the TDP-43 is observed in 18-70% of Alzheimer's cases.[16,117–123] Interestingly, TDP-43 fragments of 25 kDa have also been found in the inclusions present in the brain of AD patients.[16] The involvement of TDP-43 leads to an increase in the risk of dementia, and it is known that TDP-43-associated AD pathology increases muscular atrophy and more significant memory loss in patients suffering from AD.[118] The deposition of TDP-43 is subtype-specific, with the highest frequency present in the limbic predominant subtype.[120] Interestingly, almost all the AD brain samples showed the presence of TDP-43 positive inclusions in the later stages of the disease, implying the debilitating role played by TDP-43.[119]

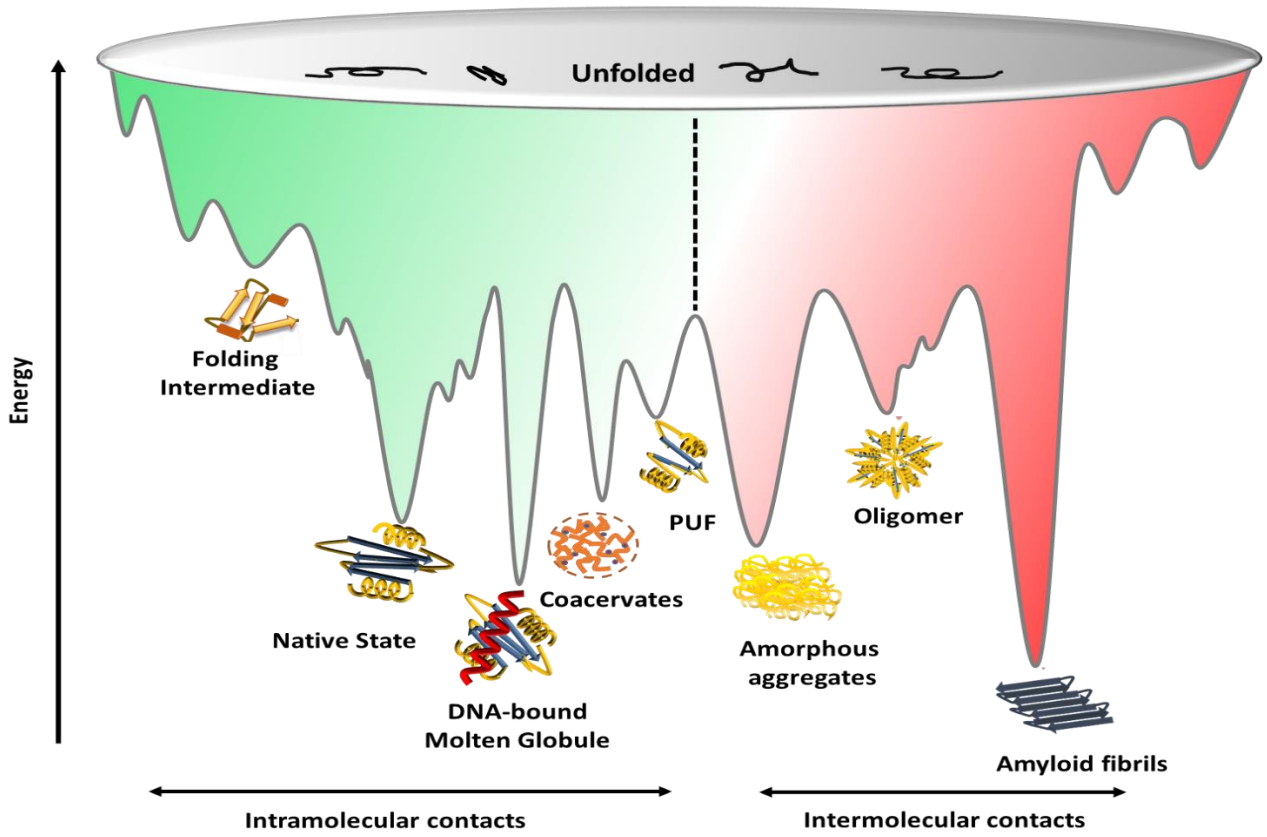

Figure 1.3 Coupled folding and aggregation landscape of the protein. The folding energy landscape (green) shows the progression of the protein from its initial unfolded state (U) to intermediate states and ultimately to its native folded conformation. The folding energy landscape also shows certain different stable conformers like DNA-bound molten globules and coacervates, which are accessed by the protein in different environmental conditions. The formation of partially unfolded forms (PUFs) allows the protein to access the aggregation energy landscape (red), leading to the formation of various misfolded species, for example, oligomers, amyloid fibrils, and amorphous aggregates. The various energy minima on the landscape represent the possibility of formation of different intermediates and their respective stability.

1.4 Understanding proteinopathies onset from energy landscape model of protein folding and aggregation

The previous sections have dealt with how protein misfolding is linked to neurodegenerative disorders. However, misfolded conformation is one of the many conformations a protein can acquire during its lifetime. All the accessible conformations are described by the energy landscape model (Figure 1.3). The energy landscape model suggests that the native conformation is achieved

by an unfolded peptide by following a funnel-shaped energy landscape.[124,125] The native conformation is generally the most stable, with minimum conformational entropy.[126,127] The landscape of the model is unique for a polypeptide under a specific set of conditions. Longer polypeptides (a.a~100) fold through a rougher (rugged) energy landscape.[125] The rugged model postulates that the native conformation is achieved via a series of partially folded intermediates. If the intermediates assist in achieving the native conformation, they are called on-pathway intermediates. On the contrary, off-pathway intermediates trap the polypeptide, thereby not allowing it to access native conformation without significant reorganization.[125] Noteworthily, it is not necessary for the natively folded protein to remain in its folded state. It instead experiences fluctuations in various degrees and timescales. These dynamics are crucial for protein, allowing it to access alternate functional conformers by partial unfolding. However, the partial unfolding can expose aggregation-prone regions, creating a risk of the formation of non-native interactions, which could form oligomers or larger particles which trigger the amyloid cascade.[58] In addition, environmental factors can also trigger a wide array of structural changes.[128] Under physiological conditions, the fully folded conformers are favored, while environmental stress conditions shift the equilibrium towards the partially unfolded forms (PUFs) or fully unfolded state. The PUFs have exposed hydrophobic patches, which make them aggregation-prone. The energy landscape under such conditions will be rough, depicting the presence of certain energy minima which a protein can access depending on its immediate microenvironment.[129]

1.4.1 Modulation of the energy landscape

Figure 1.3 shows a 2D coupled folding and aggregation energy landscape of a typical protein describing various accessible conformers (energy minima) in a set of specific conditions. The depth of the energy minima describes the thermodynamic stability, while the height of the energy barrier separating various energy minima describes the kinetic stability of a protein. Both thermodynamic and kinetic stabilities may be correlated.[130] The thermodynamic and kinetic stabilities determine how easily a polypeptide can access different conformations.[129] The energy landscape model suggests that the interplay of the thermodynamic and the kinetic stability of a conformer determines its population under a set of conditions.[129] The thermodynamic and kinetic stabilities are sensitive to various genetic and environmental parameters like pH, temperature, ions,

post-translational modifications, mutations etc., which could challenge the balance between the native, misfolded, and intermediate states.[131,132] If the native state is destabilized relative to unfolded (U) or PUFs, it will result in a shift in the equilibrium towards non-native U-state and PUFs. Also, if the transition state is not destabilized, it will increase the kinetic accessibility of the U and PUFs. The equilibrium shift from native conformers to non-native conformers has debilitating effects and marks the onset of protein misfolding diseases. For instance, a couple of reports studied the decrease in the thermodynamic stability of the natively folded protein (ΔG_{FU}) is associated with aggregation promotion and, ultimately, disease.[131,133–136]

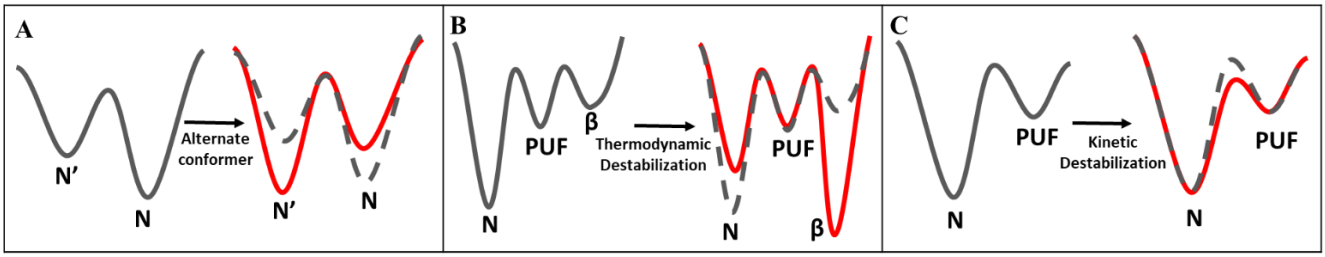

Figure 1.4 Changes in the native energy well of protein. (A) changes in the native conformations. (B) destabilization of the native state. (C) decrease in the kinetic barrier.

1.5 Environmental factors modulating the energy landscape

Some obvious question remains: Which factors cause TDP-43 to divert to a pathological pathway? Which conformers are toxic and non-toxic? What confers the aggressiveness to TDP-43 proteinopathies? It is, therefore, crucial to study different mechanisms by which TDP-43 can aggregate to design suitable drugs against their aggregation.

Approximately 90% of the disease cases are caused due to environmental stresses experienced by the cells during their lifetime.[6,7] These factors modulate the energy landscape such that aggregation-prone species get populated, which promotes aggregation. The aggregation could be triggered by the formation of alternate aggregation-prone conformers, destabilization of the native states, or by providing the energy required for navigation through the energy landscape (Figure 1.4). As a result, the conformation equilibrium shifts towards misfolded states, increasing the danger of aggregation.

The majority of the disease-linked proteins that can sense environmental stress are marginally soluble in the cytosol. These proteins are termed supersaturated proteins. They remain highly sensitive to environmental conditions and can undergo misfolding with mild fluctuations in environmental conditions. TDP-43 has also been studied to be affected by various environmental stresses like oxidation, low pH, temperature etc. The various stresses encountered by the TDP-43 and their effects are listed below:

1.5.1 Post-translational modifications (PTMs)

PTMs are covalent chemical adducts to the primary structure of proteins that changes their chemical composition.[137] Various PTMs have been observed in the case of ALS and FTLD-TDP, including acetylation, phosphorylation, ubiquitination, and SUMOylation.[2,3,138,139] PTMs are the one important environmental change that can modulate the energy landscape,[140,141] thereby bringing conformational changes in the protein molecules.[141] PTMs are generally involved in the regulation of protein functions, and their dysregulation is implicated in various diseases.[142] The most common types of PTMs of TDP-43 are ubiquitination and phosphorylation.[2,3,143,144]

Phosphorylation is involved in many aspects of cells, including the splicing function, nuclear localization, aggregation, and neurotoxicity of TDP-43.[83,145–148] Either casein kinases mediate the phosphorylation (CK1/2)[144] or glycogen synthase kinase (GSK). Importantly, phosphorylation introduces a -2 charge on the protein molecule under physiological conditions, which could introduce electrostatic perturbation, thereby affecting the free energy landscape of proteins.[149,150] The modulation triggers conformational changes in the protein, which may or may not be more stable than the unmodified state. It is speculated that the phosphorylated TDP-43 becomes more prone to aggregation, directly impacting the disease onset (Figure 1.7). There are 64 potential phosphorylation targets in the TDP-43, out of which phosphorylation of S379, S403/404, and S409/410 have been shown to occur in brain samples of patients who have ALS and FTLD.[143,144,151]

Another important PTM modulating the energy landscape is ubiquitination. The E3 ubiquitin ligase is shown to ubiquitinate TDP-43 via the ubiquitin lysines K48 and K63. This facilitates the cytoplasmic accumulation of TDP-43. RRM1 contains four different ubiquitination sites (K102, K114, K145, and K181), which could assist in the self-assembly of TDP-43.[152] Moreover,

mutation of these sites is shown to decrease the cytoplasmic accumulation of the TDP-43 thereby implicating ubiquitination in modulating TDP-43 aggregation.[152] Protein destabilization due to site-specific ubiquitination has been studied to dictate protein degradation.[140] Interestingly, Hagai and Levy presented that the effect on the thermodynamic stability of the protein depends on the type of ubiquitin moiety and the modification site.[153]

1.5.2 Oxidative stress

Oxidative stress is a phenomenon caused as a result of excessive reactive oxygen species formed during physiological and pathological processes.[154] Studies suggest that oxidative stress is a prime factor in ALS disease progression and pathogenesis.[155] Environmental stress like smoking, physical stress, chronic brain injury, and agricultural chemicals generates oxidative stress at the cellular level.[155] Oxidative stress mediates pathology by various routes. The prime targets of oxidative stress are the thiol group of cysteine residues. For instance, oxidative stress promotes disulfide bond linkage of the cysteine residues, which promotes aggregation.[156] Cohen et al. showed that C173- C175, and C198-C244 are involved in the formation of disulfide-linked aggregates.[157] It is speculated that oxidation might stabilize the partially unfolded intermediates exposing the aggregation-prone region (166-173 in RRM1 and 246-255 in RRM2) leading to aggregation.[156] Oxidative stress also favors the SG formation of TDP-43.[158] Neuronal studies confirm that induced depletion of glutathione (mimic of oxidative stress) triggers phosphorylation of TDP-43 at Ser 403/404 and Ser 409/410. Furthermore, it increased the fragmentation of TDP-43 to 25 kDa fragments with enhanced cytoplasmic mislocalization.[159] Fragments of 35 kDa were also formed due to caspase activation due to oxidation stress.[160] Furthermore, TDP-43 aggregation and global mitochondrial imbalance trigger a cascade that enhances TDP-43 aggregation.[161] These results signify that oxidative stress modulates the equilibrium between native and alternate conformers and triggers aggregation.

1.5.3. Thermal stress

An increase in the temperature is known to accelerate the protein unfolding.[162] The energy landscape evolves with temperature change. The temperature fluctuations modulate the strength of the hydrogen bond and the hydrophobic interactions.[163,164] Moreover, the temperature increase destabilizes the low-energy ensembles and populates the high-energy states.[165] TDP-43 is studied to undergo reversible nuclear aggregation upon experiencing heat shock mediated by its C-terminal domain. The aggregated protein loses its ability to interact with its binding partner, therefore impacting its function.[166] In addition, RRM domains of TDP-43 are also shown to undergo amyloid-like aggregation in the presence of thermal stress.[167] Increased misfolding at elevated temperatures also increases the burden on protein quality control, resulting in the accumulation of misfolded protein molecules.[168]

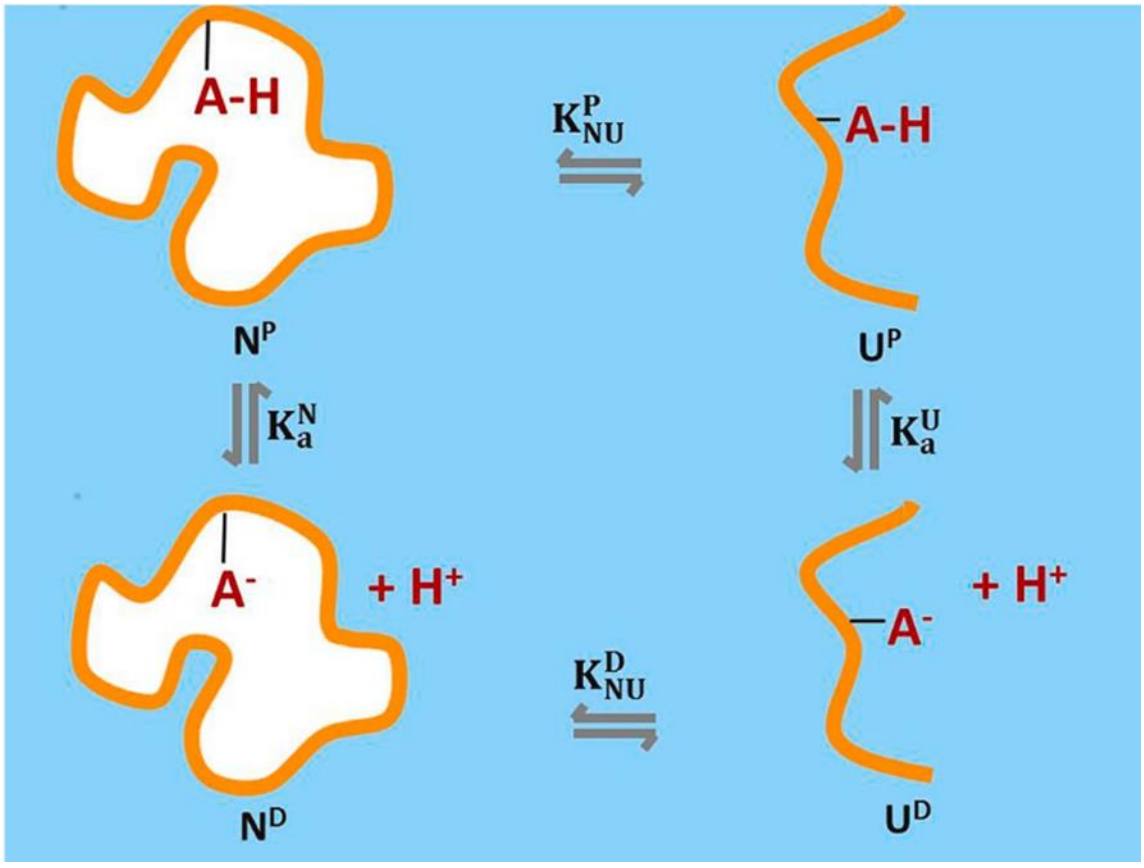

Figure 1.5 The coupling of the ionization of a buried ionizable amino acid residue with the folding / unfolding cycle of proteins. The orange lines in the figure represent the protein backbone. A-H is the protonated acidic ionizable residue in its neutral form buried inside the core (white patch) of

the fully folded protein and exposed in its unfolded counterpart. A^- refers to the deprotonated / charged state of the acidic residue. N^P and U^P, respectively, refer to the folded and unfolded state of protein when the ionizable amino acid is protonated and K_{NU}^P is the equilibrium constant between them. N^D and U^D are, respectively, the folded and unfolded conformations of the protein when the ionizable amino acid is deprotonated / charged and K_{NU}^D refers to their equilibrium constant. K_a^N is the equilibrium acid dissociation constant between the charged and neutral states of the native protein. Similarly, the acid dissociation constant for the equilibrium between the charged and the neutral states of the unfolded protein is represented by K_a^U. The image has been adapted from reference no. 169.

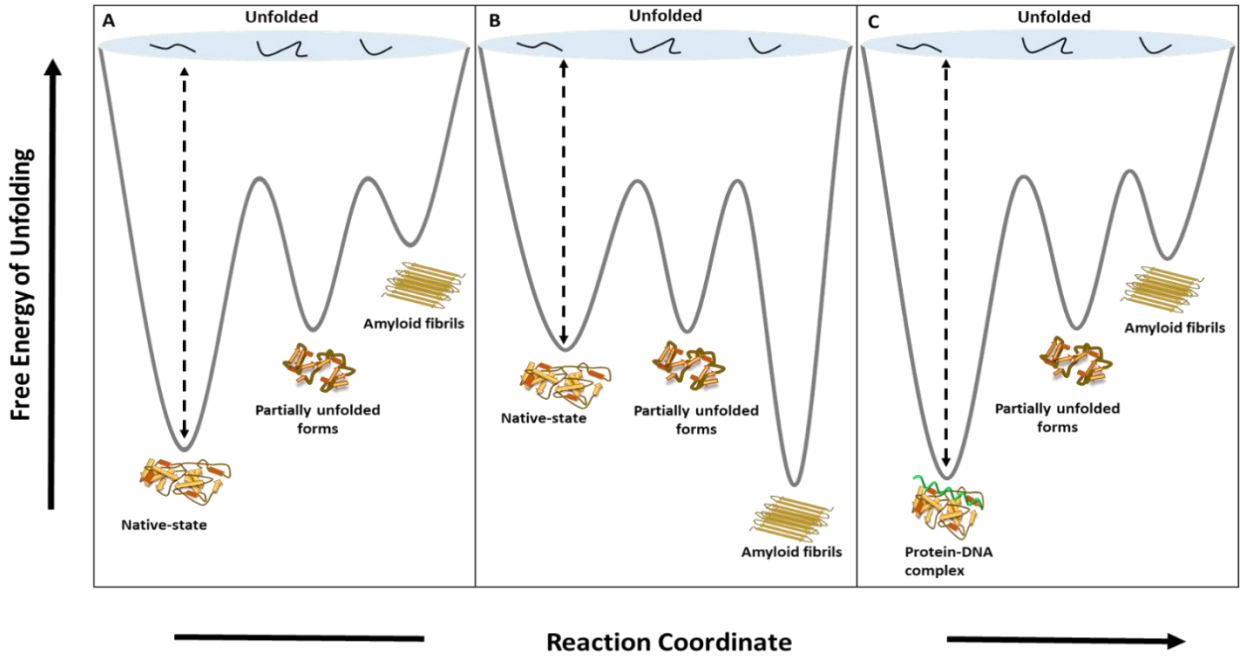

Figure 1.6 Free energy landscape model of TDP-43^{tRRM} in (A) native conditions (pH 7.5), (B) low pH stress conditions, and (C) $ss(TG)_6$ bound in native and stress conditions. The image has been adapted from reference no. 170.

1.5.4 pH stress

pH stress modulates the electrostatics of the protein molecule.[169] A buried ionizable residue can titrate differently in the folded and unfolded conformation and, therefore can affect the thermodynamic stability of the folded and unfolded protein differently, giving rise to pH-dependent stability (Figure 1.5). The pH modulation destabilizes the native state of the protein, allowing it to access the aggregation energy landscape (Figure 1.6 A,B).[170] Very recently, Slek et al. showed pH decrease (acidosis) in the cellular model of TDP-43 proteinopathy and fibroblasts

of the ALS patients, which increased the aggregation and cytoplasmic localization of TDP-43.[171] A previous in-vitro study from our lab established that the TDP-43^{tRRM} senses pH-stress and triggers the protonation of a critical amino acid residue (H166). The amyloid-like aggregation of TDP-43^{tRRM} follows this event.[60]

1.5.5 Mutations

Approximately 50 mutations have been studied in the TARDBP gene,[172] majorities of which lie in the CTD,[78] which could play a role in the pathogenesis of TDP-43. The mutations could affect different pathways, which could trigger pathogenesis (Figure 1.7). Kabashi et al. identified eight different mutations in the TARDBP gene, out of which five were found to increase the phosphorylation tendency of the protein.[63] Interestingly, Barmada et al. suggested increased cytoplasmic mislocalization as a cause of increased toxicity due to mutations.[173] A single point mutation in the NLS (A90V) disturbs the nucleocytoplasmic shuttling of TDP-43 and has been shown to be mislocalized to the cytoplasm.[174] Another study claimed enhanced neurotoxicity as a result of a single mutation (A315T).[175] M337V mutation is reported to increase the fragmentation of TDP-43, leading to cytotoxicity.[100]

Thermodynamically, mutations to the protein sequence have been notoriously known to affect protein folding, stability, and dynamics. Research on the NTD of TDP-43 and its associated mutations (L27A, L28A, and V31R) suggested that the mutations disrupt the conformational stability and dynamics of the NTD and populate the unstable metastable states. The predominance of unstable states results in the early unfolding of mutants.[176] Conversely, point mutations in the prion-like domain or CTD of TDP-43 (TDP43^{G298S}, TDP43^{Q331K}, and TDP43^{M337V}) increase the stability of the mutant variants.[177] In addition, disease mutations in RRM domains (D169G and K263E) also have higher stability than the wild-type variant.[178,179] D169G is also more prone to caspase3 cleavage, resulting in the formation of 35 kDa fragments. The aberrant increase in stability allows the protein to skip the degradation pathway and accumulate as aggregates in the cell. Interestingly, in one of our previous studies, we established that the mutation of a critical ionizable amino acid residue, histidine located at 166 position to a neutral amino acid glutamine, prevents the amyloid-like aggregation of TDP-43^{tRRM}.[60] We propose that the protonation of the histidine residue upon the partial unfolding of the protein triggers the amyloid cascade. We observe

that the glutamine mutation forms an alternate conformer (native-like molten globule) that does not aggregate under stress conditions. We speculate that the changes in the conformation increase the kinetic barrier and inhibit aggregation.

In addition, ALS-associated mutations have been reportedly shown to increase mitochondrial localization of TDP-43.[39,180] The impairment causes mitochondrial dysfunction and hence neurodegeneration.[39]

1.5.6 Nucleic acids

TDP-43 is a nucleic-acid binding protein and is involved in many essential functions in the cell. The most widely accepted model of ligand binding suggests that the ligand interacts with the protein conformer to form an energetically favorable complex (ligand-protein complex), shifting the population towards the favored conformer.[181–184] The increased stabilization prevents the misfolding of the protein molecule. We have quantitatively shown that the thermodynamic stabilization of the native state of TDP-43^{tRRM} in both native and stress-like conditions by natural binding partners prevents its amyloid-like aggregation (Figure 5).[170] The protein-DNA complex formed is even more stable than the native state and does not allow the formation of the partially unfolded forms in both native and stress-like conditions, thereby preventing TDP-43^{tRRM} from accessing the aggregation energy landscape. Therefore, stabilization of the native state holds immense potential in therapeutics.

However, in the cases of failed ligand binding, the bound conformer is not favored, which might populate the aggregation-prone species under stress conditions, which could trigger the aggregation (Figure 1.7). Mutations that could hamper the nucleic-acid binding could lead to the accumulation of TDP-43 in the nucleus and the cytoplasm. One such residue identified by Chen et al. is K181E, located in the RRM1 domain. The positively charged lysine residue binds to the negatively charged guanine nucleotide, assisting in RNA binding. Substitution by negatively charged glutamate residue increases electrostatic repulsion between RNA and TDP-43, thereby decreasing the affinity of TDP-43 and RNA. Acetylation of K181 is also reported to decrease nucleic-acid binding. Additionally, K181E and K263E have a higher tendency to phosphorylate and form intra-nuclear aggregates. Moreover, K181E aggregates were able to recruit WT-TDP-43 interfering with RNA processing. These results suggest the fatal role played by the mutations in proteinopathies.[62]

1.6 Toxic conformers related to pathogenesis

TDP-43 forms heterogeneous assemblies in diseased neurons. Electron microscopy images suggest that the aggregates are either filamentous[98,144] or granulo-filamentous with diameters of 10-15 nm. On the other hand, a separate study observed heterogeneous spheroidal or elongated and coiled, short proteinaceous filaments of TDP-43 which were 5–8 nm thick and 30–50 nm long.[14] In addition, TDP-43 is also observed to form non-fibrillar aggregates inside the affected brain tissue of FTLD-TDP patients.[185]

Generally, the aggregates of protein are classified into amyloid and amorphous.[186] Amyloid aggregates are elongated aggregates of protein characterized by ordered, cross β-rich structures. They bind to thioflavin T (ThT) dye and showcase specific optical behavior.[186] The amorphous aggregates are non-ordered and do not bind to ThT dye.[186] Preliminary studies suggested that the aggregates of TDP-43 are non-amyloid (amorphous) in nature.[74,187] Following studies suggest that the aggregates present in the spinal cord and not in the brain of ALS patients are ThS positive, confirming their amyloid-like nature.[188] However, a recent study on the aggregates harvested from the brain samples of the patients presents the amyloid nature of the aggregates,[22,189] where TDP-43 forms a double spiral-shaped fold.[22] In vitro studies on CTD and RRMs also demonstrated the ability to form amyloid fibrils in vitro.[25,26,58–60,167,190] The amyloid fibrils formed from the CTD were able to seed aggregation of the WT TDP-43 in cells.[191] The difference in the consensus on the nature of aggregates depends on how the aggregates are analyzed in the study. The different morphologies of the aggregates suggest that various factors determine aggregation.[192]

The following section deals with various assemblies implicated in pathology associated with TDP-43 proteinopathies.

1.6.1 Cytoplasmic inclusions

Insoluble cytoplasmic inclusions of TDP-43 have been a unifying feature of various TDP-43 proteinopathies.[2] The inclusions in the affected cells suggest that these inclusions could act as an end product of the disease. The cytoplasmic inclusions are higher-order assemblies of various TDP-43 species, forming large, insoluble structures. For example, TDP-35 can form cytoplasmic

inclusions and can also sequester TDP-43 with the help of RNA.[193] The presence of different species makes it unclear as to which species is responsible for toxicity.

The exact role of TDP-43 cytoplasmic inclusions in toxicity is debated. Various studies exist which confirm the toxic nature of the TDP-43 inclusions. Nonaka et al. reported that when cells transfected with WT TDP-43 are treated with inclusions from ALS and FTLD patients, they show an increase in cell death.[98] Transfection studies of the pre-formed TDP-43 inclusions in the murine neuroblastoma cells showed increased reactive oxygen species and apoptotic caspase-3 activation.[195] Similarly, the TDP-43 extracts from the FTLD-TDP patients triggered the pathology in the CNS of the infected mice.[195,196] However, some studies suggest that the mislocalization of the TDP-43 to cytoplasm rather than inclusion formation causes toxicity.[173] Another study demonstrated that the deposition of the inclusions in the cytoplasm instead acts as the protective mechanism employed by the cells to store the inert species.[147]

1.6.2 TDP-43 oligomers

Oligomers refer to the soluble intermediate state between the dimeric protein and the multimers, which can provide a scaffold for further protein aggregation.[197] In addition to acting as a template for aggregation, oligomerization might also interfere with the RNA/DNA binding function of the TDP-43, which may affect its normal function.[198] Montalbano et al. have demonstrated the presence of the TDP-43 oligomers in the brain samples of ALS, FTLD, and Alzheimer's patients, signifying their presence in the diseased conditions.[199] Fang et al. have also demonstrated the presence of the TDP-43 oligomers in FTLD-TDP patients.[198]

TDP-43 oligomers purified from the spinal cord extracts induced cytotoxicity, specifically in the human motor neurons.[200] TDP-43 oligomers have also been repeatedly shown capable of seeding and worsening the aggregation of other disease-associated proteins. For example, injection of oligomeric TDP-43 in the brains of APP/PS1ΔE9 mice showed inflammation and increased Aβ associated phenotype.[201] TDP-43 also promotes cross-association of TDP-43 oligomers with β-amyloid and tau oligomers in-vitro.[199] In another research, full-length TDP-43 was shown to undergo oligomerization which could further seed the oligomerization of Aβ.[198] The hippocampal injection of the oligomeric TDP-43 led to neuronal loss in the mouse cells.[198] TDP-43 oligomers

have been demonstrated to showcase seeding activity and intercellular spreading of oligomers.[202] These results collectively suggest that the TDP-43 oligomers could play a role in proteinopathies, and targeting them in therapeutics could lead to the discovery of potent drugs. However, care should be taken not to clear TDP-43 oligomers entirely. The oligomers are functionally important physiologically.[203] Therefore, their removal might hamper their normal functioning.

1.6.3 Intranuclear inclusions

Intranuclear inclusions are a rare kind of species, predominately associated with FTLD-U.[204] Nuclear aggregates could result from stress like heat shock,[166] overexpression of TDP-43 fragments,[205] or disruption of localization of TDP-43.[206] In addition, mutations in the progranulin (GRN) and VCP gene have been associated with TDP-43 positive intranuclear inclusions in the FTLD-TDP.[109,204,207,208] Knockout of the VCP gene leads to disruption of the protein degradation pathway culminating in the aggregation of TDP-43, setting a mechanistic link between the VCP gene and TDP-43 aggregation.[209,210]. The toxicity of neuronal aggregates is associated with the loss of function upon aggregation in the nucleus.

Interestingly, the intraneuronal aggregates can exist as both granular and fibrillar structures, with the length of fibrils extending to a mean value of 18 nm.[211] The nuclear aggregates formed from the over-expression of TDP-43 fragments are reported to form punctuate structures ranging from 4 μm to 7 μm.[205]

Apart from the nucleus, aggregation of TDP-43 has been shown in adjacent structures. The exciting finding showing the formation of the TDP-43 inclusions in association with the LeuR domain of the endogenous RGNEF in the micronuclei suggests a mechanism of aggregation in the presence of metabolic stress.[212]

1.6.4 Stress granules

Postmortem tissues of TDP-43 or phosphorylated TDP-43 have been reported to co-localize with SG makers TIA-1/PABP-1/eIF3 in ALS and FTLD patients.[213–216] In addition, the formation of SGs might also be responsible for diseases in cellular and animal models of ALS and FTLD.[217–219] Stress granules (SGs) are primarily transient structures formed as a result of the inhibition of

translation initiation due to drugs or stress response.[220] SGs are formed due to liquid-liquid phase separation driven by either one molecule (simple coacervation) or interactions between two oppositely charged molecules (complex coacervation).[221] Based on the proteome analysis, ~50% of the components of SGs are a subset of RNA-binding proteins.[222] Generally, these granules have liquid-like dynamics and dissolve upon stress removal. However, aberrations such as mutations, continued stress, and disruption of granules removal impair the dynamics of the globules, making them crucibles with high protein concentrations.[223] The slowed dynamics trigger fibrillization, which is hypothesized as one of the pathways for protein aggregation. Several studies have suggested the indispensable role of the RRMs and C-terminal domain, more specifically, residues 216-315[224] or 268-324[160], for the recruitment of TDP-43 into SGs. Interesting studies on the low-complexity domain CTD of TDP-43 report that phase separation paves the path for amyloid-like aggregates.[225–227] The droplets were shown to accelerate the amyloid-like aggregation of fragments.[228,229] Zhang et al. presented the repetitive formation of stress granules capable of forming aggregates, providing a mechanistic link between the granules and aggregation.[230] Ding et al. claimed that the SG containing mutant TDP-43 does not disassemble after 24 hours of stress removal, thereby acting as a seed for aggregation.[231] Recent work on full-length TDP-43 also showed the maturation of the previously liquid globules upon persistent stress.[225]

1.7 The dual role of stress granules

Stress granules are generally formed in response to cellular stress, thereby employing a protective role.[232–236] These granules store the untranslated mRNA and associated proteins to save the energy demand of the cell.[232,237–239] Conventionally, the SGs are entirely reversible and can occur physiologically in the nucleus or by induced stress in the cytoplasm. However, these structures could have a range of dynamics, from fast dynamics in the case of the liquid-like interior to slow dynamics in the solid-like interior.[240–244] The pathogenic nature of SGs is a result of the altered dynamics. It is suspected that the mutations and aging of neurons disrupt the dynamics of the stress granules leading to their reduced disassembly.[177,245]

However, in contrast to the established literature, we demonstrated that the phase separation of TDP-43^{tRRM} in the presence of ss(DNA) inhibits its amyloid-like aggregation, emphasizing its protective role (Chapter 4). By multiparametric analysis, we demonstrated that the phase

separation of TDP-43^{tRRM} in the presence of ss(DNA) is driven by electrostatic and hydrophobic interactions. Another study from Staderini et al. reported a similar observation, where full-length TDP-43 was studied to undergo phase separation to less dynamic globules inhibiting amyloid-like aggregation.[246] The observation emphasizes the protective role played by the assemblies in inhibiting aggregation.

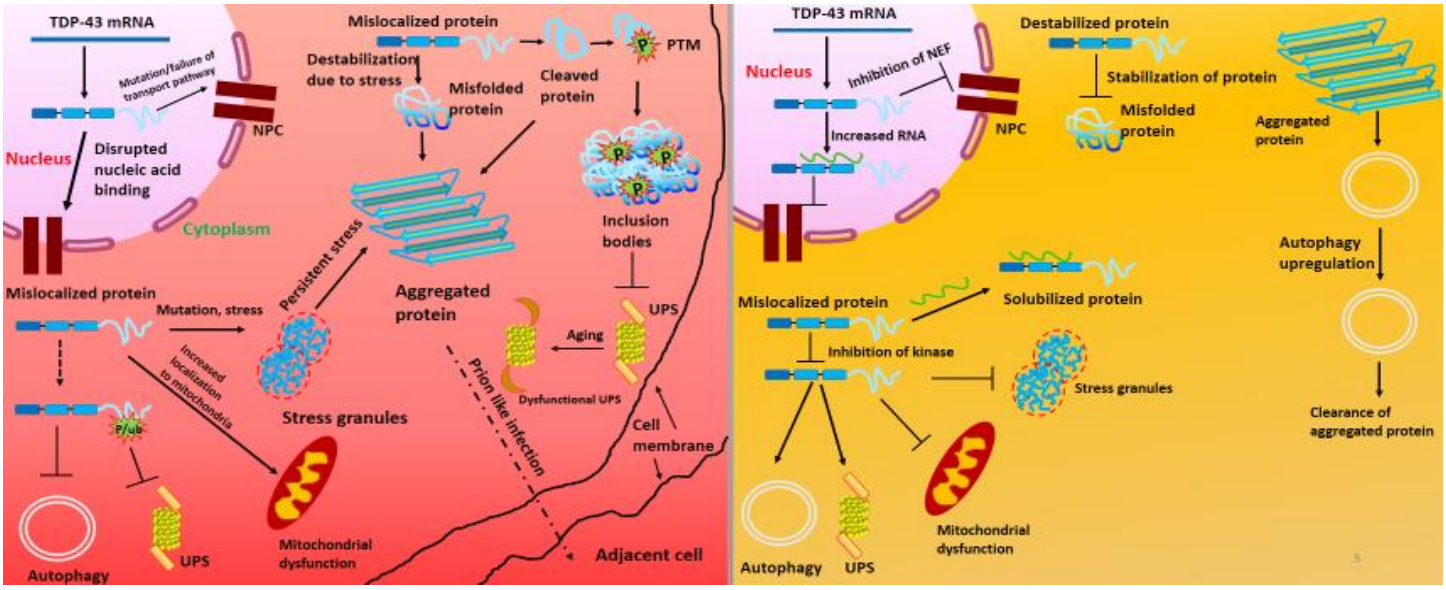

Figure 1.7 Graphical representation of the pathomechanism (left) and the therapeutic strategies (right).

1.8 Therapeutic strategies

Preventing protein aggregation is of paramount importance for treating fatal protein misfolding diseases.[247] Despite decades of extensive research, therapeutic options for TDP-43 proteinopathies are in their infancy.[248] The energy landscape view of protein folding, function, and misfolding has various practical applications in drug discovery. Enhanced exploration of the accessible conformational space of the protein under diseased conditions could prove fruitful in developing the therapeutic strategy (Figure 1.7). We argue that the consideration of the modulation of the energy landscape while optimizing drugs could be helpful in the development of more potent therapeutics. Since TDP-43 proteinopathies are caused due to aggregation of TDP-43, strategies that either target and remove the misfolded/aggregated TDP-43 or prevent their formation hold

immense potential in therapeutic intervention. In this section, we present a few promising strategies which could be considered in therapeutics.

1.8.1 Protein stabilization strategy

One of the strategies that could be considered for treating protein aggregation is the stabilization of the native functional state or other non-pathogenic forms. Protein destabilization has been linked to their aberrant misfolding.[133,134,249–252] A conceptual advantage of the protein stabilization strategy is that stabilizing the native protein conformations prevent the formation of all the non-native conformations, thereby having a mass effect on disease control (Figure 1.7).

The motivation behind the development of this approach comes from human genetic evidence related to the Transthyretin (TTR) protein with the T119M mutation.[253] The monomeric form of TTR is aggregation-prone. However, these T119M subunits get included in the tetramer, thereby increasing the kinetic barrier of the tetramer dissociation.[253–255] The stabilization of the tetramer due to the inclusion of the T119M monomer reduced the number of TTR capable of dissociation, preventing disease onset.[256] Therefore, screening the small molecules that could stabilize the native tetramer by selectively binding to it led to the discovery of tafamidis, which could efficiently delay the tetramer dissociation. Tafamidis was approved in 2011 by the FDA and EMA as a treatment for stage 1 polyneuropathy.[257]

1.8.2 Modulation of phosphorylation

Insoluble inclusions of the phosphorylated TDP-43 are a hallmark of different proteinopathies.[2,3] Neumann et al. have established that the phosphorylation of S409/410 is a common feature of all TDP-43-associated proteinopathies.[143] Different kinases have been studied that phosphorylate TDP-43. The best-studied kinases include protein casein kinase-1 (CK-1),[258] tau tubulin kinase 1 (TTBK1),[259] and cell division cycle kinase 7 (CDC7).[260]

The role of phosphorylation in disease control has always been hotly debated. However, recently Gonzalez et al. have identified that selective inhibition of the CK-1δ could reduce phosphorylation of the TDP-43 in both mouse and human models, thereby increasing the nuclear

presence of the TDP-43.[261] On a similar line, inhibitors of TTBK1 have also been identified recently, which manage to restore the nucleocytoplasmic level of the TDP-43.[262]

Nonetheless, the discovery of inhibitors remains in a very primitive stage, and further trials are required to confirm their efficacy as drugs.

1.8.3 Tuning stress granules

TDP-43 can associate with the SGs however, prolonged exposure to stress may lead to the formation of toxic conformations inside the SGs, leading to neurodegeneration.[263,264] ALS spinal cord tissue has been shown to be enriched with the TDP-43 localized with cytosolic SG markers. Therefore, strategies that could promote SG disassembly or inhibit their assembly could be used in therapeutics. As mentioned earlier, the formation of the SGs is mediated by the phosphorylation of different kinases, for example, c-Jun N-terminal kinase (JNK).[158] One such molecule whose phosphorylation has been associated with SG formation is eIF2α.[265–267] Interestingly, the small molecule N, N′-trans-(cyclohexane-1,4-diyl)-bis-(2-(4-chlorophenoxy)acetamide (ISRIB) has been reported to prevent translational inhibition by eIF2α and is also shown to reduce SG formation in the diseased mice infected with prion.[268,269] It would be great to check the effect of ISRIB on TDP-43 proteinopathies (Figure 1.7). In addition, inhibition of the extracellular signal-regulated kinase (ERK) prevents the formation of the paraquat-induced SG formation.[158] Parker et al. demonstrated that the copper complexes have an inhibitory role in SG formation as they reduce the accumulation of TDP-43 into early SGs in the neuronal cells.[270]

These studies are in their nascent stages; however, they hold promise in developing effective drugs against neurodegeneration.

1.8.4 Gene therapy

Introduction of functional genetic material to the cells, which mitigates the effects of the defective gene is called gene therapy Gene therapy works by replacing the defective gene, silencing the mutant allele, gene editing, or introducing a disease-modifying gene.[271–273] One of the most prominent examples of gene therapy is the administration of the functional SMN1 gene for the treatment of spinal muscular atrophy.[274,275] Alternatively, gene editing comprises of adding,

removing, or altering DNA sequences in a specific manner. Gene editing could prove helpful in removing or adding point mutations to the gene. Gene editing makes use of the endogenous repair pathway, which can be triggered by directed double-strand breaks in DNA (DSBs). The break can be repaired by non-homologous end joining (NHEJ) or native homology-dependent repair (HDJ).[276] Precise DNA DSBs can be introduced by employing engineered nucleases. The most common nuclease is the RNA guide clustered regulatory interspaced short palindromic repeats (CRISPR) and CRISPR-associated system 9 (Cas9) (CRISPR/Cas9).[276] CRISPR/Cas9 has already proved beneficial in the reduction of amyloid β level (implicated in AD) in human fibroblasts.[277] The G4C2 repeat in the cC9orf2 (implicated in ALS) gene was successfully deleted in the transfection of patient-derived iPSc cells.[278] In the case of HD, mutant Huntingtin and its aggregates were permanently suppressed in the HD. The gene therapy could prove specifically applicable Q-knock in mice.[279] A similar strategy can be employed for reducing the aggregation of TDP-43. CRISPR/Cas9 holds immense potential, but significant challenges must be overcome for its release in the market.

Another gene therapy strategy that could be employed for the reduction, restoration, or modification of protein expression is by employing antisense oligonucleotides (ASOs). These are synthetic and short single-stranded nucleic acids about 20-25 bases long, which specifically bind to the complementary mRNA.[280] Once bound to ASO, the mRNA-DNA hybrid becomes the substrate for the enzyme RNase H resulting in its degradation.[281] Several studies have shown the efficacy of the ASOs in the reduction of the targeted transcripts, but none have been approved for disease treatment.

Gene therapy is in its initial stage, yet it holds promise to change the world of therapeutics in the coming years.

1.8.5 Induction of protein degradation pathway

Targeting the accumulated TDP-43 species, when coupled with other therapeutic strategies, hold the potential to treat neurodegeneration even at later stages of the disease. From a therapeutic point of view, targeting the Ubiquitin proteasome system will remove small misfolded peptides, while targeting autophagy will work on removing large misfolded inclusions.[282] However, targeting both pathways might prove better in removing the toxic misfolded species (Figure 1.7).

Since prolonged induction of autophagy could hamper mitochondrial respiratory function, a balance between autophagy induction and mitochondrial function should be considered.

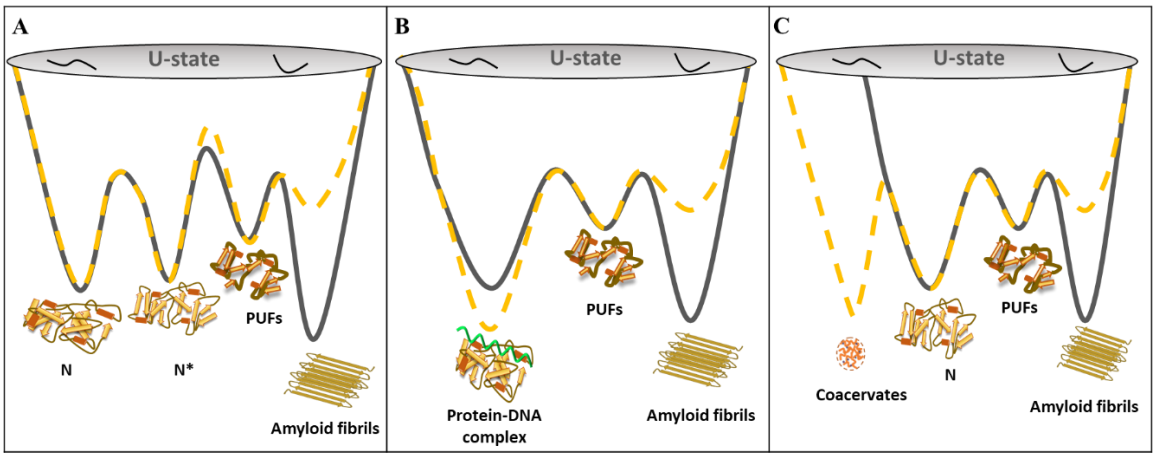

Figure 1.8 The coupled folding and aggregation energy landscape of TDP-43^{tRRM} in low pH stress conditions (gray line). Energy minima suggest that amyloid-like β form, the most stable state, populates in stress conditions. The yellow dashed line in A, B, and C represents the modulated energy landscape as a result of mutation (A: Dashed yellow line) and DNA (B, C: Dashed yellow line). These factors promote native-like conformers, which are either kinetically (A) or thermodynamically stable (B) than the native TDP-43^{tRRM}. DNA can also direct the flux towards a phase-separated conformer (C), which prevents TDP-43^{tRRM} aggregation.

1.9 Conclusions

TDP-43^{tRRM} is known to sense stress and undergo amyloid-like aggregation. However, we do not understand the thermodynamic basis of stress sensing by the protein. How does stress modulate the free energy landscape of protein? What are the initial molecular and thermodynamic changes a protein experiences upon stress sensing? How the modulation of energy landscape directs the flux towards amyloid-like aggregation? What role do mutations and nucleic acid binding molecules have on the energy landscape? Can protein access different energy minima which are native-like? How can they be used to redesign the energy landscape of proteins? Can a potent aggregation inhibitor be designed based on this knowledge? This thesis aims to answer some of these exciting questions (Figure 1.8). In this cumulative study, we have tried to study the modulation of the energy landscape of TDP-43^{tRRM} in different solution conditions. We emphasize the conformers that could populate due to the change. We quantitatively propose that

destabilization of TDP-43^{tRRM}, as it experiences low pH stress, results in its partial misfolding, which exposes a critical amino acid residue, H166. The coupling of protonation-deprotonation of H166 is linked to the amyloid-like aggregation of TDP-43^{tRRM}. We further studied the role of mutation and DNA on the energy landscape of TDP-43^{tRRM}. The mutant (H166Q) forms a molten globule that remains resistant to misfolding (Figure 1.8A). Additionally, we report that the DNA binding inhibits the amyloid-like aggregation of TDP-43^{tRRM} by forming a more stable soluble monomeric native-like DNA-protein complex even in low-pH stress conditions which resists aggregation (Figure 1.8B). Furthermore, we report that under a particular specific set of conditions, TDP-43^{tRRM} undergoes complex coacervation in the presence of DNA to soluble native-like light phase and an insoluble protein-DNA rich dense phase (coacervates) (Figure 1.8C). The phenomenon prevents the aggregation of TDP-43^{tRRM}.

1.10 References

(1) Prasad, A.; Bharathi, V.; Sivalingam, V.; Girdhar, A.; Patel, B. K. Molecular Mechanisms of TDP-43 Misfolding and Pathology in Amyotrophic Lateral Sclerosis. *Front. Mol. Neurosci.* **2019**, *12*. https://doi.org/10.3389/fnmol.2019.00025.

(2) Neumann, M.; Sampathu, D. M.; Kwong, L. K.; Truax, A. C.; Micsenyi, M. C.; Chou, T. T.; Bruce, J.; Schuck, T.; Grossman, M.; Clark, C. M.; McCluskey, L. F.; Miller, B. L.; Masliah, E.; Mackenzie, I. R.; Feldman, H.; Feiden, W.; Kretzschmar, H. A.; Trojanowski, J. Q.; Lee, V. M.-Y. Ubiquitinated TDP-43 in Frontotemporal Lobar Degeneration and Amyotrophic Lateral Sclerosis. *Science* **2006**, *314* (5796), 130–133. https://doi.org/10.1126/science.1134108.

(3) Arai, T.; Hasegawa, M.; Akiyama, H.; Ikeda, K.; Nonaka, T.; Mori, H.; Mann, D.; Tsuchiya, K.; Yoshida, M.; Hashizume, Y.; Oda, T. TDP-43 is a Component of Ubiquitin-Positive Tau-Negative Inclusions in Frontotemporal Lobar Degeneration and Amyotrophic Lateral Sclerosis. *Biochem. Biophys. Res. Commun.* **2006**, *351* (3), 602–611. https://doi.org/10.1016/j.bbrc.2006.10.093.

(4) Zhang, L.; Chen, Y.; Liu, M.; Wang, Y.; Peng, G. TDP-43 and Limbic-Predominant Age-Related TDP-43 Encephalopathy. *Front. Aging Neurosci.* **2020**, *11*, 376. https://doi.org/10.3389/fnagi.2019.00376.

(5) Majoor-Krakauer, D.; Willems, P. J.; Hofman, A. Genetic Epidemiology of Amyotrophic Lateral Sclerosis. *Clin. Genet.* **2003**, *63* (2), 83–101. https://doi.org/10.1046/j.0009-9163.2002.00001.x.

(6) Ling, S.-C.; Polymenidou, M.; Cleveland, D. W. Converging Mechanisms in ALS and FTD: Disrupted RNA and Protein Homeostasis. *Neuron* **2013**, *79* (3), 416–438. https://doi.org/10.1016/j.neuron.2013.07.033.

(7) Sun, Y.; Chakrabartty, A. Phase to Phase with TDP-43. *Biochemistry* **2017**, *56* (6), 809–823. https://doi.org/10.1021/acs.biochem.6b01088.

(8) Bang, J.; Spina, S.; Miller, B. L. Non-Alzheimer's Dementia 1. *Lancet Lond. Engl.* **2015**, *386* (10004), 1672–1682. https://doi.org/10.1016/S0140-6736(15)00461-4.

(9) Rascovsky, K.; Hodges, J. R.; Knopman, D.; Mendez, M. F.; Kramer, J. H.; Neuhaus, J.; van Swieten, J. C.; Seelaar, H.; Dopper, E. G. P.; Onyike, C. U.; Hillis, A. E.; Josephs, K. A.; Boeve, B. F.; Kertesz, A.; Seeley, W. W.; Rankin, K. P.; Johnson, J. K.; Gorno-Tempini, M.-L.; Rosen, H.; Prioleau-Latham, C. E.; Lee, A.; Kipps, C. M.; Lillo, P.; Piguet, O.; Rohrer, J. D.; Rossor, M. N.; Warren, J. D.; Fox, N. C.; Galasko, D.; Salmon, D. P.; Black, S. E.; Mesulam, M.; Weintraub, S.; Dickerson, B. C.; Diehl-Schmid, J.; Pasquier, F.; Deramecourt, V.; Lebert, F.; Pijnenburg, Y.; Chow, T. W.; Manes, F.; Grafman, J.; Cappa, S. F.; Freedman, M.; Grossman, M.; Miller, B. L. Sensitivity of Revised Diagnostic Criteria for the Behavioural Variant of Frontotemporal Dementia. *Brain* **2011**, *134* (9), 2456–2477. https://doi.org/10.1093/brain/awr179.

(10) Lough, S.; Kipps, C. M.; Treise, C.; Watson, P.; Blair, J. R.; Hodges, J. R. Social Reasoning, Emotion and Empathy in Frontotemporal Dementia. *Neuropsychologia* **2006**, *44* (6), 950–958. https://doi.org/10.1016/j.neuropsychologia.2005.08.009.

(11) Rankin, K. P.; Gorno-Tempini, M. L.; Allison, S. C.; Stanley, C. M.; Glenn, S.; Weiner, M. W.; Miller, B. L. Structural Anatomy of Empathy in Neurodegenerative Disease. *Brain J. Neurol.* **2006**, *129* (Pt 11), 2945–2956. https://doi.org/10.1093/brain/awl254.

(12) Sturm, V. E.; Rosen, H. J.; Allison, S.; Miller, B. L.; Levenson, R. W. Self-Conscious Emotion Deficits in Frontotemporal Lobar Degeneration. *Brain J. Neurol.* **2006**, *129* (Pt 9), 2508–2516. https://doi.org/10.1093/brain/awl145.

(13) Takeuchi, R.; Tada, M.; Shiga, A.; Toyoshima, Y.; Konno, T.; Sato, T.; Nozaki, H.; Kato, T.; Horie, M.; Shimizu, H.; Takebayashi, H.; Onodera, O.; Nishizawa, M.; Kakita, A.; Takahashi, H. Heterogeneity of Cerebral TDP-43 Pathology in Sporadic Amyotrophic Lateral Sclerosis: Evidence for Clinico-Pathologic Subtypes. *Acta Neuropathol. Commun.* **2016**, *4* (1), 61. https://doi.org/10.1186/s40478-016-0335-2.

(14) Laferrière, F.; Maniecka, Z.; Pérez-Berlanga, M.; Hruska-Plochan, M.; Gilhespy, L.; Hock, E.-M.; Wagner, U.; Afroz, T.; Boersema, P. J.; Barmettler, G.; Foti, S. C.; Asi, Y. T.; Isaacs, A. M.; Al-Amoudi, A.; Lewis, A.; Stahlberg, H.; Ravits, J.; De Giorgi, F.; Ichas, F.; Bezard, E.; Picotti, P.; Lashley, T.; Polymenidou, M. TDP-43 Extracted from Frontotemporal Lobar Degeneration Subject Brains Displays Distinct Aggregate Assemblies and Neurotoxic Effects Reflecting Disease Progression Rates. *Nat. Neurosci.* **2019**, *22* (1), 65–77. https://doi.org/10.1038/s41593-018-0294-y.

(15) *The basis of clinicopathological heterogeneity in TDP-43 proteinopathy - PMC*. https://www.ncbi.nlm.nih.gov/pmc/articles/PMC6800885/#CR89 (accessed 2022-11-03).

(16) Amador-Ortiz, C.; Lin, W.-L.; Ahmed, Z.; Personett, D.; Davies, P.; Duara, R.; Graff-Radford, N. R.; Hutton, M. L.; Dickson, D. W. TDP-43 Immunoreactivity in Hippocampal Sclerosis and Alzheimer's Disease. *Ann. Neurol.* **2007**, *61* (5), 435–445. https://doi.org/10.1002/ana.21154.

(17) Hasegawa, M.; Arai, T.; Akiyama, H.; Nonaka, T.; Mori, H.; Hashimoto, T.; Yamazaki, M.; Oyanagi, K. TDP-43 is Deposited in the Guam Parkinsonism-Dementia Complex Brains. *Brain J. Neurol.* **2007**, *130* (Pt 5), 1386–1394. https://doi.org/10.1093/brain/awm065.

(18) Nakashima-Yasuda, H.; Uryu, K.; Robinson, J.; Xie, S. X.; Hurtig, H.; Duda, J. E.; Arnold, S. E.; Siderowf, A.; Grossman, M.; Leverenz, J. B.; Woltjer, R.; Lopez, O. L.; Hamilton, R.; Tsuang, D. W.; Galasko, D.; Masliah, E.; Kaye, J.; Clark, C. M.; Montine, T. J.; Lee, V. M.-Y.; Trojanowski, J. Q. Co-Morbidity of TDP-43 Proteinopathy in Lewy Body Related Diseases. *Acta Neuropathol. (Berl.)* **2007**, *114* (3), 221–229. https://doi.org/10.1007/s00401-007-0261-2.

(19) Geser, F.; Winton, M. J.; Kwong, L. K.; Xu, Y.; Xie, S. X.; Igaz, L. M.; Garruto, R. M.; Perl, D. P.; Galasko, D.; Lee, V. M.-Y.; Trojanowski, J. Q. Pathological TDP-43 in Parkinsonism-Dementia Complex and Amyotrophic Lateral Sclerosis of Guam. *Acta Neuropathol. (Berl.)* **2008**, *115* (1), 133–145. https://doi.org/10.1007/s00401-007-0257-y.

(20) Zhang, Y.-J.; Xu, Y.; Dickey, C. A.; Buratti, E.; Baralle, F.; Bailey, R.; Pickering-Brown, S.; Dickson, D.; Petrucelli, L. Progranulin Mediates Caspase-Dependent Cleavage of TAR DNA Binding Protein-43. *J. Neurosci.* **2007**, *27* (39), 10530–10534. https://doi.org/10.1523/JNEUROSCI.3421-07.2007.

(21) Zhang, Y.-J.; Xu, Y.-F.; Cook, C.; Gendron, T. F.; Roettges, P.; Link, C. D.; Lin, W.-L.; Tong, J.; Castanedes-Casey, M.; Ash, P.; Gass, J.; Rangachari, V.; Buratti, E.; Baralle, F.; Golde, T. E.; Dickson, D. W.; Petrucelli, L. Aberrant Cleavage of TDP-43 Enhances Aggregation and Cellular Toxicity. *Proc. Natl. Acad. Sci.* **2009**, *106* (18), 7607–7612. https://doi.org/10.1073/pnas.0900688106.

(22) Arseni, D.; Hasegawa, M.; Murzin, A. G.; Kametani, F.; Arai, M.; Yoshida, M.; Ryskeldi-Falcon, B. Structure of Pathological TDP-43 Filaments from ALS with FTLD. *Nature* **2022**, *601* (7891), 139–143. https://doi.org/10.1038/s41586-021-04199-3.

(23) Shodai, A.; Ido, A.; Fujiwara, N.; Ayaki, T.; Morimura, T.; Oono, M. Conserved Acidic Amino Acid Residues in a Second RNA Recognition Motif Regulate Assembly and Function of TDP-43. **2012**, *7* (12). https://doi.org/10.1371/journal.pone.0052776.

(24) Shodai, A.; Morimura, T.; Ido, A.; Uchida, T.; Ayaki, T.; Takahashi, R.; Kitazawa, S.; Suzuki, S.; Shirouzu, M.; Kigawa, T.; Muto, Y.; Yokoyama, S.; Takahashi, R.; Kitahara, R.; Ito, H.; Fujiwara, N.; Urushitani, M. Aberrant Assembly of RNA Recognition Motif 1

Links to Pathogenic Conversion of TAR DNA-Binding Protein of 43 kDa (TDP-43). *J. Biol. Chem.* **2013**, *288* (21), 14886–14905. https://doi.org/10.1074/jbc.M113.451849.

(25) Agrawal, S.; Kuo, P.-H.; Chu, L.-Y.; Golzarroshan, B.; Jain, M.; Yuan, H. S. RNA Recognition Motifs of Disease-Linked RNA-Binding Proteins Contribute to Amyloid Formation. *Sci. Rep.* **2019**, *9*, 6171. https://doi.org/10.1038/s41598-019-42367-8.

(26) Shenoy, J.; El Mammeri, N.; Dutour, A.; Berbon, M.; Saad, A.; Lends, A.; Morvan, E.; Grélard, A.; Lecomte, S.; Kauffmann, B.; Theillet, F.-X.; Habenstein, B.; Loquet, A. Structural Dissection of Amyloid Aggregates of TDP-43 and its C-Terminal Fragments TDP-35 and TDP-16. *FEBS J.* **2020**, *287* (12), 2449–2467. https://doi.org/10.1111/febs.15159.

(27) Wright, G. S. A. Purification and Structural Characterization of Aggregation-Prone Human TDP-43 Involved in Neurodegenerative Diseases. iScience. **2020**, 23 (6), 101159. https://doi.org/10.1016/j.isci.2020.101159.

(28) Ou, S. H.; Wu, F.; Harrich, D.; García-Martínez, L. F.; Gaynor, R. B. Cloning and Characterization of a Novel Cellular Protein, TDP-43, That Binds to Human Immunodeficiency Virus Type 1 TAR DNA Sequence Motifs. *J. Virol.* **1995**, *69* (6), 3584–3596. https://doi.org/10.1128/JVI.69.6.3584-3596.1995.

(29) Sephton, C. F.; Good, S. K.; Atkin, S.; Dewey, C. M.; Mayer, P.; Herz, J.; Yu, G. TDP-43 is a Developmentally Regulated Protein Essential for Early Embryonic Development. *J. Biol. Chem.* **2010**, *285* (9), 6826–6834. https://doi.org/10.1074/jbc.M109.061846.

(30) Pinarbasi, E. S.; Cağatay, T.; Fung, H. Y. J.; Li, Y. C.; Chook, Y. M.; Thomas, P. J. Active Nuclear Import and Passive Nuclear Export are the Primary Determinants of TDP-43 Localization. *Sci. Rep.* **2018**, *8* (1), 7083. https://doi.org/10.1038/s41598-018-25008-4.

(31) Mompeán, M.; Romano, V.; Pantoja-Uceda, D.; Stuani, C.; Baralle, F. E.; Buratti, E.; Laurents, D. V. The TDP-43 N-Terminal Domain Structure at High Resolution. *FEBS J.* **2016**, *283* (7), 1242–1260. https://doi.org/10.1111/febs.13651.

(32) Jiang, L.-L.; Xue, W.; Hong, J.-Y.; Zhang, J.-T.; Li, M.-J.; Yu, S.-N.; He, J.-H.; Hu, H.-Y. The N-Terminal Dimerization is Required for TDP-43 Splicing Activity. *Sci. Rep.* **2017**, *7* (1), 6196. https://doi.org/10.1038/s41598-017-06263-3.

(33) Lukavsky, P. J.; Daujotyte, D.; Tollervey, J. R.; Ule, J.; Stuani, C.; Buratti, E.; Baralle, F. E.; Damberger, F. F.; Allain, F. H. T. Molecular Basis of UG-Rich RNA Recognition by the Human Splicing Factor TDP-43. *Nat. Struct. Mol. Biol.* **2013**, *20* (12), 1443–1449. https://doi.org/10.1038/nsmb.2698.

(34) Mompeán, M.; Baralle, M.; Buratti, E.; Laurents, D. V. An Amyloid-Like Pathological Conformation of TDP-43 is Stabilized by Hypercooperative Hydrogen Bonds. *Front. Mol. Neurosci.* **2016**, *9*, 125. https://doi.org/10.3389/fnmol.2016.00125.

(35) François-Moutal, L.; Perez-Miller, S.; Scott, D. D.; Miranda, V. G.; Mollasalehi, N.; Khanna, M. Structural Insights into TDP-43 and Effects of Post-Translational Modifications. *Front. Mol. Neurosci.* **2019**, *12*. https://doi.org/10.3389/fnmol.2019.00301.

(36) Mompeán, M.; Buratti, E.; Guarnaccia, C.; Brito, R. M. M.; Chakrabartty, A.; Baralle, F. E.; Laurents, D. V. Structural Characterization of the Minimal Segment of TDP-43 Competent for Aggregation. *Arch. Biochem. Biophys.* **2014**, *545*, 53–62. https://doi.org/10.1016/j.abb.2014.01.007.

(37) Cassel, J. A.; Reitz, A. B. Ubiquilin-2 (UBQLN2) Binds with High Affinity to the C-Terminal Region of TDP-43 and Modulates TDP-43 Levels in H4 Cells: Characterization of Inhibition by Nucleic Acids and 4-Aminoquinolines. *Biochim. Biophys. Acta* **2013**, *1834* (6), 964–971. https://doi.org/10.1016/j.bbapap.2013.03.020.

(38) Majumder, P.; Chu, J.-F.; Chatterjee, B.; Swamy, K. B. S.; Shen, C.-K. J. Co-Regulation of mRNA Translation by TDP-43 and Fragile X Syndrome Protein FMRP. *Acta Neuropathol. (Berl.)* **2016**, *132* (5), 721–738. https://doi.org/10.1007/s00401-016-1603-8.

(39) Wang, W.; Wang, L.; Lu, J.; Siedlak, S. L.; Fujioka, H.; Liang, J.; Jiang, S.; Ma, X.; Jiang, Z.; da Rocha, E. L.; Sheng, M.; Choi, H.; Lerou, P. H.; Li, H.; Wang, X. The Inhibition of TDP-43 Mitochondrial Localization Blocks its Neuronal Toxicity. *Nat. Med.* **2016**, *22* (8), 869–878. https://doi.org/10.1038/nm.4130.

(40) Shiina, Y.; Arima, K.; Tabunoki, H.; Satoh, J. TDP-43 Dimerizes in Human Cells in Culture. *Cell. Mol. Neurobiol.* **2010**, *30* (4), 641–652. https://doi.org/10.1007/s10571-009-9489-9.

(41) Vivoli-Vega, M.; Guri, P.; Chiti, F.; Bemporad, F. Insight into the Folding and Dimerization Mechanisms of the N-Terminal Domain from Human TDP-43. *Int. J. Mol. Sci.* **2020**, *21* (17), 6259. https://doi.org/10.3390/ijms21176259.

(42) Chang, C. ke; Wu, T. H.; Wu, C. Y.; Chiang, M. hui; Toh, E. K. W.; Hsu, Y. C.; Lin, K. F.; Liao, Y. heng; Huang, T. huang; Huang, J. J. T. The N-Terminus of TDP-43 Promotes its Oligomerization and Enhances DNA Binding Affinity. *Biochem. Biophys. Res. Commun.* **2012**, *425* (2), 219–224. https://doi.org/10.1016/j.bbrc.2012.07.071.

(43) Zhang, Y.-J.; Caulfield, T.; Xu, Y.-F.; Gendron, T. F.; Hubbard, J.; Stetler, C.; Sasaguri, H.; Whitelaw, E. C.; Cai, S.; Lee, W. C.; Petrucelli, L. The Dual Functions of the Extreme N-Terminus of TDP-43 in Regulating its Biological Activity and Inclusion Formation. *Hum. Mol. Genet.* **2013**, *22* (15), 3112–3122. https://doi.org/10.1093/hmg/ddt166.

(44) Koehler, L. C.; Grese, Z. R.; Bastos, A. C. S.; Mamede, L. D.; Heyduk, T.; Ayala, Y. M. TDP-43 Oligomerization and Phase Separation Properties are Necessary for Autoregulation. *Front. Neurosci.* **2022**, *16*, 818655. https://doi.org/10.3389/fnins.2022.818655.

(45) Wang, A.; Conicella, A.E.; Schmidt, H.B.; Martin, E.W.; Rhoads, S.N.; Reeb, A.N.; Nourse, A.; Ramirez Montero, D.; Ryan, V.H.; Rohatgi, R.; Shewmaker, F.; Naik, M.T.; Mittag, T.; Ayala, Y.M.; Fawzi, N.L.; A Single N-Terminal Phosphomimic Disrupts TDP-43

Polymerization, Phase Separation, And RNA Splicing. *EMBO J.* **2018,** 37 (5), e97452. https://doi.org/10.15252/embj.201797452.

(46) Carter, G. C.; Hsiung, C.-H.; Simpson, L.; Yang, H.; Zhang, X. N-Terminal Domain of TDP43 Enhances Liquid-Liquid Phase Separation of Globular Proteins. *J. Mol. Biol.* **2021**, *433* (10), 166948. https://doi.org/10.1016/j.jmb.2021.166948.

(47) Afroz, T.; Hock, E.-M.; Ernst, P.; Foglieni, C.; Jambeau, M.; Gilhespy, L. A. B.; Laferriere, F.; Maniecka, Z.; Plückthun, A.; Mittl, P.; Paganetti, P.; Allain, F. H. T.; Polymenidou, M. Functional and Dynamic Polymerization of the ALS-Linked Protein TDP-43 Antagonizes its Pathologic Aggregation. *Nat. Commun.* **2017**, *8* (1), 45. https://doi.org/10.1038/s41467-017-00062-0.

(48) Suzuki, H.; Lee, K.; Matsuoka, M. TDP-43-Induced Death is Associated with Altered Regulation of BIM and Bcl-XL and Attenuated by Caspase-Mediated TDP-43 Cleavage. *J. Biol. Chem.* **2011**, *286* (15), 13171–13183. https://doi.org/10.1074/jbc.M110.197483.

(49) Nishimoto, Y.; Ito, D.; Yagi, T.; Nihei, Y.; Tsunoda, Y.; Suzuki, N. Characterization of Alternative Isoforms and Inclusion Body of the TAR DNA-Binding Protein-43. *J. Biol. Chem.* **2010**, *285* (1), 608–619. https://doi.org/10.1074/jbc.M109.022012.

(50) Nishino, K.; Watanabe, S.; Shijie, J.; Murata, Y.; Oiwa, K.; Komine, O.; Endo, F.; Tsuiji, H.; Abe, M.; Sakimura, K.; Mishra, A.; Yamanaka, K. Mice Deficient in the C-Terminal Domain of TAR DNA-Binding Protein 43 Develop Age-Dependent Motor Dysfunction Associated with Impaired Notch1−Akt Signaling Pathway. *Acta Neuropathol. Commun.* **2019**, *7* (1), 118. https://doi.org/10.1186/s40478-019-0776-5.

(51) Maris, C.; Dominguez, C.; Allain, F. H.-T. The RNA Recognition Motif, a Plastic RNA-Binding Platform to Regulate Post-Transcriptional Gene Expression. *FEBS J.* **2005**, *272* (9), 2118–2131. https://doi.org/10.1111/j.1742-4658.2005.04653.x.

(52) Cléry, A.; Allain, F. H.-T. From Structure To Function of RNA Binding Domains. Landes Bioscience, 2013.

(53) Kuo, P.-H.; Chiang, C.-H.; Wang, Y.-T.; Doudeva, L. G.; Yuan, H. S. The Crystal Structure of TDP-43 RRM1-DNA Complex Reveals the Specific Recognition for UG- and TG-Rich Nucleic Acids. *Nucleic Acids Res.* **2014**, *42* (7), 4712–4722. https://doi.org/10.1093/nar/gkt1407.

(54) Buratti, E.; Baralle, F. E. Characterization and Functional Implications of the RNA Binding Properties of Nuclear Factor TDP-43, a Novel Splicing Regulator of CFTR Exon 9. *J. Biol. Chem.* **2001**, *276* (39), 36337–36343. https://doi.org/10.1074/jbc.M104236200.

(55) Buratti, E.; Dörk, T.; Zuccato, E.; Pagani, F.; Romano, M.; Baralle, F. E. Nuclear Factor TDP-43 and SR Proteins Promote in Vitro and in Vivo CFTR Exon 9 Skipping. *EMBO J.* **2001**, *20* (7), 1774–1784. https://doi.org/10.1093/emboj/20.7.1774.

(56) Mackness, B. C.; Tran, M. T.; McClain, S. P.; Matthews, C. R.; Zitzewitz, J. A. Folding of the RNA Recognition Motif (RRM) Domains of the Amyotrophic Lateral Sclerosis (ALS)-Linked Protein TDP-43 Reveals an Intermediate State. *J. Biol. Chem.* **2014**, *289* (12), 8264–8276. https://doi.org/10.1074/jbc.M113.542779.

(57) Cookson, M. R. RNA-Binding Proteins Implicated in Neurodegenerative Diseases. *Wiley Interdiscip. Rev. RNA* **2017**, *8* (1), 10.1002/wrna.1397. https://doi.org/10.1002/wrna.1397.

(58) Pillai, M.; Jha, S. K. The Folding and Aggregation Energy Landscapes of Tethered RRM Domains of Human TDP-43 are Coupled Via a Metastable Molten Globule-Like Oligomer. *Biochemistry* **2019**, *58* (6), 608–620. https://doi.org/10.1021/acs.biochem.8b01013.

(59) Pillai, M.; Jha, S. K. Early Metastable Assembly During the Stress-Induced Formation of Worm-Like Amyloid Fibrils of Nucleic Acid Binding Domains of TDP-43. *Biochemistry* **2020**, *59* (3), 315–328. https://doi.org/10.1021/acs.biochem.9b00780.

(60) Patni, D.; Jha, S. K. Protonation–Deprotonation Switch Controls the Amyloid-like Misfolding of Nucleic-Acid-Binding Domains of TDP-43. *J. Phys. Chem. B* **2021**, *125* (30), 8383–8394. https://doi.org/10.1021/acs.jpcb.1c03262.

(61) Kumar, V.; Wahiduzzaman; Prakash, A.; Tomar, A. K.; Srivastava, A.; Kundu, B.; Lynn, A. M.; Imtaiyaz Hassan, Md. Exploring the Aggregation-Prone Regions from Structural Domains of Human TDP-43. *Biochim. Biophys. Acta BBA - Proteins Proteomics* **2019**, *1867* (3), 286–296. https://doi.org/10.1016/j.bbapap.2018.10.008.

(62) Chen, H.-J.; Topp, S. D.; Hui, H. S.; Zacco, E.; Katarya, M.; McLoughlin, C.; King, A.; Smith, B. N.; Troakes, C.; Pastore, A.; Shaw, C. E. RRM Adjacent TARDBP Mutations Disrupt RNA Binding and Enhance TDP-43 Proteinopathy. *Brain* **2019**, *142* (12), 3753–3770. https://doi.org/10.1093/brain/awz313.

(63) Kabashi, E.; Valdmanis, P. N.; Dion, P.; Spiegelman, D.; McConkey, B. J.; Velde, C. V.; Bouchard, J.-P.; Lacomblez, L.; Pochigaeva, K.; Salachas, F.; Pradat, P.-F.; Camu, W.; Meininger, V.; Dupre, N.; Rouleau, G. A. TARDBP Mutations in Individuals with Sporadic and Familial Amyotrophic Lateral Sclerosis. *Nat. Genet.* **2008**, *40* (5), 572–574. https://doi.org/10.1038/ng.132.

(64) Kovacs, G. G.; Murrell, J. R.; Horvath, S.; Haraszti, L.; Majtenyi, K.; Molnar, M. J.; Budka, H.; Ghetti, B.; Spina, S. TARDBP Variation Associated with Frontotemporal Dementia, Supranuclear Gaze Palsy, and Chorea. *Mov. Disord.* **2009**, *24* (12), 1842–1847. https://doi.org/10.1002/mds.22697.

(65) Maurel, C.; Madji-Hounoum, B.; Thepault, R.-A.; Marouillat, S.; Brulard, C.; Danel-Brunaud, V.; Camdessanche, J.-P.; Blasco, H.; Corcia, P.; Andres, C. R.; Vourc'h, P. Mutation in the RRM2 Domain of TDP-43 in Amyotrophic Lateral Sclerosis with Rapid Progression Associated with Ubiquitin Positive Aggregates in Cultured Motor Neurons. *Amyotroph. Lateral Scler. Front. Degener.* **2018**, *19* (1–2), 149–151. https://doi.org/10.1080/21678421.2017.1349152.

(66) Moreno, F.; Rabinovici, G. D.; Karydas, A.; Miller, Z.; Hsu, S. C.; Legati, A.; Fong, J.; Schonhaut, D.; Esselmann, H.; Watson, C.; Stephens, M. L.; Kramer, J.; Wiltfang, J.; Seeley, W. W.; Miller, B. L.; Coppola, G.; Grinberg, L. T. A Novel Mutation P112H in the TARDBP Gene Associated with Frontotemporal Lobar Degeneration without Motor Neuron Disease and Abundant Neuritic Amyloid Plaques. *Acta Neuropathol. Commun.* **2015**, *3* (1), 19. https://doi.org/10.1186/s40478-015-0190-6.

(67) Nonaka, T.; Kametani, F.; Arai, T.; Akiyama, H.; Hasegawa, M. Truncation and Pathogenic Mutations Facilitate the Formation of Intracellular Aggregates of TDP-43. *Hum. Mol. Genet.* **2009**, *18* (18), 3353–3364. https://doi.org/10.1093/hmg/ddp275.

(68) Igaz, L. M.; Kwong, L. K.; Chen-Plotkin, A.; Winton, M. J.; Unger, T. L.; Xu, Y.; Neumann, M.; Trojanowski, J. Q.; Lee, V. M.-Y. Expression of TDP-43 C-Terminal Fragments in Vitro Recapitulates Pathological Features of TDP-43 Proteinopathies. *J. Biol. Chem.* **2009**, *284* (13), 8516–8524. https://doi.org/10.1074/jbc.M809462200.

(69) Huang, Y. C.; Lin, K. F.; He, R. Y.; Tu, P. H.; Koubek, J.; Hsu, Y. C.; Huang, J. J. T. Inhibition of TDP-43 Aggregation by Nucleic Acid Binding. *PLoS ONE* **2013**, *8* (5). https://doi.org/10.1371/journal.pone.0064002.

(70) Buratti, E.; Brindisi, A.; Giombi, M.; Tisminetzky, S.; Ayala, Y. M.; Baralle, F. E. TDP-43 Binds Heterogeneous Nuclear Ribonucleoprotein A/B through its C-Terminal Tail: An Important Region for the Inhibition of Cystic Fibrosis Transmembrane Conductance Regulator Exon 9 Splicing *. *J. Biol. Chem.* **2005**, *280* (45), 37572–37584. https://doi.org/10.1074/jbc.M505557200.

(71) Ayala, Y. M.; Pantano, S.; D'Ambrogio, A.; Buratti, E.; Brindisi, A.; Marchetti, C.; Romano, M.; Baralle, F. E. Human, Drosophila, and C.Elegans TDP43: Nucleic Acid Binding Properties and Splicing Regulatory Function. *J. Mol. Biol.* **2005**, *348* (3), 575–588. https://doi.org/10.1016/j.jmb.2005.02.038.

(72) Abhyankar, M. M.; Urekar, C.; Reddi, P. P. A Novel CPG-Free Vertebrate Insulator Silences the Testis-Specific Sp-10 Gene in Somatic Tissues: Role for TDP-43 in Insulator Function*. *J. Biol. Chem.* **2007**, *282* (50), 36143–36154. https://doi.org/10.1074/jbc.M705811200.

(73) Udan, M.; Baloh, R. H. Implications of the Prion-Related Q/N Domains in TDP-43 and FUS. *Prion* **2011**, *5* (1), 1–5. https://doi.org/10.4161/pri.5.1.14265.

(74) Johnson, B. S.; Snead, D.; Lee, J. J.; McCaffery, J. M.; Shorter, J.; Gitler, A. D. TDP-43 is Intrinsically Aggregation-Prone, and Amyotrophic Lateral Sclerosis-Linked Mutations Accelerate Aggregation and Increase Toxicity *. *J. Biol. Chem.* **2009**, *284* (30), 20329–20339. https://doi.org/10.1074/jbc.M109.010264.

(75) Johnson, B. S.; McCaffery, J. M.; Lindquist, S.; Gitler, A. D. A Yeast TDP-43 Proteinopathy Model: Exploring the Molecular Determinants of TDP-43 Aggregation and Cellular

Toxicity. *Proc. Natl. Acad. Sci.* **2008**, *105* (17), 6439–6444. https://doi.org/10.1073/pnas.0802082105.

(76) Mackenzie, I. R. A.; Rademakers, R. The Role of TDP-43 in Amyotrophic Lateral Sclerosis and Frontotemporal Dementia. *Curr. Opin. Neurol.* **2008**, *21* (6), 693–700. https://doi.org/10.1097/WCO.0b013e3283168d1d.

(77) van Es, M. A.; Hardiman, O.; Chio, A.; Al-Chalabi, A.; Pasterkamp, R. J.; Veldink, J. H.; van den Berg, L. H. Amyotrophic Lateral Sclerosis. *The Lancet* **2017**, *390* (10107), 2084–2098. https://doi.org/10.1016/S0140-6736(17)31287-4.

(78) Lattante, S.; Rouleau, G. A.; Kabashi, E. TARDBP and FUS Mutations Associated with Amyotrophic Lateral Sclerosis: Summary and Update. *Hum. Mutat.* **2013**, *34* (6), 812–826. https://doi.org/10.1002/humu.22319.

(79) Jiang, L.-L.; Che, M.-X.; Zhao, J.; Zhou, C.-J.; Xie, M.-Y.; Li, H.-Y.; He, J.-H.; Hu, H.-Y. Structural Transformation of the Amyloidogenic Core Region of TDP-43 Protein Initiates its Aggregation and Cytoplasmic Inclusion. *J. Biol. Chem.* **2013**, *288* (27), 19614–19624. https://doi.org/10.1074/jbc.M113.463828.

(80) Jiang, L.-L.; Zhao, J.; Yin, X.-F.; He, W.-T.; Yang, H.; Che, M.-X.; Hu, H.-Y. Two Mutations G335D and Q343R within the Amyloidogenic Core Region of TDP-43 Influence its Aggregation and Inclusion Formation. *Sci. Rep.* **2016**, *6* (1), 23928. https://doi.org/10.1038/srep23928.

(81) Chen, A. K.-H.; Lin, R. Y.-Y.; Hsieh, E. Z.-J.; Tu, P.-H.; Chen, R. P.-Y.; Liao, T.-Y.; Chen, W.; Wang, C.-H.; Huang, J. J.-T. Induction of Amyloid Fibrils by the C-Terminal Fragments of TDP-43 in Amyotrophic Lateral Sclerosis. *J. Am. Chem. Soc.* **2010**, *132* (4), 1186–1187. https://doi.org/10.1021/ja9066207.

(82) Saini, A.; Chauhan, V. S. Delineation of the Core Aggregation Sequences of TDP-43 C-Terminal Fragment. *Chembiochem Eur. J. Chem. Biol.* **2011**, *12* (16), 2495–2501. https://doi.org/10.1002/cbic.201100427.

(83) Yamashita, T.; Hideyama, T.; Hachiga, K.; Teramoto, S.; Takano, J.; Iwata, N.; Saido, T. C.; Kwak, S. A Role for Calpain-Dependent Cleavage of TDP-43 in Amyotrophic Lateral Sclerosis Pathology. *Nat. Commun.* **2012**, *3* (1), 1307. https://doi.org/10.1038/ncomms2303.

(84) Conicella, A. E.; Zerze, G. H.; Mittal, J.; Fawzi, N. L. ALS Mutations Disrupt Phase Separation Mediated by α-Helical Structure in the TDP-43 Low-Complexity C-Terminal Domain. *Structure* **2016**, *24* (9), 1537–1549. https://doi.org/10.1016/j.str.2016.07.007.

(85) Uryu, K.; Nakashima-Yasuda, H.; Forman, M. S.; Kwong, L. K.; Clark, C. M.; Grossman, M.; Miller, B. L.; Kretzschmar, H. A.; Lee, V. M.-Y.; Trojanowski, J. Q.; Neumann, M. Concomitant TAR-DNA-Binding Protein 43 Pathology is Present in Alzheimer Disease and

Corticobasal Degeneration but Not in Other Tauopathies. *J. Neuropathol. Exp. Neurol.* **2008**, *67* (6), 555–564. https://doi.org/10.1097/NEN.0b013e31817713b5.

(86) Markopoulou, K.; Dickson, D. W.; McComb, R. D.; Wszolek, Z. K.; Katechalidou, L.; Avery, L.; Stansbury, M. S.; Chase, B. A. Clinical, Neuropathological and Genotypic Variability in SNCA A53T Familial Parkinson's Disease. Variability in Familial Parkinson's Disease. *Acta Neuropathol. (Berl.)* **2008**, *116* (1), 25–35. https://doi.org/10.1007/s00401-008-0372-4.

(87) Schwab, C.; Arai, T.; Hasegawa, M.; Yu, S.; McGeer, P. L. Colocalization of Transactivation-Responsive DNA-Binding Protein 43 and Huntingtin in Inclusions of Huntington Disease. *J. Neuropathol. Exp. Neurol.* **2008**, *67* (12), 1159–1165. https://doi.org/10.1097/NEN.0b013e31818e8951.

(88) Kosaka, T.; Fu, Y.-J.; Shiga, A.; Ishidaira, H.; Tan, C.-F.; Tani, T.; Koike, R.; Onodera, O.; Nishizawa, M.; Kakita, A.; Takahashi, H. Primary Lateral Sclerosis: Upper-Motor-Predominant Amyotrophic Lateral Sclerosis with Frontotemporal Lobar Degeneration - Immunohistochemical and Biochemical Analyses of TDP-43: Primary Lateral Sclerosis and TDP-43. *Neuropathology* **2012**, *32* (4), 373–384. https://doi.org/10.1111/j.1440-1789.2011.01271.x.

(89) Riku, Y.; Atsuta, N.; Yoshida, M.; Tatsumi, S.; Iwasaki, Y.; Mimuro, M.; Watanabe, H.; Ito, M.; Senda, J.; Nakamura, R.; Koike, H.; Sobue, G. Differential Motor Neuron Involvement in Progressive Muscular Atrophy: A Comparative Study with Amyotrophic Lateral Sclerosis. *BMJ Open* **2014**, *4* (5), e005213. https://doi.org/10.1136/bmjopen-2014-005213.

(90) Nelson, P. T.; Dickson, D. W.; Trojanowski, J. Q.; Jack, C. R.; Boyle, P. A.; Arfanakis, K.; Rademakers, R.; Alafuzoff, I.; Attems, J.; Brayne, C.; Coyle-Gilchrist, I. T. S.; Chui, H. C.; Fardo, D. W.; Flanagan, M. E.; Halliday, G.; Hokkanen, S. R. K.; Hunter, S.; Jicha, G. A.; Katsumata, Y.; Kawas, C. H.; Keene, C. D.; Kovacs, G. G.; Kukull, W. A.; Levey, A. I.; Makkinejad, N.; Montine, T. J.; Murayama, S.; Murray, M. E.; Nag, S.; Rissman, R. A.; Seeley, W. W.; Sperling, R. A.; White III, C. L.; Yu, L.; Schneider, J. A. Limbic-Predominant Age-Related TDP-43 Encephalopathy (LATE): Consensus Working Group Report. *Brain* **2019**, *142* (6), 1503–1527. https://doi.org/10.1093/brain/awz099.

(91) Menzies, F. M.; Moreau, K.; Rubinsztein, D. C. Protein Misfolding Disorders and Macroautophagy. *Curr. Opin. Cell Biol.* **2011**, *23* (2), 190–197. https://doi.org/10.1016/j.ceb.2010.10.010.

(92) Rowland, L. P.; Shneider, N. A. Amyotrophic Lateral Sclerosis. *N. Engl. J. Med.* **2001**, *344* (22), 1688–1700. https://doi.org/10.1056/NEJM200105313442207.

(93) Scotter, E. L.; Chen, H.-J.; Shaw, C. E. TDP-43 Proteinopathy and ALS: Insights into Disease Mechanisms and Therapeutic Targets. *Neurother. J. Am. Soc. Exp. Neurother.* **2015**, *12* (2), 352–363. https://doi.org/10.1007/s13311-015-0338-x.

(94) Abrahams, S.; Newton, J.; Niven, E.; Foley, J.; Bak, T. H. Screening for Cognition and Behaviour Changes in ALS. *Amyotroph. Lateral Scler. Front. Degener.* **2014**, *15* (1–2), 9–14. https://doi.org/10.3109/21678421.2013.805784.

(95) Mackenzie, I. R. A.; Bigio, E. H.; Ince, P. G.; Geser, F.; Neumann, M.; Cairns, N. J.; Kwong, L. K.; Forman, M. S.; Ravits, J.; Stewart, H.; Eisen, A.; McClusky, L.; Kretzschmar, H. A.; Monoranu, C. M.; Highley, J. R.; Kirby, J.; Siddique, T.; Shaw, P. J.; Lee, V. M.-Y.; Trojanowski, J. Q. Pathological TDP-43 Distinguishes Sporadic Amyotrophic Lateral Sclerosis from Amyotrophic Lateral Sclerosis with SOD1 Mutations. *Ann. Neurol.* **2007**, *61* (5), 427–434. https://doi.org/10.1002/ana.21147.

(96) Igaz, L. M.; Kwong, L. K.; Xu, Y.; Truax, A. C.; Uryu, K.; Neumann, M.; Clark, C. M.; Elman, L. B.; Miller, B. L.; Grossman, M.; McCluskey, L. F.; Trojanowski, J. Q.; Lee, V. M.-Y. Enrichment of C-Terminal Fragments in TAR DNA-Binding Protein-43 Cytoplasmic Inclusions in Brain but Not in Spinal Cord of Frontotemporal Lobar Degeneration and Amyotrophic Lateral Sclerosis. *Am. J. Pathol.* **2008**, *173* (1), 182–194. https://doi.org/10.2353/ajpath.2008.080003.

(97) Riku, Y. Reappraisal of the Anatomical Spreading and Propagation Hypothesis about TDP-43 Aggregation in Amyotrophic Lateral Sclerosis and Frontotemporal Lobar Degeneration. *Neuropathology* **2020**, *40* (5), 426–435. https://doi.org/10.1111/neup.12644.

(98) Nonaka, T.; Masuda-Suzukake, M.; Arai, T.; Hasegawa, Y.; Akatsu, H.; Obi, T.; Yoshida, M.; Murayama, S.; Mann, D. M. A.; Akiyama, H.; Hasegawa, M. Prion-like Properties of Pathological TDP-43 Aggregates from Diseased Brains. *Cell Rep.* **2013**, *4* (1), 124–134. https://doi.org/10.1016/j.celrep.2013.06.007.

(99) Pesiridis, G. S.; Lee, V. M.-Y.; Trojanowski, J. Q. Mutations in TDP-43 Link Glycine-Rich Domain Functions to Amyotrophic Lateral Sclerosis. *Hum. Mol. Genet.* **2009**, *18* (R2), R156–R162. https://doi.org/10.1093/hmg/ddp303.

(100) Sreedharan, J.; Blair, I. P.; Tripathi, V. B.; Hu, X.; Vance, C.; Rogelj, B.; Ackerley, S.; Durnall, J. C.; Williams, K. L.; Buratti, E.; Baralle, F.; de Belleroche, J.; Mitchell, J. D.; Leigh, P. N.; Al-Chalabi, A.; Miller, C. C.; Nicholson, G.; Shaw, C. E. TDP-43 Mutations in Familial and Sporadic Amyotrophic Lateral Sclerosis. *Science* **2008**, *319* (5870), 1668–1672. https://doi.org/10.1126/science.1154584.

(101) Gitcho, M. A.; Baloh, R. H.; Chakraverty, S.; Mayo, K.; Norton, J. B.; Levitch, D.; Hatanpaa, K. J.; White, C. L.; Bigio, E. H.; Caselli, R.; Baker, M.; Al-Lozi, M. T.; Morris, J. C.; Pestronk, A.; Rademakers, R.; Goate, A. M.; Cairns, N. J. TDP-43 A315T Mutation in Familial Motor Neuron Disease. *Ann. Neurol.* **2008**, *63* (4), 535–538. https://doi.org/10.1002/ana.21344.

(102) Yokoseki, A.; Shiga, A.; Tan, C.F.; Tagawa, A.; Kaneko, H.; Koyama, A.; Eguchi, H.; Tsujino, A.; Ikeuchi, T.; Kakita, A.; Okamoto, K.; Nishizawa, M.; Takahashi, H.; Onodera,

O. TDP-43 Mutation in Familial Amyotrophic Lateral Sclerosis. Ann Neurol. **2008**, 63 (4), 538-42. doi: 10.1002/ana.21392.

(103) Snowden, J. S.; Neary, D.; Mann, D. M. A. Frontotemporal Dementia. *Br. J. Psychiatry* **2002**, *180* (2), 140–143. https://doi.org/10.1192/bjp.180.2.140.

(104) Rabinovici, G. D.; Miller, B. L. Frontotemporal Lobar Degeneration. *CNS Drugs* **2010**, *24* (5), 375–398. https://doi.org/10.2165/11533100-000000000-00000.

(105) Nana, A. L.; Sidhu, M.; Gaus, S. E.; Hwang, J.-H. L.; Li, L.; Park, Y.; Kim, E.-J.; Pasquini, L.; Allen, I. E.; Rankin, K. P.; Toller, G.; Kramer, J. H.; Geschwind, D. H.; Coppola, G.; Huang, E. J.; Grinberg, L. T.; Miller, B. L.; Seeley, W. W. Neurons Selectively Targeted in Frontotemporal Dementia Reveal Early Stage TDP-43 Pathobiology. *Acta Neuropathol. (Berl.)* **2019**, *137* (1), 27–46. https://doi.org/10.1007/s00401-018-1942-8.

(106) Kim, E.-J.; Sidhu, M.; Gaus, S. E.; Huang, E. J.; Hof, P. R.; Miller, B. L.; DeArmond, S. J.; Seeley, W. W. Selective Frontoinsular von Economo Neuron and Fork Cell Loss in Early Behavioral Variant Frontotemporal Dementia. *Cereb. Cortex N. Y. NY* **2012**, *22* (2), 251–259. https://doi.org/10.1093/cercor/bhr004.

(107) Mackenzie, I. R.; Rademakers, R.; Neumann, M. TDP-43 and FUS in Amyotrophic Lateral Sclerosis and Frontotemporal Dementia. *Lancet Neurol.* **2010**, *9* (10), 995–1007. https://doi.org/10.1016/S1474-4422(10)70195-2.

(108) Jo, M.; Lee, S.; Jeon, Y.-M.; Kim, S.; Kwon, Y.; Kim, H.-J. The Role of TDP-43 Propagation in Neurodegenerative Diseases: Integrating Insights from Clinical and Experimental Studies. *Exp. Mol. Med.* **2020**, *52* (10), 1652–1662. https://doi.org/10.1038/s12276-020-00513-7.

(109) Mackenzie, I. R. A.; Neumann, M.; Baborie, A.; Sampathu, D. M.; Plessis, D. D.; Jaros, E.; Perry, R. H.; Trojanowski, J. Q.; Mann, D. M. A.; Lee, V. M. Y. A Harmonized Classification System for FTLD-TDP Pathology. *Acta Neuropathol. (Berl.)* **2011**, *122* (1), 111–113. https://doi.org/10.1007/s00401-011-0845-8.

(110) Lee, E. B.; Porta, S.; Baer, G. M.; Xu, Y.; Suh, E.; Kwong, L. K.; Elman, L.; Grossman, M.; Lee, V. M.-Y.; Irwin, D. J.; Van Deerlin, V. M.; Trojanowski, J. Q. Expansion of the Classification of FTLD-TDP: Distinct Pathology Associated with Rapidly Progressive Frontotemporal Degeneration. *Acta Neuropathol. (Berl.)* **2017**, *134* (1), 65–78. https://doi.org/10.1007/s00401-017-1679-9.

(111) Kouli A.; Torsney K.M.; Kuan W.L.; Parkinson's Disease: Etiology, Neuropathology, and Pathogenesis. In: Stoker TB, Greenland JC, editors. Parkinson's Disease: Pathogenesis and Clinical Aspects [Internet]. Brisbane (AU): Codon Publications; 2018. Chapter 1. doi: 10.15586/codonpublications.parkinsonsdisease.2018.ch1.

(112) Rayaprolu, S.; Fujioka, S.; Traynor, S.; Soto-Ortolaza, A. I.; Petrucelli, L.; Dickson, D. W.; Rademakers, R.; Boylan, K. B.; Graff-Radford, N. R.; Uitti, R. J.; Wszolek, Z. K.; Ross, O.

A. TARDBP Mutations in Parkinson's Disease. *Parkinsonism Relat. Disord.* **2013**, *19* (3), 312–315. https://doi.org/10.1016/j.parkreldis.2012.11.003.

(113) MacDonald, M. E.; Ambrose, C. M.; Duyao, M. P.; Myers, R. H.; Lin, C.; Srinidhi, L.; Barnes, G.; Taylor, S. A.; James, M.; Groot, N.; MacFarlane, H.; Jenkins, B.; Anderson, M. A.; Wexler, N. S.; Gusella, J. F.; Bates, G. P.; Baxendale, S.; Hummerich, H.; Kirby, S.; North, M.; Youngman, S.; Mott, R.; Zehetner, G.; Sedlacek, Z.; Poustka, A.; Frischauf, A.-M.; Lehrach, H.; Buckler, A. J.; Church, D.; Doucette-Stamm, L.; O'Donovan, M. C.; Riba-Ramirez, L.; Shah, M.; Stanton, V. P.; Strobel, S. A.; Draths, K. M.; Wales, J. L.; Dervan, P.; Housman, D. E.; Altherr, M.; Shiang, R.; Thompson, L.; Fielder, T.; Wasmuth, J. J.; Tagle, D.; Valdes, J.; Elmer, L.; Allard, M.; Castilla, L.; Swaroop, M.; Blanchard, K.; Collins, F. S.; Snell, R.; Holloway, T.; Gillespie, K.; Datson, N.; Shaw, D.; Harper, P. S. A Novel Gene Containing a Trinucleotide Repeat That is Expanded and Unstable on Huntington's Disease Chromosomes. *Cell* **1993**, *72* (6), 971–983. https://doi.org/10.1016/0092-8674(93)90585-E.

(114) Sanchez, I. I.; Nguyen, T. B.; England, W. E.; Lim, R. G.; Vu, A. Q.; Miramontes, R.; Byrne, L. M.; Markmiller, S.; Lau, A. L.; Orellana, I.; Curtis, M. A.; Faull, R. L. M.; Yeo, G. W.; Fowler, C. D.; Reidling, J. C.; Wild, E. J.; Spitale, R. C.; Thompson, L. M. Huntington's Disease Mice and Human Brain Tissue Exhibit Increased G3BP1 Granules and TDP43 Mislocalization. *J. Clin. Invest.* **2021**, *131* (12). https://doi.org/10.1172/JCI140723.

(115) Sampedro, F.; Martínez-Horta, S.; Pérez-Pérez, J.; Pérez-González, R.; Horta-Barba, A.; Campolongo, A.; Izquierdo, C.; Aracil-Bolaños, I.; Rivas, E.; Puig-Davi, A.; Pagonabarraga, J.; Gómez-Ansón, B.; Kulisevsky, J. Plasma TDP-43 Reflects Cortical Neurodegeneration and Correlates with Neuropsychiatric Symptoms in Huntington's Disease. *Clin. Neuroradiol.* **2022**. https://doi.org/10.1007/s00062-022-01150-5.

(116) Matej, R.; Tesar, A.; Rusina, R. Alzheimer's Disease and Other Neurodegenerative Dementias in Comorbidity: A Clinical and Neuropathological Overview. *Clin. Biochem.* **2019**, *73*, 26–31. https://doi.org/10.1016/j.clinbiochem.2019.08.005.

(117) James, B. D.; Wilson, R. S.; Boyle, P. A.; Trojanowski, J. Q.; Bennett, D. A.; Schneider, J. A. TDP-43 Stage, Mixed Pathologies, and Clinical Alzheimer's-Type Dementia. *Brain* **2016**, *139* (11), 2983–2993. https://doi.org/10.1093/brain/aww224.

(118) Josephs, K. A.; Whitwell, J. L.; Weigand, S. D.; Murray, M. E.; Tosakulwong, N.; Liesinger, A. M.; Petrucelli, L.; Senjem, M. L.; Knopman, D. S.; Boeve, B. F.; Ivnik, R. J.; Smith, G. E.; Jack, C. R.; Parisi, J. E.; Petersen, R. C.; Dickson, D. W. TDP-43 is a Key Player in the Clinical Features Associated with Alzheimer's Disease. *Acta Neuropathol. (Berl.)* **2014**, *127* (6), 811–824. https://doi.org/10.1007/s00401-014-1269-z.

(119) Josephs, K. A.; Murray, M. E.; Whitwell, J. L.; Tosakulwong, N.; Weigand, S. D.; Petrucelli, L.; Liesinger, A. M.; Petersen, R. C.; Parisi, J. E.; Dickson, D. W. Updated TDP-

43 in Alzheimer's Disease Staging Scheme. *Acta Neuropathol. (Berl.)* **2016**, *131* (4), 571–585. https://doi.org/10.1007/s00401-016-1537-1.

(120) Josephs, K. A.; Whitwell, J. L.; Tosakulwong, N.; Weigand, S. D.; Murray, M. E.; Serie, A. M.; Petrucelli, L.; Senjem, M. L.; Ivnik, R. J.; Parisi, J. E.; Petersen, R. C.; Dickson, D. W. TDP-43 and Pathological Subtype of Alzheimer's Disease Impact Clinical Features. *Ann. Neurol.* **2015**, *78* (5), 697–709. https://doi.org/10.1002/ana.24493.

(121) McAleese, K. E.; Walker, L.; Erskine, D.; Thomas, A. J.; McKeith, I. G.; Attems, J. TDP-43 Pathology in Alzheimer's Disease, Dementia with Lewy Bodies and Ageing. *Brain Pathol.* **2016**, *27* (4), 472–479. https://doi.org/10.1111/bpa.12424.

(122) Josephs, K. A.; Dickson, D. W.; Tosakulwong, N.; Weigand, S. D.; Murray, M. E.; Petrucelli, L.; Liesinger, A. M.; Senjem, M. L.; Spychalla, A. J.; Knopman, D. S.; Parisi, J. E.; Petersen, R. C.; Jack, C. R.; Whitwell, J. L. Rates of Hippocampal Atrophy and Post-Mortem TDP-43 in Alzheimer's Disease: A Longitudinal Retrospective Study. *Lancet Neurol.* **2017**, *16* (11), 917–924. https://doi.org/10.1016/S1474-4422(17)30284-3.

(123) Herman, A. M.; Khandelwal, P. J.; Stanczyk, B. B.; Rebeck, G. W.; Moussa, C. E.-H. β-Amyloid Triggers ALS-Associated TDP-43 Pathology in AD Models. *Brain Res.* **2011**, *1386*, 191–199. https://doi.org/10.1016/j.brainres.2011.02.052.

(124) Dill, K.; Maccallum, J. The Protein-Folding Problem, 50 Years On. *Science* **2012**, *338*, 1042–1046. https://doi.org/10.1126/science.1219021.

(125) Jahn, T. R.; Radford, S. E. The Yin and Yang of Protein Folding. *FEBS J.* **2005**, *272* (23), 5962–5970. https://doi.org/10.1111/j.1742-4658.2005.05021.x.

(126) Wong, K.-B.; Yu, T.-H.; Chan, C.-H. 3.2 Energetics of Protein Folding. In *Comprehensive Biophysics*; Elsevier, 2012; pp 19–33. https://doi.org/10.1016/B978-0-12-374920-8.00302-7.

(127) Plotkin, S. S.; Onuchic, J. N. Understanding Protein Folding with Energy Landscape Theory Part I: Basic Concepts. *Q. Rev. Biophys.* **2002**, *35* (2), 111–167. https://doi.org/10.1017/S0033583502003761.

(128) Uversky, V. N.; Finkelstein, A. V. Life in Phases: Intra- and Inter- Molecular Phase Transitions in Protein Solutions. *Biomolecules* **2019**, *9* (12), 842. https://doi.org/10.3390/biom9120842.

(129) Gershenson, A.; Gierasch, L. M.; Pastore, A.; Radford, S. E. Energy Landscapes of Functional Proteins are Inherently Risky. *Nat. Chem. Biol.* **2014**, *10* (11), 884–891. https://doi.org/10.1038/nchembio.1670.

(130) Brissos, V.; Gonçalves, N.; Melo, E. P.; Martins, L. O. Improving Kinetic or Thermodynamic Stability of an Azoreductase by Directed Evolution. *PLoS ONE* **2014**, *9* (1), e87209. https://doi.org/10.1371/journal.pone.0087209.

(131) Chiti, F.; Dobson, C. M. Amyloid Formation by Globular Proteins Under Native Conditions. *Nat. Chem. Biol.* **2009**, *5* (1), 15–22. https://doi.org/10.1038/nchembio.131.

(132) Finkel, T. Radical Medicine: Treating Ageing to Cure Disease. *Nat. Rev. Mol. Cell Biol.* **2005**, *6* (12), 971–976. https://doi.org/10.1038/nrm1763.

(133) Booth, D. R.; Sunde, M.; Bellotti, V.; Robinson, C. V.; Hutchinson, W. L.; Fraser, P. E.; Hawkins, P. N.; Dobson, C. M.; Radford, S. E.; Blake, C. C. F.; Pepys, M. B. Instability, Unfolding and Aggregation of Human Lysozyme Variants Underlying Amyloid Fibrillogenesis. *Nature* **1997**, *385* (6619), 787–793. https://doi.org/10.1038/385787a0.

(134) Raffen, R.; Dieckman, L. J.; Szpunar, M.; Wunschl, C.; Pokkuluri, P. R.; Dave, P.; Wilkins Stevens, P.; Cai, X.; Schiffer, M.; Stevens, F. J. Physicochemical Consequences of Amino Acid Variations That Contribute to Fibril Formation by Immunoglobulin Light Chains. *Protein Sci. Publ. Protein Soc.* **1999**, *8* (3), 509–517.

(135) Stathopulos, P. B.; Rumfeldt, J. a. O.; Scholz, G. A.; Irani, R. A.; Frey, H. E.; Hallewell, R. A.; Lepock, J. R.; Meiering, E. M. Cu/Zn Superoxide Dismutase Mutants Associated with Amyotrophic Lateral Sclerosis Show Enhanced Formation of Aggregates in Vitro. *Proc. Natl. Acad. Sci. U. S. A.* **2003**, *100* (12), 7021–7026. https://doi.org/10.1073/pnas.1237797100.

(136) Sekijima, Y.; Wiseman, R. L.; Matteson, J.; Hammarström, P.; Miller, S. R.; Sawkar, A. R.; Balch, W. E.; Kelly, J. W. The Biological and Chemical Basis for Tissue-Selective Amyloid Disease. *Cell* **2005**, *121* (1), 73–85. https://doi.org/10.1016/j.cell.2005.01.018.

(137) Keenan, E. K.; Zachman, D. K.; Hirschey, M. D. Discovering the Landscape of Protein Modifications. *Mol. Cell* **2021**, *81* (9), 1868–1878. https://doi.org/10.1016/j.molcel.2021.03.015.

(138) Cohen, T. J.; Hwang, A. W.; Restrepo, C. R.; Yuan, C.-X.; Trojanowski, J. Q.; Lee, V. M. Y. An Acetylation Switch Controls TDP-43 Function and Aggregation Propensity. *Nat. Commun.* **2015**, *6* (1), 5845. https://doi.org/10.1038/ncomms6845.

(139) Maraschi, A.; Gumina, V.; Dragotto, J.; Colombrita, C.; Mompeán, M.; Buratti, E.; Silani, V.; Feligioni, M.; Ratti, A. SUMOylation Regulates TDP-43 Splicing Activity and Nucleocytoplasmic Distribution. *Mol. Neurobiol.* **2021**, *58* (11), 5682–5702. https://doi.org/10.1007/s12035-021-02505-8.

(140) Carroll, E. C.; Greene, E. R.; Martin, A.; Marqusee, S. Ubiquitination Modulates a Protein Energy Landscape Site-Specifically with Consequences for Proteasomal Degradation. *Nat. Chem. Biol.* **2020**, 16, 866–875. https://doi.org/10.1038/s41589-020-0556-3.

(141) Xin, F.; Radivojac, P. Post-Translational Modifications Induce Significant yet Not Extreme Changes to Protein Structure. *Bioinformatics* **2012**, *28* (22), 2905–2913. https://doi.org/10.1093/bioinformatics/bts541.

(142) Vellosillo, P.; Minguez, P. A Global Map of the Impact of Deletion of Post-Translational Modification Sites in Genetic Diseases. bioRxiv. **2021**, p 2020.12.20.423666. https://doi.org/10.1101/2020.12.20.423666.

(143) Neumann, M.; Kwong, L. K.; Lee, E. B.; Kremmer, E.; Flatley, A.; Xu, Y.; Forman, M.; Troost, D.; Kretzschmar, H. A.; Trojanowski, J. Q.; Lee, V. M.-Y. Phosphorylation of S409/410 of TDP-43 is a Consistent Feature in All Sporadic and Familial Forms of TDP-43 Proteinopathies. *Acta Neuropathol. (Berl.)* **2009**, *117* (2), 137–149. https://doi.org/10.1007/s00401-008-0477-9.

(144) Hasegawa, M.; Arai, T.; Nonaka, T.; Kametani, F.; Yoshida, M.; Hashizume, Y.; Beach, T. G.; Buratti, E.; Baralle, F.; Morita, M.; Nakano, I.; Oda, T.; Tsuchiya, K.; Akiyama, H. Phosphorylated TDP-43 in Frontotemporal Lobar Degeneration and Amyotrophic Lateral Sclerosis. *Ann. Neurol.* **2008**, *64* (1), 60–70. https://doi.org/10.1002/ana.21425.

(145) Li, W.; Reeb, A. N.; Lin, B.; Subramanian, P.; Fey, E. E.; Knoverek, C. R.; French, R. L.; Bigio, E. H.; Ayala, Y. M. Heat Shock-Induced Phosphorylation of TAR DNA-Binding Protein 43 (TDP-43) by MAPK/ERK Kinase Regulates TDP-43 Function. *J. Biol. Chem.* **2017**, *292* (12), 5089–5100.

(146) Sun, L.; Zhang, K.; Zhai, W.; Li, H.; Shen, H.; Yu, Z.; Chen, G. TAR DNA Binding Protein-43 Loss of Function Induced by Phosphorylation at S409/410 Blocks Autophagic Flux and Participates in Secondary Brain Injury After Intracerebral Hemorrhage. *Front. Cell. Neurosci.* **2018**, *12*, 79. https://doi.org/10.3389/fncel.2018.00079.

(147) Walker, A. K.; Spiller, K. J.; Ge, G.; Zheng, A.; Xu, Y.; Zhou, M.; Tripathy, K.; Kwong, L. K.; Trojanowski, J. Q.; Lee, V. M.-Y. Functional Recovery in New Mouse Models of ALS/FTLD after Clearance of Pathological Cytoplasmic TDP-43. *Acta Neuropathol. (Berl.)* **2015**, *130* (5), 643–660. https://doi.org/10.1007/s00401-015-1460-x.

(148) Yamashita, T.; Teramoto, S.; Kwak, S. Phosphorylated TDP-43 Becomes Resistant to Cleavage by Calpain: A Regulatory Role for Phosphorylation in TDP-43 Pathology of ALS/FTLD. *Neurosci. Res.* **2016**, *107*, 63–69. https://doi.org/10.1016/j.neures.2015.12.006.

(149) Groban, E. S.; Narayanan, A.; Jacobson, M. P. Conformational Changes in Protein Loops and Helices Induced by Post-Translational Phosphorylation. *PLOS Comput. Biol.* **2006**, *2* (4), e32. https://doi.org/10.1371/journal.pcbi.0020032.

(150) Narayanan, A.; Jacobson, M. P. Computational Studies of Protein Regulation by Post-Translational Phosphorylation. *Curr. Opin. Struct. Biol.* **2009**, *19* (2), 156–163. https://doi.org/10.1016/j.sbi.2009.02.007.

(151) Kametani, F.; Obi, T.; Shishido, T.; Akatsu, H.; Murayama, S.; Saito, Y.; Yoshida, M.; Hasegawa, M. Mass Spectrometric Analysis of Accumulated TDP-43 in Amyotrophic Lateral Sclerosis Brains. *Sci. Rep.* **2016**, *6*, 23281. https://doi.org/10.1038/srep23281.

(152) Dammer, E. B.; Fallini, C.; Gozal, Y. M.; Duong, D. M.; Rossoll, W.; Xu, P.; Lah, J. J.; Levey, A. I.; Peng, J.; Bassell, G. J.; Seyfried, N. T. Coaggregation of RNA-Binding Proteins in a Model of TDP-43 Proteinopathy with Selective RGG Motif Methylation and a Role for RRM1 Ubiquitination. *PLOS ONE* **2012**, *7* (6), e38658. https://doi.org/10.1371/journal.pone.0038658.

(153) Hagai, T.; Levy, Y. Ubiquitin Not Only Serves as a Tag but Also Assists Degradation by Inducing Protein Unfolding. *Proc. Natl. Acad. Sci.* **2010**, *107* (5), 2001–2006. https://doi.org/10.1073/pnas.0912335107.

(154) Pizzino, G.; Irrera, N.; Cucinotta, M.; Pallio, G.; Mannino, F.; Arcoraci, V.; Squadrito, F.; Altavilla, D.; Bitto, A. Oxidative Stress: Harms and Benefits for Human Health. *Oxid. Med. Cell. Longev.* **2017**, *2017*, 8416763. https://doi.org/10.1155/2017/8416763.

(155) D'Amico, E.; Factor-Litvak, P.; Santella, R. M.; Mitsumoto, H. Clinical Perspective of Oxidative Stress in Sporadic ALS. *Free Radic. Biol. Med.* **2013**, *65*, 10.1016/j.freeradbiomed.2013.06.029. https://doi.org/10.1016/j.freeradbiomed.2013.06.029.

(156) Lévy, E.; El Banna, N.; Baïlle, D.; Heneman-Masurel, A.; Truchet, S.; Rezaei, H.; Huang, M.-E.; Béringue, V.; Martin, D.; Vernis, L. Causative Links between Protein Aggregation and Oxidative Stress: A Review. *Int. J. Mol. Sci.* **2019**, *20* (16), 3896. https://doi.org/10.3390/ijms20163896.

(157) Cohen, T. J.; Hwang, A. W.; Unger, T.; Trojanowski, J. Q.; Lee, V. M. Y. Redox Signalling Directly Regulates TDP-43 via Cysteine Oxidation and Disulphide Cross-Linking. *EMBO J.* **2012**, *31* (5), 1241–1252. https://doi.org/10.1038/emboj.2011.471.

(158) Meyerowitz, J.; Parker, S. J.; Vella, L. J.; Ng, D. C.; Price, K. A.; Liddell, J. R.; Caragounis, A.; Li, Q.-X.; Masters, C. L.; Nonaka, T.; Hasegawa, M.; Bogoyevitch, M. A.; Kanninen, K. M.; Crouch, P. J.; White, A. R. C-Jun N-Terminal Kinase Controls TDP-43 Accumulation in Stress Granules Induced by Oxidative Stress. *Mol. Neurodegener.* **2011**, *6*, 57. https://doi.org/10.1186/1750-1326-6-57.

(159) Iguchi, Y.; Katsuno, M.; Takagi, S.; Ishigaki, S.; Niwa, J.; Hasegawa, M.; Tanaka, F.; Sobue, G. Oxidative Stress Induced by Glutathione Depletion Reproduces Pathological Modifications of TDP-43 Linked to TDP-43 Proteinopathies. *Neurobiol. Dis.* **2012**, *45* (3), 862–870. https://doi.org/10.1016/j.nbd.2011.12.002.

(160) Dewey, C. M.; Cenik, B.; Sephton, C. F.; Dries, D. R.; Mayer, P.; Good, S. K.; Johnson, B. A.; Herz, J.; Yu, G. TDP-43 is Directed to Stress Granules by Sorbitol, a Novel Physiological Osmotic and Oxidative Stressor. *Mol. Cell. Biol.* **2011**, *31* (5), 1098–1108. https://doi.org/10.1128/MCB.01279-10.

(161) Zuo, X.; Zhou, J.; Li, Y.; Wu, K.; Chen, Z.; Luo, Z.; Zhang, X.; Liang, Y.; Esteban, M. A.; Zhou, Y.; Fu, X.-D. TDP-43 Aggregation Induced by Oxidative Stress Causes Global

Mitochondrial Imbalance in ALS. *Nat. Struct. Mol. Biol.* **2021**, *28* (2), 132–142. https://doi.org/10.1038/s41594-020-00537-7.

(162) Day, R.; Bennion, B. J.; Ham, S.; Daggett, V. Increasing Temperature Accelerates Protein Unfolding without Changing the Pathway of Unfolding. *J. Mol. Biol.* **2002**, *322* (1), 189–203. https://doi.org/10.1016/s0022-2836(02)00672-1.

(163) Hummer, G.; Garde, S.; García, A. E.; Paulaitis, M. E.; Pratt, L. R. The Pressure Dependence of Hydrophobic Interactions is Consistent with the Observed Pressure Denaturation of Proteins. *Proc. Natl. Acad. Sci.* **1998**, *95* (4), 1552–1555. https://doi.org/10.1073/pnas.95.4.1552.

(164) Mallamace, F.; Corsaro, C.; Mallamace, D.; Vasi, S.; Vasi, C.; Baglioni, P.; Buldyrev, S. V.; Chen, S.-H.; Stanley, H. E. Energy Landscape in Protein Folding and Unfolding. *Proc. Natl. Acad. Sci.* **2016**, *113* (12), 3159–3163. https://doi.org/10.1073/pnas.1524864113.

(165) Shah, P.; Gilchrist, M. A. Is Thermosensing Property of RNA Thermometers Unique? *PLOS ONE* **2010**, *5* (7), e11308. https://doi.org/10.1371/journal.pone.0011308.

(166) Udan-Johns, M.; Bengoechea, R.; Bell, S.; Shao, J.; Diamond, M. I.; True, H. L.; Weihl, C. C.; Baloh, R. H. Prion-like Nuclear Aggregation of TDP-43 during Heat Shock is Regulated by HSP40/70 Chaperones. *Hum. Mol. Genet.* **2014**, *23* (1), 157–170. https://doi.org/10.1093/hmg/ddt408.

(167) Zacco, E.; Martin, S. R.; Thorogate, R.; Pastore, A. The RNA-Recognition Motifs of TAR DNA-Binding Protein 43 May Play a Role in the Aberrant Self-Assembly of the Protein. *Front. Mol. Neurosci.* **2018**, *11*, 372. https://doi.org/10.3389/fnmol.2018.00372.

(168) Zhang, T.; Mullane, P. C.; Periz, G.; Wang, J. TDP-43 Neurotoxicity and Protein Aggregation Modulated by Heat Shock Factor and Insulin/IGF-1 Signaling. *Hum. Mol. Genet.* **2011**, *20* (10), 1952–1965. https://doi.org/10.1093/hmg/ddr076.

(169) Mishra, P.; Patni, D.; Jha, S.K. A pH Dependent Protein Stability Switch Coupled to the Perturbed pKa of a Single Ionizable Residue. *Biophys. Chem.* **2021**, 2741 106591. https://doi.org/10.1016/j.bpc.2021.106591

(170) Patni, D.; Jha, S.K. Thermodynamic Modulation of Folding and Aggregation Energy Landscape by DNA Binding of Functional Domains of TDP-43. *Biochim. Biophys. Acta BBA-Proteins Proteom.* **2023**, 140916. (*In Press*) https://doi.org/10.1016/j.bbapap.2023.140916.

(171) Slek, C.; Ojaimi, Y. A.; Marouillat, S.; Vourc'h, P.; Lanznaster, D.; Blasco, H. Relation between PH Alterations in Cellular Models of Amyotrophic Lateral Sclerosis and TDP-43 Protein Aggregation. bioRxiv **2022**, 12.21.521010. https://doi.org/10.1101/2022.12.21.521010.

(172) Buratti, E. Chapter One - Functional Significance of TDP-43 Mutations in Disease. In *Advances in Genetics*; Friedmann, T., Dunlap, J. C., Goodwin, S. F., Eds.; Academic Press, 2015; Vol. 91, pp 1–53. https://doi.org/10.1016/bs.adgen.2015.07.001.

(173) Barmada, S. J.; Skibinski, G.; Korb, E.; Rao, E. J.; Wu, J. Y.; Finkbeiner, S. Cytoplasmic Mislocalization of TDP-43 is Toxic to Neurons and Enhanced by a Mutation Associated with Familial Amyotrophic Lateral Sclerosis. *J. Neurosci.* **2010**, *30* (2), 639–649. https://doi.org/10.1523/JNEUROSCI.4988-09.2010.

(174) Winton, M. J.; Van Deerlin, V. M.; Kwong, L. K.; Yuan, W.; Wood, E. M.; Yu, C.-E.; Schellenberg, G. D.; Rademakers, R.; Caselli, R.; Karydas, A.; Trojanowski, J. Q.; Miller, B. L.; Lee, V. M.-Y. A90V TDP-43 Variant Results in the Aberrant Localization of TDP-43 in Vitro. *FEBS Lett.* **2008**, *582* (15), 2252–2256. https://doi.org/10.1016/j.febslet.2008.05.024.

(175) Guo, W.; Chen, Y.; Zhou, X.; Kar, A.; Ray, P.; Chen, X.; Rao, E. J.; Yang, M.; Ye, H.; Zhu, L.; Liu, J.; Xu, M.; Yang, Y.; Wang, C.; Zhang, D.; Bigio, E. H.; Mesulam, M.; Shen, Y.; Xu, Q.; Fushimi, K.; Wu, J. Y. An ALS-Associated Mutation Affecting TDP-43 Enhances Protein Aggregation, Fibril Formation and Neurotoxicity. *Nat. Struct. Mol. Biol.* **2011**, *18* (7), 822–830. https://doi.org/10.1038/nsmb.2053.

(176) Kumar, V.; Pandey, P.; Idrees, D.; Prakash, A.; Lynn, Andrew. M. Delineating the Effect of Mutations on the Conformational Dynamics of N-Terminal Domain of TDP-43. *Biophys. Chem.* **2019**, *250*, 106174. https://doi.org/10.1016/j.bpc.2019.106174.

(177) Ling, S.-C.; Albuquerque, C. P.; Han, J. S.; Lagier-Tourenne, C.; Tokunaga, S.; Zhou, H.; Cleveland, D. W. ALS-Associated Mutations in TDP-43 Increase its Stability and Promote TDP-43 Complexes with FUS/TLS. *Proc. Natl. Acad. Sci.* **2010**, *107* (30), 13318–13323. https://doi.org/10.1073/pnas.1008227107.

(178) Austin, J. A.; Wright, G. S. A.; Watanabe, S.; Grossmann, J. G.; Antonyuk, S. V.; Yamanaka, K.; Hasnain, S. S. Disease Causing Mutants of TDP-43 Nucleic Acid Binding Domains Are Resistant to Aggregation and have Increased Stability and Half-Life. *Proc. Natl. Acad. Sci.* **2014**, *111* (11), 4309–4314. https://doi.org/10.1073/pnas.1317317111.

(179) Chiang, C.-H.; Grauffel, C.; Wu, L.-S.; Kuo, P.-H.; Doudeva, L. G.; Lim, C.; Shen, C.-K. J.; Yuan, H. S. Structural Analysis of Disease-Related TDP-43 D169G Mutation: Linking Enhanced Stability and Caspase Cleavage Efficiency to Protein Accumulation. *Sci. Rep.* **2016**, *6* (1), 21581. https://doi.org/10.1038/srep21581.

(180) Wang, W.; Li, L.; Lin, W.-L.; Dickson, D. W.; Petrucelli, L.; Zhang, T.; Wang, X. The ALS Disease-Associated Mutant TDP-43 Impairs Mitochondrial Dynamics and Function in Motor Neurons. *Hum. Mol. Genet.* **2013**, *22* (23), 4706–4719. https://doi.org/10.1093/hmg/ddt319.

(181) Du, X.; Li, Y.; Xia, Y.-L.; Ai, S.-M.; Liang, J.; Sang, P.; Ji, X.-L.; Liu, S.-Q. Insights into Protein–Ligand Interactions: Mechanisms, Models, and Methods. *Int. J. Mol. Sci.* **2016**, *17* (2), 144. https://doi.org/10.3390/ijms17020144.

(182) Boehr, D. D.; Nussinov, R.; Wright, P. E. The Role of Dynamic Conformational Ensembles in Biomolecular Recognition. *Nat. Chem. Biol.* **2009**, *5* (11), 789–796. https://doi.org/10.1038/nchembio.232.

(183) Gsponer, J.; Christodoulou, J.; Cavalli, A.; Bui, J. M.; Richter, B.; Dobson, C. M.; Vendruscolo, M. A Coupled Equilibrium Shift Mechanism in Calmodulin-Mediated Signal Transduction. *Struct. England1993* **2008**, *16* (5), 736–746. https://doi.org/10.1016/j.str.2008.02.017.

(184) Bernetti, M.; Cavalli, A.; Mollica, L. Protein–Ligand (Un)Binding Kinetics as a New Paradigm for Drug Discovery at the Crossroad between Experiments and Modelling. *MedChemComm* **2017**, *8* (3), 534–550. https://doi.org/10.1039/c6md00581k.

(185) Jiang, Y. X.; Cao, Q.; Sawaya, M. R.; Abskharon, R.; Ge, P.; DeTure, M.; Dickson, D. W.; Fu, J. Y.; Ogorzalek Loo, R. R.; Loo, J. A.; Eisenberg, D. S. Amyloid Fibrils in Disease FTLD-TDP are Composed of TMEM106B Not TDP-43. *Nature* **2022**, *605* (7909), 304–309. https://doi.org/10.1038/s41586-022-04670-9.

(186) Yoshimura, Y.; Lin, Y.; Yagi, H.; Lee, Y.-H.; Kitayama, H.; Sakurai, K.; So, M.; Ogi, H.; Naiki, H.; Goto, Y. Distinguishing Crystal-like Amyloid Fibrils and Glass-like Amorphous Aggregates from Their Kinetics of Formation. *Proc. Natl. Acad. Sci. U. S. A.* **2012**, *109* (36), 14446–14451. https://doi.org/10.1073/pnas.1208228109.

(187) Neumann, M. Molecular Neuropathology of TDP-43 Proteinopathies. *Int. J. Mol. Sci.* **2009**, *10* (1), 232–246. https://doi.org/10.3390/ijms10010232.

(188) Robinson, J. L.; Geser, F.; Stieber, A.; Umoh, M.; Kwong, L. K.; Van Deerlin, V. M.; Lee, V. M.-Y.; Trojanowski, J. Q. TDP-43 Skeins Show Properties of Amyloid in a Subset of ALS Cases. *Acta Neuropathol. (Berl.)* **2013**, *125* (1), 121–131. https://doi.org/10.1007/s00401-012-1055-8.

(189) Bigio, E. H.; Wu, J. Y.; Deng, H.-X.; Bit-Ivan, E. N.; Mao, Q.; Ganti, R.; Peterson, M.; Siddique, N.; Geula, C.; Siddique, T.; Mesulam, M. Inclusions in Frontotemporal Lobar Degeneration with TDP-43 Proteinopathy (FTLD-TDP) and Amyotrophic Lateral Sclerosis (ALS), but Not FTLD with FUS Proteinopathy (FTLD-FUS), Have Properties of Amyloid. *Acta Neuropathol. (Berl.)* **2013**, *125* (3), 463–465. https://doi.org/10.1007/s00401-013-1089-6.

(190) Zhuo, X.-F.; Wang, J.; Zhang, J.; Jiang, L.-L.; Hu, H.-Y.; Lu, J.-X. Solid-State NMR Reveals the Structural Transformation of the TDP-43 Amyloidogenic Region upon Fibrillation. *J. Am. Chem. Soc.* **2020**, *142* (7), 3412–3421. https://doi.org/10.1021/jacs.9b10736.

(191) Shimonaka, S.; Nonaka, T.; Suzuki, G.; Hisanaga, S.; Hasegawa, M. Templated Aggregation of TAR DNA-Binding Protein of 43 kDa (TDP-43) by Seeding with TDP-43 Peptide Fibrils. *J. Biol. Chem.* **2016**, *291* (17), 8896–8907. https://doi.org/10.1074/jbc.M115.713552.

(192) Doke, A. A.; Jha, S. K. Effect of in Vitro Solvation Conditions on Inter- and Intramolecular Assembly of Full-Length TDP-43. *J. Phys. Chem. B* **2022**, *126* (26), 4799–4813. https://doi.org/10.1021/acs.jpcb.2c02203.

(193) Che, M.-X.; Jiang, L.-L.; Li, H.-Y.; Jiang, Y.-J.; Hu, H.-Y. TDP-35 Sequesters TDP-43 into Cytoplasmic Inclusions through Binding with RNA. *FEBS Lett.* **2015**, *589* (15), 1920–1928. https://doi.org/10.1016/j.febslet.2015.06.009.

(194) Cascella, R.; Fani, G.; Bigi, A.; Chiti, F.; Cecchi, C. Partial Failure of Proteostasis Systems Counteracting TDP-43 Aggregates in Neurodegenerative Diseases. *Int. J. Mol. Sci.* **2019**, *20* (15), E3685. https://doi.org/10.3390/ijms20153685.

(195) Porta, S.; Xu, Y.; Lehr, T.; Zhang, B.; Meymand, E.; Olufemi, M.; Stieber, A.; Lee, E. B.; Trojanowski, J. Q.; Lee, V. M.-Y. Distinct Brain-Derived TDP-43 Strains from FTLD-TDP Subtypes Induce Diverse Morphological TDP-43 Aggregates and Spreading Patterns in Vitro and in Vivo. *Neuropathol. Appl. Neurobiol.* **2021**, *47* (7), 1033–1049. https://doi.org/10.1111/nan.12732.

(196) Porta, S.; Xu, Y.; Restrepo, C. R.; Kwong, L. K.; Zhang, B.; Brown, H. J.; Lee, E. B.; Trojanowski, J. Q.; Lee, V. M.-Y. Patient-Derived Frontotemporal Lobar Degeneration Brain Extracts Induce Formation and Spreading of TDP-43 Pathology in Vivo. *Nat. Commun.* **2018**, *9* (1), 4220. https://doi.org/10.1038/s41467-018-06548-9.

(197) Wells, C.; Brennan, S.; Keon, M.; Ooi, L. The Role of Amyloid Oligomers in Neurodegenerative Pathologies. *Int. J. Biol. Macromol.* **2021**, *181*, 582–604. https://doi.org/10.1016/j.ijbiomac.2021.03.113.

(198) Fang, Y.-S.; Tsai, K.-J.; Chang, Y.-J.; Kao, P.; Woods, R.; Kuo, P.-H.; Wu, C.-C.; Liao, J.-Y.; Chou, S.-C.; Lin, V.; Jin, L.-W.; Yuan, H. S.; Cheng, I. H.; Tu, P.-H.; Chen, Y.-R. Full-Length TDP-43 Forms Toxic Amyloid Oligomers that are Present in Frontotemporal Lobar Dementia-TDP Patients. *Nat. Commun.* **2014**, *5* (1), 4824. https://doi.org/10.1038/ncomms5824.

(199) Montalbano, M.; McAllen, S.; Lo Cascio, F.; Sengupta, U.; Garcia, S.; Bhatt, N.; Ellsworth, A.; Heidelman, E. A.; Johnson, O. D.; Doskocil, S.; Kayed, R. TDP-43 and Tau Oligomers in Alzheimer's Disease, Amyotrophic Lateral Sclerosis, and Frontotemporal Dementia. *Neurobiol. Dis.* **2020**, *146*, 105130. https://doi.org/10.1016/j.nbd.2020.105130.

(200) Smethurst, P.; Risse, E.; Tyzack, G. E.; Mitchell, J. S.; Taha, D. M.; Chen, Y.-R.; Newcombe, J.; Collinge, J.; Sidle, K.; Patani, R. Distinct Responses of Neurons and Astrocytes to TDP-43 Proteinopathy in Amyotrophic Lateral Sclerosis. *Brain* **2020**, *143* (2), 430–440. https://doi.org/10.1093/brain/awz419.

(201) Shih, Y.-H.; Tu, L.-H.; Chang, T.-Y.; Ganesan, K.; Chang, W.-W.; Chang, P.-S.; Fang, Y.-S.; Lin, Y.-T.; Jin, L.-W.; Chen, Y.-R. TDP-43 Interacts with Amyloid-β, Inhibits Fibrillization, and Worsens Pathology in a Model of Alzheimer's Disease. *Nat. Commun.* **2020**, *11* (1), 5950. https://doi.org/10.1038/s41467-020-19786-7.

(202) Feiler, M. S.; Strobel, B.; Freischmidt, A.; Helferich, A. M.; Kappel, J.; Brewer, B. M.; Li, D.; Thal, D. R.; Walther, P.; Ludolph, A. C.; Danzer, K. M.; Weishaupt, J. H. TDP-43 is Intercellularly Transmitted across Axon Terminals. *J. Cell Biol.* **2015**, *211* (4), 897–911. https://doi.org/10.1083/jcb.201504057.

(203) Lye, Y. S.; Chen, Y.-R. TAR DNA-Binding Protein 43 Oligomers in Physiology and Pathology. *IUBMB Life* **2022**, *74* (8), 794–811. https://doi.org/10.1002/iub.2603.

(204) Neumann, M.; Mackenzie, I. R.; Cairns, N. J.; Boyer, P. J.; Markesbery, W. R.; Smith, C. D.; Taylor, J. P.; Kretzschmar, H. A.; Kimonis, V. E.; Forman, M. S. TDP-43 in the Ubiquitin Pathology of Frontotemporal Dementia with VCP Gene Mutations. *J. Neuropathol. Exp. Neurol.* **2007**, *66* (2), 152–157. https://doi.org/10.1097/nen.0b013e31803020b9.

(205) Brady, O. A.; Meng, P.; Zheng, Y.; Mao, Y.; Hu, F. Regulation of TDP-43 Aggregation by Phosphorylation and p62/SQSTM1. *J. Neurochem.* **2011**, *116* (2), 248–259. https://doi.org/10.1111/j.1471-4159.2010.07098.x.

(206) Winton, M. J.; Igaz, L. M.; Wong, M. M.; Kwong, L. K.; Trojanowski, J. Q.; Lee, V. M.-Y. Disturbance of Nuclear and Cytoplasmic TAR DNA-Binding Protein (TDP-43) Induces Disease-like Redistribution, Sequestration, and Aggregate Formation. *J. Biol. Chem.* **2008**, *283* (19), 13302–13309. https://doi.org/10.1074/jbc.M800342200.

(207) Nishihira, Y.; Gefen, T.; Mao, Q.; Appin, C.; Kohler, M.; Walker, J.; Rademakers, R.; Rademaker, A.; Rogalski, E.; Weintraub, S.; Geula, C.; Mesulam, M.-M.; Bigio, E. H. Revisiting the Utility of TDP-43 Immunoreactive (TDP-43-ir) Pathology to Classify FTLD-TDP Subtypes. *Acta Neuropathol. (Berl.)* **2019**, *138* (1), 167–169. https://doi.org/10.1007/s00401-019-02024-w.

(208) Cairns, N. J.; Neumann, M.; Bigio, E. H.; Holm, I. E.; Troost, D.; Hatanpaa, K. J.; Foong, C.; White, C. L.; Schneider, J. A.; Kretzschmar, H. A.; Carter, D.; Taylor-Reinwald, L.; Paulsmeyer, K.; Strider, J.; Gitcho, M.; Goate, A. M.; Morris, J. C.; Mishra, M.; Kwong, L. K.; Stieber, A.; Xu, Y.; Forman, M. S.; Trojanowski, J. Q.; Lee, V. M.-Y.; Mackenzie, I. R. A. TDP-43 in Familial and Sporadic Frontotemporal Lobar Degeneration with Ubiquitin Inclusions. *Am. J. Pathol.* **2007**, *171* (1), 227–240. https://doi.org/10.2353/ajpath.2007.070182.

(209) Kustermann, M.; Manta, L.; Paone, C.; Kustermann, J.; Lausser, L.; Wiesner, C.; Eichinger, L.; Clemen, C. S.; Schröder, R.; Kestler, H. A.; Sandri, M.; Rottbauer, W.; Just, S. Loss of the Novel Vcp (Valosin Containing Protein) Interactor Washc4 Interferes with Autophagy-

Mediated Proteostasis in Striated Muscle and Leads to Myopathy in Vivo. *Autophagy* **2018**, *14* (11), 1911–1927. https://doi.org/10.1080/15548627.2018.1491491.

(210) Wani, A.; Zhu, J.; Ulrich, J. D.; Eteleeb, A.; Sauerbeck, A. D.; Reitz, S. J.; Arhzaouy, K.; Ikenaga, C.; Yuede, C. M.; Pittman, S. K.; Wang, F.; Li, S.; Benitez, B. A.; Cruchaga, C.; Kummer, T. T.; Harari, O.; Chou, T.-F.; Schröder, R.; Clemen, C. S.; Weihl, C. C. Neuronal VCP Loss of Function Recapitulates FTLD-TDP Pathology. *Cell Rep.* **2021**, *36* (3), 109399. https://doi.org/10.1016/j.celrep.2021.109399.

(211) Thorpe, J. R.; Tang, H.; Atherton, J.; Cairns, N. J. Fine Structural Analysis of the Neuronal Inclusions of Frontotemporal Lobar Degeneration with TDP-43 Proteinopathy. *J. Neural Transm. Vienna Austria 1996* **2008**, *115* (12), 1661–1671. https://doi.org/10.1007/s00702-008-0137-1.

(212) Droppelmann, C. A.; Campos-Melo, D.; Moszczynski, A. J.; Amzil, H.; Strong, M. J. TDP-43 Aggregation Inside Micronuclei Reveals a Potential Mechanism for Protein Inclusion Formation in ALS. *Sci. Rep.* **2019**, *9* (1), 19928. https://doi.org/10.1038/s41598-019-56483-y.

(213) Volkening, K.; Leystra-Lantz, C.; Yang, W.; Jaffee, H.; Strong, M. J. Tar DNA Binding Protein of 43 kDa (TDP-43), 14-3-3 Proteins and Copper/Zinc Superoxide Dismutase (SOD1) Interact to Modulate NFL mRNA Stability. Implications for Altered RNA Processing in Amyotrophic Lateral Sclerosis (ALS). *Brain Res.* **2009**, *1305*, 168–182. https://doi.org/10.1016/j.brainres.2009.09.105.

(214) Liu-Yesucevitz, L.; Bilgutay, A.; Zhang, Y.-J.; Vanderwyde, T.; Citro, A.; Mehta, T.; Zaarur, N.; McKee, A.; Bowser, R.; Sherman, M.; Petrucelli, L.; Wolozin, B. Tar DNA Binding Protein-43 (TDP-43) Associates with Stress Granules: Analysis of Cultured Cells and Pathological Brain Tissue. *PLoS ONE* **2010**, *5* (10), e13250. https://doi.org/10.1371/journal.pone.0013250.

(215) Bentmann, E.; Neumann, M.; Tahirovic, S.; Rodde, R.; Dormann, D.; Haass, C. Requirements for Stress Granule Recruitment of Fused in Sarcoma (FUS) and TAR DNA-Binding Protein of 43 kda (TDP-43). *J. Biol. Chem.* **2012**, *287* (27), 23079–23094. https://doi.org/10.1074/jbc.M111.328757.

(216) McGurk, L.; Lee, V., M.; Trojanowksi, J. Q.; Van Deerlin, V. M.; Lee, E. B.; Bonini, N. M. Poly-A Binding Protein-1 Localization to a Subset of TAR DNA-Binding Protein of 43 kDa Inclusions in Amyotrophic Lateral Sclerosis Occurs More Frequently in Patients Harboring an Expansion in C9orf72. *J. Neuropathol. Exp. Neurol.* **2014**, *73* (9), 837–845. https://doi.org/10.1097/NEN.0000000000000102.

(217) Becker, L. A.; Huang, B.; Bieri, G.; Ma, R.; Knowles, D. A.; Jafar-Nejad, P.; Messing, J.; Kim, H. J.; Soriano, A.; Auburger, G.; Pulst, S. M.; Taylor, J. P.; Rigo, F.; Gitler, A. D. Therapeutic Reduction of Ataxin-2 Extends Lifespan and Reduces Pathology in TDP-43 Mice. *Nature* **2017**, *544* (7650), 367–371. https://doi.org/10.1038/nature22038.

(218) Zhang, K.; Daigle, J. G.; Cunningham, K. M.; Coyne, A. N.; Ruan, K.; Grima, J. C.; Bowen, K. E.; Wadhwa, H.; Yang, P.; Rigo, F.; Taylor, J. P.; Gitler, A. D.; Rothstein, J. D.; Lloyd, T. E. Stress Granule Assembly Disrupts Nucleocytoplasmic Transport. *Cell* **2018**, *173* (4), 958-971.e17. https://doi.org/10.1016/j.cell.2018.03.025.

(219) Kim, H.-J.; Raphael, A. R.; LaDow, E. S.; McGurk, L.; Weber, R. A.; Trojanowski, J. Q.; Lee, V. M.-Y.; Finkbeiner, S.; Gitler, A. D.; Bonini, N. M. Therapeutic Modulation of EIF2α Phosphorylation Rescues TDP-43 Toxicity in Amyotrophic Lateral Sclerosis Disease Models. *Nat. Genet.* **2014**, *46* (2), 152–160. https://doi.org/10.1038/ng.2853.

(220) Anderson, P.; Kedersha, N. RNA Granules: Post-Transcriptional and Epigenetic Modulators of Gene Expression. *Nat. Rev. Mol. Cell Biol.* **2009**, *10* (6), 430–436. https://doi.org/10.1038/nrm2694.

(221) Alberti, S. Phase Separation in Biology. *Curr. Biol.* **2017**, *27* (20), R1097–R1102. https://doi.org/10.1016/j.cub.2017.08.069.

(222) Jain, S.; Wheeler, J. R.; Walters, R. W.; Agrawal, A.; Barsic, A.; Parker, R. ATPase-Modulated Stress Granules Contain a Diverse Proteome and Substructure. *Cell* **2016**, *164* (3), 487–498. https://doi.org/10.1016/j.cell.2015.12.038.

(223) Streit, L.; Kuhn, T.; Vomhof, T.; Bopp, V.; Ludolph, A. C.; Weishaupt, J. H.; Gebhardt, J. C. M.; Michaelis, J.; Danzer, K. M. Stress Induced TDP-43 Mobility Loss Independent of Stress Granules. *Nat. Commun.* **2022**, *13* (1), 5480. https://doi.org/10.1038/s41467-022-32939-0.

(224) Colombrita, C.; Zennaro, E.; Fallini, C.; Weber, M.; Sommacal, A.; Buratti, E.; Silani, V.; Ratti, A. TDP-43 is Recruited to Stress Granules in Conditions of Oxidative Insult. *J. Neurochem.* **2009**, *111* (4), 1051–1061. https://doi.org/10.1111/j.1471-4159.2009.06383.x.

(225) McGurk, L.; Gomes, E.; Guo, L.; Mojsilovic-Petrovic, J.; Tran, V.; Kalb, R. G.; Shorter, J.; Bonini, N. M. Poly(ADP-Ribose) Prevents Pathological Phase Separation of TDP-43 by Promoting Liquid Demixing and Stress Granule Localization. *Mol. Cell* **2018**, *71* (5), 703-717.e9. https://doi.org/10.1016/j.molcel.2018.07.002.

(226) Grese, Z. R.; Bastos, A. C.; Mamede, L. D.; French, R. L.; Miller, T. M.; Ayala, Y. M. Specific RNA Interactions Promote TDP-43 Multivalent Phase Separation and Maintain Liquid Properties. *EMBO Rep.* **2021**, *22* (12), e53632. https://doi.org/10.15252/embr.202153632.

(227) Hallegger, M.; Chakrabarti, A. M.; Lee, F. C. Y.; Lee, B. L.; Amalietti, A. G.; Odeh, H. M.; Copley, K. E.; Rubien, J. D.; Portz, B.; Kuret, K.; Huppertz, I.; Rau, F.; Patani, R.; Fawzi, N. L.; Shorter, J.; Luscombe, N. M.; Ule, J. TDP-43 Condensation Properties Specify its RNA-Binding and Regulatory Repertoire. *Cell* **2021**, *184* (18), 4680-4696.e22. https://doi.org/10.1016/j.cell.2021.07.018.

(228) Babinchak, W. M.; Haider, R.; Dumm, B. K.; Sarkar, P.; Surewicz, K.; Choi, J.-K.; Surewicz, W. K. The Role of Liquid–Liquid Phase Separation in Aggregation of the TDP-43 Low-Complexity Domain. *J. Biol. Chem.* **2019**, *294* (16), 6306–6317. https://doi.org/10.1074/jbc.RA118.007222.

(229) Pakravan, D.; Michiels, E.; Bratek-Skicki, A.; De Decker, M.; Van Lindt, J.; Alsteens, D.; Derclaye, S.; Van Damme, P.; Schymkowitz, J.; Rousseau, F.; Tompa, P.; Van Den Bosch, L. Liquid–Liquid Phase Separation Enhances TDP-43 LCD Aggregation but Delays Seeded Aggregation. *Biomolecules* **2021**, *11* (4), 548. https://doi.org/10.3390/biom11040548.

(230) Zhang, P.; Fan, B.; Yang, P.; Temirov, J.; Messing, J.; Kim, H. J.; Taylor, J. P. Chronic Optogenetic Induction of Stress Granules is Cytotoxic and Reveals the Evolution of ALS-FTD Pathology. *eLife 8*, e39578. https://doi.org/10.7554/eLife.39578.

(231) Ding, Q.; Chaplin, J.; Morris, M. J.; Hilliard, M. A.; Wolvetang, E.; Ng, D. C. H.; Noakes, P. G. TDP-43 Mutation Affects Stress Granule Dynamics in Differentiated Nsc-34 Motoneuron-like Cells. *Front. Cell Dev. Biol.* **2021**, *9*.

(232) Buchan, J. R.; Parker, R. Eukaryotic Stress Granules: The Ins and Out of Translation. *Mol. Cell* **2009**, *36* (6), 932. https://doi.org/10.1016/j.molcel.2009.11.020.

(233) Anderson, P.; Kedersha, N. Stress Granules. *Curr. Biol. CB* **2009**, *19* (10), R397-398. https://doi.org/10.1016/j.cub.2009.03.013.

(234) Protter, D. S. W.; Parker, R. Principles and Properties of Stress Granules. *Trends Cell Biol.* **2016**, *26* (9), 668–679. https://doi.org/10.1016/j.tcb.2016.05.004.

(235) Souquere, S.; Mollet, S.; Kress, M.; Dautry, F.; Pierron, G.; Weil, D. Unravelling the Ultrastructure of Stress Granules and Associated P-Bodies in Human Cells. *J. Cell Sci.* **2009**, *122* (20), 3619–3626. https://doi.org/10.1242/jcs.054437.

(236) Kedersha, N.; Stoecklin, G.; Ayodele, M.; Yacono, P.; Lykke-Andersen, J.; Fritzler, M. J.; Scheuner, D.; Kaufman, R. J.; Golan, D. E.; Anderson, P. Stress Granules and Processing Bodies are Dynamically Linked Sites of mRNP Remodeling. *J. Cell Biol.* **2005**, *169* (6), 871–884. https://doi.org/10.1083/jcb.200502088.

(237) Anderson, P.; Kedersha, N. RNA Granules. *J. Cell Biol.* **2006**, *172* (6), 803–808. https://doi.org/10.1083/jcb.200512082.

(238) Cherkasov, V.; Hofmann, S.; Druffel-Augustin, S.; Mogk, A.; Tyedmers, J.; Stoecklin, G.; Bukau, B. Coordination of Translational Control and Protein Homeostasis During Severe Heat Stress. *Curr. Biol. CB* **2013**, *23* (24), 2452–2462. https://doi.org/10.1016/j.cub.2013.09.058.

(239) Farny, N. G.; Kedersha, N. L.; Silver, P. A. Metazoan Stress Granule Assembly is Mediated by P-EIF2α-Dependent and -Independent Mechanisms. *RNA* **2009**, *15* (10), 1814–1821. https://doi.org/10.1261/rna.1684009.

(240) Kato, M.; Han, T. W.; Xie, S.; Shi, K.; Du, X.; Wu, L. C.; Mirzaei, H.; Goldsmith, E. J.; Longgood, J.; Pei, J.; Grishin, N. V.; Frantz, D. E.; Schneider, J. W.; Chen, S.; Li, L.; Sawaya, M. R.; Eisenberg, D.; Tycko, R.; McKnight, S. L. Cell-Free Formation of RNA Granules: Low Complexity Sequence Domains Form Dynamic Fibers within Hydrogels. *Cell* **2012**, *149* (4), 753–767. https://doi.org/10.1016/j.cell.2012.04.017.

(241) Lin, Y.; Protter, D. S. W.; Rosen, M. K.; Parker, R. Formation and Maturation of Phase-Separated Liquid Droplets by RNA-Binding Proteins. *Mol. Cell* **2015**, *60* (2), 208–219. https://doi.org/10.1016/j.molcel.2015.08.018.

(242) Molliex, A.; Temirov, J.; Lee, J.; Coughlin, M.; Kanagaraj, A.; Kim, H. J.; Mittag, T.; Taylor, J. P. Phase Separation by Low Complexity Domains Promotes Stress Granule Assembly and Drives Pathological Fibrillization. *Cell* **2015**, *163*, 123–133. https://doi.org/10.1016/j.cell.2015.09.015.

(243) Patel, A.; Lee, H. O.; Jawerth, L. M.; Maharana, S.; Jahnel, M.; Hein, M. Y.; Stoynov, S. S.; Mahamid, J.; Saha, S.; Franzmann, T. M.; Pozniakovski, A.; Poser, I.; Maghelli, N.; Royer, L. A.; Weigert, M.; Myers, E. W.; Grill, S. W.; Drechsel, D. N.; Hyman, A. A.; Alberti, S. A Liquid-to-Solid Phase Transition of the ALS Protein FUS Accelerated by Disease Mutation. *Cell* **2015**. https://doi.org/10.1016/j.cell.2015.07.047.

(244) Ray, S.; Singh, N.; Kumar, R.; Patel, K.; Pandey, S.; Datta, D.; Mahato, J.; Panigrahi, R.; Navalkar, A.; Mehra, S.; Gadhe, L.; Chatterjee, D.; Sawner, A. S.; Maiti, S.; Bhatia, S.; Gerez, J. A.; Chowdhury, A.; Kumar, A.; Padinhateeri, R.; Riek, R.; Krishnamoorthy, G.; Maji, S. K. α-Synuclein Aggregation Nucleates through Liquid-Liquid Phase Separation. *Nat. Chem.* **2020**, *12* (8), 705–716. https://doi.org/10.1038/s41557-020-0465-9.

(245) Khalfallah, Y.; Kuta, R.; Grasmuck, C.; Prat, A.; Durham, H. D.; Vande Velde, C. TDP-43 Regulation of Stress Granule Dynamics in Neurodegenerative Disease-Relevant Cell Types. *Sci. Rep.* **2018**, *8* (1), 7551. https://doi.org/10.1038/s41598-018-25767-0.

(246) Staderini, T.; Bigi, A.; Mongiello, D.; Cecchi, C.; Chiti, F. Biophysical Characterization of Full-Length TAR DNA-Binding Protein (TDP-43) Phase Separation. *Protein Sci. Publ. Protein Soc.* **2022**, *31* (12), e4509. https://doi.org/10.1002/pro.4509.

(247) Ajmal, M. R. Protein Misfolding and Aggregation in Proteinopathies: Causes, Mechanism and Cellular Response. *Diseases* **2023**, *11* (1), 30. https://doi.org/10.3390/diseases11010030.

(248) Forman, M. S.; Trojanowski, J. Q.; Lee, V. M.-Y. Neurodegenerative Diseases: A Decade of Discoveries Paves the Way for Therapeutic Breakthroughs. *Nat. Med.* **2004**, *10* (10), 1055–1063. https://doi.org/10.1038/nm1113.

(249) Lai, Z.; Colón, W.; Kelly, J. W. The Acid-Mediated Denaturation Pathway of Transthyretin Yields a Conformational Intermediate that can Self-Assemble into Amyloid. *Biochemistry* **1996**, *35* (20), 6470–6482. https://doi.org/10.1021/bi952501g.

(250) Guijarro, J. I.; Sunde, M.; Jones, J. A.; Campbell, I. D.; Dobson, C. M. Amyloid Fibril Formation by an SH3 Domain. *Proc. Natl. Acad. Sci. U. S. A.* **1998**, *95* (8), 4224–4228. https://doi.org/10.1073/pnas.95.8.4224.

(251) Kad, N. M.; Thomson, N. H.; Smith, D. P.; Smith, D. A.; Radford, S. E. Beta(2)-Microglobulin and its Deamidated Variant, N17D Form Amyloid Fibrils with a Range of Morphologies in Vitro. *J. Mol. Biol.* **2001**, *313* (3), 559–571. https://doi.org/10.1006/jmbi.2001.5071.

(252) McParland, V. J.; Kad, N. M.; Kalverda, A. P.; Brown, A.; Kirwin-Jones, P.; Hunter, M. G.; Sunde, M.; Radford, S. E. Partially Unfolded States of Beta(2)-Microglobulin and Amyloid Formation in Vitro. *Biochemistry* **2000**, *39* (30), 8735–8746. https://doi.org/10.1021/bi000276j.

(253) Coelho, T.; Carvalho, M.; Saraiva, M.; Alves, C.; Almeida, M.; Costa, P.; Almeida; Araùjo, P. C. A Strikingly Benign Evolution of FAP in an Individual Found to be a Compound Heterozygote for Two TTR Mutations: TTR MET 30 and TTR MET 119. **1993**.

(254) Hammarström, P.; Wiseman, R. L.; Powers, E. T.; Kelly, J. W. Prevention of Transthyretin Amyloid Disease by Changing Protein Misfolding Energetics. *Science* **2003**, *299* (5607), 713–716. https://doi.org/10.1126/science.1079589.

(255) Hammarström, P.; Schneider, F.; Kelly, J. W. Trans-Suppression of Misfolding in an Amyloid Disease. *Science* **2001**, *293* (5539), 2459–2462. https://doi.org/10.1126/science.1062245.

(256) Yee, A. W.; Aldeghi, M.; Blakeley, M. P.; Ostermann, A.; Mas, P. J.; Moulin, M.; de Sanctis, D.; Bowler, M. W.; Mueller-Dieckmann, C.; Mitchell, E. P.; Haertlein, M.; de Groot, B. L.; Boeri Erba, E.; Forsyth, V. T. A Molecular Mechanism for Transthyretin Amyloidogenesis. *Nat. Commun.* **2019**, *10*, 925. https://doi.org/10.1038/s41467-019-08609-z.

(257) Bulawa, C. E.; Connelly, S.; Devit, M.; Wang, L.; Weigel, C.; Fleming, J. A.; Packman, J.; Powers, E. T.; Wiseman, R. L.; Foss, T. R.; Wilson, I. A.; Kelly, J. W.; Labaudinière, R. Tafamidis, a Potent and Selective Transthyretin Kinetic Stabilizer that Inhibits the Amyloid Cascade. *Proc. Natl. Acad. Sci. U. S. A.* **2012**, *109* (24), 9629–9634. https://doi.org/10.1073/pnas.1121005109.

(258) Kametani, F.; Nonaka, T.; Suzuki, T.; Arai, T.; Dohmae, N.; Akiyama, H.; Hasegawa, M. Identification of Casein Kinase-1 Phosphorylation Sites on TDP-43. *Biochem. Biophys. Res. Commun.* **2009**, *382* (2), 405–409. https://doi.org/10.1016/j.bbrc.2009.03.038.

(259) Liachko, N. F.; McMillan, P. J.; Strovas, T. J.; Loomis, E.; Greenup, L.; Murrell, J. R.; Ghetti, B.; Raskind, M. A.; Montine, T. J.; Bird, T. D.; Leverenz, J. B.; Kraemer, B. C. The Tau Tubulin Kinases TTBK1/2 Promote Accumulation of Pathological TDP-43. *PLOS Genet.* **2014**, *10* (12), e1004803. https://doi.org/10.1371/journal.pgen.1004803.

(260) Liachko, N. F.; McMillan, P. J.; Guthrie, C. R.; Bird, T. D.; Leverenz, J. B.; Kraemer, B. C. CDC7 Inhibition Blocks Pathological TDP-43 Phosphorylation and Neurodegeneration. *Ann. Neurol.* **2013**, *74* (1), 39–52. https://doi.org/10.1002/ana.23870.

(261) Martínez-González, L.; Rodríguez-Cueto, C.; Cabezudo, D.; Bartolomé, F.; Andrés-Benito, P.; Ferrer, I.; Gil, C.; Martín-Requero, Á.; Fernández-Ruiz, J.; Martínez, A.; de Lago, E. Motor Neuron Preservation and Decrease of in Vivo TDP-43 Phosphorylation by Protein CK-1δ Kinase Inhibitor Treatment. *Sci. Rep.* **2020**, *10* (1), 4449. https://doi.org/10.1038/s41598-020-61265-y.

(262) Nozal, V.; Martínez-González, L.; Gomez-Almeria, M.; Gonzalo-Consuegra, C.; Santana, P.; Chaikuad, A.; Pérez-Cuevas, E.; Knapp, S.; Lietha, D.; Ramírez, D.; Petralla, S.; Monti, B.; Gil, C.; Martín-Requero, A.; Palomo, V.; de Lago, E.; Martinez, A. TDP-43 Modulation by Tau-Tubulin Kinase 1 Inhibitors: A New Avenue for Future Amyotrophic Lateral Sclerosis Therapy. *J. Med. Chem.* **2022**, *65* (2), 1585–1607. https://doi.org/10.1021/acs.jmedchem.1c01942.

(263) Ramaswami, M.; Taylor, J. P.; Parker, R. Altered "Ribostasis": RNA-Protein Granule Formation or Persistence in the Development of Degenerative Disorders. *Cell* **2013**, *154* (4), 10.1016/j.cell.2013.07.038. https://doi.org/10.1016/j.cell.2013.07.038.

(264) Li, Y. R.; King, O. D.; Shorter, J.; Gitler, A. D. Stress Granules as Crucibles of ALS Pathogenesis. *J. Cell Biol.* **2013**, *201* (3), 361–372. https://doi.org/10.1083/jcb.201302044.

(265) RNA Granules: The Good, the Bad and the Ugly. *Cell. Signal.* **2011**, *23* (2), 324–334. https://doi.org/10.1016/j.cellsig.2010.08.011.

(266) Kedersha, N. L.; Gupta, M.; Li, W.; Miller, I.; Anderson, P. RNA-Binding Proteins TIA-1 and TIAR Link the Phosphorylation of eIF-2α to the Assembly of Mammalian Stress Granules. *J. Cell Biol.* **1999**, *147* (7), 1431–1442. https://doi.org/10.1083/jcb.147.7.1431.

(267) Kedersha, N.; Anderson, P. Regulation of Translation by Stress Granules and Processing Bodies. *Prog. Mol. Biol. Transl. Sci.* **2009**, *90*, 155–185. https://doi.org/10.1016/S1877-1173(09)90004-7.

(268) Halliday, M.; Radford, H.; Sekine, Y.; Moreno, J.; Verity, N.; le Quesne, J.; Ortori, C. A.; Barrett, D. A.; Fromont, C.; Fischer, P. M.; Harding, H. P.; Ron, D.; Mallucci, G. R. Partial Restoration of Protein Synthesis Rates by the Small Molecule ISRIB Prevents Neurodegeneration without Pancreatic Toxicity. *Cell Death Dis.* **2015**, *6*, e1672. https://doi.org/10.1038/cddis.2015.49.

(269) Sidrauski, C.; McGeachy, A. M.; Ingolia, N. T.; Walter, P. The Small Molecule ISRIB Reverses the Effects of eIF2α Phosphorylation on Translation and Stress Granule Assembly. *eLife* **2015**, *4*, e05033. https://doi.org/10.7554/eLife.05033.

(270) Parker, S. J.; Meyerowitz, J.; James, J. L.; Liddell, J. R.; Nonaka, T.; Hasegawa, M.; Kanninen, K. M.; Lim, S.; Paterson, B. M.; Donnelly, P. S.; Crouch, P. J.; White, A. R.

Inhibition of TDP-43 Accumulation by Bis(Thiosemicarbazonato)-Copper Complexes. *PLoS ONE* **2012**, *7* (8), e42277. https://doi.org/10.1371/journal.pone.0042277.

(271) Grimm, D.; Kay, M. A. RNAi and Gene Therapy: A Mutual Attraction. *Hematol. Am. Soc. Hematol. Educ. Program* **2007**, 473–481. https://doi.org/10.1182/asheducation-2007.1.473.

(272) Dow, L. E.; Fisher, J.; O'Rourke, K. P.; Muley, A.; Kastenhuber, E. R.; Livshits, G.; Tschaharganeh, D. F.; Socci, N. D.; Lowe, S. W. Inducible in Vivo Genome Editing with CRISPR-Cas9. *Nat. Biotechnol.* **2015**, *33* (4), 390–394. https://doi.org/10.1038/nbt.3155.

(273) Saraiva, J.; Nobre, R. J.; Pereira de Almeida, L. Gene Therapy for the CNS Using AAVs: The Impact of Systemic Delivery by AAV9. *J. Control. Release Off. J. Control. Release Soc.* **2016**, *241*, 94–109. https://doi.org/10.1016/j.jconrel.2016.09.011.

(274) Zolgensma-Epar-Public-Assessment Report_en.Pdf. https://www.ema.europa. eu/en/ documents/assessment-report/zolgensma-epar-public-assessment-report_en.pdf (accessed 2023-03-13).

(275) Dominguez, E.; Marais, T.; Chatauret, N.; Benkhelifa-Ziyyat, S.; Duque, S.; Ravassard, P.; Carcenac, R.; Astord, S.; Pereira de Moura, A.; Voit, T.; Barkats, M. Intravenous scAAV9 Delivery of a Codon-Optimized SMN1 Sequence Rescues SMA Mice. *Hum. Mol. Genet.* **2011**, *20* (4), 681–693. https://doi.org/10.1093/hmg/ddq514.

(276) Gupta, R. M.; Musunuru, K. Expanding the Genetic Editing Tool Kit: ZFNs, TALENs, and CRISPR-Cas9. *J. Clin. Invest.* **2014**, *124* (10), 4154–4161. https://doi.org/10.1172/JCI72992.

(277) Gyorgy, B.; Ingelsson, M.; Lööv, C.; Takeda, S.; Lannfelt, L.; Hyman, B. T.; Breakefield, X. O. CRISPR-Cas9 Mediated Gene Editing in a Monogenic Form of Alzheimer Disease. *Mol. Ther.* **2016**, *24*, S226–S227. https://doi.org/10.1016/S1525-0016(16)33375-5.

(278) Pribadi, M.; Yang, Z.; Kim, T. S.; Swartz, E. W.; Huang, A. Y.; Chen, J. A.; Dokuru, D.; Baek, J.; Gao, F.; Fua, A. T.; Wojta, K.; Wang, Q.; Karydas, A.; Fong, J.; Lezcano, E.; Ng, S.; Chehab, F. F.; Vinters, H. V.; Miller, B. L.; Coppola, G. CRISPR-Cas9 Targeted Deletion of the C9orf72 Repeat Expansion Mutation Corrects Cellular Phenotypes in Patient-Derived IPS Cells. bioRxiv **2016**, p 051193. https://doi.org/10.1101/051193.

(279) Yang, S.; Chang, R.; Yang, H.; Zhao, T.; Hong, Y.; Kong, H. E.; Sun, X.; Qin, Z.; Jin, P.; Li, S.; Li, X.-J. CRISPR/Cas9-Mediated Gene Editing Ameliorates Neurotoxicity in Mouse Model of Huntington's Disease. *J. Clin. Invest.* **2017**, *127* (7), 2719–2724. https://doi.org/10.1172/JCI92087.

(280) Rinaldi, C.; Wood, M. J. A. Antisense Oligonucleotides: The next Frontier for Treatment of Neurological Disorders. *Nat. Rev. Neurol.* **2018**, *14* (1), 9–21. https://doi.org/10.1038/nrneurol.2017.148.

(281) Wu, H.; Lima, W. F.; Zhang, H.; Fan, A.; Sun, H.; Crooke, S. T. Determination of the Role of the Human RNase H1 in the Pharmacology of DNA-like Antisense Drugs. *J. Biol. Chem.* **2004**, *279* (17), 17181–17189. https://doi.org/10.1074/jbc.M311683200.

(282) Scotter, E. L.; Vance, C.; Nishimura, A. L.; Lee, Y.-B.; Chen, H.-J.; Urwin, H.; Sardone, V.; Mitchell, J. C.; Rogelj, B.; Rubinsztein, D. C.; Shaw, C. E. Differential Roles of the Ubiquitin Proteasome System and Autophagy in the Clearance of Soluble and Aggregated TDP-43 Species. *J. Cell Sci.* **2014**, *127* (6), 1263–1278. https://doi.org/10.1242/jcs.140087.

Chapter 2

Protonation-deprotonation switch controls the amyloid-like misfolding of nucleic acid binding domains of TDP-43

Reprinted with permission from Patni D., and Jha S.K. ***(2021)****. Protonation-deprotonation switch controls the amyloid-like misfolding of nucleic acid binding domains of TDP-43.* ***J. Phy. Chem. B.*** *125 (30), 8383-8394.*

2.1 Introduction

The misfolding of TDP-43 (transactive response DNA binding protein 43 kDa) into pathogenic aggregates has been linked to two fatal neurodegenerative diseases, Amyotrophic lateral sclerosis (ALS) and Frontotemporal lobar degeneration (FTLD).[1,2] ALS is a progressive neurodegenerative disease causing damage to neurons in brain and spinal cord[3,4] and FTLD is marked by progressive decrease in language and behavior.[5–8] In addition to the above two diseases, aberrant aggregates of TDP-43 have also been reported in various other neurodegenerative diseases, together referred to as TDP-43 proteinopathies.[9–12] The hallmark of these proteinopathies is the depletion of TDP-43 from the nucleus and its subsequent aggregation into the cytosol of neurons and glia cells.[9] In particular in ALS, around 97% of the patients examined till date have been reported to contain inclusions of TDP-43 in the affected areas.[13,14] It has been shown that under stress like conditions, TDP-43 form protein assemblies referred to as stress granules.[15–18] These assemblies can form disease associated aggregates in persistent chronic stress.[19] Not surprisingly, almost 90% of the cases of ALS occur due to sporadic factors, and chronic environmental stress is believed to play a major role in the aggregation of TDP-43.[4,12,20] However, the molecular mechanism of how different types of stress are detected by protein molecules and how they trigger protein misfolding remains very poorly understood.

TDP-43 belongs to a family of highly conserved nuclear RNA binding proteins known as heterogeneous nuclear ribonucleoprotein (hnRNP).[21–23] It is a 43 kDa protein composed of 414 amino acids and is divided into four domains (Figure 2.1): N-terminal, two RNA binding domains RRM1 and RRM2 connected with a 15 amino acid long linker (called TDP-43^{tRRM} hereafter) and a glycine-rich, prion-like C-terminal domain.[24–26] (UniProtKB/Swiss-Prot entry Q13148). The N-terminal contains a nuclear localization sequence (NLS) and TDP-43^{tRRM} contains a nuclear export sequence (NES). N-terminal is required for dimerization.[27] Low complexity C-terminal is required for the protein-protein interaction.[28] NLS and NES are responsible for the shuttling of TDP-43 into and out of the nucleus.[29] TDP-43^{tRRM} is the principal functional domain and is responsible for binding to pyrimidine rich nucleic acids.[12,25,30,31] It performs various crucial functions in the cells like mRNA stability, mRNA splicing etc.[32–40] under physiological conditions but has been recently reported to form disease associated aggregates in stress-like destabilizing conditions.[41–43]

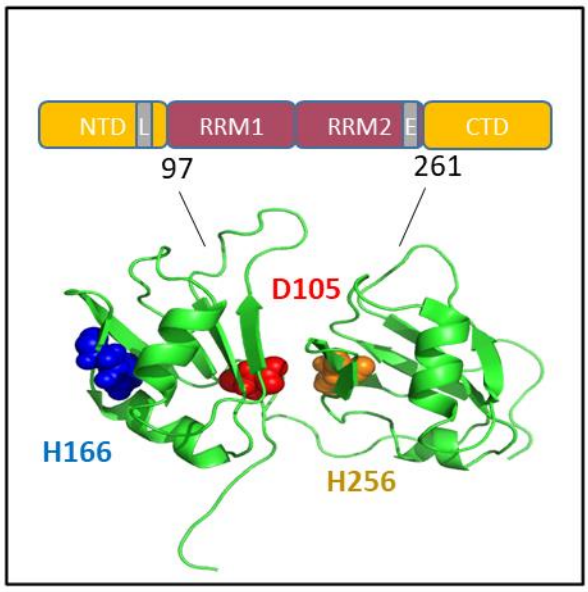

Figure 2.1 Schematic depiction of the four domains of the TDP-43. NTD: N-terminal domain; RRM1, RRM2: two RNA Recognition Motifs (collectively called TDP-43^{tRRM} in this chapter); CTD: C-terminal domain. The letters L and E correspond to the nuclear localization and nuclear export sequence, respectively. Structural representation of TDP-43^{tRRM} (amino acid residues 97-261) is shown below. The locations of the side-chains of the amino acid residues D105, H166 and H256 are highlighted. The side chains of D105, H166 and H256 are buried to the extents of 97%, 93%, and 91.5%, respectively. The image is produced using PyMOL with the PDB file 4BS2.

Cells experience a variety of stress-like conditions and each stress changes the physiochemical and solvation environment inside the cells in a different manner.[44–47] In particular, nutrient starvation stress acidifies the cytosol and increases the cytosolic proton ion concentration due to the reduced efficiency of ATP proton pump.[48–50] Some proteins or protein domains inside the cells can function as biosensors.[46,47,49,51] It has been proposed that cells sense starvation stress at the molecular level by protonating the side-chains of biosensor protein molecules that triggers their inter-molecular assembly.[47,49] Cells are believed to mitigate the starvation stress by coupling the protonation-deprotonation of proteins with their assembly-disassembly reaction, but under persistent stress these large protein assemblies lead to the formation of disease-associated amyloid-like aggregates.[15,44–47,49,51] In line with this hypothesis, we observed in a previous study that TDP-43^{tRRM} could function as a biosensor and sense pH stress but undergoes misfolding to form β-sheet rich amyloid-like fibrils on prolonged stress[41,44] in the presence of salt. However, the identity of

protein side-chains whose protonation is coupled to misfolding and aggregation of TDP-43^{tRRM} remains unknown. The side-chains of the ionizable amino acid residues buried inside the protein structure have differential pKa in the folded and unfolded states,[52] and can protonate or deprotonate only upon partial or complete unfolding. They are promising candidates to function as gatekeeper residues for protein aggregation as it often begin with partial unfolding of the protein. It has been also shown recently that pathogenicity in case of multiple disease-related proteins are more frequently associated with the buried amino acid residues.[53] In this study, we have systematically mutated the three buried ionizable amino acids to neutral amino acids whose side-chains cannot undergo protonation-deprotonation reaction (D105A, H166Q and H256Q). We compared the aggregation behavior of the mutant proteins to that of the TDP-43^{tRRM}. We observed that while the mutant protein variants D105A and H256Q show the misfolding behavior similar to the TDP-43^{tRRM}, H166Q retains the native-like (N-like) secondary structure under low pH conditions and does not misfold to the β-sheet rich, β form. Instead, H166Q predominantly forms a molten globule that binds to ANS. Our results shed important light on how site-specific modification of proteins under stress-like conditions could trigger the misfolding into amyloid-like forms in neurodegenerative diseases.

2.2 Materials and Methods

Buffers and chemicals

All the chemicals used are of highest purity grade and were obtained from the Sigma and Sisco Research Laboratories (SRL). For the pH dependent experimental studies, the following buffers for different pH range are used: 20 mM glycine-HCl (pH 1.5-3.5), 20 mM sodium acetate (pH 3.8-5.0), 20 mM 2-(N-Morpholino) ethanesulfonic acid (MES) (pH 5.5-6.0), 20 mM 3-(N-Morpholino) propanesulfonic acid (MOPS) (pH 7.0, 7.5) and 20 mM Tris (pH 8.0). All the buffers contained 150 mM KCl and 1 mM DTT (dithiothreitol). The buffers were filtered with 0.2 µm filter before use.

Expression and purification of TDP-43^{tRRM}

TDP-43^{tRRM} was purified as described previously[41] and stored in the storage buffer (10 mM potassium phosphate, 150 mM KCl, 1 mM DTT and 5% glycerol at pH 7.2). The protein was

highly pure as checked by SDS-PAGE (sodium dodecyl sulfate−polyacrylamide gel electrophoresis). The concentration of the protein was determined by measuring the absorbance at 280 nm using the extinction coefficient of 15,470 M^{-1} cm^{-1}.[54]

Site-directed mutagenesis

Primers containing the desired mutations were constructed with the help of QuikChange primer design program (https://www.agilent.com/store/primerDesignProgram.jsp). The designed primers were procured from IDT Technologies. QuikChange lightning kit from Agilent was used to generate the single site mutants of TDP-43^{tRRM} using the protocol provided with it. The mutations were confirmed by the DNA sequencing. The three mutant variants studied are D105A, H166Q and H256Q. The mutant proteins D105A and H256Q were purified using the same protocol as that of TDP-43^{tRRM}. Both of the proteins were highly pure as checked by SDS-PAGE.

Purification of H166Q

H166Q showed a different expression profile and was found in inclusion bodies and hence was extracted from the cell pellet. The BL21 cells were transformed with the mutation containing plasmid, and grown in Luria Bertani (LB) agar containing 100 µg/mL of ampicillin. Single cell colony was used to grow primary culture in LB media containing 100 µg/mL of ampicillin. The primary culture was then used to inoculate secondary culture, where cells were allowed to grow till the OD_{600} reached 0.7 in LB media. To overexpress the protein, the cells were induced by 1 mM isopropyl β-D-1-thiogalactopyranoside (IPTG) and spun at 20 °C for 24 h. The cells were pelleted at 4500 rpm for 30 minutes at 4 °C and then lysed by sonication in lysis buffer (20 mM sodium phosphate, 300 mM NaCl, 30 mM imidazole, DNaseI at pH 7.4). The lysed cells were centrifuged to separate them from the supernatant at 14,000 rpm for 45 minutes. The cell pellets were dissolved in urea containing lysis buffer (7.2 M urea, 20 mM sodium phosphate, 300 mM NaCl, 30 mM imidazole, DNaseI at pH 7.4) for 30 minutes. The cell debris was separated from the supernatant by centrifugation at 14,000 rpm for 45 minutes. The supernatant was filtered through 0.2 µm filter. Filtered supernatant was passed through Ni Sepharose™ 6-Fast Flow beads (GE Healthcare) pre-equilibrated with the urea containing lysis buffer. The bound mutant protein was eluted in the elution buffer (7.2 M urea, 20 mM sodium phosphate, 300 mM NaCl, 300 mM

imidazole at pH 7.4). The eluted protein was further desalted using a HiPrep™ 26/10 desalting column (GE Healthcare) into 7.2 M urea, 20 mM sodium phosphate buffer followed by anion exchange chromatography on a HiPrep™ Q FF 16/10 column (GE Healthcare). Finally, the protein was buffer exchanged in the storage buffer (10 mM potassium phosphate, 7.2 M urea, 1 mM DTT at pH 7.2) by passing the protein through a PD10 desalting column. 5% glycerol was further added to the protein solution. The purity of the purified protein was checked by SDS-PAGE and found to be highly pure. The protein was refolded in the desired buffer just before performing the experiments. The concentration of the protein was determined by measuring the absorbance at 280 nm, using an extinction coefficient of 15,470 M^{-1} cm^{-1}.

pH-induced formation of the β form

The buffers used at different pH are described above. For the pH-induced formation of the β form, the proteins were incubated in the desired buffer for at least 4 h at the room temperature before taking any measurement.

Circular dichroism

All the circular dichroism (CD) measurements were performed on Jasco J-815 spectropolarimeter. The instrument setting used for collecting spectra are as follows: data integration time of 4 s, bandwidth of 2 nm, data pitch of 1 nm and scan speed of 20 nm/min. Each CD spectrum collected was an average of 2 accumulations. For far-UV CD spectra, the data were collected in the wavelength range 205-250 nm and cuvette of path length 0.1 cm was used. For all the equilibrium and kinetics measurements the concentration of the protein used was in the range of 8-20 µM. The buffer spectra were taken under similar settings and were subtracted from the acquired CD spectra. The signals obtained from CD were used to calculate fraction misfolded for all the mutant variants using the equation:

$$\text{Fraction misfolded} = \frac{S_N - S_O}{S_N - S_M} \qquad (2.1)$$

where, S_N is the signal of native protein, S_O is the observed signal and S_M refers to the signal of misfolded protein.

8-anilino-1-naphthalenesulfonic acid (ANS) fluorescence assay

A stock solution of 10 mM ANS was prepared in Dimethyl Sulfoxide (DMSO). The concentration of ANS was measured by monitoring the absorbance at 350 nm and using an extinction coefficient of 5000 M^{-1} cm^{-1}.[55] TDP-43^{tRRM} (2 µM) was incubated with ANS (60 µM) for 15 minutes. The experiments were carried out on FluoroMax-4® spectrofluorometer (Horiba Scientific). The fluorescence spectrum for each sample was measured by exciting ANS at 380 nm and acquiring emission from 400-600 nm. The slits used were 1 nm and 8 nm for the excitation and the emission, respectively. Some of the ANS experiments were also performed on Perkin Elmer Fluorescence spectrometer LS55. For those experiments, the slits used were 8 nm for the excitation and 9 nm for the emission, respectively.

Analysis of the pH dependence of the N⇌ β transition

Kinetic experiments in the previous studies[44] have shown that the pH dependent N⇌ β transition occurs in multiple steps. However, at equilibrium, the N⇌ β transition monitored by CD signal at 216 nm and ANS fluorescence signal at 469 nm for TDP-43^{tRRM}, D105A and H256Q showed an apparently two-state sigmoidal change as a function of pH. This result suggests that only the N form or the β are stable enough to be populated at equilibrium under the experimental conditions used in this study (in the presence of 150 mM KCl). In view of this result, we fitted the pH dependent equilibrium data to a simplified apparently two-state model in which the formation of the misfolded β form was coupled to the protonation of a single critical residue of the N form, with a dissociation constant of K_a, as shown in the following scheme:

$$N + H^+ \rightleftharpoons NH^+ \rightleftharpoons \beta \qquad \text{(Scheme 2.1)}$$

It is assumed in the model that only NH^+ is competent to transform into the β form. In that case, the pH dependence is that of the protonation of N, and is given by a transformation of the Henderson-Hasselbalch equation:

$$Y_{obs} = \frac{Y_{NH^+} + Y_N 10^{(pH-pK_a)}}{1+10^{(pH-pK_a)}} \qquad (2.2)$$

where, Y_{obs} corresponds to the observed spectroscopic signal at a particular pH value; Y_N and Y_{NH^+} correspond to the signals of the N form and the protonated NH^+ form, respectively. It is assumed that under the experimental conditions and the protein concentrations used in this study,

$NH^+ \rightleftharpoons \beta$ equilibrium completely favors the β form and hence, the amount of NH^+ is equal to the amount of the β form.

The fraction of the protonated NH^+ form, i.e., the fraction of protein protonated at the critical titrating residue, as a function pH will be given by:

$$\text{Fraction of } NH^+ = \frac{1}{1+10^{(pH-pKa)}} \qquad (2.3)$$

Estimation of solvent accessibility of acidic amino acid residues

The absolute solvent accessible surface area (ASA) of each amino acid residue was calculated using DSSP program.[56] The relative solvent accessible surface area (RSA) was calculated by dividing absolute solvent accessible surface area by total surface area of the amino acid residue.[57,58]

Size exclusion chromatography

Size exclusion chromatography (SEC) was performed on a Superdex™ 75 10/300 GL column having fractionation range from 3 kDa to 70 kDa with a void volume of 7.2 mL and bed volume of 23.5 mL. For the SEC experiments, an AKTA Pure M FPLC system (GE Healthcare) was used. SEC experiment on the N form was performed at pH 7.5. The concentration of the protein used was 20 µM. SEC experiment on the misfolded β form was performed at pH 3.0. The concentration of the protein used was 15 µM. The flow rate used was 0.8 mL/min. All the experiments were performed at 4 °C.

In order to determine the apparent molecular weight (M_W^{app}) of the N form, we first created a calibration curve (Figure 2.S1) between the partition coefficient (K_{av}) of the five standard biomolecules (bovine serum albumin (BSA), ovalbumin, ribonuclease A, aprotonin and vitamin B12) and their respective molecular weights, as described in the GE Healthcare manual. The value of K_{av} was calculated by using the below mentioned equation:

$$K_{av} = \frac{V_e - V_o}{V_t - V_o} \qquad (2.4)$$

where, V_e refers to the elution volume of the protein molecule, V_o refers to the void volume of the column and V_t refers to the to the total bed volume of the column. The value of V_o and V_t were taken from the column specifications provided in the manual for Superdex™ 75 10/300 GL column. V_e and molecular weight of different standards were also taken from the instruction

manual provided along with the column. We used the experimentally measured elution volumes of the N form to calculate the partition coefficient and in turn determined its M_W^{app} from the calibration curve.

Transmission electron microscopy (TEM)

TEM was used to visualize the morphology of the β form. The β form (10 µL of 1 µM concentration) was loaded onto the 300-mesh carbon coated grid (Electron Microscopy Science) and allowed to get absorbed for 5 minutes. Excess sample was removed. Uranyl acetate (2%) was used for 1.5 minutes to negatively stain the samples. Excess stain was removed. This was followed by a wash by milliQ water for 1 minute to wash off any extra stain stuck on the grid. The sample was then covered and allowed to dry overnight and imaged under transmission electron microscope (Technai-T20) at an accelerating voltage of 200 kV.

Guanidinium chloride (GdmCl) induced equilibrium unfolding experiments

All the equilibrium unfolding experiments were performed at pH 7.5. Proteins (4 µM) were equilibrated in the presence of different concentration of GdmCl. The samples were excited at 280 nm and the emission was collected from 295 to 400 nm. The slit width of 1 nm was used for excitation and 8-12 nm for emission. Buffer spectra were acquired under similar settings and were subtracted from the protein spectra. The data were converted to fraction unfolded as a function of [GdmCl] and analyzed using a N⇌U two-state model, as described previously.[59]

Thioflavin T (ThT) fluorescence assay

The ThT assay was performed on the N form and the β form of all the proteins. The N form or the β form was added to the ThT buffer (50 mM Tris, pH 8.0) so that the final concentration of the protein and ThT were 2 µM and 40 µM, respectively. The ThT fluorescence was acquired within one minute of mixing. The experiments were performed on a Perkin Elmer Fluorescence spectrometer LS55. The slit width used for excitation was 8 nm and for emission was 11 nm, respectively. Excitation was carried out at 440 nm and emission spectra was monitored from 460

nm to 600 nm. Buffer spectra were acquired under the similar settings and were subtracted from the protein spectra.

2.3 Results

2.3.1 TDP-43^{tRRM} undergoes pH dependent misfolding

We monitored the changes in the secondary structure content of TDP-43^{tRRM} as a function of pH using far-UV CD (Figure 2.2A). At pH 8.0, the far-UV CD spectrum displayed minima at 208 and 222 nm. The mean value of mean residue ellipticity (MRE) at 222 nm was -4700 deg. cm^2. dmol^{-1}. The secondary structure of TDP-43^{tRRM} contains α-helices, β-sheets and disordered loops (Figure 2.1) and the far-UV CD spectrum at pH 8.0 is characteristic of TDP-43^{tRRM} in its native state.[41] We observed that the far-UV CD spectra of TDP-43^{tRRM} remains highly identical to the spectrum of the native protein in the pH range 8.0 – 5.0 (Figure 2.2A). As the pH is decreased below 5.0, the far-UV CD spectra gradually shifts to a spectrum of a β-sheet with a minima at 216 nm. This result indicates that at low pH and physiological concentration of salt (150 mM KCl), TDP-43^{tRRM} transitions into an alternative misfolded conformation that is rich in β-sheet (β form). Interestingly, both native and urea-unfolded TDP-43^{tRRM} form almost identical β form when transferred to low pH (Figure 2.S2), indicating that the β form is thermodynamically the most stable form at low pH. At pH 3.0, the value of MRE at 216 nm is -12645 deg. cm^2. dmol^{-1}. Such an increase in the value of MRE at the low pH is indicative of a disorder to order transition in the protein molecules.[41]

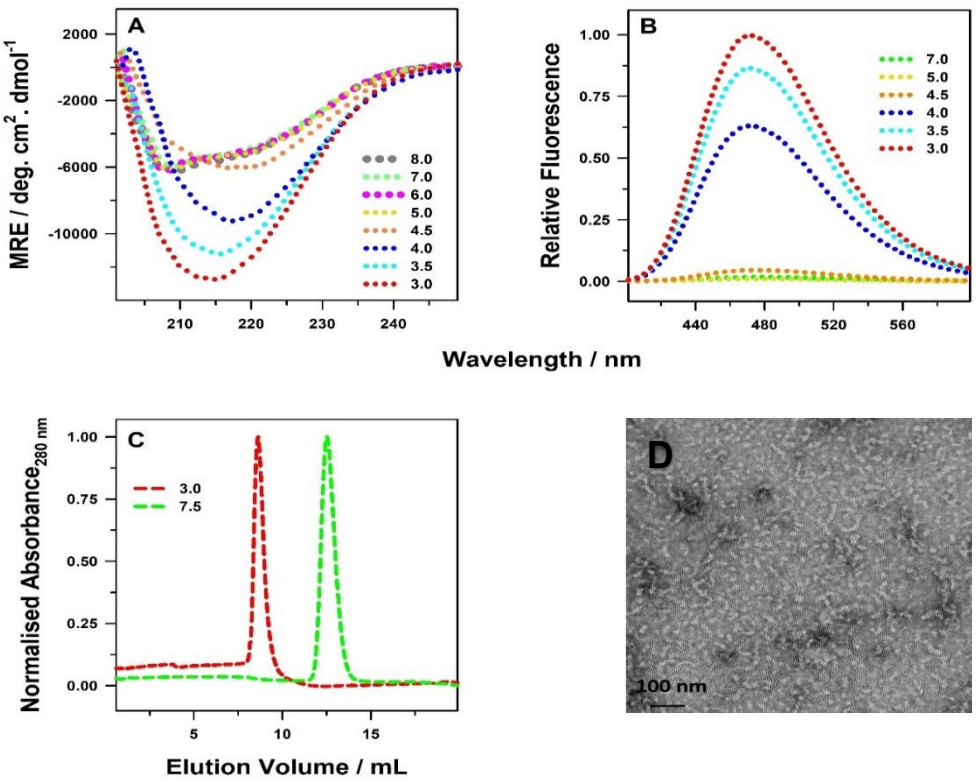

Figure 2.2 TDP-43^{tRRM} undergoes pH dependent misfolding and aggregation. (A) Far-UV CD spectra of TDP-43^{tRRM} as a function of pH. (B) Changes in the fluorescence spectrum of ANS in the presence of TDP-43^{tRRM} as a function of pH. (C) Elution profile of TDP-43^{tRRM} in SEC, in the N form (pH 7.5) and in the β form (pH 3.0). (D) TEM image of the β form.

The N⇌ β transition is also accompanied by a large change in the tertiary structure of the protein molecules, in addition to the secondary structure. Figure 2.2B shows the changes in the tertiary structure of TDP-43^{tRRM} as a function of pH as probed by the ANS binding assay. ANS is a dye that binds to the exposed hydrophobic patches of the protein resulting in its increased fluorescence signal. We observed that in the pH range 8.0-5.0, ANS does not bind to TDP-43^{tRRM} as indicated by a near zero fluorescence signal (Figure 2.2B). In contrast, the fluorescence of ANS increases dramatically as the pH is decreased in the range of 5.0-3.0. These results indicate that the misfolded β form has exposed hydrophobic patches.

2.3.2 β form is an amyloid-like protein assembly

In order to understand, if the misfolding is accompanied by inter-molecular self-assembly, we performed SEC of TDP-43^{tRRM} at different pH on a Superdex™ 75 10/300 GL column (Figure 2.2C). TDP-43^{tRRM} under native conditions at pH 7.5 elutes at 12.5 mL, corresponding to a molecular weight of 19952 Da (see Materials and Methods section), which suggests it to be a monomer. However, at pH 3.0, the elution of the TDP-43^{tRRM} occurs at 8.6 mL which is near to void volume (7.2 mL) of the column. These results indicate that the misfolded β form is a large size protein assembly.

We examined the external morphology of the β form using TEM (Figure 2.2D). In the TEM micrograph, the β form appears to be curly amyloid-like protein assembly which are around hundred nanometers long, as observed in a previous study.[44] These results indicate that the β form has amyloid-like ordered morphology.

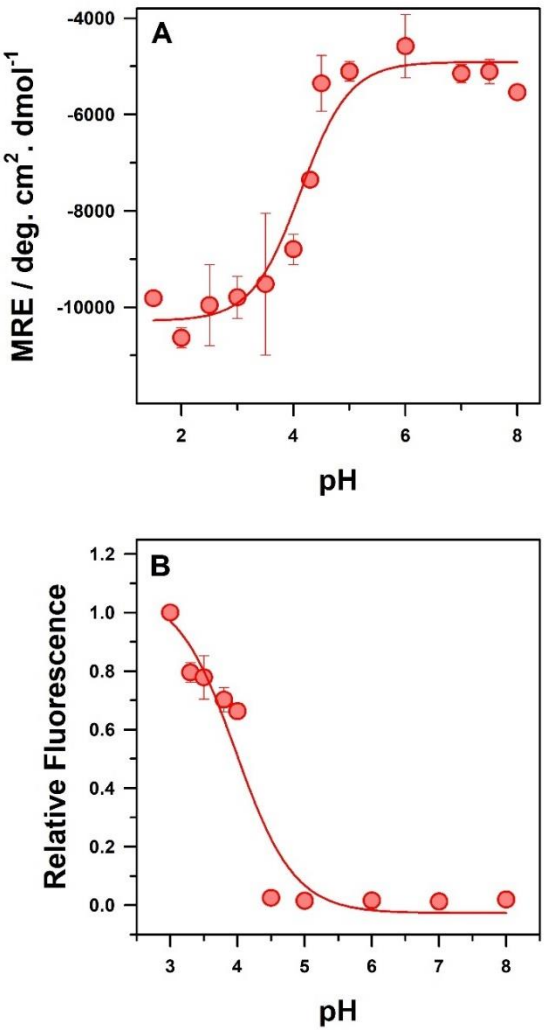

Figure 2.3 pH dependence of the misfolding transition. Changes in values of (A) MRE at 216 nm obtained by far-UV CD and (B) ANS fluorescence emission at 469 nm as a function of pH. In both the panels, the solid line through the data is a least square fit to equation 2.2. The error bars in both the panels are standard deviation in values of the data points from three independent experiments.

2.3.3 pH dependence of the N⇌ β transition

Above results show that when the monomeric N form of TDP-43^{tRRM} is subjected to low pH in the presence of 150 mM KCl, it transforms into an amyloid-like protein assembly, β form, which is rich in β sheet and has exposed hydrophobic patches. Figure 2.3A shows the pH dependence of the change in CD signal at 216 nm during the N⇌ β transition. Figure 2.3B does likewise for the change in the signal of ANS fluorescence at 469 nm. We observed that in both the cases the signal

changes in an apparently sigmoidal manner as a function of pH. These results suggest that the structural changes in the protein molecules during the N⇌ β transition, is coupled to the ionization of at least one ionizable residue. The results of the ANS experiments (Figure 2.2B and 3B) show that the disruption of side-chain packing in the hydrophobic core is required for ionization. This result suggests that the ionizing side-chain residue is buried in the protein core. We fitted the data on pH dependence of misfolding (Figure 2.3) to a model in which the formation of the misfolded β form was coupled to the protonation of at least one critical residue of the N form (see Materials and Methods). A fit of the data in Figure 2.3 to equation 2.2, yielded the pKa of the critical titrating residue to be ~4.0. This result suggests that the titration of a buried aspartate, glutamate or a histidine residue with a perturbed pKa might be coupled to the formation of the β form. There are 12 glutamate, 13 aspartate and 3 histidine residues in the primary sequence of TDP-43^{tRRM}. Out of these, only one aspartate (D105) and two histidine (H166 and H256) residues are almost completely buried in the protein structure (Figure 2.1, Table 2.S1). We targeted these three residues to check whether the ionization of any one of them is coupled to the formation of the β form. We mutated them to a neutral amino acid, one at a time, by site-directed mutagenesis to abolish the protonation-deprotonation equilibrium of their side-chains in the acidic pH. Aspartate was mutated to alanine and both the histidine residues were mutated to the glutamine because of their similar size. The three mutant protein variants are named D105A, H256Q and H166Q.

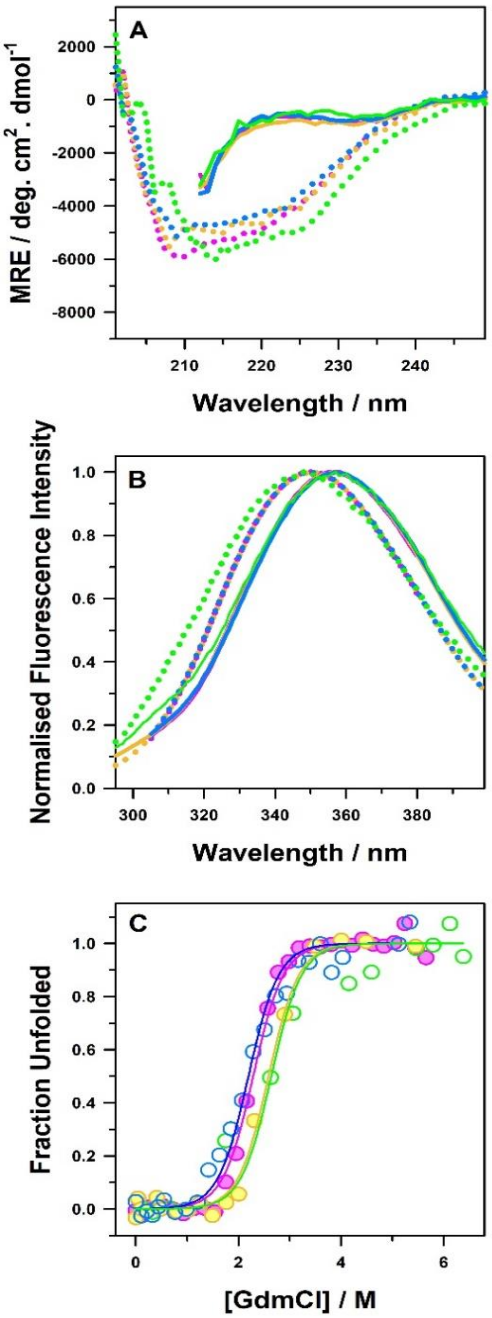

Figure 2.4 The mutant protein variants and TDP-43^{tRRM} have similar structure and thermodynamic stability. (A) Far-UV CD spectra, and (B) Fluorescence spectra of TDP-43^{tRRM} (pink lines), D105A (yellow lines), H166Q (green lines) and H256Q (blue lines), in the N form (dotted lines) and the GdmCl unfolded U form (6.2 M GdmCl) (solid lines) at pH 7.5. (C) Fraction unfolded as a function of [GdmCl] obtained from GdmCl induced equilibrium unfolding at pH 7.5 is plotted for TDP-43^{tRRM} (filled pink circles), D105A (filled yellow circles), H166Q (empty green circles)

and H256Q (empty blue circles). The solid lines through the data are fits to a two-state, N⇌U model.[59,60]

2.3.4 The single-site mutant variants have similar structure and thermodynamic stability

It was important to first check whether the single-site mutations affect the structure and stability of the N form. Figure 2.4A compares the far-UV CD spectra of D105A, H256Q and H166Q to that of the TDP-43^{tRRM} in the N form and the GdmCl unfolded U form. The far-UV CD spectra of all the mutant variants are very similar to the TDP-43^{tRRM}, both in the N form and the U form. These results indicate that the mutant variants have a very similar secondary structure to that of the TDP-43^{tRRM} and that they are completely and similarly unfolded in 6.2 M GdmCl.

Figure 2.4B compares the maximum wavelength of fluorescence emission (λ_{max}) of the D105A, H256Q and H166Q, to that of the TDP-43^{tRRM} protein in the N form and the U form. There are two tryptophan residues, W113 and W172, in the three dimensional structure of TDP-43^{tRRM}. Solvent accessibility calculations (Materials and Methods) suggest that W113 is 52% exposed and W172 is 41% exposed to the solvent. We observed that all the proteins in the N form showed similar λ_{max} of ~347 nm (Figure 2.4B), indicating that the side-chains of tryptophan residues are buried to a similar extent in the mutant variants and in the TDP-43^{tRRM}.[44] Similarly, in the U form all the proteins show similar λ_{max} of ~357 nm (Figure 2.4B), indicating that in the U form of all the proteins, tryptophan residues are completely exposed to solvent.

We measured the thermodynamic stabilities of the proteins using GdmCl induced equilibrium unfolding experiments. Figure 2.4C shows that all the three mutant variants display an apparent two-state unfolding behavior. The free energy of unfolding of TDP-43^{tRRM}, D105A, H256Q and H166Q is 4.6 kcal mol^{-1}, 5.2 kcal mol^{-1}, 4.4 kcal mol^{-1}, and 5.2 kcal mol^{-1}, respectively (Table 2.S2). These results suggest that the effect of mutations on protein stability is very minimal. These results conclude that all the mutant variants have similar secondary and tertiary structure (Figure 2.4A and 2.4B) and thermodynamic stability (Figure 2.4C) to that of the TDP-43^{tRRM}. Hence, the mutations do not alter the overall structure and stability of TDP-43^{tRRM} and all the variants can be directly compared to each other.

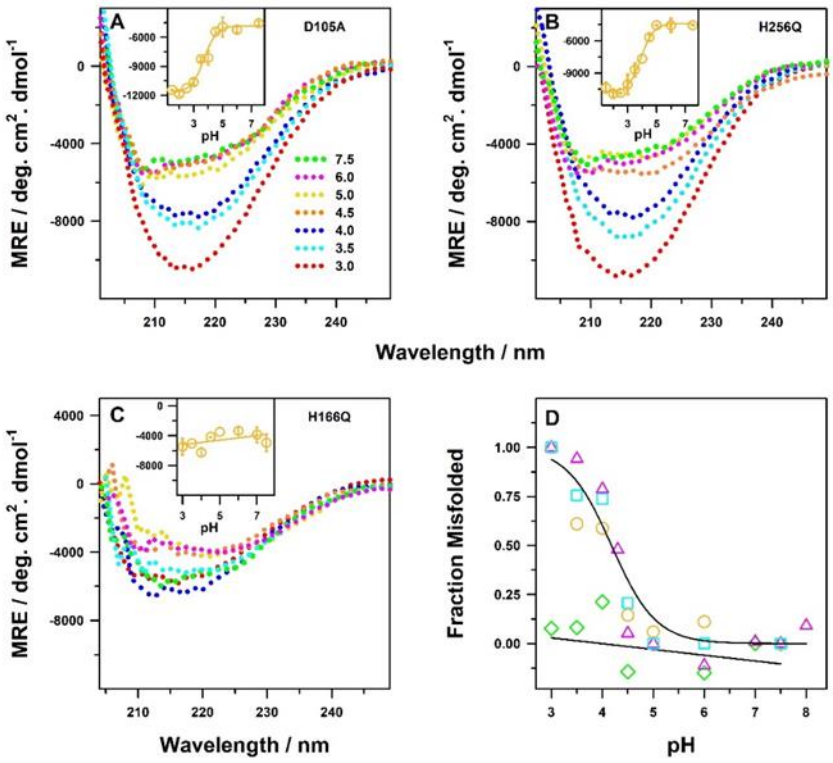

Figure 2.5 Effect of site-specific mutations on the N⇌β transition. Changes in the far-UV CD spectra of (A) D105A, (B) H256Q and (C) H166Q, as a function of pH. In panels (A) to (C) the different colors of the dotted lines denote different pH, as indicated in panel A. The insets in panels (A) to (C) show the changes in values of MRE at 216 nm as a function of pH, for the corresponding protein. The solid yellow line through the data in the insets of panel (A) and (B) is a fit to equation 2.2. The solid yellow line through the data in the inset of panel (C) is drawn to guide the eye. The error bars are the spread in values of the data points from two independent experiments. (D) Fraction of the misfolded protein as a function of pH is compared for TDP-43^{tRRM} (pink triangles), D105A (yellow circles), H256Q (blue squares) and H166Q (green diamonds). The solid black line through the data for TDP-43^{tRRM}, D105A and H256Q is a global fit to equation 2.3. The solid black line through the data for H166Q is drawn to guide the eye.

2.3.5 D105A and H256Q shows pH dependent misfolding similar to TDP-43^{tRRM}

Figure 2.5A and Figure 2.5B displays the changes in far-UV CD spectra of D105A and H256Q, respectively, as a function of pH. The pH-dependent changes in secondary structure is strikingly similar to that of the TDP-43^{tRRM} (Figure 2.2A), for both the mutant variants. The far-UV CD spectra of the N form gradually shifts to the spectrum of a β sheet, with a minima at 216 nm, as

the pH is decreased from 7.5 to 3.0. Both the mutant variants display an apparently sigmoidal change in CD signal at 216 nm with mid-point of transition at pH 4.0 (inset: Figure 2.5A and 2.5B), similar to the TDP-43^{tRRM} (Figure 2.3A). These results indicate that D105A and H256Q undergo N⇌β transition, akin to TDP-43^{tRRM}. Hence, the ionization of D105 and H256 is not coupled to the misfolding of TDP-43^{tRRM}.

2.3.6 H166Q does not show pH dependent misfolding

Interestingly, we observed that in contrast to D105A, H256Q and TDP-43^{tRRM}, the mutant variant H166Q does not undergo pH dependent misfolding. Figure 2.5C shows the changes in the far-UV CD spectra of H166Q, as a function of pH. The far-UV CD spectrum of H166Q in the N form, does not change to a spectrum of β sheet as the pH is decreased from 7.5 to 3.0. Instead, the far-UV CD spectrum remains N-like throughout the range of pH, indicating that H166Q maintains N-like secondary structure in the pH range 7.5 to 3.0. The mean value of MRE at 216 nm does not show a sigmoidal behavior as a function of pH (inset: Figure 2.5C) and remains roughly the same across the pH range (7.5 to 3.0). The average of the mean value of MRE across the pH range is -4571 deg. cm^2. dmol^{-1} and the standard deviation is -1028 deg. cm^2. dmol^{-1}. These results indicate that H166Q does not undergo N⇌β transition. Hence, the pH dependent ionization of H166Q is coupled to the misfolding of TDP-43^{tRRM} and is a key trigger for the formation of amyloid-like β form.

We calculated the fraction of misfolded β form, formed by each protein, as a function of pH from the changes in value of MRE at 216 nm (see Materials and Methods). Figure 2.5D compares the fraction misfolded as a function of pH, for all the four proteins. Remarkably, the change in the fraction of the misfolded β form during N⇌β transition of D105A and H256Q is highly comparable to that of TDP-43^{tRRM} with midpoint of transition near ~4.0. In contrast, the fraction of misfolded β form for H166Q is almost near zero in the pH range 7.5 to 3.0.

2.3.7 D105A and H256Q show similar kinetics of misfolding as TDP-43^{tRRM}

Figure 2.6A shows the kinetics of misfolding of TDP-43^{tRRM} to the β form at pH 7.5 and pH 3.0 as measured by the change in far-UV CD signal at 216 nm. At pH 7.5, the far-UV CD signal remains constant at the value of MRE of the N form as a function of time, indicating that the N-

like structure is maintained and that the rate of misfolding is negligible under N-like conditions. Upon transferring the protein under aggregation condition at pH 3.0, there appears to be a fast change in the MRE signal during the dead-time of mixing (~20-30 s), in which ~10-15% of the total expected amplitude of the MRE signal is lost. This is followed by a double exponential change in the MRE signal with time. Both the observable phases have roughly equal amplitudes. These results indicate that TDP-43^{tRRM} misfolds in at least three steps during the formation of the β form. The time constant of the two observable steps were estimated to be ~6.3 minutes and ~65 minutes at pH 3.0.

The mutant variants, D105A (Figure 2.6B), and H256Q (Figure 2.6C) show strikingly similar pH-dependent kinetics of misfolding at pH 3.0 as TDP-43^{tRRM} (Figure 2.6A). For both the proteins, there is a fast change in the MRE signal at 216 nm within the dead-time of mixing in which ~15-25 % of the total expected change in MRE signal is lost. This is followed by a double exponential change in the MRE signal with time with roughly equal amplitudes. The time-constant of the two observable phases at pH 3.0 was estimated to be ~7.1 minutes and 60 minutes for D105A and ~4.5 minutes and ~50 minutes for H256Q. At pH 7.5, for both the proteins the far-UV CD signal remains constant at the value of MRE of the N form, indicating that both the proteins maintain their native structure for a long time in N-like conditions. These results indicate that D105A and H256Q display similar pH-dependent kinetics of misfolding as TDP-43^{tRRM}.

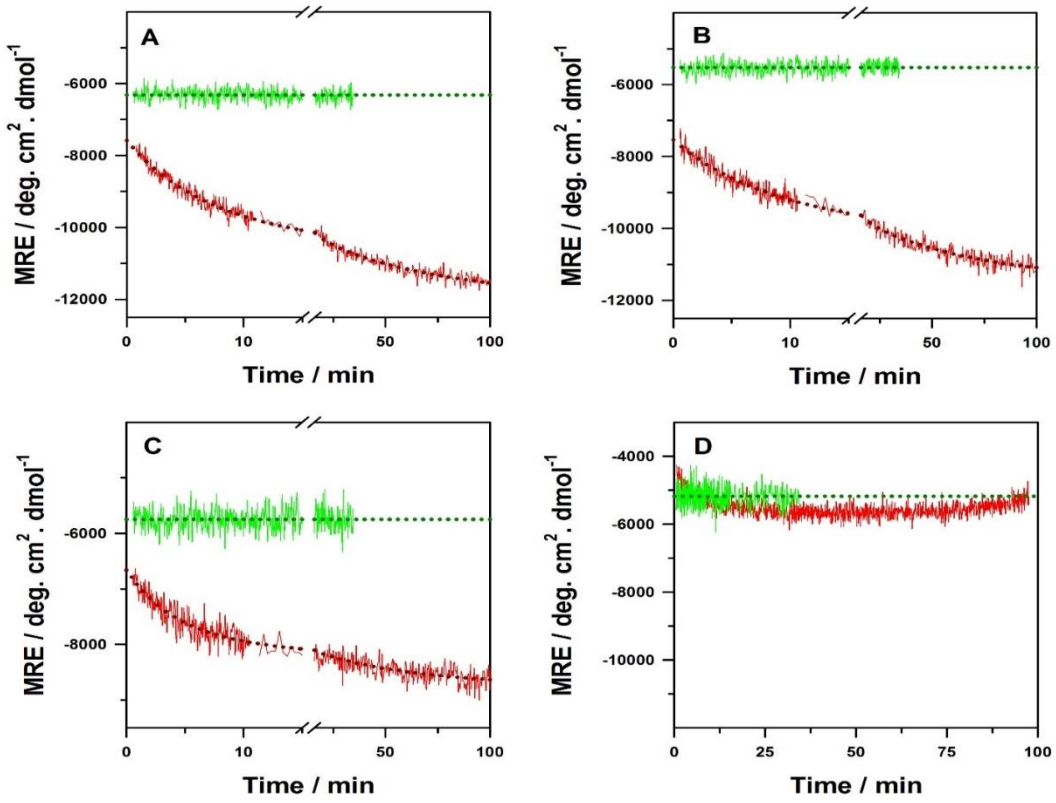

Figure 2.6 Comparison of the pH-dependent kinetics of misfolding of TDP-43^{tRRM} and the three mutant protein variants. The change in far-UV CD MRE signal at 216 nm with time is shown for (A) TDP-43^{tRRM}, (B) D105A, (C) H256Q, and (D) H166Q when each of the protein variant is transferred to pH 7.5 (green line) and pH 3.0 (red line). In panels (A), (B) and (C) the dotted red lines through the data for pH 3.0 are fits to a double exponential equation. In all the panels, the dotted green line through the data for pH 7.5 is shown to guide the eye.

2.3.8 H166Q does not show pH dependent kinetics of misfolding

In contrast to TDP-43^{tRRM}, D105A and H256Q, the N form of H166Q does not transition to the misfolded β form when transferred to pH 3.0 (Figure 2.6D). The far-UV CD signal of H166Q remains constant at the value of MRE of the N form at both pH 7.5 and pH 3.0. These results indicate that H166Q does not undergo a change in its secondary structure and retains its N-like secondary structure even at low pH, for a long time. Hence, the process of pH-dependent misfolding is highly arrested for H166Q mutant protein.

2.3.9 The low pH form of H166Q shows very little binding to amyloid staining dye ThT but has disrupted side-chain packing

H166Q maintains its N-like secondary structure under pH stress and does not misfold to form amyloid-like misfolded β form as shown by far-UV CD experiments (Figure 2.5C, Figure 2.5D and Figure 2.6D). We further probed the nature of the structure formed by H166Q at the physiological and low pH by measuring its ability to bind ThT and ANS dyes. ThT dye binds strongly to amyloid-like cross-β structure[61] and upon binding, gives an increased fluorescence at 482 nm. ThT dye has also been shown to bind weakly to non-amyloid N-like oligomers of some variants of TDP-43[62] and amorphous aggregates of other proteins.[63] Figure 2.7A and its inset compares the ThT binding efficiency of the species populated at pH 3.0 and pH 7.5 for H166Q with that of TDP-43^{tRRM}, D105A and H256Q. For all the four proteins, no ThT fluorescence was observed for the N form at pH 7.5, indicating that no amyloidogenic structures are present under N-like conditions. For the misfolded β forms formed by TDP-43^{tRRM}, D105A and H256Q at pH 3.0, a huge and similar increase in ThT fluorescence was observed, indicating the presence of amyloid like β-sheet rich structure. In contrast, the N-like species formed by H166Q at pH 3.0, showed very minimal binding to the ThT dye (~20 %). As the low pH form of H166Q does not contain amyloid like β-sheet rich structure as indicated by far-UV CD experiments (Figure 2.5C, 2.5D and Figure 2.6D), the small binding to the ThT dye might be due to the association of a small fraction of TDP-43^{tRRM} in N-like oligomers as shown previously[44,62] or amorphous aggregates[63] *via* its strand regions.

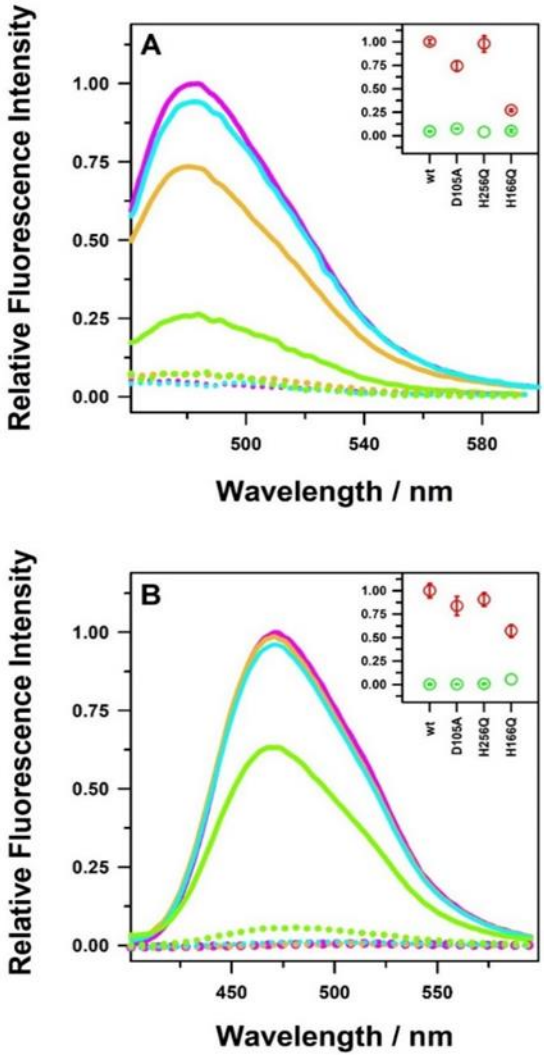

Figure 2.7 Comparison of the binding of ThT and ANS dyes to TDP-43^{tRRM} and the three mutant protein variants. TDP-43^{tRRM} (pink), D105A (yellow), H166Q (green) and H256Q (blue) were transferred to pH 7.5 (dotted lines) and pH 3.0 (solid lines) and (A) ThT fluorescence and (B) ANS fluorescence spectra were obtained for the species populated at both the pH. The inset in panel (A) compares the ThT fluorescence emission at 482 nm for all the proteins for the species populated at pH 7.5 (green circles) and pH 3.0 (red circles). The inset in panel (B) compares the ANS fluorescence emission at 469 nm for all the proteins for the species populated at pH 7.5 (green circles) and pH 3.0 (red circles). The error bars in the insets are the spread in values of the data points from two independent experiments.

ANS assay was performed to compare the tertiary structure and packing of hydrophobic core[64] of H166Q in the N form and the low pH form to that of TDP-43^{tRRM}, D105A and H256Q. Figure 2.7B and its inset compares the binding efficiency of the ANS dye to the species populated at pH

3.0 and pH 7.5 for H166Q with that of TDP-43^{tRRM}, D105A and H256Q. For all the four proteins, near zero fluorescence was observed for the N form at pH 7.5, indicating that the hydrophobic core is tightly packed in the N form of all the proteins. For the misfolded β forms formed by TDP-43^{tRRM}, D105A and H256Q at pH 3.0, a huge and similar increase in ANS fluorescence was observed, indicating that the β forms of all the proteins have similar but large amount of exposed hydrophobic patches. The N-like species formed by H166Q at pH 3.0 also binds to the ANS dye but the ANS fluorescence in this case is only about 50-60% to that of the β form of the other three proteins. This result indicates that the N-like species formed by H166Q at pH 3.0 have disrupted side-chain packing and exposed hydrophobic patches. The intact secondary structure and disrupted tertiary structure suggests that H166Q forms a molten globular structure at low pH.

The ANS binding signal of the molten globular structure formed by H166Q at low pH is around 50-60 % of the amyloid-like β forms formed for other three proteins. This is because the amyloid-like β forms have a sheeted structure and likely to have more exposed hydrophobic surface and ANS binding sites compared to a molten globule.

2.4 Discussion and Conclusions

For the proper functioning of the cells, neutral pH is required. For maintaining the neutral cytosolic pH, cells employ hydrolysis of ATP and proton pumps to export protons into the extracellular space.[47] However, during nutrient starvation stress, the ATP level decreases thereby affecting the proton pump which fails to export protons out of the cell.[65] These events lead to increase in the concentration of protons and acidification of the cytosol.[45,47,49,50] It has been suggested that one of the energy efficient ways cells employ to negate the effect of starvation stress and increased concentration of protons is the formation of large reversible protein assemblies, like stress granules.[46,47,49,51] According to this hypothesis, certain biosensors proteins in the cell (for example, Pab1,[46] Pub1[45] and Sup 35,[51] etc.) sense and mitigate starvation stress at the molecular level by coupling the protonation-deprotonation equilibrium of their side-chains with their assembly-disassembly reaction.[47,49,51] These assemblies are metastable and aggregation prone and could misfold to form amyloid-like aggregates under persistent stress. However, the experimental evidence for this hypothesis remains limited.[44–47,51] In particular, it is critical to identify the side-

chain residues whose protonation is important for formation of large assemblies and trigger misfolding.

TDP-43 is known to associate with stress granule proteins and nucleic acids *via* its TDP-43^{tRRM} and C-terminal regions under stress-like conditions[16,66,67] and misfold to form aberrant aggregates.[15] In this chapter, we showed that the monomeric N form of TDP-43^{tRRM} forms a misfolded amyloid-like protein assembly, β form, in a pH-dependent manner (Figure 2.2 and Figure 2.3). The change in secondary structure to β sheet during N to β transition occurs concomitantly with the disruption of the side-chain packing in the hydrophobic core (Figure 2.3). Both the events follow the same pH dependence with pKa around 4.0. These results suggest that ionization of a protein side-chain buried in the protein structure might be coupled to the formation of the misfolded β form. An examination of the protein structure revealed that out of all the amino acid residues whose side-chain could titrate in the acidic pH range, only D105, H166 and H256 are almost completely buried in the protein structure (Figure 2.1). We systematically mutated these residues, one at a time, to neutral amino acids to block the pH-dependent protonation-deprotonation titration of their side-chain and studied their effect on the N to β transition. All the four proteins have similar structure and thermodynamic stability under native conditions (Figure 2.4). We observed that D105A and H256Q resembled TDP-43^{tRRM} (Figure 2.2A and 3A) in their pH-dependent misfolding behavior, both in the equilibrium (Figure 2.5A, 2.5B and 2.5D) and the kinetic experiments (Figure 2.6A, 2.6B and 2.6C). However, in the case of H166Q, the pH-dependent misfolding of the N form to the β form is highly arrested (Figure 2.5C, 2.5D and 2.6D). These results indicate that H166 is the critical side-chain residue whose protonation triggers the misfolding of TDP-43^{tRRM} to the β form.

The observation that the protonation of a histidine residue triggers the misfolding of TDP-43^{tRRM} at low pH is surprising. Histidine residues usually have a pKa near 6.5 and their protonation-deprotonation is known to play important roles in protein function.[68–70] However, the pKa of the H166 in TDP-43^{tRRM} is near ~4.0 (Figure 2.3). H166 is around 93% buried in the protein structure (Figure 2.1). A positively charged arginine residue, R165, is just next to H166 in the primary sequence and it has spatial proximity with the side-chains of Q164, C173 and C175. It appears that these residues create a complex microenvironment around H166 that results in the decrease of its pKa. It is important to note that out of the other two histidine residues of TDP-

43^{tRRM}, H143 participates in DNA binding[25] at the near-neutral physiological pH whereas H256 does not participate in either the function or the misfolding. Hence, decreasing the pKa of the sole histidine residue, H166, whose protonation triggers the misfolding might be nature's way of protecting the protein from aggregation under mild starvation stress. The protonation of a single histidine residue near pH 4.0 has also been shown recently to partially control the misfolding of the mouse prion protein at low pH.[71]

We observed that H166Q forms a molten globule at low pH and a small fraction of the protein forms N-like oligomers (Figure 2.5C and Figure 2.7). We have shown earlier that TDP-43^{tRRM} can sense pH stress and form reversible metastable assemblies,[41,44] that form amyloid-like aggregate upon persistent stress. We observed that at low pH in the presence of small amount of salt (~5 mM KCl), TDP-43^{tRRM} partially unfolds to form a molten globule that slowly transforms into metastable N-like oligomers.[44] Upon increasing the concentration of salt to more than 20 mM, the N-like oligomers transform to the misfolded β form.[44] At 150 mM KCl, β form is the predominantly populated form of the protein.[44] In the case of H166Q, under these conditions only molten globule form is predominantly populated with a small amount of N-like oligomers (Figure 2.5C, Figure 2.6D and Figure 2.7), but not the β form. These results indicate that the protonation of H166 functions as a critical trigger switch that controls the amyloid-like misfolding of TDP-43^{tRRM} upon pH stress sensing. It appears that the protonation of H166 results in proximal or distal conformational changes that initiate the misfolding of the protein. The result of this study that protonation-deprotonation of a single side-chain residue controls the misfolding is an important step for understanding how the stress-induced misfolding of proteins can begin from site-specific triggers[44,45,47] and the design of site-specific therapeutics. The results of this study also hold significance for misfolding of prion proteins and prion diseases where the misfolding of protein begins in the low pH conditions encountered in the endocytic pathways.[72–74]

2.5 References

(1) Neumann, M.; Sampathu, D. M.; Kwong, L. K.; Truax, A. C.; Micsenyi, M. C.; Chou, T. T.; Bruce, J.; Schuck, T.; Grossman, M.; Clark, C. M., et al. Ubiquitinated TDP-43 in Frontotemporal Lobar Degeneration and Amyotrophic Lateral Sclerosis. *Science* **2006**, *314* (5796), 130–133. https://doi.org/10.1126/science.1134108.

(2) Arai, T.; Hasegawa, M.; Akiyama, H.; Ikeda, K.; Nonaka, T.; Mori, H.; Mann, D.; Tsuchiya, K.; Yoshida, M.; Hashizume, Y., et al. TDP-43 is a Component of Ubiquitin-Positive Tau-Negative Inclusions in Frontotemporal Lobar Degeneration and Amyotrophic Lateral Sclerosis. *Biochem. Biophys. Res. Commun.* **2006**, *351* (3), 602–611. https://doi.org/10.1016/j.bbrc.2006.10.093.

(3) Strong, M. J.; Kesavapany, S.; Pant, H. C. The Pathobiology of Amyotrophic Lateral Sclerosis: A Proteinopathy? *J. Neuropathol. Exp. Neurol.* **2005**, *64* (8), 649–664. https://doi.org/10.1097/01.jnen.0000173889.71434.ea.

(4) Rowland, L. P.; Shneider, N. A. Amyotrophic Lateral Sclerosis. *N. Engl. J. Med.* **2001**, *344* (22), 1688–1700. https://doi.org/10.1056/NEJM200105313442207.

(5) Rabinovici, G. D.; Miller, B. L. Frontotemporal Lobar Degeneration. *CNS Drugs* **2010**, *24* (5), 375–398. https://doi.org/10.2165/11533100-000000000-00000.

(6) Cairns, N. J.; Neumann, M.; Bigio, E. H.; Holm, I. E.; Troost, D.; Hatanpaa, K. J.; Foong, C.; White, C. L.; Schneider, J. A.; Kretzschmar, H. A. et al. TDP-43 in Familial and Sporadic Frontotemporal Lobar Degeneration with Ubiquitin Inclusions. *Am. J. Pathol.* **2007**, *171* (1), 227–240. https://doi.org/10.2353/ajpath.2007.070182.

(7) Neary, D.; Snowden, J. S.; Mann, D. M. Classification and Description of Frontotemporal Dementias. *Ann. N. Y. Acad. Sci.* **2000**, *920*, 46–51. https://doi.org/10.1111/j.1749-6632.2000.tb06904.x.

(8) Neary, D.; Snowden, J. S.; Mann, D. M.; Northen, B.; Goulding, P. J.; Macdermott, N. Frontal Lobe Dementia and Motor Neuron Disease. *J. Neurol. Neurosurg. Psychiatry* **1990**, *53* (1), 23–32. https://doi.org/10.1136/jnnp.53.1.23.

(9) Lee, E. B.; Lee, V. M.-Y.; Trojanowski, J. Q. Gains or Losses: Molecular Mechanisms of TDP43-Mediated Neurodegeneration. *Nat. Rev. Neurosci.* **2012**, *13* (1), 38–50. https://doi.org/10.1038/nrn3121.

(10) Dugger, B. N.; Dickson, D. W. Pathology of Neurodegenerative Diseases. *Cold Spring Harb. Perspect. Biol.* **2017**, *9* (7), a028035. https://doi.org/10.1101/cshperspect.a028035.

(11) Davidson, Y. S.; Raby, S.; Foulds, P. G.; Robinson, A.; Thompson, J. C.; Sikkink, S.; Yusuf, I.; Amin, H.; DuPlessis, D.; Troakes, C., et al. TDP-43 Pathological Changes in Early Onset Familial and Sporadic Alzheimer's Disease, Late Onset Alzheimer's Disease and Down's Syndrome: Association with Age, Hippocampal Sclerosis and Clinical Phenotype. *Acta Neuropathol. (Berl.)* **2011**, *122* (6), 703–713.

(12) Sun, Y.; Chakrabartty, A. Phase to Phase with TDP-43. *Biochemistry* **2017**, *56* (6), 809–823. https://doi.org/10.1021/acs.biochem.6b01088.

(13) Ling, S.-C.; Polymenidou, M.; Cleveland, D. W. Converging Mechanisms in ALS and FTD: Disrupted RNA and Protein Homeostasis. *Neuron* **2013**, *79* (3), 416–438. https://doi.org/10.1016/j.neuron.2013.07.033.

(14) Tan, R. H.; Ke, Y. D.; Ittner, L. M.; Halliday, G. M. ALS/FTLD: Experimental Models and Reality. *Acta Neuropathol. (Berl.)* **2017**, *133* (2), 177–196. https://doi.org/10.1007/s00401-016-1666-6.

(15) Dewey, C. M.; Cenik, B.; Sephton, C. F.; Johnson, B. A.; Herz, J.; Yu, G. TDP-43 Aggregation in Neurodegeneration: Are Stress Granules The Key? *Brain Res.* **2012**, *1462*, 16–25. https://doi.org/10.1016/j.brainres.2012.02.032.

(16) Colombrita, C.; Zennaro, E.; Fallini, C.; Weber, M.; Sommacal, A.; Buratti, E.; Silani, V.; Ratti, A. TDP-43 is Recruited to Stress Granules in Conditions of Oxidative Insult. *J. Neurochem.* **2009**, *111* (4), 1051–1061. https://doi.org/10.1111/j.1471-4159.2009.06383.x.

(17) Aulas, A.; Vande Velde, C. Alterations in Stress Granule Dynamics Driven by TDP-43 and FUS: A Link to Pathological Inclusions in ALS? *Front. Cell. Neurosci.* **2015**, *9*. https://doi.org/10.3389/fncel.2015.00423.

(18) Liu-Yesucevitz, L.; Bilgutay, A.; Zhang, Y.-J.; Vanderwyde, T.; Citro, A.; Mehta, T.; Zaarur, N.; McKee, A.; Bowser, R.; Sherman, M., et al. Tar DNA Binding Protein-43 (TDP-43) Associates with Stress Granules: Analysis of Cultured Cells and Pathological Brain Tissue. *PLoS ONE* **2010**, *5* (10), e13250. https://doi.org/10.1371/journal.pone.0013250.

(19) Parker, S. J.; Meyerowitz, J.; James, J. L.; Liddell, J. R.; Crouch, P. J.; Kanninen, K. M.; White, A. R. Endogenous TDP-43 Localized to Stress Granules Can Subsequently Form Protein Aggregates. *Neurochem. Int.* **2012**, *60* (4), 415–424. https://doi.org/10.1016/j.neuint.2012.01.019.

(20) Hergesheimer, R. C.; Chami, A. A.; de Assis, D. R.; Vourc'h, P.; Andres, C. R.; Corcia, P.; Lanznaster, D.; Blasco, H. The Debated Toxic Role of Aggregated TDP-43 in Amyotrophic Lateral Sclerosis: A Resolution in Sight? *Brain* **2019**, *142* (5), 1176–1194. https://doi.org/10.1093/brain/awz078.

(21) Dreyfuss, G.; Matunis, M. J.; Piñol-Roma, S.; Burd, C. G. hnRNP Proteins and the Biogenesis of mRNA. *Annu. Rev. Biochem.* **1993**, *62*, 289–321. https://doi.org/10.1146/annurev.bi.62.070193.001445.

(22) Geuens, T.; Bouhy, D.; Timmerman, V. The hnRNP Family: Insights into Their Role in Health and Disease. *Hum. Genet.* **2016**, *135*, 851–867. https://doi.org/10.1007/s00439-016-1683-5.

(23) Wang, H.-Y.; Wang, I.-F.; Bose, J.; Shen, C.-K. J. Structural Diversity and Functional Implications of the Eukaryotic TDP Gene Family. *Genomics* **2004**, *83* (1), 130–139. https://doi.org/10.1016/s0888-7543(03)00214-3.

(24) Kuo, P.-H.; Chiang, C.-H.; Wang, Y.-T.; Doudeva, L. G.; Yuan, H. S. The Crystal Structure of TDP-43 RRM1-DNA Complex Reveals the Specific Recognition for UG- and TG-Rich Nucleic Acids. *Nucleic Acids Res.* **2014**, *42* (7), 4712–4722. https://doi.org/10.1093/nar/gkt1407.

(25) Lukavsky, P. J.; Daujotyte, D.; Tollervey, J. R.; Ule, J.; Stuani, C.; Buratti, E.; Baralle, F. E.; Damberger, F. F.; Allain, F. H. T. Molecular Basis of UG-Rich RNA Recognition by the Human Splicing Factor TDP-43. *Nat. Struct. Mol. Biol.* **2013**, *20* (12), 1443–1449. https://doi.org/10.1038/nsmb.2698.

(26) Qin, H.; Lim, L.-Z.; Wei, Y.; Song, J. TDP-43 N Terminus Encodes a Novel Ubiquitin-Like Fold and its Unfolded Form in Equilibrium That Can Be Shifted by Binding to ssDNA. *Proc. Natl. Acad. Sci.* U.S.A. **2014**, *111* (52), 18619–18624. https://doi.org/10.1073/pnas.1413994112.

(27) Jiang, L.-L.; Xue, W.; Hong, J.-Y.; Zhang, J.-T.; Li, M.-J.; Yu, S.-N.; He, J.-H.; Hu, H.-Y. The N-Terminal Dimerization is Required for TDP-43 Splicing Activity. *Sci. Rep.* **2017**, *7* (1), 6196. https://doi.org/10.1038/s41598-017-06263-3.

(28) Conicella, A. E.; Zerze, G. H.; Mittal, J.; Fawzi, N. L. ALS Mutations Disrupt Phase Separation Mediated by -Helical Structure in the TDP-43 Low Complexity C-Terminal Domain. *Struct. Lond. Engl. 1993* **2016**, *24* (9), 1537–1549. https://doi.org/10.1016/j.str.2016.07.007.

(29) Winton, M. J.; Igaz, L. M.; Wong, M. M.; Kwong, L. K.; Trojanowski, J. Q.; Lee, V. M.-Y. Disturbance of Nuclear and Cytoplasmic TAR DNA-Binding Protein (TDP-43) Induces Disease-Like Redistribution, Sequestration, and Aggregate Formation. *J. Biol. Chem.* **2008**, *283* (19), 13302–13309. https://doi.org/10.1074/jbc.M800342200.

(30) Ou, S. H.; Wu, F.; Harrich, D.; García-Martínez, L. F.; Gaynor, R. B. Cloning and Characterization of a Novel Cellular Protein, TDP-43, That Binds to Human Immunodeficiency Virus Type 1 Tar DNA Sequence Motifs. *J. Virol.* **1995**, *69* (6), 3584–3596. https://doi.org/10.1128/JVI.69.6.3584-3596.1995.

(31) François-Moutal, L.; Perez-Miller, S.; Scott, D. D.; Miranda, V. G.; Mollasalehi, N.; Khanna, M. Structural Insights into TDP-43 and Effects of Post-Translational Modifications. *Front. Mol. Neurosci.* **2019**, *12*. https://doi.org/10.3389/fnmol.2019.00301.

(32) Ratti, A.; Buratti, E. Physiological Functions and Pathobiology of TDP-43 and FUS/TLS Proteins. *J. Neurochem.* **2016**, *138* (S1), 95–111. https://doi.org/10.1111/jnc.13625.

(33) Ayala, Y. M.; Pantano, S.; D'Ambrogio, A.; Buratti, E.; Brindisi, A.; Marchetti, C.; Romano, M.; Baralle, F. E. Human, Drosophila, and C.Elegans TDP43: Nucleic Acid Binding Properties and Splicing Regulatory Function. *J. Mol. Biol.* **2005**, *348* (3), 575–588. https://doi.org/10.1016/j.jmb.2005.02.038.

(34) Lagier-Tourenne, C.; Polymenidou, M.; Cleveland, D. W. TDP-43 and FUS/TLS: Emerging Roles in RNA Processing and Neurodegeneration. *Hum. Mol. Genet.* **2010**, *19* (R1), R46–R64. https://doi.org/10.1093/hmg/ddq137.

(35) Buratti, E.; Dörk, T.; Zuccato, E.; Pagani, F.; Romano, M.; Baralle, F. E. Nuclear Factor TDP-43 and SR Proteins Promote in Vitro and in Vivo CFTR Exon 9 Skipping. *EMBO J.* **2001**, *20* (7), 1774–1784. https://doi.org/10.1093/emboj/20.7.1774.

(36) Deshaies, J.-E.; Shkreta, L.; Moszczynski, A. J.; Sidibé, H.; Semmler, S.; Fouillen, A.; Bennett, E. R.; Bekenstein, U.; Destroismaisons, L.; Toutant, J., et al. TDP-43 Regulates the Alternative Splicing of hnRNP A1 to Yield an Aggregation-Prone Variant in Amyotrophic Lateral Sclerosis. *Brain* **2018**, *141* (5), 1320–1333. https://doi.org/10.1093/brain/awy062.

(37) Ayala, Y. M.; De Conti, L.; Avendaño-Vázquez, S. E.; Dhir, A.; Romano, M.; D'Ambrogio, A.; Tollervey, J.; Ule, J.; Baralle, M.; Buratti, E., et al. TDP-43 Regulates its mRNA Levels Through a Negative Feedback Loop. *EMBO J.* **2011**, *30* (2), 277–288. https://doi.org/10.1038/emboj.2010.310.

(38) Buratti, E.; Baralle, F. E. Characterization and Functional Implications of the RNA Binding Properties of Nuclear Factor TDP-43, A Novel Splicing Regulator of CFTR Exon 9. *J. Biol. Chem.* **2001**, *276* (39), 36337–36343. https://doi.org/10.1074/jbc.M104236200.

(39) Sephton, C. F.; Cenik, B.; Cenik, B. K.; Herz, J.; Yu, G. TDP-43 in Central Nervous System Development and Function: Clues to TDP-43-Associated Neurodegeneration. *Biol. Chem.* **2012**, *393* (7), 589–594. https://doi.org/10.1515/hsz-2012-0115.

(40) Sephton, C. F.; Good, S. K.; Atkin, S.; Dewey, C. M.; Mayer, P.; Herz, J.; Yu, G. TDP-43 is a Developmentally Regulated Protein Essential for Early Embryonic Development. *J. Biol. Chem.* **2010**, *285* (9), 6826–6834. https://doi.org/10.1074/jbc.M109.061846.

(41) Pillai, M.; Jha, S. K. The Folding and Aggregation Energy Landscapes of Tethered RRM Domains of Human TDP-43 are Coupled Via a Metastable Molten Globule-Like Oligomer. *Biochemistry* **2019**, *58* (6), 608–620. https://doi.org/10.1021/acs.biochem.8b01013.

(42) Zacco, E.; Graña-Montes, R.; Martin, S. R.; de Groot, N. S.; Alfano, C.; Tartaglia, G. G.; Pastore, A. RNA as a Key Factor in Driving or Preventing Self-Assembly of the TAR DNA-Binding Protein 43. *J. Mol. Biol.* **2019**, *431* (8), 1671–1688. https://doi.org/10.1016/j.jmb.2019.01.028.

(43) Garnier, C.; Devred, F.; Byrne, D.; Puppo, R.; Roman, A. Y.; Malesinski, S.; Golovin, A. V.; Lebrun, R.; Ninkina, N. N.; Tsvetkov, P. O. Zinc Binding to RNA Recognition Motif of TDP-43 Induces the Formation of Amyloid-Like Aggregates. *Sci. Rep.* **2017**, *7* (1), 6812. https://doi.org/10.1038/s41598-017-07215-7.

(44) Pillai, M.; Jha, S. K. Early Metastable Assembly During the Stress-Induced Formation of Worm-Like Amyloid Fibrils of Nucleic Acid Binding Domains of TDP-43. *Biochemistry* **2020**, *59* (3), 315–328. https://doi.org/10.1021/acs.biochem.9b00780.

(45) Kroschwald, S.; Munder, M. C.; Maharana, S.; Franzmann, T. M.; Richter, D.; Ruer, M.; Hyman, A. A.; Alberti, S. Different Material States of Pub1 Condensates Define Distinct Modes of Stress Adaptation and Recovery. *Cell Rep.* **2018**, *23* (11), 3327–3339. https://doi.org/10.1016/j.celrep.2018.05.041.

(46) Riback, J. A.; Katanski, C. D.; Kear-Scott, J. L.; Pilipenko, E. V.; Rojek, A. E.; Sosnick, T. R.; Drummond, D. A. Stress-Triggered Phase Separation is an Adaptive, Evolutionarily Tuned Response. *Cell* **2017**, *168* (6), 1028-1040.e19. https://doi.org/10.1016/j.cell.2017.02.027.

(47) Rabouille, C. Cell Adaptation Upon Stress: The Emerging Role of Membrane-Less Compartments. *Curr. Opin. Cell Biol.* **2017**, 9.

(48) Petrovska, I.; Nüske, E.; Munder, M. C.; Kulasegaran, G.; Malinovska, L.; Kroschwald, S.; Richter, D.; Fahmy, K.; Gibson, K.; Verbavatz, J.-M., et al. Filament Formation by Metabolic Enzymes is a Specific Adaptation to an Advanced State of Cellular Starvation. *eLife* **2014**. https://doi.org/10.7554/eLife.02409.

(49) Kroschwald, S.; Alberti, S. Gel or Die: Phase Separation as a Survival Strategy. *Cell* **2017**, *168* (6), 947–948. https://doi.org/10.1016/j.cell.2017.02.029.

(50) Munder, M. C.; Midtvedt, D.; Franzmann, T.; Nüske, E.; Otto, O.; Herbig, M.; Ulbricht, E.; Müller, P.; Taubenberger, A.; Maharana, S., et al. A pH-Driven Transition of the Cytoplasm from a Fluid- to a Solid-Like State Promotes Entry into Dormancy. *eLife* **2016**, *5*, e09347. https://doi.org/10.7554/eLife.09347.

(51) Franzmann, T. M.; Jahnel, M.; Pozniakovsky, A.; Mahamid, J.; Holehouse, A. S.; Nüske, E.; Richter, D.; Baumeister, W.; Grill, S. W.; Pappu, R. V., et al. Phase Separation of a Yeast Prion Protein Promotes Cellular Fitness. *Science* **2018**, *359* (6371). https://doi.org/10.1126/science.aao5654.

(52) Mishra, P.; Patni, D.; Jha, S. K. A pH-Dependent Protein Stability Switch Coupled to the Perturbed pka of a Single Ionizable Residue. *Biophys. Chem.* **2021**, *274*, 106591. https://doi.org/10.1016/j.bpc.2021.106591.

(53) C, S.; G, B.; Pl, M.; R, C. Mapping OMIM Disease-Related Variations on Protein Domains Reveals an Association Among Variation Type, Pfam Models, and Disease Classes. *Front. Mol. Biosci.* **2021**, *8*, 617016–617016. https://doi.org/10.3389/fmolb.2021.617016.

(54) Gill, S. C.; von Hippel, P. H. Calculation of Protein Extinction Coefficients from Amino Acid Sequence Data. *Anal. Biochem.* **1989**, *182* (2), 319–326. https://doi.org/10.1016/0003-2697(89)90602-7.

(55) Stryer, L. The Interaction of a Naphthalene Dye with Apomyoglobin and Apohemoglobin. A Fluorescent Probe of Non-Polar Binding Sites. *J. Mol. Biol.* **1965**, *13* (2), 482–495. https://doi.org/10.1016/s0022-2836(65)80111-5.

(56) Kabsch, W.; Sander, C. Dictionary of Protein Secondary Structure: Pattern Recognition of Hydrogen-Bonded and Geometrical Features. *Biopolymers* **1983**, *22* (12), 2577–2637. https://doi.org/10.1002/bip.360221211.

(57) Gong, H.; Zhang, H.; Zhu, J.; Wang, C.; Sun, S.; Zheng, W.-M.; Bu, D. Improving Prediction of Burial State of Residues by Exploiting Correlation Among Residues. *BMC Bioinformatics* **2017**, *18* (S3), 70. https://doi.org/10.1186/s12859-017-1475-5.

(58) Tien, M. Z.; Meyer, A. G.; Sydykova, D. K.; Spielman, S. J.; Wilke, C. O. Maximum Allowed Solvent Accessibilites of Residues in Proteins. *PLoS ONE* **2013**, *8* (11), e80635. https://doi.org/10.1371/journal.pone.0080635.

(59) Mishra, P.; Jha, S. K. An Alternatively Packed Dry Molten Globule-Like Intermediate in the Native State Ensemble of a Multidomain Protein. *J. Phys. Chem. B* **2017**, *121* (40), 9336–9347. https://doi.org/10.1021/acs.jpcb.7b07032.

(60) Bolen, D. W; Santoro, M.M. Unfolding Free Energy Changes Determined by the Linear Extrapolation Method. 2. Incorporation of ΔG^{o}_{N-U} Values in a Thermodynamic Cycle. *Biochemistry* **1988**, *27* (21), 8069-8074. https://doi.org/10.1021/bi00421a015

(61) Naiki, H.; Gejyo, F. Kinetic Analysis of Amyloid Fibril Formation. *Methods Enzymol.* **1999**, *309*, 305–318. https://doi.org/10.1016/s0076-6879(99)09022-9.

(62) Sun, Y.; Medina Cruz, A.; Hadley, K. C.; Galant, N. J.; Law, R.; Vernon, R. M.; Morris, V. K.; Robertson, J.; Chakrabartty, A. Physiologically Important Electrolytes as Regulators of TDP-43 Aggregation and Droplet-Phase Behavior. *Biochemistry* **2019**, *58* (6), 590–607. https://doi.org/10.1021/acs.biochem.8b00842.

(63) Adachi, M.; Noji, M.; So, M.; Sasahara, K.; Kardos, J.; Naiki, H.; Goto, Y. Aggregation-Phase Diagrams of β 2-Microglobulin Reveal Temperature and Salt Effects on Competitive Formation of Amyloids Versus Amorphous Aggregates. *J. Biol. Chem.* **2018**, *293* (38), 14775–14785. https://doi.org/10.1074/jbc.RA118.004683.

(64) Khurana, R.; Udgaonkar, J. B. Equilibrium Unfolding Studies of Barstar: Evidence for an Alternative Conformation Which Resembles a Molten Globule. *Biochemistry* **1994**, *33* (1), 106–115. https://doi.org/10.1021/bi00167a014.

(65) Orij, R.; Brul, S.; Smits, G. J. Intracellular pH is a Tightly Controlled Signal in Yeast. *Biochim. Biophys. Acta* **2011**, *1810* (10), 933–944. https://doi.org/10.1016/j.bbagen.2011.03.011.

(66) Bentmann, E.; Neumann, M.; Tahirovic, S.; Rodde, R.; Dormann, D.; Haass, C. Requirements for Stress Granule Recruitment of Fused in Sarcoma (FUS) and Tar DNA-Binding Protein of 43 kDa (TDP-43). *J. Biol. Chem.* **2012**, *287* (27), 23079–23094. https://doi.org/10.1074/jbc.M111.328757.

(67) Mann, J. R.; Gleixner, A. M.; Mauna, J. C.; Gomes, E.; DeChellis-Marks, M. R.; Needham, P. G.; Copley, K. E.; Hurtle, B.; Portz, B.; Pyles, N. J., et al. RNA Binding Antagonizes Neurotoxic Phase Transitions of TDP-43. *Neuron* **2019**, *102* (2), 321-338.e8. https://doi.org/10.1016/j.neuron.2019.01.048.

(68) Medina, E.; Villalobos, P.; Coñuecar, R.; Ramírez-Sarmiento, C. A.; Babul, J. The Protonation State of an Evolutionarily Conserved Histidine Modulates Domainswapping Stability of FoxP1. *Sci. Rep.* **2019**, *9* (1), 5441. https://doi.org/10.1038/s41598-019-41819-5.

(69) Hu, J.; Fu, R.; Nishimura, K.; Zhang, L.; Zhou, H.-X.; Busath, D. D.; Vijayvergiya, V.; Cross, T. A. Histidines, Heart of the Hydrogen Ion Channel from Influenza A Virus: Toward an

Understanding of Conductance and Proton Selectivity. *Proc. Natl. Acad. Sci. U.S.A.* **2006**, *103* (18), 6865–6870. https://doi.org/10.1073/pnas.0601944103.

(70) Rötzschke, O.; Lau, J. M.; Hofstätter, M.; Falk, K.; Strominger, J. L. A pH-Sensitive Histidine Residue as Control Element for Ligand Release from HLA-DR Molecules. *Proc. Natl. Acad. Sci. U.S.A.* **2002**, *99* (26), 16946–16950. https://doi.org/10.1073/pnas.212643999.

(71) Singh, J.; Udgaonkar, J. B. Unraveling the Molecular Mechanism of pH-Induced Misfolding and Oligomerization of the Prion Protein. *J. Mol. Biol.* **2016**, *428* (6), 1345–1355. https://doi.org/10.1016/j.jmb.2016.01.030.

(72) Borchelt, D. R.; Taraboulos, A.; Prusiner, S. B. Evidence for Synthesis of Scrapie Prion Proteins in the Endocytic Pathway. *J. Biol. Chem.* **1992**, *267* (23), 16188–16199.

(73) Arnold, J. E.; Tipler, C.; Laszlo, L.; Hope, J.; Landon, M.; Mayer, R. J. The Abnormal Isoform of the Prion Protein Accumulates in Late-Endosome-Like Organelles in Scrapie-Infected Mouse Brain. *J. Pathol.* **1995**, *176* (4), 403–411. https://doi.org/10.1002/path.1711760412.

(74) Sunyach, C.; Jen, A.; Deng, J.; Fitzgerald, K. T.; Frobert, Y.; Grassi, J.; McCaffrey, M. W.; Morris, R. The Mechanism of Internalization of Glycosylphosphatidylinositol-Anchored Prion Protein. *EMBO J.* **2003**, *22* (14), 3591–3601. https://doi.org/10.1093/emboj/cdg344.

2.6 Supporting figures

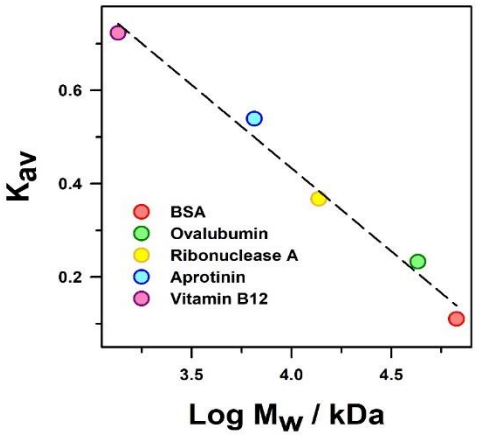

Figure 2.S1 Calibration curve for the determination of the apparent molecular weight (M_w^{app}) of the N form from the size exclusion chromatography. Log of molecular weight of five standard biomolecules is plotted against their respective partition coefficient (K_{av}). The K_{av} for all the standard biomolecules is calculated from their respective elution volumes noted from the manufacturer provided manual for Superdex™ 75 10/300 GL column using equation 2.4.The dashed line is a linear fit to the data and used to calculate the $M_w^{app}$of the N form in figure 2.2C (main text).

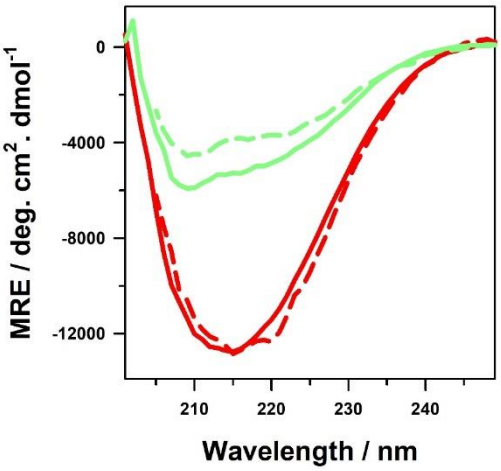

Figure 2.S2 Both native and urea unfolded TDP-43^{tRRM} form almost identical β form when transferred to low pH. Far-UV CD spectra acquired after native TDP-43^{tRRM} was transferred to pH 7.0 (solid green line) and pH 3.0 (solid red line) buffer. Far-UV CD spectra acquired after urea unfolded TDP-43^{tRRM} (in 8.2 M urea, pH 7.5) was transferred to pH 7.0 (dashed green) and pH 3.0 (dashed red line) buffer. All the buffers contain 150 mM KCl and 1 mM DTT.

Table 2.S1 Table of relative solvent accessibility of acidic residues of TDP-43^{tRRM}

Residues	ASA (DSSP)[1] (Å^2)	Total surface area[2] (Å^2)	% relative surface accessible area (% RSA)	% surface buried
D105	6	193	3.1	96.9
D119	46	193	23.8	76.2
D138	33	193	17.1	82.9
D169	105	193	54.4	45.6
D174	84	193	43.5	56.5
D185	141	193	73.1	26.9
D201	92	193	47.7	52.3
D205	117	193	60.6	39.4
D216	104	193	53.9	46.1
D219	97	193	50.3	49.7
D236	58	193	30.1	69.9
D237	90	193	46.6	53.4
D247	4	193	2.1	97.9
E117	63	223	28.2	71.7
E122	111	223	49.8	50.2
E129	116	223	52.0	48.0
E154	86	223	38.6	61.4
E156	80	223	35.9	64.1
E186	152	223	68.2	31.8
E200	161	223	72.2	27.8
E204	66	223	29.6	70.4
E206	69	223	30.9	69.1
E209	139	223	62.3	37.4
E246	112	223	50.2	49.8
E261	168	223	75.3	24.7
H143	117	224	52.2	47.8
H166	16	224	7.1	92.9
H256	19	224	8.5	91.5

* D105, D247, H166 and H256 are the four acidic residues which are more than 90% buried in protein structure. D247 was not considered in this study as its role in protein stability and aggregation has been studied in detail in a previous work.[3]

Table 2.S2 Table of thermodynamic parameters for the equilibrium unfolding of the N form of the protein variants used in this study

variant	ΔG (kcal mol^{-1})	m (kcal $mol^{-1}M^{-1}$)	C_m (M)
$TDP\text{-}43^{tRRM}$	4.6	2.0	2.3
D105A	5.2	2.0	2.6
H256Q	4.4	2.0	2.2
H166Q	5.2	2.0	2.6

References

(1) Kabsch, W.; Sander, C. Dictionary of Protein Secondary Structure: Pattern Recognition of Hydrogen-Bonded and Geometrical Features. *Biopolymers* **1983**, *22* (12), 2577–2637. https://doi.org/10.1002/bip.360221211.

(2) Tien, M. Z.; Meyer, A. G.; Sydykova, D. K.; Spielman, S. J.; Wilke, C. O. Maximum Allowed Solvent Accessibilites of Residues in Proteins. *PLoS ONE* **2013**, *8* (11), e80635. https://doi.org/10.1371/journal.pone.0080635.

(3) Shodai, A.; Ido, A.; Fujiwara, N.; Ayaki, T.; Morimura, T.; Oono, M.; Uchida, T.; Takahashi, R.; Ito, H.; Urushitani, M. Conserved Acidic Amino Acid Residues in a Second RNA Recognition Motif Regulate Assembly and Function of TDP-43. *PLoS ONE* **2012**, *7* (12), e52776. https://doi.org/10.1371/journal.pone.0052776.

Chapter 3

Thermodynamic modulation of folding and aggregation energy landscape by DNA binding of functional domains of TDP-43

Reprinted with permission from Patni D., and Jha S.K. ***(2023)****. Thermodynamic modulation of folding and aggregation energy landscape by DNA binding of functional domains of TDP-43.* ***Biochim. Biophys. Acta- BBA Proteins Proteom.*** *1871 (4), 140196. https://doi.org/10.1016/j.bbapap.2023.140916.*

3.1 Introduction

TAR DNA binding protein (TDP-43) is a ubiquitously expressed member of the heterogeneous nuclear ribonucleoprotein family (hnRNP).[1,2] It is a 414 amino acid-long multidomain protein (Figure 3.1). It consists of an N-terminal domain (NTD), two tandem RNA Recognition Motifs (RRM 1 and RRM 2, referred to as TDP-43^{tRRM}), and a C-terminal domain (CTD).[3] TDP-43^{tRRM} is the primary functional domain of the protein, which associates explicitly with the UG and TG-rich nucleic acid sequences.[4] These motifs were highly conserved throughout evolution.[5,6] Under normal physiological conditions, TDP-43 predominately resides in the nucleus but often shuttles to the cytoplasm to perform some of its functions.[7,8] In its native state, TDP-43, with the help of TDP-43^{tRRM}, performs crucial functions like mRNA splicing,[9–11] mRNA transcription,[12,13] non-coding RNA processing,[14] embryonic development,[15] and CNS development.[16] TDP-43 is also involved in mRNA stability,[17–20] and mRNA transport,[21] along with self-regulating its level in the cells.[22] However, it has been observed that TDP-43 loses its natively folded conformation under stress conditions.[23,24] Cytoplasmic aggregates of the TDP-43 have been predominately found in Amyotrophic Lateral Sclerosis (ALS), the adult-onset motor neuron disease[25], and Frontotemporal Lobar Degeneration (FTLD), the second most common form of pre-senile dementia.[23,26,27] In addition to these diseases, aggregates of TDP-43 have also been associated with Huntington's disease,[28] Alzheimer's disease,[29,30] and Parkinson's disease.[31] These diseases are collectively termed TDP-43 proteinopathies.[32–35] It is noteworthy that due to the lack of understanding of the mechanism of TDP-43 aggregation and aggregation inhibition under stress conditions, these neurodegenerative disorders remain incurable till date.

The majority of the research has focused on deciphering the role of both N and C-terminal domains on the aggregation of TDP-43.[36–42] A few studies on the C-terminal fragments suggest that the glycine-rich region and the Q/N (glutamine/aspargine) rich region of CTD play an important role in the aggregation.[37–41] Interestingly, small peptides in the CTD have also been shown to undergo fibrilization in vitro.[40,43] Moreover, C-terminal fragments of various lengths have been implicated in TDP-43-associated pathogenesis.[44–50] Furthermore, CTD has also been shown to undergo liquid-liquid phase separation.[51,52] On the other hand, NTD facilitates dimer and higher-order oligomer formation.[53–56] NTD oligomerization is also involved in droplet formation by full-length TDP-43.[57] Removal of the first few residues of NTD annihilates the aggregation

propensity of the TDP-43.[58] N-terminal fragments were found lethal as they trigger motor dysfunction in mice.[42] However, the role of TDP-43^{tRRM} in aggregation is poorly understood. With the increased association of TDP-43 with different neurodegenerative diseases, it becomes crucial to study the role of different domains in disease onset. Recent accumulating evidence suggests the role of RRMs in the formation of aberrant aggregates.[40,59–63] As TDP-43^{tRRM} associates with the nucleic acids to perform its functions, dissecting their impact on the aggregation behavior of TDP-43 could help establish the role of TDP-43^{tRRM} and their interaction with nucleic acids in aggregation control.

The binding with nucleic acids has been shown to modulate the self-assembly energy landscape of TDP-43 and its multiple fragments and variants.[64–66] It has been observed that binding to single-stranded (ss) DNA enhances the solubility of TDP-43 purified from a rabbit reticulocyte cell-free system.[66] The binding to ss$(TG)_{12}$ also enhances the solubility of a yellow fluorescent protein (YFP)-tagged TDP-43.[65] RNA binding has also been shown to promote liquid-liquid phase separation of SUMO-tagged TDP-43 and low complexity domain of TDP-43.[64] Interestingly, in a separate study, it has been observed using an optogenetic approach that RNA binding antagonizes the phase transition of various variants of TDP-43 containing the RRM domains.[67] Recently, it has been observed that nucleic acid binding inhibits the thermal aggregation of a variant consisting of N-terminal along with TDP-43^{tRRM} (N-RRM1-2).[68] However, the underlying thermodynamic and molecular basis of aggregation and how the energy landscape of folding, stability, and aggregation are coupled and modulated by nucleic acid binding is not well understood. This knowledge could help in the identification of the natural binding partners, which could prove beneficial in designing the therapeutic strategy against the detrimental aggregation of proteins.

TDP-43^{tRRM} has been shown to undergo pH-dependent amyloid-like aggregation in the presence of physiological salt concentration.[62,69,70] In the current study, we show that the specific binding of a single-stranded DNA oligo (ss$(TG)_6$) inhibits the pH-dependent amyloid-like aggregation of TDP-43^{tRRM}. We also observed that DNA-binding keeps the protein in the native-like monomeric state even at low pH as measured by circular dichroism (CD), ANS assay, and size exclusion chromatography (SEC). TEM studies show that in the DNA-bound protein does not show the ordered morphology of amyloid-like fibrils under aggregation conditions. We observed that pH decreases the thermodynamic stability of TDP-43^{tRRM} and reduces the mid-point of

unfolding (C_m) from 2.2 to 1.3 M [GdmCl] as we go down from pH 7.5 to 5.0. This destabilization initiates the amyloid-like aggregation below pH 5.0. The ss$(TG)_6$ binding increases the thermodynamic stability of TDP-43^{tRRM}, making it more stable even at low pH and hence, ss$(TG)_6$ bound TDP-43^{tRRM} (ss$(TG)_6$-TDP-43^{tRRM}) does not undergo amyloid-like aggregation. Our study suggests that modulation of the self assembly energy landscape by natural binding ligands could be exploited for therapeutic strategies against aggregation-prone proteins.

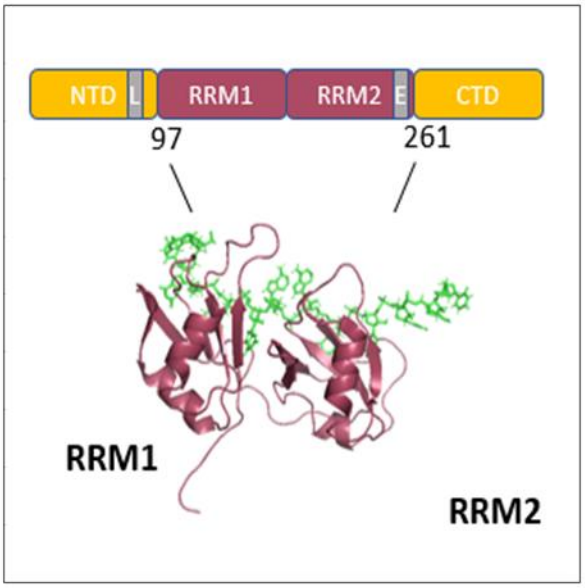

Figure 3.1 TDP-43 binds to nucleic acid. Schematic depiction of the full-length TDP-43 constituting NTD: N-terminal domain-involved in dimerization; RRM1, RRM2: two tethered RNA Recognition Motifs (tRRM)-binds specifically to UG-rich RNA and TG-rich DNA [6] and therefore are the major functional domains of TDP-43; CTD: C-terminal domain-involved in the protein-protein interactions; L and E: nuclear localization and nuclear export sequence, respectively, which shuttles TDP-43 in and out of the nucleus. A structural representation of the nucleic acid binding domain of TDP-43 with its binding partner RNA (PDB ID: 4BS2) is shown below. The green color depicts RNA. The image is created from the PDB file 4BS2 using PyMOL Molecular Graphics System.

3.2 Materials and Methods

Chemicals and buffers

All the chemicals and buffers were procured from HiMedia, Sigma, and Sisco Research Laboratories (SRL) and were used directly without further purification. The buffers that were used for pH-dependent studies are as follows: 20 mM glycine-HCl (pH 3.0-3.5), 20 mM sodium acetate (pH 3.8-5.0), 20 mM 2-(N-Morpholino) ethanesulfonic acid (MES) (pH 5.5-6.0), 20 mM 3-(N-Morpholino) propanesufonic acid (MOPS) (pH 6.5-7.5) and 20 mM Tris (pH 8.0). All the buffers contained 150 mM KCl. 1 mM DTT (dithiothreitol) was added to the buffers before the experiments. All the buffers were filtered with a 0.2 µm filter before use.

Expression and purification of TDP-43^{tRRM}

We followed the previously reported protocol to express and purify TDP-43^{tRRM} (UniProtKB/Swiss-Prot entry Q13148).[62] In brief, the induced BL21(DE3) *Escherichia coli* cells were sonicated, and the supernatant was passed through Ni Sepharose 6-Fast Flow beads (GE Healthcare) to separate His_6-tagged TDP-43^{tRRM}. The eluted protein was buffer exchanged in protease cleavage buffer followed by overnight cleavage of the His_6-tag by PreScission protease at 15 °C. The purified His_6-tag cleaved TDP-43^{tRRM} was stored in a storage buffer (10 mM KPi, 150 mM KCl, 5% glycerol, and 1 mM DTT). The purity of the protein was confirmed by SDS-PAGE (sodium dodecyl sulfate-polyacrylamide gel electrophoresis). The protein concentration was measured by UV-VIS spectroscopy using an extinction coefficient of 15,470 M^{-1} cm^{-1} at 280 nm. The molecular weight of the purified and His_6 tagged-cleaved TDP-43^{tRRM} protein as determined by Synapt G2 HD mass spectrometer (Waters) was 19429 Da.

Preparation of DNA bound sample

Single-stranded (ss) $ss(TG)_6$, $ss(CA)_6$, and $ss(TG)_{12}$ DNA oligos were procured from Integrated DNA Technologies (IDT). The 1 M DNA oligos stock was prepared in HyPure™ Molecular Biology Grade Water (nuclease-free, deionized, distilled-GE Lifesciences). Further dilutions were made as per the requirement and their concentrations were checked using an extinction coefficient of 113,000 M^{-1} cm^{-1} for $ss(TG)_6$, 119,200 M^{-1} cm^{-1} for $ss(CA)_6$ and 225,800 M^{-1} cm^{-1} for $ss(TG)_{12}$ at 260 nm. The values of the extinction coefficients were taken from the manual provided along

with DNA oligos. For the preparation of the DNA-bound TDP-43^{tRRM} samples (ss(DNA)-TDP-43^{tRRM}), the required ratios of the ss(DNA) and TDP-43^{tRRM} were mixed and allowed to incubate at pH 7.2 for 2 hours, followed which all the experiments were performed.

Steady-state fluorescence anisotropy measurements

Steady-state fluorescence anisotropy was measured on a Fluoromax-4 spectrofluorometer from HORIBA Scientific, coupled to the FM4-Pol polarization accessory in the L-format configuration. The ss(TG)$_6$ conjugated with 6-carboxyfluorescein at its 5' end (labeled ss(TG)$_6$) was purchased from IDT. The oligo was dissolved in HyPure™ Molecular Biology Grade Water. The concentration of the labeled ss(TG)$_6$ was confirmed by taking the absorbance at 260 nm and using an extinction coefficient of 133,960 M^{-1} cm^{-1}. To estimate the anisotropy, an increasing concentration of TDP-43^{tRRM} (0-2 µM) was incubated with 30 nM of labeled ss(TG)$_6$. The incubation was conducted in pH 7.5 buffer for 2.5 hours at room temperature. The anisotropy data was acquired by exciting the labeled ss(TG)$_6$ at 482 nm and collecting the emission at 515 nm.. All the measurements were carried out in a quartz cuvette with a path length of 1 cm. The fluorescence anisotropy (r) and emission intensity (I) are related to each other by

$$r = \frac{I_{VV} - I_{VH}G}{I_{VV} + 2I_{VH}G} \qquad (3.1)$$

where subscript V (vertical) and H (horizontal) refer to the position of the polarizer in the excitation beam (first subscript) and emission beam (second subscript) for every measurement performed. G refers to the instrumental correction factor and is given by I_{HV}: I_{HH}.

The binding affinity of the 6-carboxyfluorescein labeled ss(TG)$_6$ for TDP-43^{tRRM} was calculated by fitting the obtained binding curve to the equation:

$$\Delta r = n \frac{[TDP-43^{tRRM}]}{[TDP-43^{tRRM}]+K_d} \qquad (3.2)$$

where Δr is the buffer subtracted anisotropy signal, [TDP-43^{tRRM}] is the protein concentration, n is the valency of the interaction of DNA and protein, and K_d refers to the dissociation constant.

Size exclusion chromatography

The size exclusion chromatography (SEC) of the free and the ss(TG)$_6$-TDP-43^{tRRM} was performed on the AKTA Pure M FPLC system (GE Healthcare). A Superdex™ 75 10/300 GL size

exclusion column having a fractionation range of 3 kDa–70 kDa was used. The bed and void volume of the column is 23.5 mL and 7.2 mL, respectively. Free TDP-43^{tRRM} (8 µM - 10 µM) was incubated with pH 3.0 and pH 7.5 buffer. For the SEC study of the bound sample, ss$(TG)_6$-TDP-43^{tRRM} complex was prepared at pH 7.5 and later incubated with pH 3.0 and pH 7.5 buffer for 30 minutes. The final concentration of the TDP-43^{tRRM} and ss$(TG)_6$ was 8 µM and 10 µM, respectively. All the buffers used in the SEC contained 150 mM KCl. The column was pre-equilibrated with required buffers of respective pH. The flow rate used was 0.8 mL/min. All the experiments were performed at 4°C.

To determine the apparent molecular weight (M_W^{app}) of the TDP-43^{tRRM} under different conditions, we created the calibration curve between the partition coefficient (K_{av}) of the five standard biomolecules (bovine serum albumin (BSA), ovalbumin, ribonuclease A, aprotinin and vitamin B12) and their respective molecular weights.[70] The calibration curve was further used to deduce M_W^{app} based on the elution volume of the sample.

Circular dichroism (CD)

The far-UV CD measurements were performed on a Jasco J-815 spectropolarimeter using a data integration time of 4 s, bandwidth of 2 nm, data pitch of 1 nm, and a scan speed of 20 nm/min at a constant temperature of 20 °C. Each CD spectrum collected was an average of at least two accumulations and was acquired with the help of a quartz cuvette with a path length of 1 mm. The spectra were collected in the wavelength range from 205-250 nm. The concentration of free TDP-43^{tRRM} used was 8 µM. For acquiring the far-UV CD of ss(DNA)-TDP-43^{tRRM}, their preformed complex was diluted with respective buffers to make a final concentration of 10-11 µM of ssDNA and 8-10 µM of TDP-43^{tRRM}. Buffer spectra were acquired under similar conditions for all the buffer conditions and were subtracted from the CD spectra of each sample.

Analysis of the pH dependence of the N⇌ β transition

We have fitted the pH-dependent spectroscopic data by assuming the protonation of a single critical residue in the transition of the native state (N) to β form, as discussed previously[70] using the scheme:

$$N + H^+ \rightleftharpoons NH^+ \rightleftharpoons \beta \qquad \text{(Scheme 3.1)}$$

In the above scheme, it is assumed that only NH^+ is capable of transitioning to β.[71] In that case, the pH dependence is that of the protonation of N and is given by a transformation of the Henderson-Hasselbalch equation:

$$Y_{obs} = \frac{Y_{NH^+} + Y_N 10^{(pH-pK_a)}}{1+10^{(pH-pK_a)}} \quad (3.3)$$

where Y_{obs} corresponds to the observed spectroscopic signal at a particular pH value; Y_N and Y_{NH^+} correspond to the N form and the protonated NH^+ form signals, respectively. It is assumed that under the experimental conditions and the protein concentrations used in this study, $NH^+ \rightleftharpoons$ β equilibrium ultimately favors the β form. Hence, the amount of NH^+ is equal to the amount of the β form.

Dissociation kinetics of the β⇌ N transition

We monitored the dissociation kinetics of β⇌N transition using ThT assay. The β form (80 µM) was prepared from the N-state by performing pH jump from pH 7.5 to pH 3.8. The sample was allowed to incubate for 2 hours. The incubation was followed by a 10-fold jump to pH 7.5 (β to N) and to pH 3.8 (β to β). For the native control, the N-state (80 µM) was prepared from the N-state by performing pH jump from pH 7.5 to pH 7.5. The final sample was prepared by performing 10-fold jump to the pH 7.5 buffer. The final concentration of the protein was 8 µM.

At different times of the reaction, the required amount of the protein was taken from the above samples and assayed for the amount of the β form using ThT assay. The ThT fluorescence assay was performed in 50 mM pH 8.0 Tris buffer. The concentration of the protein was 1 µM while that of ThT was 40 µM. The ThT fluorescence was measured within 1 minute of protein addition. The samples were excited at 440 nm, and emission was collected from 460 nm to 600 nm. The excitation and emission slit widths used were 4 nm. Fluorescence of the free ThT dye was also acquired under similar settings before every ThT acquisition. All the data have been buffer subtracted.

Far-UV CD spectra of the samples were also acquired at the end of the reaction using similar settings as mentioned above at 25 °C, and all the spectra were buffer subtracted.

Reversibility of N⇌β transition

The reversibility of the N⇌β transition was monitored using circular dichroism. The β form (62.6 µM) was prepared from the N-state by performing pH jump from pH 7.5 to pH 3.0. The sample was allowed to incubate for 2 hours. The incubation was followed by a 10-fold jump to different pH (7.5-3.0). For control, the N-state was also prepared using a similar sequence of dilution in the native buffer. The final concentration of the protein was 6.26 µM.

Equilibrium far-UV CD signals were acquired at 216 nm using a data integration time of 2 s, bandwidth of 2 nm, and data pitch of 1 s. The values plotted are an average of data acquired for 30 s. All the signals were buffer subtracted.

Transmission electron microscopy

The free TDP-43^{tRRM} (1 µM) and ss(TG)$_6$-TDP-43^{tRRM} (1.5 µM ss(TG)$_6$ and 1 µM TDP-43^{tRRM}) were incubated at pH 3.8 buffer for 45 minutes. 10 µL of these samples were placed on the copper-coated 300 mesh grid (Electron Microscopy Science) for 5 minutes. The excess sample was removed, followed by a milliQ wash for 30 sec. 2% uranyl acetate was used for 1.5 minutes to stain the samples negatively. The excess stain was removed with MilliQ water. The samples were then covered and allowed to dry overnight and imaged under Technai-T20 at an accelerating voltage of 200 kV.

8-anilino-1-naphthalenesulfonic acid (ANS) fluorescence assay

A stock solution of 10 mM ANS was prepared in Dimethyl Sulfoxide (DMSO). The concentration of the ANS solution was confirmed using absorbance measurement at 350 nm with an extinction coefficient of 5000 M^{-1} cm^{-1}.[72] Pre-equilibrated free TDP-43^{tRRM} (2 µM), and ss(TG)$_6$ -TDP-43^{tRRM} (2 µM TDP-43^{tRRM} and 5 µM ss(TG)$_6$) were incubated in 60 µM ANS for 15 minutes. The fluorescence spectrum for each sample was measured by exciting ANS at 380 nm and obtaining emissions from 400-600 nm.

GdmCl-mediated equilibrium unfolding experiments

The GdmCl-mediated equilibrium unfolding experiments were performed under different pH conditions (3.0-8.0). TDP-43^{tRRM} (4 µM) was incubated with a gradient of GdmCl concentration for 3 hours at room temperature. Tryptophan present in TDP-43^{tRRM} was excited at 280 nm, and

the emission spectrum was acquired from 295 nm to 380 nm. The fluorescence spectra of buffers were collected under similar settings and were subtracted from each fluorescence spectrum. Fluoromax-4 spectrofluorometer from HORIBA Scientific was used for the measurements.

The transitions were analyzed using a two-step N⇋U model. The fraction of unfolded states (f_U) at any particular denaturant concentration were calculated using the following equation:

$$f_U = \frac{Y_o - (Y_N + m_N * [D])}{(Y_U + m_U * [D]) - (Y_N + m_N * [D])} \quad (3.4)$$

where Y_O is the observed MRE signal being measured at different denaturant concentrations [D]. Y_N and Y_U refer to the intercepts, whereas m_N and m_U are the slopes of native and unfolded baseline, respectively.[73,74]

f_U is related to the equilibrium constant (K_{eq}) by the relationship: $K_{eq} = f_U/(1-f_U)$. K_{eq} is further related to free energy ΔG_{NU} by the relationship: $\Delta G_{NU} = -RTlnK_{eq}$. f_U and ΔG_{NU} are related by a modification of Gibbs Helmholtz equation:

$$f_U = \frac{e^{\frac{-\triangle G_{NU}}{RT}}}{1 + e^{\frac{-\triangle G_{NU}}{RT}}} \quad (3.5)$$

where R refers to the gas constant and ΔG_{NU} is the free energy of N⇋U transition. It is related to denaturant concentration [D] by the equation

$$\triangle G_{NU} = \triangle G_{NU}^{H_2O} + m_{NU}[D] \quad (3.6)$$

where $\triangle G_{NU}^{H_2O}$ and m_{NU} are the standard free energy at 0 M denaturant and slope of the N⇋U transition.[73–75]

Reversibility of N⇌U transition

The U-state (40 µM) was prepared from the N-state by performing a jump to 5 M GdmCl (U buffer; pH 7.5). For the native control, the N-state (40 µM) was prepared from the N-state by performing a jump to pH 7.5 (no GdmCl). The samples were allowed to incubate for 3 hours. The N and the U-state were further incubated in a gradient of GdmCl concentrations for 3 hours by performing a 10-fold jump by manual mixing. Following incubation, the changes in the fluorescence signals were monitored by exciting TDP-43^{tRRM} at 280 nm and obtaining emission from 300-400 nm. The excitation and emission slit widths used were 1 nm and 8 nm, respectively. The final TDP-43^{tRRM} concentration was 4 µM. All the signals were acquired at pH 7.5 in the presence of 150 mM KCl and were buffer subtracted accordingly.

Calculation of N and U populations

K_{eq} and population of the N and the U-state ([N] and [U]) are related by equation:

$$K_{eq} = \frac{[N]}{[U]} \qquad (3.7)$$

The population of different ensembles can be calculated by:

$$\triangle G_{NU}^{H_2O} = -RT \ln K_{eq} \quad \text{or} \quad \triangle G_{NU}^{H_2O} = -RT \ln \frac{[N]}{[U]} \qquad (3.8)$$

where R is the universal gas constant and T refers to the temperature of measurement in Kelvin.

Characterization of the thermal stability

The heat-induced unfolding of TDP-43^{tRRM} was used to measure the thermal stability of the free and ss$(TG)_6$-TDP-43^{tRRM} from pH 5.0-7.5. A PTC-424S/15 Peltier system was attached to the CD instrument for temperature ramping. The temperature was ramped up by 1 °C/min. Far-UV CD signals were acquired at 222 nm from 25 °C to 70 °C in a cuvette with a path length of 1 mm. The concentration of the free TDP-43^{tRRM} used was 8 µM. ss(DNA)-TDP-43^{tRRM} were incubated in pH 7.2 to make a final concentration of 10 µM of ss$(TG)_6$ and 8 µM of TDP-43^{tRRM}. Samples were incubated in their respective buffers for at least 30 minutes. Respective buffer spectra were acquired at similar settings, and the buffer subtraction was carried out for all the CD spectra.

The mean residue ellipticity (MRE) values obtained were converted to fraction unfolded (f_U) using the following equation:

$$f_U = \frac{Y_o - (Y_N + m_N * T)}{(Y_U + m_U * T) - (Y_N + m_N * T)} \qquad (3.9)$$

where Y_O is the observed MRE signal being measured at different temperatures (T). Y_N and Y_U refers to the intercepts, whereas m_N and m_U are the slopes of native and unfolded baseline, respectively.

The f_U versus temperature plots were fitted to the equation:

$$f_U = \frac{\exp\left[\frac{\Delta H\left(\frac{T}{Tm}-1\right) + \Delta C\left[Tm - T + T\ln\left(\frac{T}{Tm}\right)\right]}{RT}\right]}{1 + \exp\left[\left(\Delta H\left(\frac{T}{Tm}-1\right) + \Delta C\left[Tm - T + T\ln\left(\frac{T}{Tm}\right)\right]\right)/RT\right]} \qquad (3.10)$$

where ΔH is enthalpy and ΔC refers to specific heat capacity (ΔC_P). T refers to different temperatures and T_m is the midpoint of unfolding transition.[73–75]

Reversibility of β⇌U transition

The β form and the U state were incubated in the gradient of GdmCl at pH 3.8 for 3 hrs. The fluorescence signal of the samples was acquired using similar settings as mentioned above.

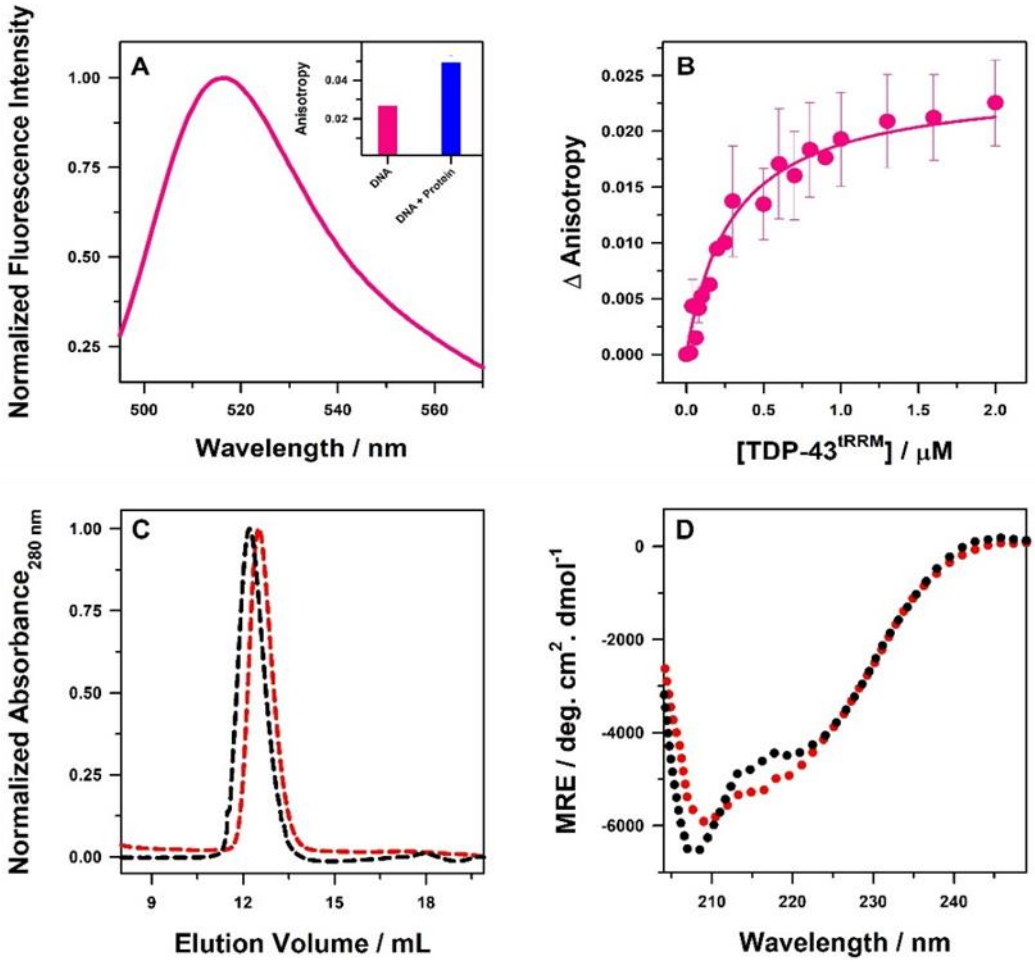

Figure 3.2 ss(TG)$_6$ binds to TDP-43^{tRRM}. (A) Fluorescence emission spectra of labeled ss(TG)$_6$ upon excitation at 482 nm. Mean anisotropy values of free and bound labeled ss(TG)$_6$ (Figure 3.2A, inset). (B) Binding curve of TDP-43^{tRRM} with labeled ss(TG)$_6$ as a function of TDP-43^{tRRM} concentration as monitored by fluorescence anisotropy assay. The error bars represent the spread in values of the data points from three independent sets of experiments. (C) Normalized chromatograms obtained from SEC plotted at 280 nm for the free TDP-43^{tRRM} (red) and ss(TG)$_6$-TDP-43^{tRRM} (black) at pH 7.5. (D) Far-UV CD spectra of the free TDP-43^{tRRM} (red) and ss(TG)$_6$-TDP-43^{tRRM} (black) at pH 7.5.

3.3 Results

3.3.1 TDP-43^{tRRM} binds strongly to TG-rich DNA

Figure 3.2A shows the emission spectrum of fluorescently labeled ss$(TG)_6$ upon excitation at 482 nm. The wavelength of the maximum fluorescence emission (λ_{max}^{em}) was observed at 515 nm. Figure 3.2A, inset, compares the mean value of steady-state anisotropy at 515 nm of labeled ss$(TG)_6$ in free and bound form at pH 7.5. The mean steady-state anisotropy of free and bound forms are 0.026 ± 0.001 and 0.049 ± 0.003, respectively.

Figure 3.2B shows the relative change in the anisotropy values of labeled ss$(TG)_6$ as a function of increasing TDP-43^{tRRM} concentration at 515 nm. The curve shows a hyperbolic increase in the signal. We observed that the relative value of steady-state anisotropy of the labeled ss$(TG)_6$ has increased from 0.0 to 0.023 upon increasing TDP-43^{tRRM} concentration from 0 μM to 2 μM. The low value of the anisotropy of the free labeled ss$(TG)_6$ indicates free tumbling of the fluorophore owing to the smaller size of the attached ssDNA. The gradual increase in the value of anisotropy with an increase in TDP-43^{tRRM} concentration could be attributed to the slowed movement of the fluorophore upon binding of ssDNA to TDP-43^{tRRM}. Upon fitting the data to equation 3.2, we obtained a K_d value of 0.3±0.05 μM, indicating a strong binding affinity of TDP-43^{tRRM} towards ss$(TG)_6$. Our results are in accordance (0.28±.09 μM) to the K_d values of the TDP-43^{tRRM} and unlabeled $(TG)_6$ measured using change in fluorescence lifetime of tryptophan residues present in the protein.[76] These results suggest that the 6-carboxyfluorescein does not interfere with the measurement of the binding constant.

The binding constant reported in our study is very similar (0.28±.09 μM) to the binding constant of the TDP-43^{tRRM} and unlabeled $(TG)_6$ measured using change in fluorescence lifetime of tryptophan residues present in protein.

3.3.2 The molecular size of TDP-43^{tRRM} increases upon binding to ss$(TG)_6$

We employed size exclusion chromatography to estimate the molecular mass of TDP-43^{tRRM} in its free and ss$(TG)_6$ bound form at pH 7.5. Figure 3.2C shows their normalized elution profile monitored at 280 nm. We observed that the free TDP-43^{tRRM} elutes at 12.51 mL, corresponding to a molecular weight of 19.4±0.5 kDa. The obtained molecular weight is similar to that obtained

with the mass spectrometer of monomeric TDP-43^{tRRM}. This data suggests that TDP-43^{tRRM} exists as a monomer under physiological conditions.

ss(TG)$_6$-TDP-43^{tRRM}, on the other hand, eluted at 12.13±0.07 mL, which corresponds to a molecular weight of 23.3±0.6 kDa. The early elution and higher molecular weight of ss(TG)$_6$-TDP-43^{tRRM} indicate that DNA is bound to the protein.

3.3.3 The secondary structure of TDP-43^{tRRM} remains native-like upon DNA binding

Figure 3.2D compares the far-UV CD spectra for both free and ss(TG)$_6$-TDP-43^{tRRM} at pH 7.5. The secondary structure of free TDP-43^{tRRM} is rich in α-helix, β-sheet, and the disordered region. The signal minima at 208 nm and 222 nm with MRE values of -5764 and -4550 deg.cm^2.dmol^{-1} suggests the presence of both α-helix and β-sheet rich structures (referred to hereafter as the native state). Interestingly, we also observed similar far-UV CD spectra for ss(TG)$_6$-TDP-43^{tRRM} with a MRE value of -6584 deg.cm^2.dmol^{-1} at 208 nm and -4340 deg.cm^2.dmol^{-1} at 222 nm. The similar MRE values imply that upon binding to ss(TG)$_6$, the secondary structure of TDP-43^{tRRM} remains similar to the native state. Thus, DNA binding induces no significant secondary structural changes under physiological conditions. Therefore, both free and bound TDP-43^{tRRM} can be compared directly.

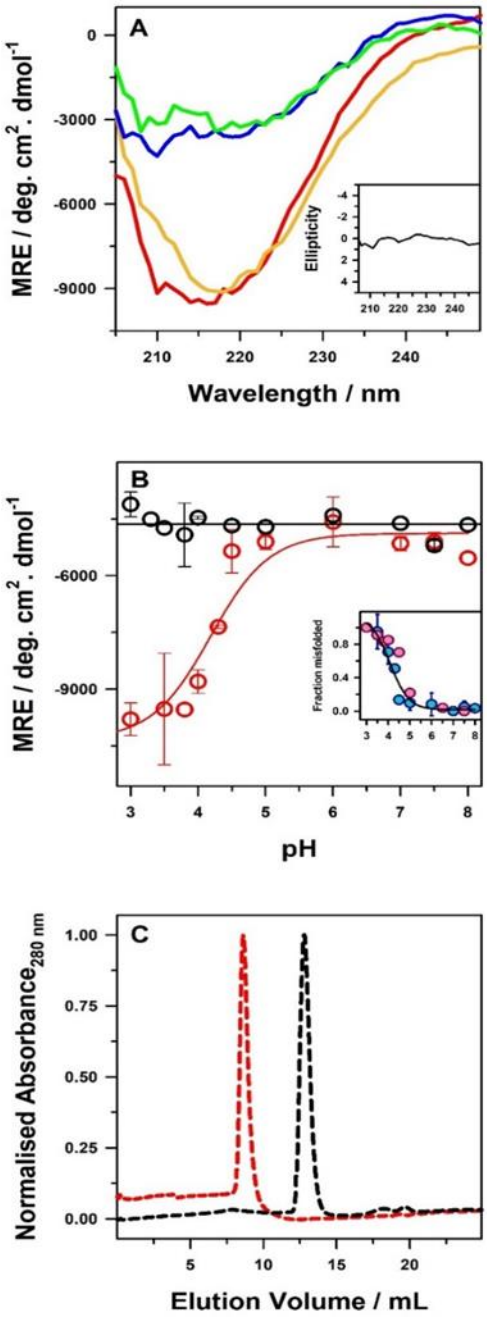

Figure 3.3 ss(TG)$_6$ binding inhibits the pH-induced misfolding of TDP-43^{tRRM}. (A) Far-UV CD spectra of free (red), ss(TG)$_6$ (blue), ss(TG)$_{12}$ (green) and ss(CA)$_6$ (yellow) bound TDP-43^{tRRM} at pH 3.8. Inset shows the ellipticity of ss(TG)$_6$ at pH 3.8. (B) Changes in the mean residue ellipticity at 216 nm as a function of pH for the free TDP-43^{tRRM} (red) and ss(TG)$_6$-TDP-43^{tRRM} (black). The error bars represent the spread in values of the data points from at least two independent sets of experiments. The solid line through the free TDP-43^{tRRM} data is a fit to equation 3.3, while that of ss(TG)$_6$-TDP-43^{tRRM} is drawn to guide the eye. Inset demonstrates that the N⇌β transition is

reversible. Fraction misfolded calculated upon jumping β form to different pH (pink, circle) are compared with the fraction misfolded calculated from jumping N-state to different pH (blue, circle). The fraction misfolded is calculated as discussed previously.[70] The solid line is a fit to equation 3.3. (C) Normalized size-exclusion chromatograms for the free TDP-43^{tRRM} (red) and ss(TG)$_6$-TDP-43^{tRRM} (black).

3.3.4 pH-dependent misfolding of TDP-43^{tRRM} is abolished upon ss(TG)$_6$ binding

Previously, we have shown that free TDP-43^{tRRM} undergoes a transition to soluble amyloid-like conformation at low pH stress conditions (aggregation conditions), which is predominately rich in β sheeted structure.[62,69,70] The far-UV CD spectrum of free TDP-43^{tRRM} at pH 3.8 (Figure 3.3A) shows a shift in the signal minima to 216 nm, which signifies the dominance of β sheets (β form) in the protein sample. The shift is accompanied by an increase in the signal with an MRE value of -9536 deg. cm^2. dmol^{-1}. We observed that the β form binds to the amyloid-staining dye ThT (Figure 3.S1A).[77] Together, these results indicate that the aggregates observed in this study are amyloid-like.

To study the effect of the ssDNA on the secondary structure of TDP-43^{tRRM} under aggregation conditions, we have used ss(TG)$_6$ and ss(TG)$_{12,}$ which are specific binding partners of TDP-43^{tRRM}.[6] We measured the far-UV signal of the free ss(TG)$_6$ and did not observe any appreciable absorbance, suggesting the lack of structure (Figure 3.3A, inset). We observed a far-UV CD spectrum similar to the native TDP-43^{tRRM} with minima at 208 and 222 nm for the ss(TG)$_n$-TDP-43^{tRRM} (Figure 3.3A). The observed values of the MRE at 216 nm for ss(TG)$_6$ and ss(TG)$_{12}$ bound TDP-43^{tRRM} were -4401 deg. cm^2. dmol^{-1} and -3031 deg. cm^2. dmol^{-1}, respectively. These results imply that the transition to β form is abolished in the presence of ss(TG)$_6$ and ss(TG)$_{12,}$ and TDP-43^{tRRM} maintains its native-like form under aggregation conditions.

We also used ss(CA)$_6$ to look for the effect of non-specific nucleic acid sequences.[6] We observed signal minima at 216 nm in the far-UV CD spectrum with an MRE value of -9052 deg cm^2 dmol^{-1}. The appearance of the far-UV CD spectrum and the signal strength resembles that of free TDP-43^{tRRM} under aggregation conditions. These results provide an important observation that suggests that the specific binding of ss(TG)$_6$ and ss(TG)$_{12}$ plays a vital role in abolishing the misfolding behavior of the TDP-43^{tRRM} under the studied conditions.

We measured the pH-induced structural transition under equilibrium conditions of the native state to β form at 216 nm using far-UV CD spectroscopy (Figure 3.3B). We observed that the secondary structure of the TDP-43^{tRRM} remains native-like from pH 7.5 to pH 5.0. The average MRE value at 216 nm was -5096 ± 340 deg cm^2 dmol^{-1}. However, with a further decrease in the pH, we observed an increase in the MRE, which saturated at pH 3.0. This increase in the signal at 216 nm signifies the transition to β form. The transition from native-state to β form as a function of pH has a steep slope, and the midpoint of the transition is pH 4.0. The plot was fitted using equation 3.3. It is crucial to point out that the N⇌β transition is reversible (Figure 3.3B, inset). The β form dissociates and acquires a native-like secondary structure upon stress removal (Figure 3.S1).

However, ss(TG)$_6$-TDP-43^{tRRM} did not show any such transition under low pH conditions and retained an average MRE value of -4591 ± 271 deg cm^2 dmol^{-1} at 216 nm throughout the studied pH range. The results suggest that the ss(TG)$_6$ binding to the TDP-43^{tRRM} inhibits the conformation conversion of TDP-43^{tRRM} to β form while retaining its native structure.

3.3.5 DNA binding inhibits oligomerization of TDP-43^{tRRM}

To characterize the size of ss(TG)$_6$-TDP-43^{tRRM}, we compared the elution profile of the free and ss(TG)$_6$ -TDP-43^{tRRM} at low pH (Figure 3.3C). Free TDP-43^{tRRM} eluted at 8.69 mL. The void volume of the SEC column employed is comparable to the elution volume, due to which the exact molecular weight of free TDP-43^{tRRM} cannot be deduced. However, this suggests that the β form is much larger than the monomeric TDP-43^{tRRM}. Interestingly, the ss(TG)$_6$-TDP-43^{tRRM} eluted at 12.7 mL corresponding to a molecular mass of 18.6 kDa, which is similar to the molecular mass of the monomeric TDP-43^{tRRM} at pH 7.5. The delayed elution of ss(TG)$_6$-TDP-43^{tRRM} at pH 3.0 suggests the formation of a compact structure at pH 3.0. The results in Figure 3.3 confirm that DNA binding inhibits structural change and prevents oligomerization of TDP-43^{tRRM} under aggregation conditions. An intact secondary structure with a compact size suggests that ss(DNA) could induce the formation of compact native-like states under aggregation conditions.

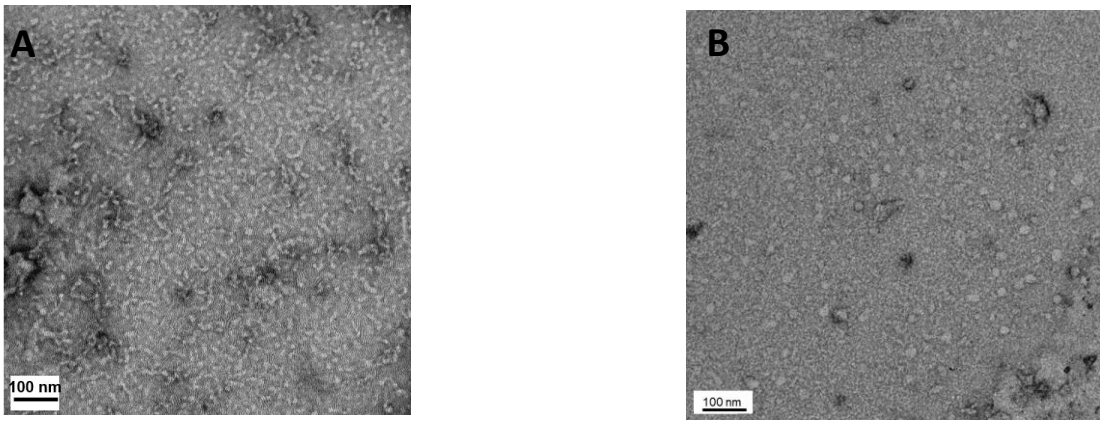

Figure 3.4 DNA binding inhibits the worm-like fibril formation of TDP-43^{tRRM}. TEM image of (A) free TDP-43^{tRRM} (B) ss(TG)$_6$-TDP-43^{tRRM}.

3.3.6 ss(TG)$_6$ abolishes the formation of worm-like β form

We examined the effect of DNA binding on the morphology of the amyloid-like aggregates at low pH. Figure 3.4 compares the TEM image of the free and ss(TG)$_6$ -TDP-43^{tRRM}. In the case of free TDP-43^{tRRM}, we observed small worm-like assemblies of approximately 50-70 nm. The observed small fibrils are similar to the fibrils of mouse prion protein observed previously in a separate study.[78] The result suggests that the oligomeric β form appears to be worm-like fibrils. In contrast, no visible assemblies were observed in the presence of ss(TG)$_6$ (Figure 3.4B). The absence of visible assemblies proves that the formation of the worm-like β form is abolished in the presence of ss(TG)$_6$.

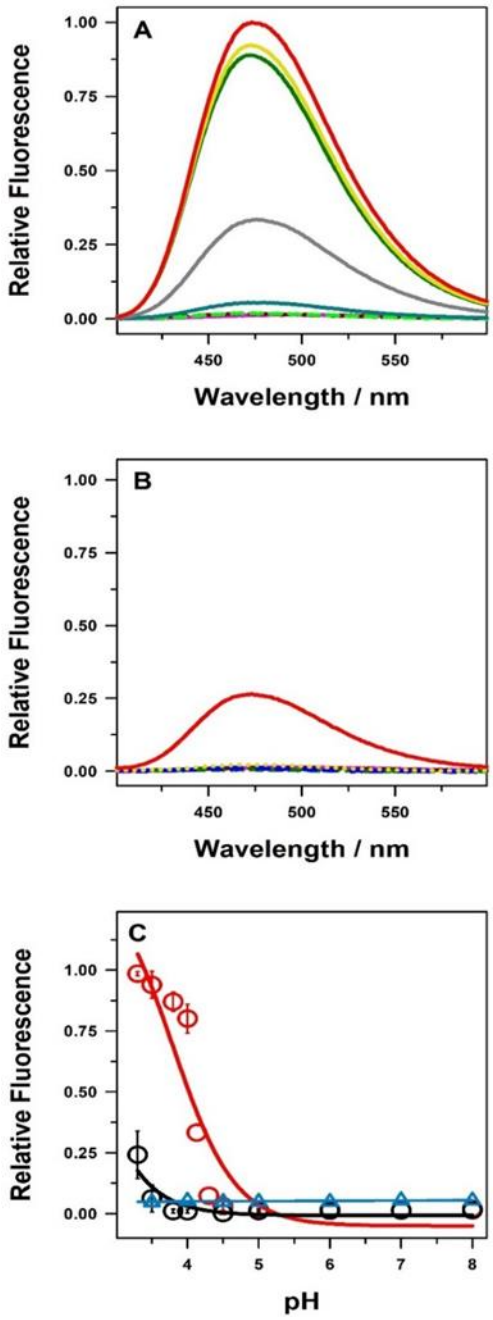

Figure 3.5 ss$(TG)_6$-TDP-43^{tRRM} averts changes in the tertiary structure by forming a molten globule. (A) Normalized ANS fluorescence spectra for free TDP-43^{tRRM}. pH 3.3 (red), pH 3.5 (yellow), 4.0 (dark green), 4.1 (grey) 4.3 (dark cyan), 4.5 (light green) 5.0 (maroon), 7.5 (pink). (B) Normalized ANS fluorescence spectra for ss$(TG)_6$-TDP-43^{tRRM}. (C) Relative comparison of the fluorescence points at 480 nm for free (red), ss$(TG)_6$-TDP-43^{tRRM} (black), and buffer (teal blue) as a function of pH. Error bars represent the spread of at least two independent data sets.

3.3.7 ss(TG)$_6$ binding preserves the tertiary structure of TDP-43^{tRRM} under stress-like conditions

We performed pH-dependent ANS binding assay on the free and ss(TG)$_6$-TDP-43^{tRRM} to study the effect of DNA binding on the tertiary structure of TDP-43^{tRRM} under aggregation conditions. ANS is a dye that binds to the solvent-exposed hydrophobic amino acids and fluoresces. Figure 3.5A shows the relative ANS fluorescence signal of the free TDP-43^{tRRM}. We did not observe ANS fluorescence under native conditions (pH 5.0-pH 7.5). The result indicates that the native state of TDP-43^{tRRM} is appropriately folded, and no exposed hydrophobic patches are present. However, we observed a gradual increase in the ANS fluorescence below pH 5.0. The λ_{max}^{em} of the fluorescence emission was observed at 472 nm. An increase in the fluorescence signal indicates an increase in the exposed hydrophobic patches, a characteristic of the misfolded state of proteins. The gradual increase with a decrease in the pH indicates a higher amount of misfolded species under low pH conditions.

In contrast, we observed a negligible ANS fluorescence signal for the ss(TG)$_6$-TDP-43^{tRRM} across the studied pH range (Figure 3.5B). The inability of ANS dye to bind and fluoresce suggests that the native structure of TDP-43^{tRRM} is intact under various pH stress in the presence of ss(TG)$_6$. However, ss(TG)$_6$-TDP-43^{tRRM} at pH 3.3 showed 20% ANS fluorescence than its free counterpart (Figure 3.5B). As the secondary structure of ss(TG)$_6$-TDP-43^{tRRM} is similar to the native state at pH 3.3, the results indicate that some molten globular structure is forming at very low pH conditions.

Figure 3.5C compares the ANS fluorescence during pH-induced equilibrium transition of free and ssDNA bound TDP-43^{tRRM}. The increase in the ANS fluorescence with a decrease in the pH indicates the exposure of the hydrophobic patches of free TDP-43^{tRRM}. However, ss(TG)$_6$-TDP-43^{tRRM} shows no increase in the ANS fluorescence until pH 3.5. The results indicate that ss(TG)$_6$ binding keeps the native tertiary structure TDP-43^{tRRM} intact. The figure also shows the relative signal of the buffer containing ANS in different pH conditions. We virtually observed no change in the ANS fluorescence as a function of pH.

These results together conclude that the presence of ss(TG)$_6$ prevents side-chain breaking and keeps the tertiary structure of TDP-43^{tRRM} intact.

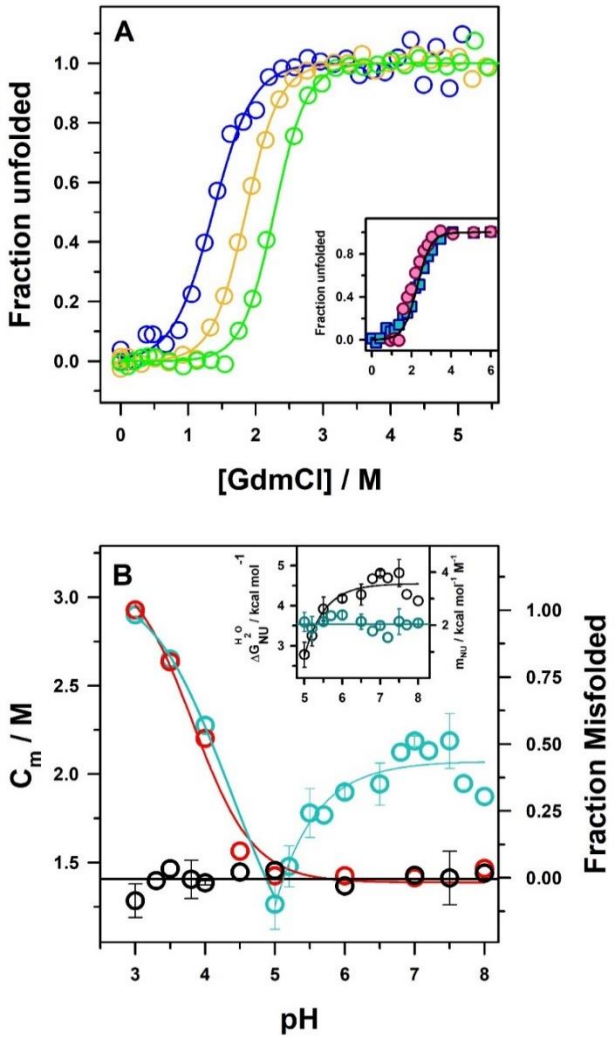

Figure 3.6 pH-induced misfolding is coupled to pH-induced destabilization. (A) Representative plots show fraction unfolded as the function of GdmCl concentration at pH 5.0 (blue), 6.0 (yellow), 7.5 (green). The inset shows the N⇌U transition is reversible. Fraction unfolded calculated from the unfolding transition of the N-state (blue, square) as a function of GdmCl concentration are compared with fraction unfolded calculated from the refolding transition of the U-state (pink, circle) at 340 nm at pH 7.5. The fraction unfolded is calculated using equation 3.4. The solid line is a simulated fit to equation 3.5. (B) C_m of free TDP-43^{tRRM} (dark cyan) is compared with the fraction misfolded of free TDP-43^{tRRM} (red) and ss$(TG)_6$-TDP-43^{tRRM} (black) as a function of pH. ΔG_{NU}^{H2O} (black) and m_{NU} (dark cyan) dependence on pH (Figure 3.6B, inset). The error bars represent the spread in values of the data points from at least two independent sets of experiments.

3.3.8 TDP-43^{tRRM} exhibits pH-dependent thermodynamic stability

In order to understand the effect of pH on the thermodynamic stability of TDP-43^{tRRM}, we employed fluorescence spectroscopy. Two tryptophan residues are located at positions 113 and 172 in the RRM1 domain of TDP-43^{tRRM}. We observed that these tryptophans fluoresce differently in the native and chemically unfolded states. Their fluorescence was found to decrease upon protein unfolding due to increased quenching as a result of the solvation environment. Also, the λ_{max}^{em} of emission was observed at 347 nm and 357 nm for the native and unfolded states, respectively. These two results signify the solvation of the tryptophans. We utilized this difference in the spectroscopic properties of the native and unfolded states of the protein to calculate the population distribution and hence the thermodynamic stability of the TDP-43^{tRRM}. The unfolding curves obtained as a function of GdmCl concentration were converted to the fraction of unfolded protein (f_U) using equation 3.4. Figure 3.6A shows the representative plots of the f_U as a function of GdmCl concentration for pH 5.0, 6.0, and 7.5. The plots were fitted to equation 3.5 to calculate the associated thermodynamic parameters.

Figure 3.6A demonstrates that the midpoint of the unfolding transition (C_m) changes as a function of pH in the pH range of 5.0-7.5. C_m is a measure of protein stability.[79] For pH 7.5, we noticed that the native baseline (N-baseline) extends till ~ 1.5 M, and C_m is reached at 2.2 ± 0.15 M.

In contrast, the N-baseline decreases to 1.1 M for pH 6.0, and C_m was achieved at ~ 1.9 M. With a further decrease in the pH to 5.0, the transition zone begins early at 0.65 M, and C_m is achieved at 1.3 M. These results confirm that TDP-43^{tRRM} exhibits pH-dependent thermodynamic stability, which starts decreasing upon decreasing the pH below 7.5. It is important to note that the m_{NU} value remains constant (2.1±0.2 kcal mol^{-1} M^{-1}) throughout the pH range studied (Figure 3.6B, inset). The observation suggests that the pH-dependent changes in the stability are not due to the structural changes.

It is also important to point out that the N⇌U transition is reversible (Figure 3.6A, inset). We observed the expected change in the fraction of the unfolded protein population upon dilution of the U-state in a gradient of GdmCl, demonstrating the reversibility of the N⇌U transition.
Figure 3.6B shows the variations in the value of C_m value as a function of pH under equilibrium conditions. The mean value of C_m remains 2.16 ± 0.03 M [GdmCl] for the pH range 6.8-8.0. Below

pH 6.8, the C_m value starts decreasing. It achieves a minimum at pH 5.0 with a value of 1.26 ± 0.14 M. We observed that C_m increases below pH 5.0. Figure 3.6B, inset shows the value of ΔG_{NU}^{H2O} as a function of pH. We noticed a decrease in the ΔG_{NU}^{H2O} (4.8 to 2.8 kcal mol^{-1}) with decrease in the pH from pH 7.5 to 5.0. The previous results from Figures 3.3B and 3.5C show that the TDP-43^{tRRM} begins to form an amyloid-like assembly below pH 5.0. Hence, the increase in the C_m values below pH 5.0 represents the structural unfolding of the heterogeneous mixture of the native and aggregated state.

The data presented in Figure 3.3B were utilized to calculate the fraction of misfolded protein as a function of pH (Figure 3.6B), as discussed previously.[70] Interestingly, we observed that misfolding of TDP-43^{tRRM} starts below pH 5.0, the point of minimum thermodynamic stability of TDP-43^{tRRM}. These results together convey that misfolding of TDP-43^{tRRM} happens as a result of its destabilization.

We also converted the MRE values obtained for ss$(TG)_6$-TDP-43^{tRRM} from Figure 3.3B to obtain the fraction misfolded as a function of pH (Figure 3.6B). We observed that the conformational conversion of the TDP-43^{tRRM} in the presence of ss$(TG)_6$ is inhibited throughout the studied pH range.

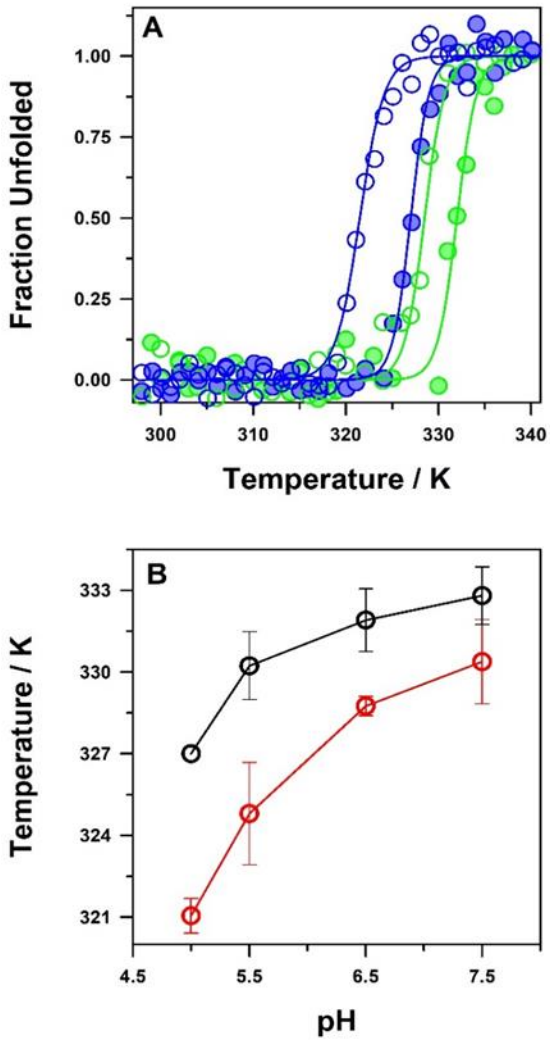

Figure 3.7 DNA binding increases the thermal stability of TDP-43^{tRRM}. (A) Fraction unfolded of TDP-43^{tRRM} at 222 nm as a function of temperature. The fraction unfolded is compared for free TDP-43^{tRRM} at pH 5.0 (blue, open), pH 7.5 (green, open) with ss(TG)$_6$-TDP-43^{tRRM} at pH 5.0 (blue, filled) and pH 7.5 (green, filled). The plots are fitted through equation 3.10. (B) T_m of free (red) and ss(TG)$_6$-TDP-43^{tRRM} (black) plotted as a function of pH. Error bars represent the spread of at least two data sets. The lines drawn are to guide the eye.

3.3.9 ss(TG)$_6$ binding increases the thermal stability of TDP-43^{tRRM}

The above results indicate that the extent of misfolding of TDP-43^{tRRM} is directly linked to its destabilization. In order to understand the effect of ss(DNA) on the thermodynamic stability, denaturant-induced unfolding could not be used as ss(DNA) does not bind to TDP-43^{tRRM} in the presence of even small amount of denaturant. Therefore, we employed temperature-mediated

unfolding experiments in the pH range of 5.0-7.5 to estimate the midpoint of thermal unfolding (T_m) as a measure of stability. We used the difference in the far-UV CD spectrum of native and unfolded states to monitor the unfolding of the TDP-43^{tRRM}. Figure 3.7A shows the representative thermal unfolding plots of free and ss$(TG)_6$-TDP-43^{tRRM} at pH 5.0 and 7.5. We observed that the transition from native to unfolded form is a two-step process, and the midpoint of unfolding changes with the pH.

In the case of free TDP-43^{tRRM}, the native baseline extends till 318 K at pH 5.0, beyond which the transition zone begins. The unfolding transition follows a sigmoidal pattern with a midpoint of unfolding at 321 K. Complete unfolding is achieved at 328 K. Interestingly, free TDP-43^{tRRM} under pH 7.5 showed higher stability than pH 5.0 as evident with a more extended native baseline till 324 K. The midpoint of transition shifted to 328.5 K. In contrast, the complete unfolding of TDP-43^{tRRM} occurred at 333 K.

On the contrary, ss$(TG)_6$-TDP-43^{tRRM} showed a difference in the midpoint of the unfolding transition. We observed extended native baselines both at pH 5.0 and 7.5. The more extended native baseline suggests an increase in the resistance to thermal unfolding. The unfolding transition was observed to begin near 324 K, and the midpoint of transition was achieved at 327 K at pH 5.0. The transition midpoint at pH 7.5 was observed to shift to 332 K. This data suggests that ss$(TG)_6$ binding increases the thermal stability of TDP-43^{tRRM} under both pH conditions.

Figure 3.7B compares the mean value of T_m as a function of pH for free and ss$(TG)_6$-TDP-43^{tRRM}. In the case of free TDP-43^{tRRM}, the mean value of T_m at pH 5.0 is 321 K. The T_m value increased with the increase in the pH, making the T_m value equivalent to 324.8 K at pH 5.5, 328.8 K at pH 6.5, and 330.4 K at pH 7.5. The presence of ss$(TG)_6$ increased the T_m to ~ 332 K, suggesting increased stability of the ss$(TG)_6$-TDP-43^{tRRM}.

3.4 Discussion

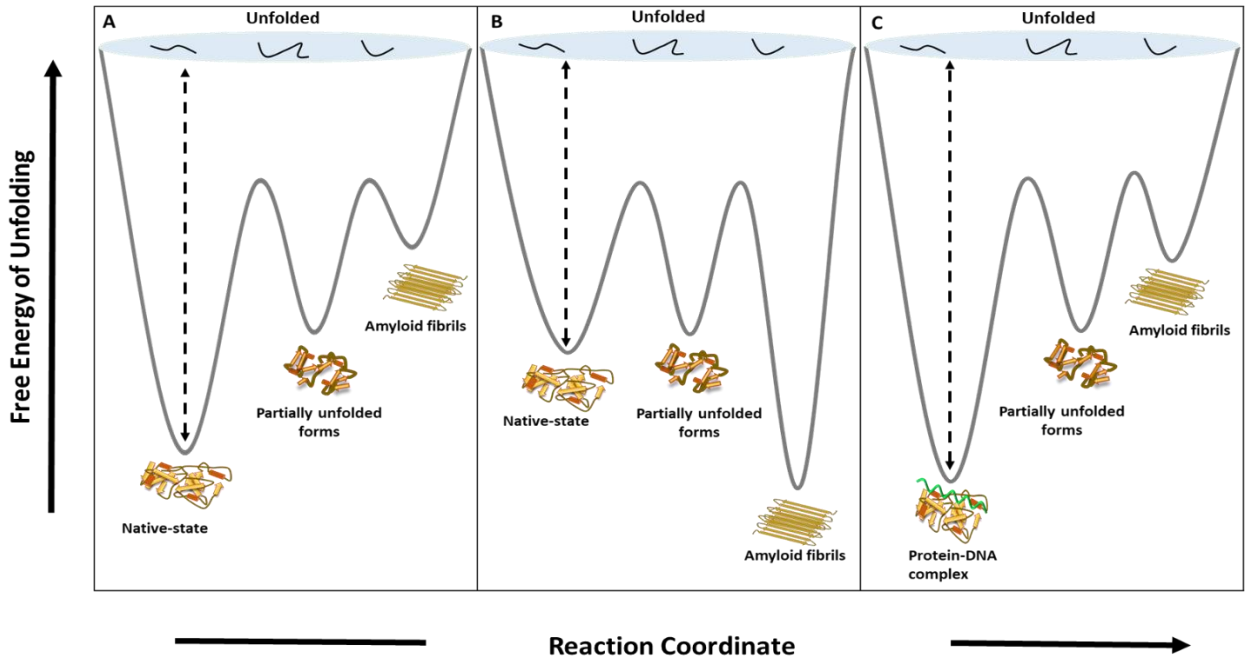

Figure 3.8 Free energy landscape model of TDP-43^{tRRM} in (A) native conditions (pH 7.5), (B) low pH stress-like conditions, and (C) ss$(TG)_6$ bound in native and stress conditions.

TDP-43 is a nucleic acid-binding protein whose aggregation has been implicated in TDP-43-associated proteinopathies.[23,26,28,30] Nucleic acids have been shown to modulate the aggregation behavior of TDP-43.[66,67,80,81] For instance, Huang et al. have shown that DNA binding increases the solubility of TDP-43 generated from a cell-free system by centrifugation and western blotting. They have also shown a decrease in the turbidity of purified TDP-43 expressed from *E.coli* in the presence of ssDNA, suggesting increased solubility.[66] Another paper by Qin et al. explores the effect of DNA binding on the N-terminal domain. However, the N-terminal domain is not the primary nucleic acid binding domain of TDP-43.[81] In addition, nucleic acids have also been shown to modulate the other self-assembly reactions of TDP-43, like phase separation. It has been shown that RNA molecules can buffer the phase separation of TDP-43.[80] In a separate study, RNA binding has been shown to antagonize the phase separation and aggregation of TDP-43 variants containing RRM domain.[67] These elegant studies have provided important observations regarding the role of nucleic acids. However, a quantitative thermodynamic basis for these observations was missing. In addition, none of these studies have studied the relationship between nucleic acid

binding and amyloid-like aggregation of the protein. One major way in which amyloid-like aggregation differs from other insoluble aggregates is that there is a large structural change in the protein from the native structure to a predominately β-sheet rich structure. It is not known how DNA binding affects this structural transition of the functional domain of TDP-43.

In this study, we have explored the role of DNA on the primary functional domain of TDP-43, TDP-43^{tRRM}. Because TDP-43^{tRRM} forms an essential part of the 35 kDa fragments (TDP-35), which is implicated in ALS and FTLD,[82,83] it becomes important to understand the TDP-43^{tRRM}-mediated aggregation and aggregation inhibition. Till now, very limited studies exist which has specifically studied the thermodynamic basis of aggregation and aggregation inhibition of the TDP-43^{tRRM}. We have used a thermodynamic approach in a systematic manner and quantitatively show how stress destabilizes the TDP-43^{tRRM} leading to large structural change to form amyloid-like aggregates, and how DNA binding inhibits the amyloid-like aggregation of the TDP-43^{tRRM} by stabilizing the native state.

We have employed fluorescence spectroscopy, circular dichroism, size exclusion chromatography, and TEM to study the structure and thermodynamics of TDP-43^{tRRM} in free and ss$(TG)_6$ bound states. The secondary and tertiary structure analysis suggests that the transition from the native state to oligomeric β form (Figure 3.3C) begins below pH 5.0, with a midpoint of the transition ~ pH 4.0 (Figures 3.3B and 3.5C). We employed GdmCl and heat-mediated denaturation under different pH conditions to probe the cause of misfolding under low pH conditions (Figures 3.6 and 3.7). The denaturation experiments suggest that the free TDP-43^{tRRM} exhibits pH-dependent stability (Figures 3.6 and 3.7). The thermodynamic parameters calculated from GdmCl mediated denaturation experiments suggest that free TDP-43^{tRRM} remains most stable in the pH range of 6.8 to 7.5 with a mean C_m value of 2.16 M [GdmCl] (Mean ΔG_{NU}^{H2O} = 4.74 kcal mol^{-1}). Below pH 6.8, C_m decreases as a function of pH and becomes 1.26 M [GdmCl] at pH 5.0 (ΔG_{NU}^{H2O} = 2.78 kcal mol^{-1}) (Figure 3.6B and inset). The thermal denaturation experiments also confirmed the pH-dependent stability of TDP-43^{tRRM} being higher at pH 7.5 (T_m = 330.38 K) compared to pH 5.0 (T_m = 321 K) (Figure 3.7A). The observed destabilization of TDP-43^{tRRM} at low pH stress conditions makes it aggregation prone as evident from the increased misfolding accompanied with destabilization (Figure 3.6B). We also observed that the specific ss$(TG)_6$ binding abolishes the pH-dependent secondary and tertiary structural changes (Figure 3.3B and 3.5C). The ss$(TG)_6$-TDP-43^{tRRM} remains in the monomeric state even at low pH (Figure 3.3C) and

does not form amyloid-like pre-fibrils (Figure 3.4, Figure 3.6B). The binding of ss$(TG)_6$ increases the stability of TDP-43^{tRRM} under native and stress-like conditions. The mean value of T_m observed for ss$(TG)_6$-TDP-43^{tRRM} in native and stress conditions was 332.8 K and 327 K, respectively (Figure 3.7B).

Our results can be explained from the model energy diagram as shown in Figure 3.8. An energy diagram postulates various species that can be populated under a specific set of conditions. Figure 3.8 shows the structural transition between the N-state, U-state, PUFs, and β form. In this study, we show that the N⇌U transition is reversible (Figure 3.6A, inset). Previous studies from our lab and the present study have established the reversibility of the β⇌U transition (Figure 3.S2).[62,70] In this study, we also point out that the N⇌β transition is reversible in nature (Figure 3.3B, inset, and 3.S1). Therefore, the different species accessed by the protein are reversible as their population depends on the solution environment. Under native conditions (Figure 3.8A), the N-state of TDP-43^{tRRM} is the most stable conformation. Therefore, this energy minima is favored by a majority of the TDP-43^{tRRM} molecules. The calculated value of ΔG_{NU}^{H2O} at pH 7.5 is 4.74 kcal mol^{-1}. This translates into 3 unfolded molecules per 10000 molecules of TDP-43^{tRRM}. This suggests that only 3 molecules are able to traverse the energy landscape to non-native minima at equilibrium, while remaining molecules populate the N-state. These molecules are not enough to trigger self-assembly to amyloid-like aggregates and therefore, aggregated conformation is not favored under native conditions. In contrast, the low-pH stress destabilizes the native-state of TDP-43^{tRRM} (Figure 3.8B). The calculated value of ΔG_{NU}^{H2O} at pH 5.0 is 2.78 kcal mol^{-1}, which translates to 91 unfolded molecules per 10000 molecules of TDP-43^{tRRM}. Therefore, compared to native conditions, a higher number of TDP-43^{tRRM} molecules (30 times higher) could traverse the energy landscape. Some of these conformers could be aggregation prone (partially unfolded forms), hence can interact with each other with their exposed hydrophobic patches to undergo amyloid-like aggregation (amyloid fibrils). Therefore, destabilization of TDP-43^{tRRM} allows it to access the aggregation energy landscape. The pH-dependent destabilization is observed by thermal denaturation experiments as well (Figure 3.7). Interestingly, we observed that ss$(TG)_6$ binding stabilizes N-state of TDP-43^{tRRM} in both the native and the stress-like conditions (Figure 3.7). The T_m of DNA-bound protein at pH 5.0 is 327 K which is similar to the T_m of the unbound protein at pH 6.5 (328.75) (Figure 3.7B). Hence, for the DNA-bound protein the N-state of TDP-43^{tRRM} is thermodynamically favored even at low pH conditions. It is also interesting to note that the change in T_m as a function of pH is much

shallower for the DNA bound protein compared to the unbound protein. For the free protein, the value of T_m changes by ~ 9 K as we move from pH 7.5 to 5.0, but it changes only by ~ 5 K for the DNA-bound protein (Figure 3.7B). These results indicate that the DNA-bound protein is much better able to tolerate low-pH stress. Overall, our results indicate that specific ss(DNA) binding modulates the energy landscape of TDP-43^{tRRM} such that the N-state of TDP-43^{tRRM} gets populated and very few partially or fully unfolded-like molecules are available for interactions, and hence amyloid-like aggregation is inhibited even in stress conditions (Figure 3.8C).

The inhibition of amyloid-like aggregation and the stabilization of TDP-43^{tRRM} in the presence of DNA indicates that the protein regions involved in the DNA binding are also involved in the amyloid-like aggregation of the protein. It appears that the DNA binding interferes with the non-native interactions between the two protein molecules that trigger aggregation. The hydrogen-deuterium studies coupled to mass spectrometry are ongoing in the laboratory to identify the amino acid residues responsible for amyloid-like aggregation and inhibition. Nevertheless, our observations are in line with a few recent studies that show that the functionally important regions of the proteins are the same region that promotes aggregation.[84]

The stabilization of aggregation prone proteins by ligands hold therapeutic importance. A conceptual advantage of the protein stabilization strategy is that stabilizing the native protein conformation prevents the formation of all the non-native conformations (non-native monomers, oligomers, fibrils), thereby having a mass effect on disease control. It is interesting to know that a FDA approved drug, Tafamidis[85] which is used to treat transthyretin (TTR)-related hereditary amyloidosis stabilizes the tetramer of the native TTR, thereby preventing its dissociation into monomers and hence aggregation. The natural DNA aptamer reported in this study targets the monomeric TDP-43^{tRRM}, stabilizes it and inhibits amyloid-like aggregation. Therefore, we propose that nucleic acid like molecules which can modulate the thermodynamic energy landscape and hence aggregation behavior of TDP-43^{tRRM} could be prime candidates for therapeutic intervention in TDP-43-associated proteinopathies.

3.5 References

(1) D. Arseni, M. Hasegawa, A.G. Murzin, F. Kametani, M. Arai, M. Yoshida, B. Ryskeldi-Falcon, Structure of Pathological TDP-43 Filaments from ALS with FTLD, Nature. 601 (2022) 139–143. https://doi.org/10.1038/s41586-021-04199-3.

(2) B.D. Freibaum, R.K. Chitta, A.A. High, J.P. Taylor, Global Analysis of TDP-43 Interacting Proteins Reveals Strong Association with RNA Splicing and Translation Machinery, J. Proteome Res. 9 (2010) 1104–1120. https://doi.org/10.1021/pr901076y.

(3) I.-F. Wang, L.-S. Wu, C.-K.J. Shen, TDP-43: an Emerging New Player in Neurodegenerative Diseases, Trends Mol. Med. 14 (2008) 479–485. https://doi.org/10.1016/j.molmed.2008.09.001.

(4) P.-H. Kuo, C.-H. Chiang, Y.-T. Wang, L.G. Doudeva, H.S. Yuan, The Crystal Structure of TDP-43 RRM1-DNA Complex Reveals the Specific Recognition for UG- and TG-Rich Nucleic Acids, Nucleic Acids Res. 42 (2014) 4712–4722. https://doi.org/10.1093/nar/gkt1407.

(5) L. François-Moutal, S. Perez-Miller, D.D. Scott, V.G. Miranda, N. Mollasalehi, M. Khanna, Structural Insights Into TDP-43 and Effects of Post-translational Modifications, Front. Mol. Neurosci. 12 (2019). https://doi.org/10.3389/fnmol.2019.00301.

(6) P.-H. Kuo, L.G. Doudeva, Y.-T. Wang, C.-K.J. Shen, H.S. Yuan, Structural Insights into TDP-43 in Nucleic-Acid Binding and Domain Interactions, Nucleic Acids Res. 37 (2009) 1799–1808. https://doi.org/10.1093/nar/gkp013.

(7) Y.M. Ayala, P. Zago, A. D'Ambrogio, Y.-F. Xu, L. Petrucelli, E. Buratti, F.E. Baralle, Structural Determinants of the Cellular Localization and Shuttling of TDP-43, J. Cell Sci. 121 (2008) 3778–3785. https://doi.org/10.1242/jcs.038950.

(8) H. Ederle, D. Dormann, TDP-43 and FUS en Route From the Nucleus to the Cytoplasm, FEBS Lett. 591 (2017) 1489–1507. https://doi.org/10.1002/1873-3468.12646.

(9) E. Buratti, F.E. Baralle, Characterization and Functional Implications of the RNA Binding Properties of Nuclear Factor TDP-43, a Novel Splicing Regulator of CFTR Exon 9, J. Biol. Chem. 276 (2001) 36337–36343. https://doi.org/10.1074/jbc.M104236200.

(10) J.R. Tollervey, T. Curk, B. Rogelj, M. Briese, M. Cereda, M. Kayikci, J. König, T. Hortobágyi, A.L. Nishimura, V. Zupunski, R. Patani, S. Chandran, G. Rot, B. Zupan, C.E. Shaw, J. Ule, Characterizing the RNA Targets and Position-Dependent Splicing Regulation by TDP-43, Nat. Neurosci. 14 (2011) 452–458. https://doi.org/10.1038/nn.2778.

(11) M. Polymenidou, C. Lagier-Tourenne, K.R. Hutt, S.C. Huelga, J. Moran, T.Y. Liang, S.-C. Ling, E. Sun, E. Wancewicz, C. Mazur, H. Kordasiewicz, Y. Sedaghat, J.P. Donohue, L. Shiue, C.F. Bennett, G.W. Yeo, D.W. Cleveland, Long pre-mRNA Depletion and RNA Missplicing Contribute to Neuronal Vulnerability from Loss of TDP-43, Nat. Neurosci. 14 (2011) 459–468. https://doi.org/10.1038/nn.2779.

(12) A.N. Coyne, B.B. Siddegowda, P.S. Estes, J. Johannesmeyer, T. Kovalik, S.G. Daniel, A. Pearson, R. Bowser, D.C. Zarnescu, Futsch/MAP1B mRNA is a Translational Target of TDP-43 and is Neuroprotective in a Drosophila Model of Amyotrophic Lateral Sclerosis, J. Neurosci. 34 (2014) 15962–15974. https://doi.org/10.1523/JNEUROSCI.2526-14.2014.

(13) A. Russo, R. Scardigli, F. La Regina, M.E. Murray, N. Romano, D.W. Dickson, B. Wolozin, A. Cattaneo, M. Ceci, Increased Cytoplasmic TDP-43 Reduces Global Protein Synthesis by Interacting with RACK1 on Polyribosomes, Hum. Mol. Genet. 26 (2017) 1407–1418. https://doi.org/10.1093/hmg/ddx035.

(14) Y. Kawahara, A. Mieda-Sato, TDP-43 Promotes microRNA Biogenesis as a Component of the Drosha and Dicer Complexes, Proc. Natl. Acad. Sci. U.S.A. 109 (2012) 3347–3352. https://doi.org/10.1073/pnas.1112427109.
(15) C.F. Sephton, S.K. Good, S. Atkin, C.M. Dewey, P. Mayer, J. Herz, G. Yu, TDP-43 is a Developmentally Regulated Protein Essential for Early Embryonic Development, J. Biol. Chem. 285 (2010) 6826–6834. https://doi.org/10.1074/jbc.M109.061846.
(16) C.F. Sephton, B. Cenik, B.K. Cenik, J. Herz, G. Yu, TDP-43 in Central Nervous System Development and Function: Clues to TDP-43-Associated Neurodegeneration, Biol. Chem. 393 (2012) 589–594. https://doi.org/10.1515/hsz-2012-0115.
(17) M.J. Strong, K. Volkening, R. Hammond, W. Yang, W. Strong, C. Leystra-Lantz, C. Shoesmith, TDP43 is a Human Low Molecular Weight Neurofilament (hNFL) mRNA-Binding Protein, Mol. Cell. Neurosci. 35 (2007) 320–327. https://doi.org/10.1016/j.mcn.2007.03.007.
(18) K. Volkening, C. Leystra-Lantz, W. Yang, H. Jaffee, M.J. Strong, TAR DNA Binding Protein of 43 kDa (TDP-43), 14-3-3 Proteins and Copper/Zinc Superoxide Dismutase (SOD1) Interact to Modulate NFL mRNA Stability. Implications for Altered RNA Processing in Amyotrophic Lateral Sclerosis (ALS), Brain Res. 1305 (2009) 168–182. https://doi.org/10.1016/j.brainres.2009.09.105.
(19) C. Colombrita, E. Onesto, F. Megiorni, A. Pizzuti, F.E. Baralle, E. Buratti, V. Silani, A. Ratti, TDP-43 and FUS RNA-Binding Proteins Bind Distinct Sets of Cytoplasmic Messenger RNAs and Differently Regulate Their Post-Transcriptional Fate in Motoneuron-Like Cells, J. Biol. Chem. 287 (2012) 15635–15647. https://doi.org/10.1074/jbc.M111.333450.
(20) L. Costessi, F. Porro, A. Iaconcig, A.F. Muro, TDP-43 Regulates β-adducin (Add2) Transcript Stability, RNA Biol. 11 (2014) 1280–1290. https://doi.org/10.1080/15476286.2014.996081.
(21) N.H. Alami, R.B. Smith, M.A. Carrasco, L.A. Williams, C.S. Winborn, S.S.W. Han, E. Kiskinis, B. Winborn, B.D. Freibaum, A. Kanagaraj, A.J. Clare, N.M. Badders, B. Bilican, E. Chaum, S. Chandran, C.E. Shaw, K.C. Eggan, T. Maniatis, J.P. Taylor, Axonal Transport of TDP-43 mRNA Granules is Impaired by ALS-Causing Mutations, Neuron. 81 (2014) 536–543. https://doi.org/10.1016/j.neuron.2013.12.018.
(22) Y.M. Ayala, L. De Conti, S.E. Avendaño-Vázquez, A. Dhir, M. Romano, A. D'Ambrogio, J. Tollervey, J. Ule, M. Baralle, E. Buratti, F.E. Baralle, TDP-43 Regulates its mRNA Levels Through a Negative Feedback Loop, EMBO J. 30 (2011) 277–288. https://doi.org/10.1038/emboj.2010.310.
(23) M. Neumann, D.M. Sampathu, L.K. Kwong, A.C. Truax, M.C. Micsenyi, T.T. Chou, J. Bruce, T. Schuck, M. Grossman, C.M. Clark, L.F. McCluskey, B.L. Miller, E. Masliah, I.R. Mackenzie, H. Feldman, W. Feiden, H.A. Kretzschmar, J.Q. Trojanowski, V.M.-Y. Lee, Ubiquitinated TDP-43 in Frontotemporal Lobar Degeneration and Amyotrophic Lateral Sclerosis, Science. 314 (2006) 130–133. https://doi.org/10.1126/science.1134108.
(24) T. Nonaka, F. Kametani, T. Arai, H. Akiyama, M. Hasegawa, Truncation and Pathogenic Mutations Facilitate the Formation of Intracellular Aggregates of TDP-43, Hum. Mol. Genet. 18 (2009) 3353–3364. https://doi.org/10.1093/hmg/ddp275.
(25) M.C. Kiernan, S. Vucic, B.C. Cheah, M.R. Turner, A. Eisen, O. Hardiman, J.R. Burrell, M.C. Zoing, Amyotrophic Lateral Sclerosis, Lancet. 377 (2011) 942–955. https://doi.org/10.1016/S0140-6736(10)61156-7.

(26) T. Arai, M. Hasegawa, H. Akiyama, K. Ikeda, T. Nonaka, H. Mori, D. Mann, K. Tsuchiya, M. Yoshida, Y. Hashizume, T. Oda, TDP-43 is a Component of Ubiquitin-Positive Tau-Negative Inclusions in Frontotemporal Lobar Degeneration and Amyotrophic Lateral Sclerosis, Biochem. Biophys. Res. Commun. 351 (2006) 602–611. https://doi.org/10.1016/j.bbrc.2006.10.093.

(27) G.D. Rabinovici, B.L. Miller, Frontotemporal Lobar Degeneration, CNS Drugs. 24 (2010) 375–398. https://doi.org/10.2165/11533100-000000000-00000.

(28) C. Schwab, T. Arai, M. Hasegawa, S. Yu, P.L. McGeer, Colocalization of Transactivation-Responsive DNA-Binding Protein 43 and Huntingtin in Inclusions of Huntington Disease, J. Neuropathol. Exp. Neurol. 67 (2008) 1159–1165. https://doi.org/10.1097/NEN.0b013e31818e8951.

(29) X.-L. Chang, M.-S. Tan, L. Tan, J.-T. Yu, The Role of TDP-43 in Alzheimer's Disease, Mol. Neurobiol. 53 (2016) 3349–3359. https://doi.org/10.1007/s12035-015-9264-5.

(30) A. Meneses, S. Koga, J. O'Leary, D.W. Dickson, G. Bu, N. Zhao, TDP-43 Pathology in Alzheimer's Disease, Mol. Neurodegener. 16 (2021) 84. https://doi.org/10.1186/s13024-021-00503-x.

(31) K. Markopoulou, D.W. Dickson, R.D. McComb, Z.K. Wszolek, L. Katechalidou, L. Avery, M.S. Stansbury, B.A. Chase, Clinical, Neuropathological and Genotypic Variability in SNCA A53T Familial Parkinson's Disease. Variability in Familial Parkinson's Disease, Acta Neuropathol. 116 (2008) 25–35. https://doi.org/10.1007/s00401-008-0372-4.

(32) A.S. Chen-Plotkin, V.M.-Y. Lee, J.Q. Trojanowski, TAR DNA-Binding Protein 43 in Neurodegenerative Disease, Nat. Rev. Neurol. 6 (2010) 211–220. https://doi.org/10.1038/nrneurol.2010.18.

(33) E.B. Lee, V.M.-Y. Lee, J.Q. Trojanowski, Gains or Losses: Molecular Mechanisms of TDP43-Mediated Neurodegeneration, Nat. Rev. Neurosci. 13 (2012) 38–50. https://doi.org/10.1038/nrn3121.

(34) F. Geser, V.M.-Y. Lee, J.Q. Trojanowski, Amyotrophic Lateral Sclerosis and Frontotemporal Lobar Degeneration: A Spectrum of TDP-43 Proteinopathies, Neuropathol. 30 (2010) 103–112. https://doi.org/10.1111/j.1440-1789.2009.01091.x.

(35) E.M.J. de Boer, V.K. Orie, T. Williams, M.R. Baker, H.M. De Oliveira, T. Polvikoski, M. Silsby, P. Menon, M. van den Bos, G.M. Halliday, L.H. van den Berg, L. Van Den Bosch, P. van Damme, M.C. Kiernan, M.A. van Es, S. Vucic, TDP-43 Proteinopathies: A New Wave of Neurodegenerative Diseases, J. Neurol. Neurosurg. Psychiatry. 92 (2020) 86-95. https://doi.org/10.1136/jnnp-2020-322983.

(36) L.-L. Jiang, M.-X. Che, J. Zhao, C.-J. Zhou, M.-Y. Xie, H.-Y. Li, J.-H. He, H.-Y. Hu, Structural Transformation of the Amyloidogenic Core Region of TDP-43 Protein Initiates its Aggregation and Cytoplasmic Inclusion, J. Biol. Chem. 288 (2013) 19614–19624. https://doi.org/10.1074/jbc.M113.463828.

(37) A.K.-H. Chen, R.Y.-Y. Lin, E.Z.-J. Hsieh, P.-H. Tu, R.P.-Y. Chen, T.-Y. Liao, W. Chen, C.-H. Wang, J.J.-T. Huang, Induction of Amyloid Fibrils by the C-Terminal Fragments of TDP-43 in Amyotrophic Lateral Sclerosis, J. Am. Chem. Soc. 132 (2010) 1186–1187. https://doi.org/10.1021/ja9066207.

(38) M. Udan, R.H. Baloh, Implications of the Prion-Related Q/N Domains in TDP-43 and FUS, Prion. 5 (2011) 1–5. https://doi.org/10.4161/pri.5.1.14265.

(39) R.A. Fuentealba, M. Udan, S. Bell, I. Wegorzewska, J. Shao, M.I. Diamond, C.C. Weihl, R.H. Baloh, Interaction with Polyglutamine Aggregates Reveals a Q/N-rich Domain in TDP-43, J. Biol. Chem. 285 (2010) 26304–26314. https://doi.org/10.1074/jbc.M110.125039.
(40) A. Saini, V.S. Chauhan, Delineation of the Core Aggregation Sequences of TDP-43 C-terminal Fragment, Chembiochem. 12 (2011) 2495–2501. https://doi.org/10.1002/cbic.201100427.
(41) M. Budini, E. Buratti, C. Stuani, C. Guarnaccia, V. Romano, L. De Conti, F.E. Baralle, Cellular Model of TAR DNA-binding Protein 43 (TDP-43) Aggregation Based on its C-Terminal Gln/Asn-rich Region, J. Biol. Chem. 287 (2012) 7512–7525. https://doi.org/10.1074/jbc.M111.288720.
(42) K. Nishino, S. Watanabe, J. Shijie, Y. Murata, K. Oiwa, O. Komine, F. Endo, H. Tsuiji, M. Abe, K. Sakimura, A. Mishra, K. Yamanaka, Mice Deficient in the C-Terminal Domain of TAR DNA-Binding Protein 43 Develop Age-Dependent Motor Dysfunction Associated with Impaired Notch1−Akt Signaling Pathway, Acta Neuropathol. Commun. 7 (2019) 118. https://doi.org/10.1186/s40478-019-0776-5.
(43) W. Guo, Y. Chen, X. Zhou, A. Kar, P. Ray, X. Chen, E.J. Rao, M. Yang, H. Ye, L. Zhu, J. Liu, M. Xu, Y. Yang, C. Wang, D. Zhang, E.H. Bigio, M. Mesulam, Y. Shen, Q. Xu, K. Fushimi, J.Y. Wu, An ALS-Associated Mutation Affecting TDP-43 Enhances Protein Aggregation, Fibril Formation and Neurotoxicity, Nat. Struct. Mol. Biol. 18 (2011) 822–830. https://doi.org/10.1038/nsmb.2053.
(44) L.M. Igaz, L.K. Kwong, A. Chen-Plotkin, M.J. Winton, T.L. Unger, Y. Xu, M. Neumann, J.Q. Trojanowski, V.M.-Y. Lee, Expression of TDP-43 C-Terminal Fragments in Vitro Recapitulates Pathological Features of TDP-43 Proteinopathies, J. Biol. Chem. 284 (2009) 8516–8524. https://doi.org/10.1074/jbc.M809462200.
(45) Y.-J. Zhang, Y.-F. Xu, C. Cook, T.F. Gendron, P. Roettges, C.D. Link, W.-L. Lin, J. Tong, M. Castanedes-Casey, P. Ash, J. Gass, V. Rangachari, E. Buratti, F. Baralle, T.E. Golde, D.W. Dickson, L. Petrucelli, Aberrant Cleavage of TDP-43 Enhances Aggregation and Cellular Toxicity, Proc. Natl. Acad. Sci. U.S.A. 106 (2009) 7607–7612. https://doi.org/10.1073/pnas.0900688106.
(46) M. Hasegawa, T. Arai, T. Nonaka, F. Kametani, M. Yoshida, Y. Hashizume, T.G. Beach, E. Buratti, F. Baralle, M. Morita, I. Nakano, T. Oda, K. Tsuchiya, H. Akiyama, Phosphorylated TDP-43 in Frontotemporal Lobar Degeneration and Amyotrophic Lateral Sclerosis, Ann. Neurol. 64 (2008) 60–70. https://doi.org/10.1002/ana.21425.
(47) M.-X. Che, Y.-J. Jiang, Y.-Y. Xie, L.-L. Jiang, H.-Y. Hu, Aggregation of the 35-kDa Fragment of TDP-43 Causes Formation of Cytoplasmic Inclusions and Alteration of RNA Processing, FASEB J. 25 (2011) 2344–2353. https://doi.org/10.1096/fj.10-174482.
(48) Y. Liu, W. Duan, Y. Guo, Z. Li, H. Han, S. Zhang, P. Yuan, C. Li, A New Cellular Model of Pathological TDP-43: The Neurotoxicity of Stably Expressed CTF25 of TDP-43 Depends on the Proteasome, Neuroscience. 281 (2014) 88–98. https://doi.org/10.1016/j.neuroscience.2014.09.043.
(49) D.X. Medina, M.E. Orr, S. Oddo, Accumulation of C-Terminal Fragments of Transactive Response DNA-Binding Protein 43 Leads to Synaptic Loss and Cognitive Deficits in Human TDP-43 Transgenic Mice, Neurobiol. Aging. 35 (2014) 79–87. https://doi.org/10.1016/j.neurobiolaging.2013.07.006.
(50) A. Prasad, V. Sivalingam, V. Bharathi, A. Girdhar, B.K. Patel, The Amyloidogenicity of a C-Terminal Region of TDP-43 Implicated in Amyotrophic Lateral Sclerosis can be Affected

by Anions, Acetylation and Homodimerization, Biochimie. 150 (2018) 76–87. https://doi.org/10.1016/j.biochi.2018.05.003.

(51) A.E. Conicella, G.H. Zerze, J. Mittal, N.L. Fawzi, ALS Mutations Disrupt Phase Separation Mediated by α-Helical Structure in the TDP-43 Low Complexity C-Terminal Domain, Structure. 1993. 24 (2016) 1537–1549. https://doi.org/10.1016/j.str.2016.07.007.

(52) H.-R. Li, T.-C. Chen, C.-L. Hsiao, L. Shi, C.-Y. Chou, J. Huang, The Physical Forces Mediating Self-Association and Phase-Separation in the C-Terminal Domain of TDP-43, Biochim. Biophys. Acta Proteins Proteom. 1866 (2018) 214–223. https://doi.org/10.1016/j.bbapap.2017.10.001.

(53) Y. Shiina, K. Arima, H. Tabunoki, J. Satoh, TDP-43 Dimerizes in Human Cells in Culture, Cell. Mol. Neurobiol. 30 (2010) 641–652. https://doi.org/10.1007/s10571-009-9489-9.

(54) M. Vivoli-Vega, P. Guri, F. Chiti, F. Bemporad, Insight into the Folding and Dimerization Mechanisms of the N-Terminal Domain from Human TDP-43, Int. J. Mol. Sci. 21 (2020) 6259. https://doi.org/10.3390/ijms21176259.

(55) C. ke Chang, T.H. Wu, C.Y. Wu, M. hui Chiang, E.K.W. Toh, Y.C. Hsu, K.F. Lin, Y. heng Liao, T. huang Huang, J.J.T. Huang, The N-Terminus of TDP-43 Promotes its Oligomerization and Enhances DNA Binding Affinity, Biochem. Biophys. Res. Commun. 425 (2012) 219–224. https://doi.org/10.1016/j.bbrc.2012.07.071.

(56) L.-L. Jiang, W. Xue, J.-Y. Hong, J.-T. Zhang, M.-J. Li, S.-N. Yu, J.-H. He, H.-Y. Hu, The N-Terminal Dimerization is Required for TDP-43 Splicing Activity, Sci. Rep. 7 (2017) 6196. https://doi.org/10.1038/s41598-017-06263-3.

(57) A. Wang, A.E. Conicella, H.B. Schmidt, E.W. Martin, S.N. Rhoads, A.N. Reeb, A. Nourse, D. Ramirez Montero, V.H. Ryan, R. Rohatgi, F. Shewmaker, M.T. Naik, T. Mittag, Y.M. Ayala, N.L. Fawzi, A Single N-Terminal Phosphomimic Disrupts TDP-43 Polymerization, Phase Separation, and RNA Splicing, EMBO J. 37 (2018) e97452. https://doi.org/10.15252/embj.201797452.

(58) Y.-J. Zhang, T. Caulfield, Y.-F. Xu, T.F. Gendron, J. Hubbard, C. Stetler, H. Sasaguri, E.C. Whitelaw, S. Cai, W.C. Lee, L. Petrucelli, The Dual Functions of the Extreme N-Terminus of TDP-43 in Regulating its Biological Activity and Inclusion Formation, Hum. Mol. Genet. 22 (2013) 3112–3122. https://doi.org/10.1093/hmg/ddt166.

(59) A. Shodai, A. Ido, N. Fujiwara, T. Ayaki, T. Morimura, M. Oono, Conserved Acidic Amino Acid Residues in a Second RNA Recognition Motif Regulate Assembly and Function of TDP-43, PloS one. 7 (2012) e52776. https://doi.org/10.1371/journal.pone.0052776.

(60) A. Shodai, T. Morimura, A. Ido, T. Uchida, T. Ayaki, R. Takahashi, S. Kitazawa, S. Suzuki, M. Shirouzu, T. Kigawa, Y. Muto, S. Yokoyama, R. Takahashi, R. Kitahara, H. Ito, N. Fujiwara, M. Urushitani, Aberrant Assembly of RNA Recognition Motif 1 Links to Pathogenic Conversion of TAR DNA-Binding Protein of 43 kDa (TDP-43), J. Biol. Chem. 288 (2013) 14886–14905. https://doi.org/10.1074/jbc.M113.451849.

(61) S. Agrawal, P.-H. Kuo, L.-Y. Chu, B. Golzarroshan, M. Jain, H.S. Yuan, RNA Recognition Motifs of Disease-Linked RNA-Binding Proteins Contribute to Amyloid Formation, Sci. Rep. 9 (2019) 6171. https://doi.org/10.1038/s41598-019-42367-8.

(62) M. Pillai, S.K. Jha, The Folding and Aggregation Energy Landscapes of Tethered RRM Domains of Human TDP-43 are Coupled Via a Metastable Molten Globule-Like Oligomer, Biochemistry. 58 (2019) 608–620. https://doi.org/10.1021/acs.biochem.8b01013.

(63) C. Yang, W. Tan, C. Whittle, L. Qiu, L. Cao, S. Akbarian, Z. Xu, The C-Terminal TDP-43 Fragments Have a High Aggregation Propensity and Harm Neurons by a Dominant-Negative Mechanism, PloS one. 5 (2010) e15878. https://doi.org/10.1371/journal.pone.0015878.
(64) Z.R. Grese, A.C. Bastos, L.D. Mamede, R.L. French, T.M. Miller, Y.M. Ayala, Specific RNA Interactions Promote TDP-43 Multivalent Phase Separation and Maintain Liquid Properties, EMBO Rep. 22 (2021) e53632. https://doi.org/10.15252/embr.202153632.
(65) Y. Sun, P.E. Arslan, A. Won, C.M. Yip, A. Chakrabartty, Binding of TDP-43 to the 3'UTR of its Cognate mRNA Enhances its Solubility, Biochemistry. 53 (2014) 5885–5894. https://doi.org/10.1021/bi500617x.
(66) Y.C. Huang, K.F. Lin, R.Y. He, P.H. Tu, J. Koubek, Y.C. Hsu, J.J.T. Huang, Inhibition of TDP-43 Aggregation by Nucleic Acid Binding, PLoS ONE. 8 (2013) e64002. https://doi.org/10.1371/journal.pone.0064002.
(67) J.R. Mann, A.M. Gleixner, J.C. Mauna, E. Gomes, M.R. DeChellis-Marks, P.G. Needham, K.E. Copley, B. Hurtle, B. Portz, N.J. Pyles, L. Guo, C.B. Calder, Z.P. Wills, U.B. Pandey, J.K. Kofler, J.L. Brodsky, A. Thathiah, J. Shorter, C.J. Donnelly, RNA Binding Antagonizes Neurotoxic Phase Transitions of TDP-43., Neuron. 102 (2019) 321-338.e8. https://doi.org/10.1016/j.neuron.2019.01.048.
(68) E. Zacco, R. Graña-Montes, S.R. Martin, N.S. de Groot, C. Alfano, G.G. Tartaglia, A. Pastore, RNA as a Key Factor in Driving or Preventing Self-Assembly of the TAR DNA-Binding Protein 43, J. Mol. Biol. 431 (2019) 1671–1688. https://doi.org/10.1016/j.jmb.2019.01.028.
(69) M. Pillai, S.K. Jha, Early Metastable Assembly During the Stress-Induced Formation of Worm-Like Amyloid Fibrils of Nucleic Acid Binding Domains of TDP-43, Biochemistry. 59 (2020) 315–328. https://doi.org/10.1021/acs.biochem.9b00780.
(70) D. Patni, S.K. Jha, Protonation–Deprotonation Switch Controls the Amyloid-like Misfolding of Nucleic-Acid-Binding Domains of TDP-43, J. Phys. Chem. B. 125 (2021) 8383–8394. https://doi.org/10.1021/acs.jpcb.1c03262.
(71) J. Singh, J.B. Udgaonkar, Unraveling the Molecular Mechanism of pH-Induced Misfolding and Oligomerization of the Prion Protein, J. Mol. Biol. 428 (2016) 1345–1355. https://doi.org/10.1016/j.jmb.2016.01.030.
(72) L. Stryer, The Interaction of a Naphthalene Dye with Apomyoglobin and Apohemoglobin. a Fluorescent Probe of Non-Polar Binding Sites, J. Mol. Biol. 13 (1965) 482–495. https://doi.org/10.1016/s0022-2836(65)80111-5.
(73) V.R. Agashe, J.B. Udgaonkar, Thermodynamics of Denaturation of Barstar: Evidence for Cold Denaturation and Evaluation of the Interaction with Guanidine Hydrochloride, Biochemistry. 34 (1995) 3286–3299. https://doi.org/10.1021/bi00010a019.
(74) R. Moulick, J.B. Udgaonkar, Thermodynamic Characterization of the Unfolding of the Prion Protein, Biophys. J. 106 (2014) 410–420. https://doi.org/10.1016/j.bpj.2013.11.4491.
(75) J.A. Schellman, The Thermodynamic Stability of Proteins, Annu. Rev. Biophys. Biophys. Chem. 16 (1987) 115–137. https://doi.org/10.1146/annurev.bb.16.060187.000555.
(76) B.C. Mackness, M.T. Tran, S.P. McClain, C.R. Matthews, J.A. Zitzewitz, Folding of the RNA Recognition Motif (RRM) Domains of the Amyotrophic Lateral Sclerosis (ALS)-Linked Protein TDP-43 Reveals an Intermediate State, J. Biol. Chem. 289 (2014) 8264–8276. https://doi.org/10.1074/jbc.M113.542779.
(77) H. Naiki, F. Gejyo, Kinetic Analysis of Amyloid Fibril Formation, Methods Enzymol. 309 (1999) 305–318. https://doi.org/10.1016/s0076-6879(99)09022-9.

(78) S. Jain, J.B. Udgaonkar, Evidence for Stepwise Formation of Amyloid Fibrils by the Mouse Prion Protein, J. Mol. Biol. 382 (2008) 1228–1241. https://doi.org/10.1016/j.jmb.2008.07.052.

(79) K. Nasreen, Z.A. Parray, S. Ahamad, F. Ahmad, A. Ahmed, S. Freeh Alamery, T. Hussain, M.I. Hassan, A. Islam, Interactions Under Crowding Milieu: Chemical-Induced Denaturation of Myoglobin is Determined by the Extent of Heme Dissociation on Interaction with Crowders, Biomolecules. 10 (2020) 490. https://doi.org/10.3390/biom10030490.

(80) S. Maharana, J. Wang, D.K. Papadopoulos, D. Richter, A. Pozniakovsky, I. Poser, M. Bickle, S. Rizk, J. Guillén-Boixet, T.M. Franzmann, M. Jahnel, L. Marrone, Y.-T. Chang, J. Sterneckert, P. Tomancak, A.A. Hyman, S. Alberti, RNA Buffers the Phase Separation Behavior of Prion-Like RNA Binding Proteins, Science. 360 (2018) 918–921. https://doi.org/10.1126/science.aar7366.

(81) H. Qin, L.-Z. Lim, Y. Wei, J. Song, TDP-43 N Terminus Encodes a Novel Ubiquitin-Like Fold and its Unfolded Form in Equilibrium that can be Shifted by Binding to ssDNA, Proc. Natl. Acad. Sci. 111 (2014) 18619–18624. https://doi.org/10.1073/pnas.1413994112.

(82) S. Xiao, T. Sanelli, H. Chiang, Y. Sun, A. Chakrabartty, J. Keith, E. Rogaeva, L. Zinman, J. Robertson, Low Molecular Weight Species of TDP-43 Generated by Abnormal Splicing form Inclusions in Amyotrophic Lateral Sclerosis and Result in Motor Neuron Death, Acta Neuropathol. (Berl.). 130 (2015) 49–61. https://doi.org/10.1007/s00401-015-1412-5.

(83) Y.-J. Zhang, Y. Xu, C.A. Dickey, E. Buratti, F. Baralle, R. Bailey, S. Pickering-Brown, D. Dickson, L. Petrucelli, Progranulin Mediates Caspase-Dependent Cleavage of TAR DNA Binding Protein-43, J. Neurosci. 27 (2007) 10530–10534. https://doi.org/10.1523/JNEUROSCI.3421-07.2007.

(84) M. Laura, N. Giuseppe, C. Lesley, V. Michele, P. Annalisa, Functional Interactions as a Survival Strategy Against Abnormal Aggregation, FASEB J. 25 (2011) 45–54. https://doi.org/10.1096/fj.10-161208.

(85) C.E. Bulawa, S. Connelly, M. Devit, L. Wang, C. Weigel, J.A. Fleming, J. Packman, E.T. Powers, R.L. Wiseman, T.R. Foss, I.A. Wilson, J.W. Kelly, R. Labaudinière, Tafamidis, a Potent and Selective Transthyretin Kinetic Stabilizer that Inhibits the Amyloid Cascade, Proc. Natl. Acad. Sci. U. S. A. 109 (2012) 9629–9634. https://doi.org/10.1073/pnas.1121005109.

3.6 Supporting figures

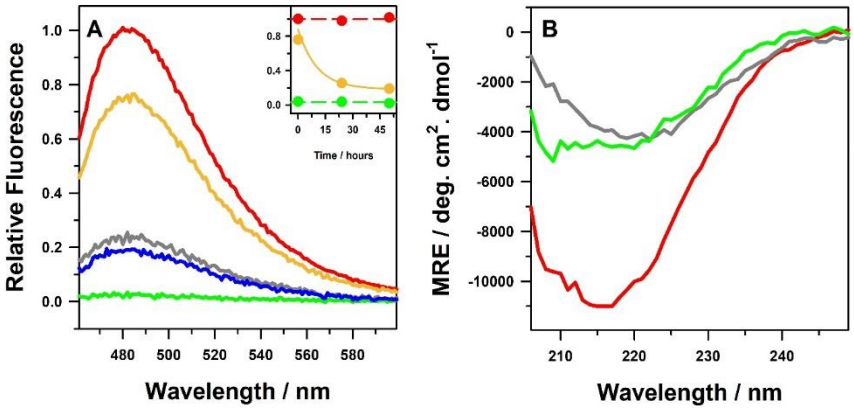

Figure 3.S1 The N⇌β transition is reversible. (A) Dissociation kinetics of the β form upon jumping to the pH 7.5 buffer monitored by ThT assay. The ThT fluorescence spectra of βtoN jump at 35 s (solid dark yellow line), 24 hours (solid dark gray line), and 50 hours (solid blue line) are compared to βtoβ jump (solid red line) and NtoN jump (solid green line). Inset shows the dissociation kinetics of β form (yellow dots) monitored at 482 nm. For comparison, the relative ThT fluorescence at 482 nm of βtoβ jump (red dots) and NtoN jump (green dots) at various time points have also been shown. (B) Far-UV CD spectrum of βtoN jump at 24 hours (dark gray) is compared with equilibrated βtoβ jump (red) and equilibrated NtoN jump (green).

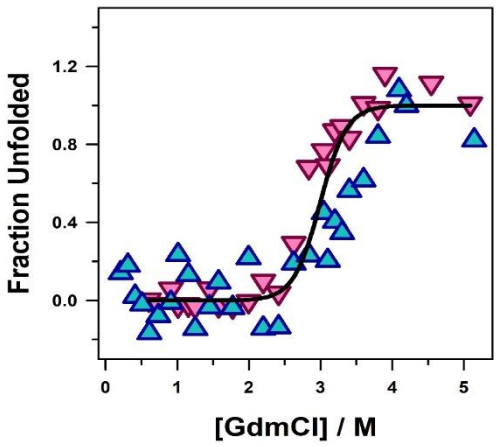

Figure 3.S2 The β⇌U transition is reversible. The fraction unfolded calculated from the unfolding transition of β form (blue, triangle-up) is compared with the fraction unfolded calculated from the misfolding transition of the U-state (pink, triangle-down). The expected changes in the fraction unfolded estimated from the misfolding transition of the U-state depict the reversibility of the β⇌U transition. The solid line is a simulated fit to equation 3.5.

Chapter 4

DNA-mediated complex coacervation of the nucleic acid-binding domain of TAR DNA binding protein (TDP-43) prevents its amyloid-like misfolding

4.1 Introduction

Environmental insults leading to cellular stress can compromise the entire homeostasis of the cell.[1] An important rapid mechanism the cells employ to recover their homeostasis is the modulation of gene expression. The modulation is achieved by stalling the translation of the mRNA associated with the housekeeping proteins and triggering the translation of the mRNA coding for repair proteins.[2–5] It has been proposed that stalled mRNA and their associated proteins sequester into a membrane-less structure called stress granules (SGs) resulting from liquid-liquid phase-separation.[3,6–9] The phase separation could be driven by one biomolecule (simple coacervation) or the opposite charge interaction of two or more different biomolecules (complex coacervation).[10] Stresses such as nutrient deprivation, oxidation stress, heat, and UV irradiation instigate reversible SGs formation in a wide range of organisms.[4,5,11–14] Interestingly, the composition of the SGs varies with the stress conditions. However, some biomolecules are consistently sequestered into the granules, including various translation initiation factors, functionally diverse proteins like RNA binding proteins, and various RNA and signaling molecules. Different RNA binding proteins sequester into the globules depending on the cell and the stress type.[21,22] Recently, it has been reported that TDP-43 (transactive response DNA binding protein – 43 kDa), a nucleic binding protein involved in neurodegenerative diseases,[23,24] is also associated with SGs.[25–28] TDP-43 is a ubiquitously expressed and conserved multidomain protein (Figure 4.S1) consisting of N-terminal domain[29] (NTD), RNA recognition motifs 1 and 2[30] (RRM1 and RRM2: primary functional domain, referred to as TDP-43^{tRRM}, hereafter), and a largely disordered C-terminal domain[31] (CTD). It performs many functions involving RNA binding in the nucleus and the cytoplasm.[32–46] The phase separation of TDP-43 upon stress sensing and its association with the SGs suggests the crucial roles played by TDP-43 in stress regulation and mitigation. However, the principles governing its phase separation are not completely known.

Though the function and formation of phase-separated coacervates are increasingly becoming evident, their link to amyloid-like aggregation remains ambiguous. Multiple groups have reported a range of achievable material states of the resultant phase-separated assemblies ranging from liquids to gels to solid-like dynamics.[47–51] Of key interest, alterations in the dynamics of the phase-separated coacervates, leading to their maturation, have been linked to various diseases.[48,52] Here, by maturation, we refer to coarsening and loss in the dynamicity of the previously dynamic phase-

separated assemblies. For instance, in-vitro and cellular studies on α-synuclein proposes that the maturation of the liquid-liquid phase separated globules leads to its amyloid-like aggregation.[51] In addition, phase separation of Tau and FUS culminates into amyloid-like aggregation.[50,53] Moreover, mutations are also reported to increase the aggregation propensity of the phase-separated SGs as a result of their maturation.[31,50,54] On the contrary, some evidence suggests that phase separation is a strategy employed by the cells to mitigate stress conditions. The studies claim that certain proteins phase separate into less dynamic globules in response to environmental stress to promote cellular fitness. For instance, Pab1 and Pub1 have been studied to undergo phase separation under pH, temperature, and nutrient starvation stress.[55,56] Ded1p and Sup35 undergo phase separation as a result of heat shock and low pH stress, respectively.[57,58] Therefore, it is not clear whether the phase-separated coacervates perform a toxic or protective role.

The role of phase-separated coacervates is also debatable in the case of TDP-43. Full-length TDP-43 (FLTDP-43) has recently been shown to phase separate to less dynamic globules.[59] In many cases, the phase separation of TDP-43 is associated with its prion-like or low-complexity C-terminal domain (CTD).[31,60,61] For instance, some studies on the low-complexity domain CTD of TDP-43 report that phase separation paves the path for amyloid-like aggregates.[62–64] The droplets were shown to accelerate the amyloid-like aggregation of fragments.[61,65] In addition to CTD, a single critical residue (S48) in NTD aids in the phase separation of TDP-43.[66,67] NTD is also reported to enhance the liquid-liquid phase separation of TDP-43.[68] However, the construct containing NTD and a linker sequence aggregated into fibril-like structures.[68] These reports suggest that various hotspots trigger the phase separation of TDP-43. However, the role of TDP-43^{tRRM} in phase separation is unequivocally answered. The molecular interactions (specific and non-specific) and physical forces driving the phase separation of TDP-43^{tRRM} are not known. In addition, the modulating effects of nucleic acid binding on the phase separation behavior of TDP-43^{tRRM} are also not fully understood. It is not clear whether phase separation of TDP-43^{tRRM} aids in its aggregation or prevents it. Since TDP-43^{tRRM} is the primary functional domain of TDP-43 and is also a crucial part of the 35 kDa fragments implicated in diseases,[69,70] understanding various conditions that favor and regulate phase separation will prove beneficial in designing therapeutic strategies.

TDP-43^{tRRM} has been shown to sense various environmental stress such as pH,[71–74] oxidation,[75] agitation,[76] and temperature.[77] It undergoes pH-dependent amyloid-like aggregation in the presence of physiological salt concentration.[71–74] In one previous study from our lab, we have demonstrated that the DNA binding stabilizes the native-state of TDP-43^{tRRM} and maintains its native-like secondary structure.[78] In the present study we explored an alternative conformer of TDP-43^{tRRM} in the presence of DNA and pH stress. The increase in the positive charge on TDP-43^{tRRM} in low pH triggers its complex coacervation (phase separation) in the presence of anionic DNA. The complex coacervation gives rise to a large and dilute light phase (soluble state) and the biomolecule-rich dense phase (complex coacervates), which remain in equilibrium with one another. The phenomenon inhibits the amyloid-like misfolding of TDP-43^{tRRM}. In this study, phase separation will be used to intend the process, where TDP-43^{tRRM}, in the presence of DNA, assembles to form coacervates independent of their liquid, gel, or solid nature. The coacervates observed in our study ranged in size from 1-5 μm and appeared globular. We report that the coacervates have limited mobility and assemble into chain-like arrangements without fusion. We further show that coacervation is a dynamic process that depends on the solution environment. The various environmental factors which could modulate the electrostatics, like macromolecule concentrations, temperature, pH, ionic strength, and the type of binding ligand, can regulate the population of the coacervates. In addition, our results suggest that the onset of coacervation is favored at high temperatures, signifying the importance of hydrophobic interactions in the formation of coacervates. Therefore, the coacervation of TDP-43^{tRRM} is driven by electrostatics and hydrophobic interactions. We studied two disease-associated mutants (D169G and P112H) and established the inhibition of their amyloid-like aggregation in the presence of DNA. Most importantly, we present that the favorable interactions between DNA and TDP-43^{tRRM} maintain the monomeric native-like state of TDP-43^{tRRM} in the light phase. DNA and TDP-43^{tRRM} interactions are mandatory for the coacervation as weakening of interactions due to denaturant inhibits coacervation and drives the amyloid-like aggregation of the unbound TDP-43^{tRRM}. The results suggest the existence of competition among the native-state, amyloid-like β form, and complex coacervates tuned by various environmental factors. Together our results illuminate an alternate function of the RNA binding domain of TDP-43 in response to pH stress in the presence of the DNA, where it could act as a stress sensor and undergo stress-triggered coacervation to save the protein from amyloid-like aggregation. We hypothesize that additional interactions between

the nucleic acids and the RRM domain could compete with the protein-protein interactions. Altogether, these events could trigger or abolish biochemical reactions, including aggregation.

4.2 Materials and Methods

Chemicals and buffers preparation

The various chemicals used for the experiments were procured from HiMedia, Sigma, and Sisco Research Laboratories (SRL) and used directly without further purification. Different buffers that were used are as follows: 20 mM glycine-HCl for pH 3.0 - pH 3.5, 20 mM sodium acetate for pH 3.8 - pH 5.0, 20 mM 2-(N-Morpholino) ethanesulfonic acid (MES) for pH 5.2 - pH 6.2, 20 mM 3-(N-Morpholino) propanesufonic acid (MOPS) for pH 6.5 - pH 7.5. All the buffers were filtered with a 0.2 μm filter, followed by the addition of 1 mM dithiothreitol (DTT) to the buffers before use.

Purification of TDP-43^{tRRM}

Purification of the TDP-43^{tRRM} was carried out using the previously mentioned protocol.[72] Purified and His_6-tag cleaved TDP-43^{tRRM} was stored in a storage buffer (10 mM KPi, 150 mM KCl, 5% glycerol, and 1 mM DTT) at -20 °C. The purity of the TDP-43^{tRRM} was assessed by SDS-PAGE (sodium dodecyl sulfate–polyacrylamide gel electrophoresis). The protein concentration was estimated using an extinction coefficient of 15,470 M^{-1} cm^{-1}. The molecular weight of the purified and His_6 tagged-cleaved TDP-43^{tRRM} protein as determined by Synapt G2 HD mass spectrometer (Waters) was 19429 Da.

Preparation of mutant A99C TDP-43^{tRRM}

QuikChange primer design program was used to design mutation-containing primers (A99C) (https://www.agilent.com/store/primerDesignProgram.jsp). The designed primers were procured from Integrated DNA Technologies (IDT). The Quikchange Lighting kit from Agilent Technologies generated the mutant A99C plasmid from a Cys-less TDP-43^{tRRM} template (all the indigenous Cys residues were removed from the TDP-43^{tRRM} by site-directed mutagenesis). The mutations were confirmed by DNA sequencing. This was followed by the purification of A99C

TDP-43^{tRRM} using the same purification protocol as wild-type TDP-43^{tRRM}. SDS-PAGE confirmed the purity of the mutant.

Labeling of A99C TDP-43^{tRRM} with Alexa 488

20x molar excess of Alexa 488 was added to A99C TDP-43^{tRRM} at pH 8.0. The reaction mixture was stirred in the dark for 2 hours, followed by concentration to 1.0 mL using a centrifugal concentrator from GE Lifesciences with a molecular weight cut-off of 10 kDa. The concentrated labeled solution was desalted into 20 mM pH 7.5 buffer. The percentage of labeled protein was calculated as discussed previously.[79]

Preparation of ss(DNA)-TDP-43^{tRRM} sample

Single-stranded (ss) ss$(TG)_6$, ss$(CA)_6$, and ss$(TG)_{12}$ DNA oligos were procured from IDT. The lyophilized oligos were dissolved in HyPure™ Molecular Biology Grade Water (nuclease-free, deionized, distilled, GE Lifesciences) to make a stock solution of 1 M. Further dilutions were made from the stock solution as needed. The concentrations of the ss(DNA) were checked by taking absorbance at 260 nm by using an extinction coefficient of 113,000 M^{-1} cm^{-1} for ss$(TG)_6$, 119,200 M^{-1} cm^{-1} for ss$(CA)_6$, and 225,800 M^{-1} cm^{-1} for ss$(TG)_{12}$ at 260 nm. (provided in the IDT oligo manual). For DNA-bound TDP-43^{tRRM} experiments, the required ratios of the DNA and TDP-43^{tRRM} were mixed and incubated at pH 7.2 for 2 hours. All the experiments were performed on the previously incubated samples.

Circular dichroism (CD)

Far-UV CD studies were carried out on a Jasco J-815 spectropolarimeter. The following parameters were used for the spectra acquisition: data integration time - 4 s, bandwidth - 2 nm, data pitch - 1 nm, and spectrum speed - 20 nm/min. All the measurements were acquired at 25 °C unless otherwise mentioned using a cuvette with a path length of 1 mm. The concentration of the free TDP-43^{tRRM} used was 10 µM. For acquiring the far-UV CD of DNA-bound TDP-43^{tRRM}, their pre-formed complex was diluted with respective buffers to make the required concentration. Equilibrium spectra were acquired from 205 to 250 nm after 30 minutes of mixing. Each spectrum was an average of 2 individual spectra.

Equilibrium and kinetic far-UV CD experiments for a single wavelength (216 nm) were performed using data integration time - 2 s, bandwidth - 2 nm, and data pitch – 2 s. The single point MRE values plotted are an average of data acquired for 30 s. Kinetic spectra were acquired after the required concentration of the free TDP-43^{tRRM} or DNA-bound TDP-43^{tRRM} was transferred to the aggregation conditions. The dead time was calculated by calculating the time difference between adding the aggregation buffer and acquiring the first CD signal. All the equilibrium and kinetics signals were buffer corrected.

Analysis of the pH dependence of the N⇌ β transition

We have fitted the pH-dependent spectroscopic data by assuming the protonation of a single critical residue in the transition of the native-state (N) to β form, as discussed previously[71] using the scheme:

$$N + H^+ \rightleftharpoons NH^+ \rightleftharpoons \beta \qquad \text{(Scheme 4.1)}$$

In the above scheme, it is assumed that only NH^+ is capable of transitioning to β.[80] In that case, the pH dependence is that of the protonation of N and is given by a transformation of the Henderson-Hasselbalch equation:

$$Y_{obs} = \frac{Y_{NH^+} + Y_N 10^{(pH-pK_a)}}{1+10^{(pH-pK_a)}} \qquad (4.1)$$

where Y_{obs} corresponds to the observed spectroscopic signal at a particular pH value; Y_N and Y_{NH^+} correspond to the N form and the protonated NH^+ form signals, respectively. It is assumed that under the experimental conditions and the protein concentrations used in this study, $NH^+ \rightleftharpoons \beta$ equilibrium ultimately favors the β form. Hence, the amount of NH^+ equals the amount of the β form.

Right angle light scattering (RALS)

RALS intensities were measured using a Fluoromax-4 spectrofluorometer from HORIBA Scientific. Excitation and emission slits were adjusted to either 0.3 and 1 or 0.5 and 1, respectively. A quartz cuvette with a path length of 10 mm was used to acquire the signals at 400 nm. The RALS intensity plotted is an average of scattering data acquired for 10 to 30 seconds with an interval of 0.5 seconds. For equilibrium experiments, the concentration of free TDP-43^{tRRM} used was 10 μM.

For the DNA-bound experiments, the pre-formed complex of DNA-bound TDP-43^{tRRM} was diluted with respective buffers to make the required concentration. All the samples were incubated in the desired buffer for 30 minutes before acquiring the RALS.

For the estimation of the RALS kinetics, samples were incubated separately in the aggregation buffer at 25 °C in 2 mL microcentrifuge tubes. The solution was taken out at regular intervals to obtain the light scattering and plotted as a function of time. The excitation and emission slit widths were adjusted to 0.3 and 1, respectively, and the light scattering value was acquired with excitation and emission at 400 nm. All the RALS values were buffer corrected.

DIC microscopy

The images of the coacervates were acquired using Leica DM6, an upright microscope system. 100 µL of the reaction mixture was prepared under different conditions (mentioned in the results section, wherever required). The solutions were immediately placed on a microscopic slide (Blue star, India) and sandwiched with a 12 mm coverslip. The sides of the coverslip were sealed with double-sided tape. The slides were observed with the help of a 100x oil immersion objective.

Fluorescence recovery after photobleaching (FRAP)

For the FRAP study, the aggregation buffer was added to the pre-formed complex of DNA-bound TDP-43^{tRRM} (4 µM ss(TG)$_6$-10 µM TDP-43^{tRRM}) in the presence of 5-10% of the labeled TDP-43^{tRRM}. The sample was immediately spotted on the microscope slides (Blue Star, India) and sandwiched with a coverslip (Blue Star, India). The fluorophore-labeled droplets were visualized using an appropriate fluorescent channel (488 nm for Alexa 488). FRAP studies were performed on Zeiss's laser scanning confocal microscope with a 100x oil immersion objective. 100% laser power was used to bleach the edge of the freshly settled coacervate (ROI-A). The fluorescence recovery of the bleached region was recorded for 25 seconds. Along with ROI-A, the fluorescence of the two more regions: the reference region of the same or nearby coacervate (ROI-B), and a region outside the droplet to correct the background noise were also measured.

UV-VIS absorbance studies

Absorbance studies were performed on a UV 3200 spectrophotometer from LAB INDIA Analytical. The reaction mixtures containing the required ratios of the DNA and TDP-43^{tRRM} were allowed to demix at 25 °C for 30 minutes. The reaction mixtures were centrifuged at 10000 rpm for 15 minutes to separate the pellet (dense phase) and the supernatant (light phase). The protein and DNA concentration in the light and the dense phase were estimated by measuring absorbance at 280 nm and 260 nm, respectively. The absorbance of the supernatant was acquired directly. For the estimation of the concentration of biomolecules in the pellets, 500 µL of 20 mM MOPS buffer at pH 7.5 containing 8 M urea was added to it to dissolve it entirely, followed by measuring the absorbance.

For the estimation of the partition of the biomolecules, the absorbance at 260 nm (DNA estimation) and 280 nm (protein estimation) of the pellet fraction was divided by the cumulative absorbance at 260 nm and 280 nm (pellet and supernatant), respectively for all the respective samples.

Bradford assay

For the Bradford assay, 11 µM ss$(TG)_6$ was incubated with a gradient of TDP-43^{tRRM} in duplicates. pH 7.5 buffer was added to one set of tubes and pH 3.8 buffer to the other set, followed by incubation for 30 mins. The samples were centrifuged at 10000 rpm for 15 minutes to separate the supernatant and the pellet. To estimate the protein concentration of the supernatant or the soluble fraction, 20 µL Bradford's reagent was added to 480 µL of the supernatant and incubated for 15 minutes in the dark, followed by fixed point signal acquisition at 595 nm.

Size exclusion chromatography

The size exclusion chromatography was performed on AKTA Pure M FPLC systems from GE Lifesciences with the help of HiLoad™ 10/300 Superdex 75 pg column with a fractionation range from 3 kDa to 70 kDa. The void and the bed volume of the column are 7.2 mL and 23.5 mL, respectively. Free and DNA-bound TDP-43^{tRRM} were incubated in a pH 7.5 buffer to estimate molecular size under native conditions. In contrast, DNA-bound TDP-43^{tRRM} was incubated in a

pH 3.8 buffer to estimate the molecular size of TDP-43^{tRRM} in the light phase. The concentration of the free TDP-43^{tRRM} used was 8-10 μM. To estimate the size of DNA-bound TDP-43^{tRRM}, a complex containing a final concentration of 10 μM TDP-43^{tRRM} and 11 μM ss$(TG)_6$ was used. The flow rate was 0.8 mL/min, and all the experiments were performed at 4 °C.

GdmCl-mediated unfolding experiments

The GdmCl-mediated equilibrium unfolding experiments were performed at pH 3.8 on a Jasco J-815 spectropolarimeter. Pre-equilibrated DNA-bound -TDP-43^{tRRM} complexes were incubated with a gradient of GdmCl concentration, making the final DNA (ss$(TG)_6$) concentration 11 μM and final TDP-43^{tRRM} concentration 10 μM. The samples were incubated for 30 minutes to 1 hour at room temperature. Far-UV CD spectra were acquired using similar settings as mentioned above. The spectra of buffers were collected under similar settings and were subtracted from each far-UV CD spectrum.

4.3 Results

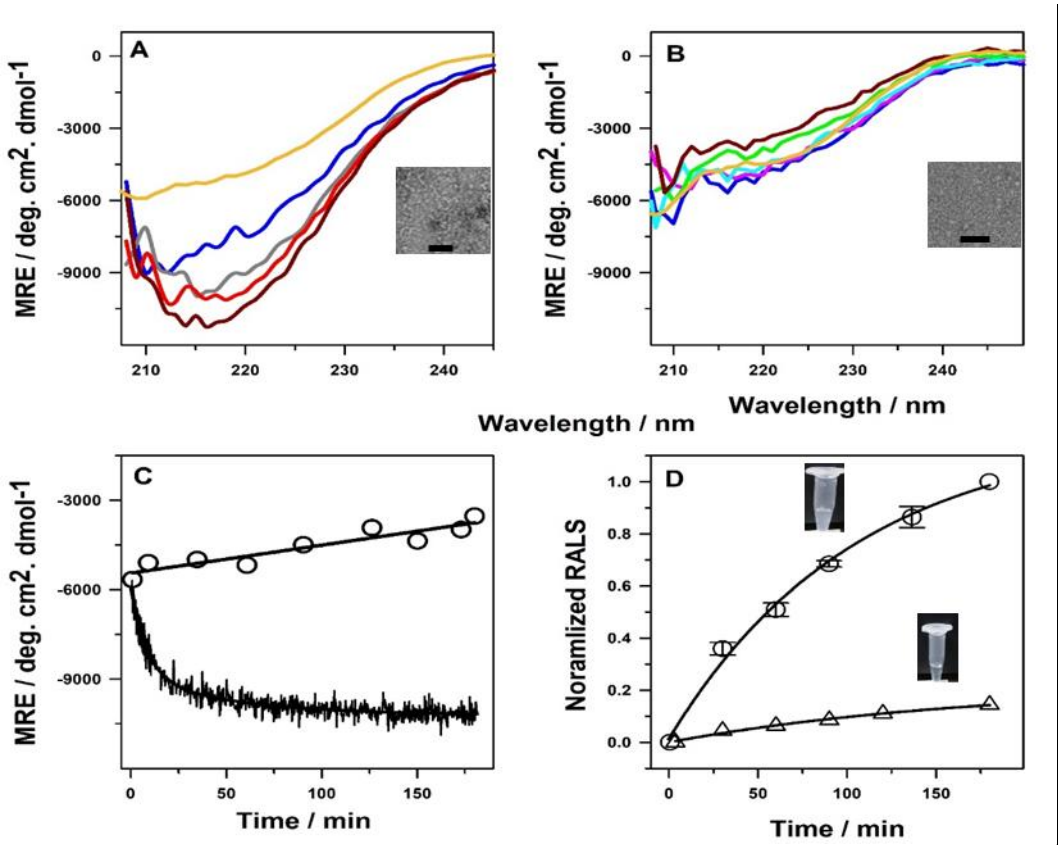

Figure 4.1 DNA mediated competition between amyloid-like aggregation and phase-separated coacervate formation. (A) Far-UV CD spectra of free TDP-43^{tRRM} acquired at pH 3.8 at different time points; 0.75 min (blue), 4 mins (gray), 7 mins (red), and 1 hour (brown). The spectra are compared with the equilibrium signal of free TDP-43^{tRRM} at pH 7.5 (yellow). Inset shows the TEM image showing the presence of small curvy assemblies at low pH. The scale represents 100 nm. (B) Far-UV CD spectra of DNA-bound TDP-43^{tRRM} acquired at pH 3.8 at different time points; 0.9 min (blue), 30 mins (pink), 1 hour (cyan), 2 hours (green), and 3 hours (brown). The spectra are compared with the equilibrium signal of DNA-bound TDP-43^{tRRM} at pH 7.5 (yellow). Inset shows the TEM image of DNA-bound TDP-43^{tRRM} at low pH. The scale represents 100 nm. (C) The comparison between the changes in the far-UV CD signal at 216 nm as a function of time of free (black; line) and DNA-bound TDP-43^{tRRM} (black; circle) at pH 3.8. (D) The RALS intensity of free (Δ) and DNA-bound TDP-43^{tRRM} (◯) at pH 3.8 as a function of time normalized relative to the RALS intensity of the DNA-bound TDP-43^{tRRM} obtained at 3 hours. The microcentrifuge tube images show a solution containing free and DNA-bound TDP-43^{tRRM} after 3 hours of incubation at pH 3.8.

4.3.1 DNA inhibits amyloid-like aggregation of TDP-43^{tRRM}

Figure 4.1A compares the changes in the secondary structure of free TDP-43^{tRRM} upon transferring it from the native condition to the low pH aggregation condition (from pH 7.5 to pH 3.8 in the presence of 150 mM KCl) at different time points. pH 3.8 in the presence of 150 mM KCl will be referred to as aggregation buffer from here onwards. The native structure of TDP-43^{tRRM} is composed of α-helix, β-sheet, and disordered loops (Figure 4.S1). These secondary structures result in a characteristic far-UV CD spectrum of native TDP-43^{tRRM} with minima at 208 and 222 nm. Upon transferring the native TDP-43^{tRRM} to the aggregation buffer, we observed a gradual increase in the MRE signals, with a shift in the signal minima to 216 nm. The changes in the signal minima suggest the conformational transition to a β-sheet-rich structure (β form). The unexpected increase in the far-UV CD signal is hypothesized to result from the structure gain of the previously disordered loops in the TDP-43^{tRRM}.[72] TEM results (Figure 4.1A, inset) suggest that the β form has a curvy, thread-like morphology that is approximately 50 nm long. This result suggests that the β form is amyloid-like, as observed in our previous study.[71–73]

In order to probe the effect of the DNA binding partner on the misfolding transition of TDP-43^{tRRM}, we performed a pH jump study on the pre-formed complex of DNA-bound TDP-43^{tRRM} (11 μM ss(TG)$_6$- 10 μM TDP-43^{tRRM}) at 25 °C (Figure 4.1B). ss(TG)$_6$ is a specific binding partner of TDP-43.[81,82] The ss(TG)$_6$-TDP-43^{tRRM} will be referred to as DNA-bound TDP-43^{tRRM} in the entire study. Interestingly, we observed that the far-UV CD spectrum of DNA-bound TDP-43^{tRRM} remains comparable to the spectrum of its native-state, signifying no measurable change in the secondary structure of DNA-bound TDP-43^{tRRM} with time. TEM images showed the absence of curvy thread-like assemblies (Figure 4.1B, inset). The results suggest that the DNA binding inhibits the transition of TDP-43^{tRRM} to β-sheet rich structure.

We utilized the difference in the MRE values at 216 nm between the native and misfolded TDP-43^{tRRM} to study the kinetics of its structural transition in the presence and absence of DNA upon pH change (Figure 4.1C). We observed that the transition from native-state to β form fits best in bi-exponential fit, suggesting the transition occurs in two steps, with a time constant of 8.36 minutes and 54 minutes, respectively. We did not observe any lag phase in the transition. The results thus signify that the secondary structure of the native TDP-43^{tRRM} changes to the misfolded β form in two distinct steps as observed previously.[72] However, we did not notice an exponential

change in the secondary structure to β-sheet in the presence of DNA at 216 nm with the far-UV CD; instead, a minute decrease in the signal intensity with time is observed. This implies that the DNA binding inhibits the transition of native-state to β form at low pH. The decrease in the signal intensity at 216 nm suggests a decrease in the protein concentration in the soluble phase due to the occurrence of a secondary process.

4.3.2 DNA aids in the formation of phase-separated coacervates in the presence of pH stress

We encountered an important observation where we noticed the onset of turbidity in the DNA-containing solution of TDP-43^{tRRM} in aggregation conditions (Figure 4.1D, microcentrifuge tube image). We studied the solution in the presence and absence of DNA using the right angle light scattering (RALS) intensity at different times to gather more information about the process. Figure 4.1D compares the normalized RALS at 400 nm as a function of time for the free and DNA-bound TDP-43^{tRRM} at 25 °C upon transfer to aggregation conditions. In the case of DNA-bound TDP-43^{tRRM}, we noticed minimal scattering at the start of the pH jump, which increased exponentially upon further incubation. The RALS is characterized by a single exponential change with a time constant of 105 min. The increase in the RALS signifies the formation of the coacervates capable of scattering light.

In contrast, free TDP-43^{tRRM} showed negligible scattering in the studied period. The signal increased only by 10% after 3 hours of incubation. The results suggest that the free TDP-43^{tRRM} cannot form coacervates independently. The aggregate (β form) formed is relatively soluble, as observed previously.[72,73] The formation of coacervates in the presence of binding ligand also suggests that the favorable interactions between DNA and TDP-43^{tRRM} are necessary for their formation.

Figure 4.1 highlights the competition between protein-protein and protein-DNA interactions controlled by ss$(TG)_6$. Free TDP-43^{tRRM} senses pH stress and undergo pH-dependent misfolding to β form (protein-protein interactions). DNA binding abolishes the pH-dependent misfolding by forming phase-separated coacervates (protein-DNA interactions).

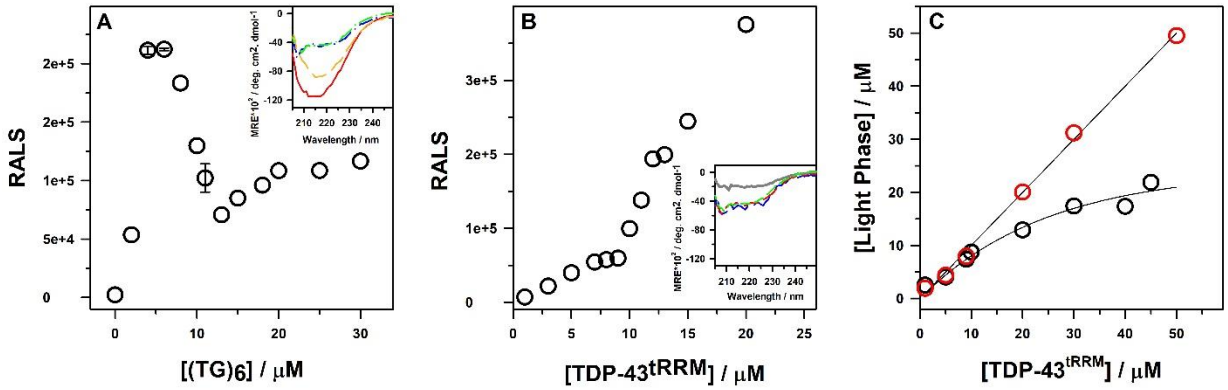

Figure 4.2 The extent of phase separation depends on protein and DNA ratio. (A) RALS intensity of the coacervates formed in the presence of 10 μM TDP-43^{tRRM} with different concentrations of DNA. Inset shows the far-UV CD spectra of 10 μM TDP-43^{tRRM} in the presence of 2 μM (yellow), 11 μM (green), and 20 μM (blue) DNA. These spectra are compared to that of β form (red). (B) RALS intensity of coacervates formed in the presence of 11 μM DNA complexed with different concentrations of TDP-43^{tRRM}. Inset shows the far-UV CD spectra of 11 μM DNA in the presence of 5 μM (blue), 8 μM (red), 10 μM (green), and 20 μM (dark gray). All the RALS intensities are obtained for pH 3.8 at 400 nm. (C) The concentration of the TDP-43^{tRRM} in the light phase obtained for pH 7.5 (red) and pH 3.8 (black) as a function of increasing TDP-43^{tRRM} concentration.

4.3.3 The ratio of DNA and TDP-43^{tRRM} determines the extent of phase separation

In order to investigate the factors determining the extent of phase separation, we studied the concentration of the participating molecules required to trigger phase separation in low pH conditions by employing RALS (Figure 4.2). Figure 4.2A compares the RALS intensity as a function of increasing DNA concentration at a constant concentration of 10 μM TDP-43^{tRRM}. In the absence of DNA, the RALS intensity is very small due to the formation of the soluble β form (Figure 4.1). The far-UV CD data confirms the presence of the β-sheet rich β form (Figure 4.2A, inset). With an increase in the DNA concentration to 2 μM, we observed an increase in the RALS. The far-UV CD spectrum of the corresponding sample appeared similar to the β form (Figure 4.2A, inset). However, it showed a decrease in the signal intensity, suggesting a change in conformation of protein and change in the population of the β form. Upon increasing the concentration of DNA further, we noticed the onset of turbidity of different orders (Figure 4.S2). A spike in the RALS intensity was also observed with an increase in the DNA concentration to 4 μM, which decreased upon increasing the DNA concentration beyond 6 μM. The far-UV CD spectra of these samples

suggest the presence of native-like TDP-43^{tRRM}. The RALS intensity becomes constant once the DNA concentration reaches 10 μM. The corresponding far-UV spectra of the samples appeared similar to the native-state. Therefore, the data suggest that DNA maintains the native-like secondary structure of the TDP-43^{tRRM} under aggregation conditions by undergoing coacervation. This increase and subsequent decrease in turbidity have been shown earlier.[83-85]

We further investigated the effect of the different concentrations of TDP-43^{tRRM} in the presence of 11 μM DNA on phase separation (Figure 4.2B). We noticed an increase in the RALS, suggesting the presence of coacervates. The far-UV CD spectra obtained under different concentrations of TDP-43^{tRRM} imply the presence of a native-like secondary structure (Figure 4.2B, inset). The results suggest that the DNA binding inhibits amyloid-like aggregation of TDP-43^{tRRM}. These ratios also correspond to the region of minimal turbidity (Figure S3). However, upon increasing the concentration of TDP-43^{tRRM} beyond 10 μM, we noticed a sigmoidal increase in the RALS, suggesting the increased formation of coacervates with increasing protein concentration. The solutions were turbid to the naked eye with different orders of milkiness (Figure 4.S3). Noteworthily, with a further increase in the TDP-43^{tRRM} to 20 μM (Figure 4.2B, inset), we noticed an overall reduction in the MRE signal owing to the increase in the turbidity of the sample. The minima at 208 nm and 222 nm still suggest the presence of the native-like secondary structure. We refrained from acquiring far-UV CD spectra at higher concentrations of TDP-43^{tRRM} due to an increase in the turbidity of the samples. The results suggest that the concentration of the DNA and TDP-43^{tRRM} and their ratio determine the extent of coacervation.

4.3.4 The coacervates are a result of complex coacervation

Figure 4.2C compares the concentration of TDP-43^{tRRM} in the light phase at pH 7.5 and 3.8. The amount of protein in the light phase increases linearly with the added protein concentration at pH 7.5. Hence, protein remains soluble, and there is no phase separation. In contrast, under aggregation conditions, the amount of soluble protein increases linearly till 10 μM TDP-43^{tRRM} and remains constant beyond it as all the protein beyond 10 μM separates into an insoluble dense phase. The results also imply that the coacervation of TDP-43^{tRRM} in the presence of DNA happens only when the protein is positively charged (pH 3.8). We, therefore, imply that the coacervates arose from complex coacervation, a class of phase separation. Complex

coacervation occurs when two differently charged polyelectrolytes undergo favorable interactions, separating into a polyelectrolyte-rich dense phase and a much larger light phase.[86-88]

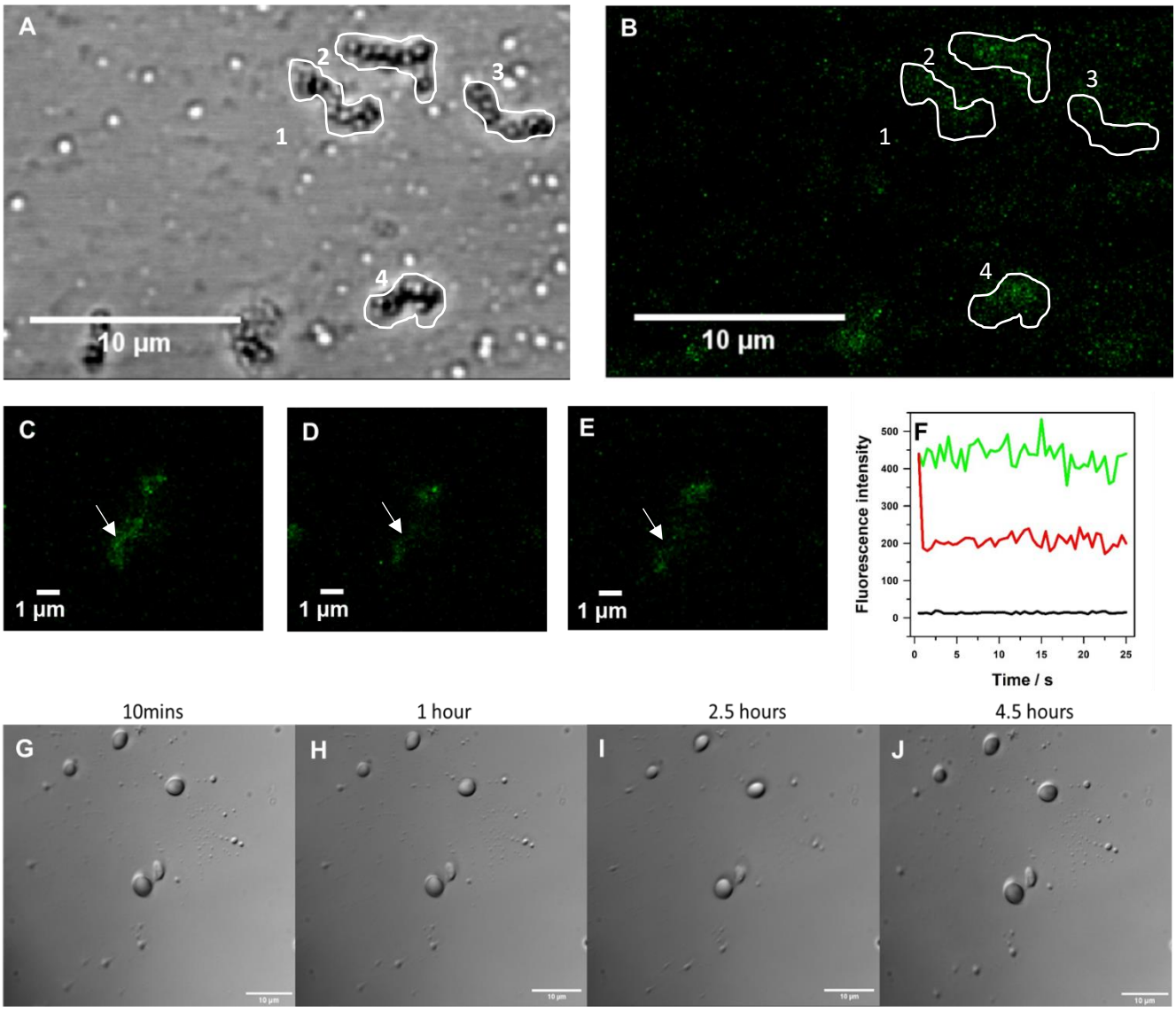

Figure 4.3 The coacervates appear spherical and are less dynamic. (A, B) images of coacervates acquired using confocal microscope show their clustered nature. The corresponding areas are marked in panel A and B. (C, D, E) images showing FRAP at different time intervals. (F) graph showing the fluorescence intensity of the coacervate: before photobleaching (green), after photobleaching (red), and the background fluorescence (black). (G-J) DIC images acquired after 10 minutes, 1 hour, 2.5 hours, and 4.5 hours, respectively.

4.3.5 The coacervates appear spherical and are less dynamic

We next employed microscopy to gather insights into the size and appearance of the coacervates. We have used two different ratios of TDP-43^{tRRM} and DNA (10 μM TDP-43^{tRRM} and 4 μM ss$(TG)_6$ / 10 μM TDP-43^{tRRM} and 11 μM ss$(TG)_6$) for the further study. These ratios will be referred to as low DNA complex and high DNA complex, respectively, from now onwards. Figures 4.3A and 4.3B show the confocal image of the coacervates of low DNA complex. These coacervates appeared clustered non-fusing beads like globules and ranged in size from 1-2 μm. The persistent clusters appeared in strings and signified that the fusion events were started but did not complete. The fluorescent globules confirm the presence of the labeled TDP-43^{tRRM} molecules (Figure 4.3B). To measure the internal dynamics of the coacervates, we performed fluorescence recovery after photobleaching (FRAP) (Figures 4.3C, 4.3D, 4.3E, and 4.3F). Figure 4.3C shows the globule before bleaching, while Figures 4.3D and 4.3E show the globule after bleaching. The coacervates did not exhibit substantial fluorescence recovery in the observed timescale (Figure 4.3F). The failed recovery of the fluorescence suggests the rigid internal dynamics of the coacervates.

On the other hand, coacervates formed by the high DNA complex appeared spherical and ranged from 2-4 μm in size (Figure 4.3G, 4.3H, 4.3I, and 4.3J). Most of the observed coacervates were distantly placed along with some closely packed ones. Interestingly, these coacervates did not fuse and showed any increase in size for the studied time range. The images altogether suggest that the coacervates are less dynamic in nature. Interestingly, we observed the formation of coacervates at other parts of the slide with time. The observation is in line with the RALS intensity shown in Figure 4.1D, confirming that the number of coacervates increases with time.

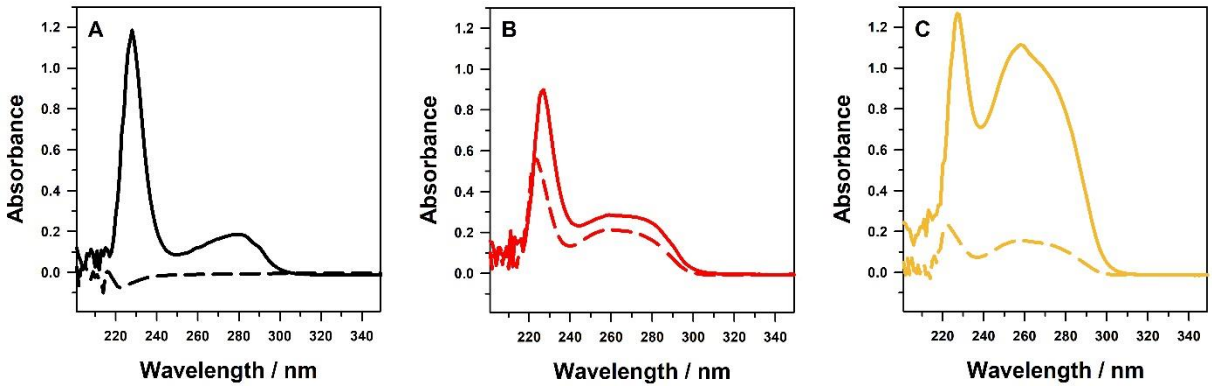

Figure 4.4 DNA and protein both partitions to coacervates. Absorbance spectra of biomolecules present in the supernatants (solid line) and pellets (dashed line) acquired for 10 μM TDP-43^{tRRM} in the presence of 0 μM (A), 4 μM, (B) and 11 μM (C) DNA.

4.3.6 Coacervates are composed of both TDP-43^{tRRM} and ss(TG)$_6$

The results suggest that nucleic acid is necessary for triggering the coacervation of TDP-43^{tRRM}. We went on to check the partitioning of the participating biomolecules into the coacervates. To do so, we employed three conditions 1) 10 μM TDP-43^{tRRM} and 0 μM ss(TG)$_6$ (no demixing), 2) 10 μM TDP-43^{tRRM} and 4 μM ss(TG)$_6$ (demixing with higher RALS intensity) and 3) 10 μM TDP-43^{tRRM} and 11 μM ss(TG)$_6$ (demixing with low RALS intensity) (Figures 4A, B, and C respectively). We followed the steps mentioned in the Materials and Methods to check the concentration of the biomolecules in the coacervates. The supernatant represents the light phase, while the pellet represents the dense phase. Fig 4A compares the absorbance spectrum of the supernatant and pellet of condition 1. We observed negligible absorbance in the pellet fraction, and the absorbance from the supernatant corresponded to 10 μM TDP-43^{tRRM}. The results indicate that all the biomolecules are in the light phase, emphasizing that no demixing has occurred in the absence of DNA.

Contrarily, we observed the absorbance at 260 nm and 280 nm in the re-dissolved pellet and the supernatant in the phase-separating conditions (Figure 4.4 B, C). The absorbance suggests the presence of both the DNA and the protein in the dense and the light phase, respectively. We calculated the fraction of biomolecules in the pellet fraction (materials and methods). We estimated that approximately 39-42% and 9-11% of the biomolecules get sequestered into the coacervates in

the low DNA and high DNA complex, respectively. The observation suggests that the biomolecules partition more into the coacervates in low-DNA conditions as compared to high-DNA.

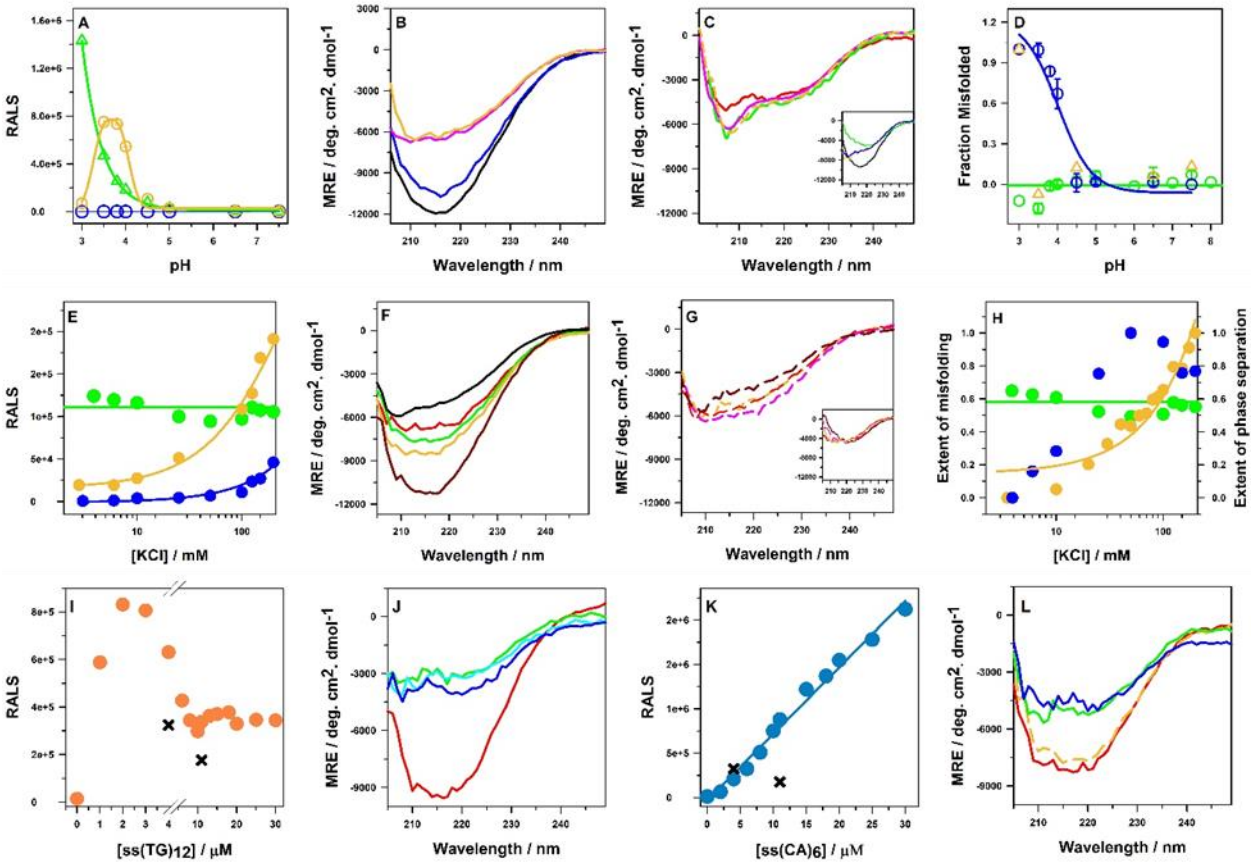

Figure 4.5 Favorable electrostatic interactions drive coacervation. (A) Comparison among the RALS intensity of free (blue), low DNA complex (yellow), and high DNA complex (green). The lines are drawn to guide the eye. (B) Far-UV CD spectra of the free TDP-43^{tRRM} at pH 7.5 (yellow), pH 5.0 (pink), pH 4.0 (blue), and pH 3.0 (black). (C) Far-UV CD spectra of the high DNA complex at pH 3.5 (red), pH 3.8 (green), pH 4.0 (blue), pH 6.0 (pink), and pH 7.0 (yellow). Inset compares far-UV CD spectra of low DNA complex at pH 3.0 (black), pH 3.8 (green), pH 4.0 (blue), pH 4.5 (dark brown), and pH 7.5 (yellow). (D) Fraction of misfolded population as a function of pH: for free (blue) and DNA bound TDP-43^{tRRM} in low (yellow) and high DNA (green) conditions. The fits through the graph are a least square fit to equation 4.1. The straight line is drawn to guide the eye. (E) RALS value of free TDP-43^{tRRM} (blue), low DNA complex (yellow), and high DNA complex (green) as a function of KCl concentration. (F) Far-UV CD spectra of the free TDP-43^{tRRM} acquired at pH 3.8 at 3.9 mM (red), 6 mM (green), 10 mM (yellow), and 150 mM (brown) KCl. The spectra are compared to the native TDP-43^{tRRM} (black). (G) Far-UV CD spectra of high DNA complex at different KCl concentrations. Inset compares the far-UV CD spectra of low DNA

complex at various KCl concentrations. The concentration of KCl in different spectrum is 3.9 mM (red), 10 mM (yellow), 50 mM (pink), 150 mM (brown). (H) Competition between misfolding and phase separation is depicted by ThT assay (blue) and normalized RALS value (yellow; low DNA complex, and green; high DNA complex) as a function of KCl concentration. (I) RALS of ss$(TG)_{12}$-TDP-43^{tRRM} as a function of ss$(TG)_{12}$ concentration (orange circles). The RALS of ss$(TG)_{12}$-TDP-43^{tRRM} is compared with RALS of ss$(TG)_6$-TDP-43^{tRRM} (black cross). (J) Far-UV CD spectra of 10 μM TDP-43^{tRRM} acquired in the presence of 11 μM (green), 15 μM (cyan), 20 μM (blue) of ss$(TG)_{12}$. The spectra are compared with that of free TDP-43^{tRRM} (red). All the spectra are acquired at pH 3.8. (I) RALS of ss$(CA)_6$-TDP-43^{tRRM} as a function of ss$(CA)_6$ concentration (teal blue circles). The RALS of ss$(CA)_6$-TDP-43^{tRRM} is compared with RALS of ss$(TG)_6$-TDP-43^{tRRM} (black cross). Far-UV CD spectra of 10 μM TDP-43^{tRRM} in the presence of 2 μM (yellow), 11 μM (green), and 20 μM (blue) compared with the β form (red) at pH 3.8.

4.3.7 The extent of coacervation is dependent on the pH of the solution environment

We first investigated the impact of pH change on TDP-43^{tRRM} in the free and DNA bound state. We monitored the process by employing RALS and far-UV CD. Figure 4.5A compares the RALS intensity of the free TDP-43^{tRRM} with high and low DNA complexes as a function of pH. We observed minimal RALS for free TDP-43^{tRRM} across the studied pH range, which suggests that free TDP-43^{tRRM} does not undergo phase separation at any studied pH and remains soluble. In addition, Figure 4.5B suggests that the free TDP-43^{tRRM} experiences pH-dependent misfolding to β form. Noteworthily, the far-UV CD spectrum suggests that the minimal RALS signal till pH 5.0 is due to the presence of soluble native TDP-43^{tRRM} (Figure 4.5B). On the contrary, the RALS signal below pH 4.5 originates due to the soluble β form (Figure 4.5B). The population of β form increases with a decrease in the pH, as evident from the increase in the far-UV CD signal (Figure 4.5B).

Interestingly, we observed differential RALS in the low and high DNA complexes at different pH (Figure 4.5A). In the case of the high DNA complex, we observed minimal RALS intensity from pH 5.0 to 7.5. The far-UV CD spectra in the pH range suggests the presence of native TDP-43^{tRRM} (Figure 4.5C). Therefore, the results indicate that the high DNA complex is soluble from pH 5.0-7.5, and TDP-43^{tRRM} remains in a native-like state. We observed an exponential increase in the RALS intensity with a further decrease in the pH below 5.0. The increase in the RALS implies the formation of coacervates upon a decrease in the pH. This phenomenon indicated that

an increase in the positive charge on protein due to low pH stress is necessary for coacervation. The far-UV CD spectra in low pH conditions were similar to native TDP-43^{tRRM} (Figure 4.5C). Upon further decrease in the pH, attractive interactions between protein and DNA increased owing to an increase in the positive charge of TDP-43^{tRRM}, promoting the formation of more coacervates. The highest RALS intensity was observed at pH 3.0. We could not acquire the far-UV CD spectrum at pH 3.0 due to high turbidity. Notably, the far-UV CD spectra suggest that the coacervation inhibits pH-dependent amyloid-like aggregation of TDP-43^{tRRM} at low pH. Another important observation from Figure 4.5A is the differential RALS intensity as a function of pH. This suggests the different populations of the coacervates. The results indicate the importance of charge density in tuning the extent of coacervation. Coacervation is favored at higher charge density for high DNA complexes.

Figure 4.5A also shows the RALS intensity as a function of the pH of the low DNA complex. We observed negligible RALS from pH 5.0 to 7.5 and a native-like secondary structure (Figure 4.5C, inset). We further observed an increase in the RALS with a decrease in the pH to 3.5 (Figure 4.5A). The far-UV CD spectrum signify the presence of a native-like secondary structure (Figure 4.5C, inset). The results are in line with the previous observation that suggests DNA binding prevents amyloid-like aggregation at low pH by forming coacervates. Intriguingly, we noticed a decrease in the RALS with a further decrease in the pH to 3.0 (Figure 4.5A). The far-UV CD spectrum resembles the β form with minima at 216 nm at pH 3.0 (Figure 4.5C, inset). The results signify that the increase in the charge on TDP-43^{tRRM} at pH 3.0 in the presence of low DNA disfavors the coacervation and favors aggregation. The imbalance in the charge density due to the low concentration of DNA decreases the attractive interactions between protein and DNA and fails to trigger coacervation leading to the misfolding of the TDP-43^{tRRM}.

Figure 4.5D compares the fraction of the misfolded population calculated from figure 4.5A as described previously[71] at different pH. Figure 4.5D suggests that free TDP-43^{tRRM} undergoes pH-dependent amyloid-like aggregation. This aggregation is inhibited in the case of high DNA complex and TDP-43^{tRRM} remains in a native-like state. Low DNA complex, on the other hand, inhibits the aggregation and remains native-like till pH 3.5, below which it undergoes a transition to β form.

The results highlight the pH and DNA concentration-dependent titration between amyloid-like aggregation, coacervation, and native-like state of TDP-43^{tRRM}.

4.3.8 The extent of coacervation is dependent on the ionic strength of the solution

Building on the results obtained in section 4.3.7, we examined the effects of increasing salt concentration on coacervation. Ionic strength is a known modulator of coacervation.[55,89] We explored the impact of KCl concentration on the free TDP-43^{tRRM} and low and high DNA complexes. The negligible scattering of the free TDP-43^{tRRM} at all the studied salt concentrations signifies their soluble nature (Figure 4.5E). The shift in the signal minima of the far-UV CD spectra to 216 nm with increased KCl concentrations implies that the free TDP-43^{tRRM} misfolds to β form with increased salt concentration (Figure 4.5F). We next investigated the effect of salt on low DNA complex. No substantial scattering was observed until 10 mM KCl, suggesting that the species in low salt conditions are soluble (Figure 4.5E). Their secondary structure resembles native-like TDP-43^{tRRM} (Figure 4.5G, inset), implicating that low ionic strength favors the equilibrium towards the native-like light phase. However, with a further increase in the salt concentration, the equilibrium shifted to the dense phase, as evident from the increasing RALS intensity, which became maximum at 200 mM KCl. The solution also turned turbid linearly with the addition of salt. Interestingly, the far-UV CD spectra of these samples signify the presence of a native-like structure.

The high DNA complex solutions show high scattering at all the studied salt concentrations (Figure 4.5E), signifying predominately the presence of the dense phase. The data suggest that a higher amount of DNA shifts the equilibrium from the soluble light phase toward the dense phase even at low salt concentrations. However, the far-UV CD spectra suggest the presence of the native-like structure till 200 mM KCl (Figure 4.5G). The results imply that the polyionic effect of DNA, which is more significant than KCl, triggers the coacervation at low KCl concentration, suggesting the role of electrostatics in modulating the demixing equilibrium.

The scattering intensity is roughly half of the maximum scattering observed for low DNA complex, indicating the different amount of coacervates in the dense phase in both the cases.

4.3.9 DNA mediates the competition between misfolding and demixing

Figure 4.5H compares the extent of misfolding of free TDP-43^{tRRM} and the extent of phase separation of low and high DNA complex as a function of KCl concentration. The misfolding of free TDP-43^{tRRM} begins with the addition of salt. In contrast, in the presence of the DNA, TDP-43^{tRRM} does not aggregate under stress but demixes to mesoscale coacervates, which scatter light. The data imply that competition between amyloid-like aggregation and demixing is controlled by the DNA and salt concentration. Therefore, DNA is necessary for the maintenance of the TDP-43^{tRRM} under stress conditions.

4.3.10 Ligands tune the coacervation by modulating the electrostatic interactions

To understand the mechanism that underlies the regulation of coacervation by ligands, we employed two different ligands, ss$(TG)_{12}$ and ss$(CA)_6$. ss$(TG)_{12}$ binds TDP-43^{tRRM} with higher affinity while ss$(CA)_6$ is a weak non-specific binding ligand as compared to ss$(TG)_6$.[81] ss$(TG)_{12}$ is a longer nucleic acid as compared to ss$(TG)_6$. The increased number of nucleotides results in more binding pockets, which can influence the phase separation behavior. Figure 4.5I shows the RALS intensity as a function of increasing ss$(TG)_{12}$ concentration. We observed a maximum spike in the RALS at 2 μM ss$(TG)_{12}$. The results suggest that the increase in the binding pockets decreases the concentration of ligands required to trigger coacervation (Figure 4.2A). We noticed a decrease in the RALS intensity with a further increase in the ss$(TG)_{12}$ concentration. The RALS becomes constant above 9 μM ss$(TG)_{12}$. Moreover, the RALS intensity is also more (2 times more) than that of ss$(TG)_6$-TDP-43^{tRRM} (Figure 4.5I-cross), suggesting the presence of either more or bigger coacervates. The far-UV CD spectra resemble that of native TDP-43^{tRRM}, suggesting the presence of native-like species in the presence of ss$(TG)_{12}$ (Figure 4.5J).

We questioned if electrostatics are essential forces in driving coacervation, will a non-specific DNA binding ligand of TDP-43^{tRRM} containing a similar charge can modulate the phase separation behavior? Figure 4.5K shows RALS with increasing ss$(CA)_6$ concentration. We observed a linear increase in the RALS intensity with an increase in the ss$(CA)_6$ concentration. The results suggest that the negatively charged ss$(CA)_6$ can trigger coacervation. The far-UV CD spectra resemble β form in the presence of 2 μM ss$(CA)_6$ and native-like at higher concentrations of ss$(CA)_6$ (Figure

4.5L). The study suggest that a non-specific ligand with similar negative charge can also trigger coacervation.

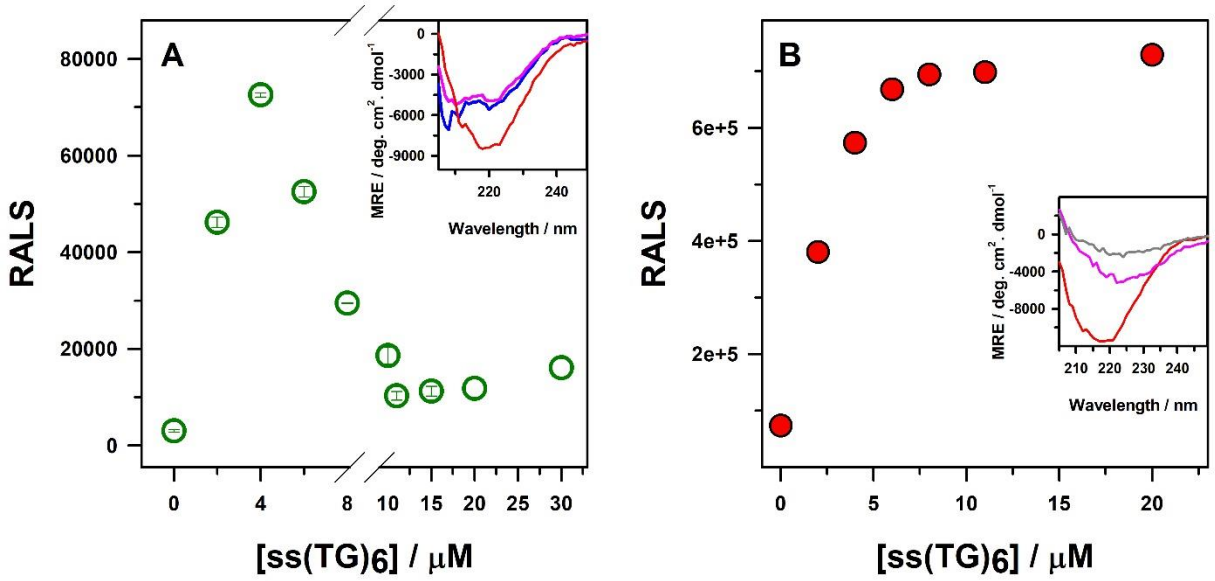

Figure 4.6 Disease mutants undergo complex coacervation. (A) RALS intensity for the coacervate formed in the presence of 10 μM D169G with different concentrations of DNA (green dots). Inset shows the far-UV CD spectra of 10 μM D169G in the presence of 4 μM (pink), 20 μM (blue) of DNA. The spectra are compared with the equilibrated β form of D169G (red). All the RALS values were obtained for pH 3.8 at 400 nm. (B) RALS intensity for the coacervate formed in the presence of 10 μM P112H with different concentrations of DNA (red dots). Inset shows the far-UV CD spectra of 10 μM P112H in the presence of 2 μM (pink), 8 μM (dark gray) of DNA. The spectra are compared with that of β form of P112H (red).

4.3.11 DNA inhibits aggregation and triggers complex coacervation of the disease mutants

TDP-43^{tRRM} harbors two disease-related mutants, D169G and P112H in its sequence. Figure 4.6 shows how these single site mutations affect the process of DNA mediated coacervation. Interestingly, we observed a very similar change in the RALS intensity for D169G as observed for TDP-43^{tRRM} (Figure 4.2A). We observed negligible scattering for the free D169G at pH 3.8 (Figure 4.6A). The far-UV CD spectra suggest the presence of β-sheet-rich structure (Figure 4.6A, inset). The results confirm that the D169G also undergoes aggregation to soluble β form in low-pH conditions. The RALS intensity increased with the addition of the DNA, which became maximum at 4 μM DNA concentration. The far-UV CD spectra show minima at 208 nm and 222 nm,

confirming the presence of a native-like secondary structure. The RALS intensity decreased with further addition of the DNA, and the far-UV spectra denote the presence of a native-like secondary structure (Figure 4.S4). Therefore, Figure 4.6A confirms that the disease mutant D169G undergoes aggregation to soluble β form in low-pH conditions. The aggregation is inhibited in the presence of DNA, which promotes complex coacervation and maintains the native-like secondary structure of D169G.

Figure 4.6B shows the RALS values for the P112H as a function of DNA concentration. P112H, in the absence of any ligand, undergoes aggregation to β form (Figure 4.6B, inset). However, we noticed that the solution containing P112H in a complex with 2 μM DNA turned turbid instantly (Figure 4.S5). The increase in the turbidity was coupled with a spike in the RALS intensity. We could not capture a reliable far-UV CD spectrum of the reaction mixture because of the noise in the far-UV CD spectrum due to high turbidity (Figure 4.6B, inset). Intriguingly, we noticed a further spike in the turbidity and the RALS intensity with the further addition of the DNA, which became constant after the addition of 6 μM of DNA. The high RALS intensity suggest the presence of a higher number of coacervates. The far-UV CD spectra, however, confirmed that the formation of β form is inhibited in the presence of DNA.

The difference in the RALS intensity between the two mutants implies the role of Histidine residue, which can impart a more positive charge to the protein molecule at pH 3.8. The increased charge density on protein favored complex coacervation even at low DNA concentrations.

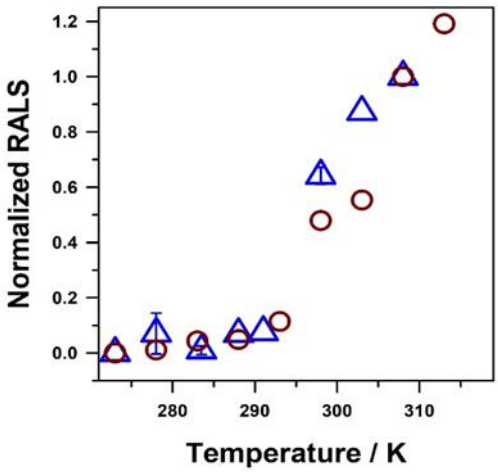

Figure 4.7 Coacervation of DNA-bound TDP-43^{tRRM} follows LCST behavior. (A) Normalized RALS intensity of low DNA complex (purple) and high DNA complex (brown) plotted as a function of temperature.

4.3.12 Coacervation of TDP-43^{tRRM} follows LCST behavior

Temperature is an important parameter that is known to modulate protein-DNA driven coacervation. Figure 4.7 compares the RALS intensity of DNA mediated coacervation of TDP-43^{tRRM} as a function of temperature. We observed negligible RALS until 293 K for the high DNA complex. The solution did not turn visibly turbid (Figure 4.S5). These two observations suggest the absence of the coacervates and predominance of the light phase till 293 K. Interestingly, we noticed a slight demixing upon an increase in the temperature to 298 K (Figure 4.S5). The turbidity increase was complemented by an increase in the RALS value, indicating coacervation onset. The solutions were found visibly turbid at all the above temperatures tested with a simultaneous increase in the RALS value suggesting a gradual shift to the dense phase. This behavior is defined as LCST (lower critical solution temperature). In LCST, the coacervation to light and the dense phase is favored above a threshold temperature, below which the components remain soluble (light phase).

We noticed a similar observation for the low DNA complex, suggesting that it follows LCST behavior (Figure 4.7). Figure 4.7 suggests that the phase separation of DNA-bound TDP-43^{tRRM} follows an LCST behavior. It also suggests that the temperature can modulate the equilibrium between the light and the dense phase.

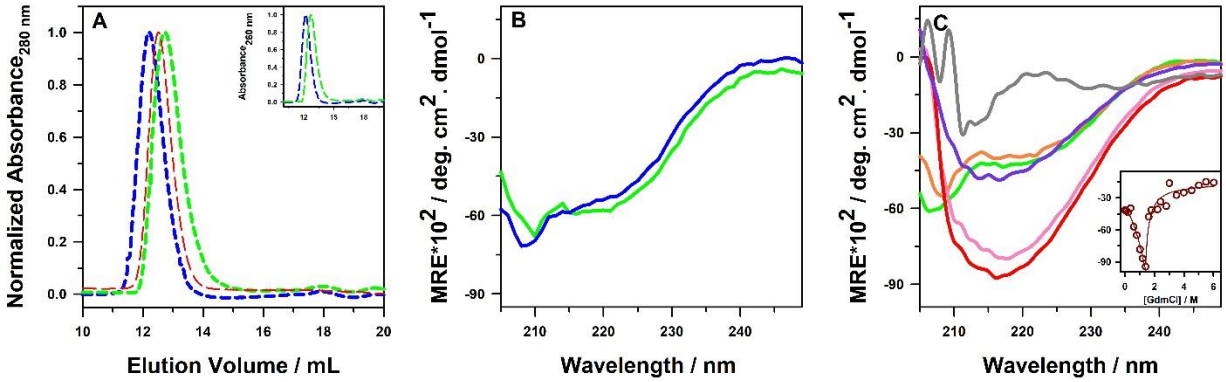

Figure 4.8 TDP-43^{tRRM} remains a native-like monomer in the light phase. (A) SEC curves of free and DNA-bound TDP-43^{tRRM} at pH 7.5 (red, blue respectively) and DNA-bound TDP-43^{tRRM} at pH 3.8 (green). Inset compares the elution at 260 nm (B) far-UV CD spectra of DNA-bound TDP-43^{tRRM} at pH 7.5 (blue), and at pH 3.8 (green). (C) far-UV CD spectra for the DNA-bound TDP-43^{tRRM} at different GdmCl concentrations: 0M (green), 0.39M (orange), 1M (pink), 1.2M (red), 1.6M (purple), 6M (grey). Inset shows the MRE values plotted at 216 nm for DNA-bound TDP-43^{tRRM} as a function of GdmCl concentration.

4.3.13 TDP-43^{tRRM} remains in the monomeric native-like state in the light phase

We were interested in knowing the oligomerization state of the TDP-43^{tRRM} in the light phase. In these experiments, we employed low temperatures to shift the equilibrium of phase separation toward the light phase. Figure 4.8A shows the size exclusion chromatography (SEC) elution profile of the free and DNA-bound TDP-43^{tRRM} in the light phase under different pH conditions. Free TDP-43^{tRRM} in pH 7.5 eluted at 12.51 mL, corresponding to a molecular weight of 19.4±0.5 kDa. Additionally, DNA-bound TDP-43^{tRRM} in pH 7.5 was eluted at 12.2 mL. The early elution of the bound form compared to the free form is linked to the increased weight of the protein due to attached DNA. The simultaneous increase in the absorbance at 260 nm at 12.2 mL suggests elution of the DNA with protein in the bound state (Figure 4.8A, inset).

The DNA-bound TDP-43^{tRRM} at pH 3.8 eluted at 12.7 mL. Since the elution is very near to the site of monomer elution, we can conclude that it remains in the monomeric form in the light phase, even under aggregation conditions. Its delayed elution at low pH could be argued as a result of the compaction of the bound protein. These results conclude that DNA maintains the monomeric state of the TDP-43^{tRRM} in the light phase.

We next went to probe the secondary structure of the DNA-bound TDP-43^{tRRM} in the light phase (Figure 4.8B). Interestingly, we observed minima at 208 and 222 nm. The MRE value at 222 nm was -5576 mdeg dmol^{-1} cm^{-1} in aggregation conditions. These values were similar to the MRE value at pH 7.5 (-5266 mdeg dmol^{-1} cm^{-1}) at 222 nm. In addition, the spectrum at pH 3.8 also looked very similar to the typical spectrum of native TDP-43^{tRRM}, suggesting the presence of the α-helix and β-sheet in the protein structure. The results imply that the light phase of demixed solution contains TDP-43^{tRRM} in its native-like state.

4.3.14 Disruption of favorable interactions between DNA and TDP-43^{tRRM} disfavors coacervation

To gain more insights into the interactions between the DNA and TDP-43^{tRRM} under low pH conditions, we studied the effect of increasing GdmCl concentration on the secondary structure of DNA-bound TDP-43^{tRRM}. Figure 4.8C compares the far-UV CD spectra of DNA-bound TDP-43^{tRRM} at different GdmCl concentrations. The far-UV CD spectra indicate that the DNA-bound TDP-43^{tRRM} maintains a native-like secondary structure till 0.39 M GdmCl. With the further addition of the GdmCl, the native-like secondary structure transitions to β form, as evident with an increase in the minima at 216 nm. The observed behavior could result from decreased DNA binding due to disruption of the attractive interactions in the presence of GdmCl. We observed the unfolding of the β form with a further increase of GdmCl. Figure 4.8C, inset, shows the MRE values of DNA-bound TDP-43^{tRRM} at 216 nm as a function of GdmCl concentration. The midpoint of N⇌β transition was 0.85 M GdmCl. The complete misfolding to β form was achieved at 1.4 M GdmCl. The unfolding of the β form followed the misfolding with a further increase of GdmCl. The complete unfolding is achieved at 4 M GdmCl.

The GdmCl melt suggests that the interactions between DNA and TDP-43^{tRRM} are necessary to maintain the native structure of TDP-43^{tRRM} under low pH aggregation conditions. Any alterations in the interactions could hamper or modulate the binding of the DNA and can trigger the misfolding of the TDP-43^{tRRM}.

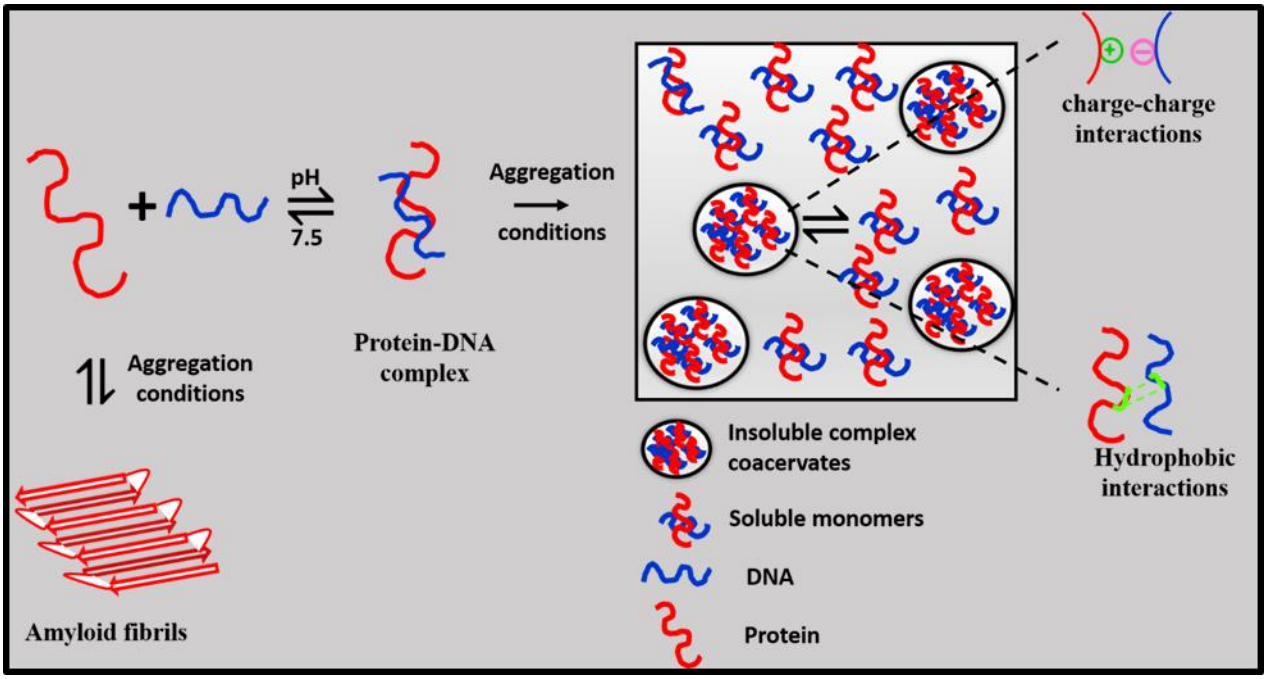

Figure 4.9 Model summarizing the events in complex coacervation of DNA and TDP-43^{tRRM}. Free TDP-43^{tRRM} experiences amyloid-like aggregation in aggregation conditions. Protein and DNA complexes, when exposed to aggregation conditions, undergo complex coacervation to dense phase and light phase. The dense phase consists of coacervates formed due to favorable electrostatic and hydrophobic interactions between protein and DNA. The light phase is made of soluble and monomeric TDP-43^{tRRM}.

4.4 Discussion

The nucleic acid binding proteins like TDP-43 are known to form coacervates.[66,90-93] However, the link between coacervate formation and amyloid-like aggregation is poorly understood. Furthermore, the majority of the literature has focused on simple coacervation of TDP-43 (coacervation driven by a single component).[59,61,94,95] Very few studies have explored its ability to coacervate in the presence of oppositely charged molecules.[63,96] Nevertheless, the underlying principles of complex coacervation of protein and nucleic acids and their regulation remains ambiguous till date. It is likely that the high concentration of the negatively charged nucleic acids and the positively charged protein molecules in the cells can trigger complex coacervation. Therefore, understanding the factors tuning coacervation is of paramount importance.

With the deepening research of phase-separated condensates, the role of nucleic acids in the formation of coacervates is increasingly becoming more clear. Typically, nucleic acids serve as a framework and offer a site for the binding of protein molecules.[97,98] Their properties such as length, composition, and expression level determine the biophysical properties of the condensates.[99–101] For instance, coacervates formed from poly (A) RNA are more viscous than that formed by poly (C) and poly (U) RNA.[100] A very interesting study from Koehler et al. on TDP-43 demonstrated the alteration in the material states of coacervates depending on the type of RNA employed.[66] In addition, long RNAs are favored in mammalian coacervates over short RNAs.[101] Furthermore, nucleic acids have been shown to buffer the phase separation of proteins depending on their concentrations.[102,103] In one experimental study, varying concentrations of RNA resulted in different behavior in a phase separating mixture of RNA and FUS.[103] In lower concentrations, RNA promotes the phase separation of FUS, whereas, at higher concentrations, it disrupts the phase separation process.[103] Noteworthily, depending on coacervation conditions, RNA binding can also completely antagonize the phase transition of TDP-43.[104] Such studies elicit how nucleic acids play an essential role in modulating protein phase separation. Notwithstanding these advancements, our comprehension of the underlying molecular forces that drive phase separation between nucleic acids and proteins remains limited.

In the present work, we have shown that the nucleic acid-binding domain (TDP-43^{tRRM}) of the disease-related protein TDP-43 can separate to protein-rich coacervates and soluble light phase by undergoing complex coacervation in the presence of DNA in low pH stress conditions. The coacervates appeared spherical, and the FRAP analysis suggests that their dynamics are rigid as they fail to exchange the TDP-43^{tRRM} under the studied time range. TDP-43^{tRRM} maintains the native-like secondary structure in the soluble light phase. In contrast, the free TDP-43^{tRRM} undergoes aggregation to an amyloid-like β form in similar stress-like conditions. The onset of coacervation depends on the concentration of the DNA and TDP-43^{tRRM} and their ratio. The favorable interactions between DNA and TDP-43^{tRRM} are necessary for coacervation as the weakening of the interactions by denaturant inhibits coacervation. The dense and the light phases remain in equilibrium, which can be tuned by environmental conditions such as temperature, pH, and salt. Altogether, we report a competition among amyloid-like β form, native-like soluble state, and insoluble complex coacervates under low pH stress conditions mediated by the environmental

conditions. Our results suggest that the complex coacervation by TDP-43^{tRRM} could be an adaptive strategy against environmental stress.

4.4.1 Complex coacervation of TDP-43^{tRRM} forms less dynamic coacervates

We showed that DNA-bound TDP-43^{tRRM} undergoes coacervation to less dynamic coacervates (Figure 4.3), which protects the TDP-43^{tRRM} against amyloid-like aggregation. The globular coacervates did not merge, signifying their rigid dynamics. The coacervates remained intact, and the monomeric native-state of the protein was maintained even under persistent stress in the measured time frame (Figures 4.1C and 4.3). These coacervates of TDP-43^{tRRM} are different from the previously observed liquid-like condensates for various constructs of TDP-43,[31,61,62,94] which undergo fibrillization under persistent stress conditions. It has been postulated that the interaction strength between the participating biomolecules determines the material state of the coacervate.[105] A rigid coacervate suggests the presence of strong and favorable associative interactions.[106] We propose that the strong, attractive forces between positively charged protein and negatively charged DNA are responsible for the rigid dynamics of the coacervates. Similar, less dynamic coacervates have also been observed for CTD and GRNs-driven phase separation as well as full-length TDP-43.[59,96] Additionally, proteins like Pab1,[55] Pub1,[56] and Sup35[58] have been shown to phase separate to globules with rigid dynamics as an adaptive stress strategy. Therefore, our study supports the notion that phase separation to the rigid coacervates due to attractive forces prevents amyloid-like aggregation. An extensive study is required to decipher the effect of the cellular environment on the material properties of the coacervates.

4.4.2 Primary forces responsible for the coacervation

The exciting aspect of our study is the inability of the DNA and TDP-43^{tRRM} to phase separate on their own (Figure 4.1D). Both the biopolymers were able to phase separate only after interacting with each other (Figure 4.1D). Moreover, the breaking of interactions between DNA and TDP-43^{tRRM} was enough to abolish the coacervation (Figure 4.8C). Therefore, the favorable interactions of TDP-43^{tRRM} with the DNA are the primary physical force driving the complex coacervation.

An important observation that stemmed from this study is that the coacervation of TDP-43^{tRRM} does not happen above pH 5.0 (Figure 4.5A). Noteworthily, the pI of the TDP-43^{tRRM} is ~6.8.

Therefore, it remains negatively charged in physiological conditions. The negatively charged protein molecule repulses the negatively charged DNA; therefore, the interactions are not enough to trigger coacervation. However, a decrease in the pH below the pI modulates the ionization state of the side chain residues of TDP-43^{tRRM}. The alteration in the ionization states leading to overall cationic charge on TDP-43^{tRRM} at low pH (~23 at pH 3.8)[107] can trigger favorable electrostatic interactions between cationic protein and the anionic (DNA), thereby triggering complex coacervation.

Building upon the above data, the multiparametric analysis carried out in our study implies that the charge density of biomolecules determines the extent of coacervation. Modulation of charge density by changing biomolecule concentration (Figure 4.2A, 4.5E), pH (Figure 4.5A), and type or type of biomolecule (Figure 4.5I-L) dictates that the imbalance in the charge density regulates the coacervation behavior. Overcharging of only one participant biomolecule could disfavor coacervation and promote solubilization (Figure 4.2A, and 4.5E), as observed previously.[83-85]

The dependence of coacervation propensity on charge emphasizes that electrostatic interactions are important for coacervation.

However, these are not the only forces responsible for the coacervation. We observed that our system followed LCST behavior. This kind of behavior has been observed previously for many molecules, both for proteins and ionic liquids.[55,108,109] In LCST, coacervation occurs above a lower critical temperature. The LCST-mediated coacervation is triggered by the interactions favored at the higher temperature, such as hydrophobic interactions. The entropy gain upon release of the water molecules from the hydration shells of the hydrophobic residues when they come together for coacervation drives coacervation. Therefore, we propose that the coacervation of TDP-43^{tRRM} is driven by multiple types of interactions, and future biophysical studies are required to determine their contribution to coacervation.

4.4.3 Amyloid-like aggregation of the disease mutants is abolished in the presence of DNA

We studied the effect of two disease-associated mutants (D169G and P112H) on coacervation. D169G undergoes complex coacervation with DNA (Figure 4.26A) in stress conditions. The

similar coacervation behavior of D169G as TDP-43^{tRRM} could be explained as a result of a similar charge on the protein molecule. In wild-type TDP-43^{tRRM}, Asp residue at 169 position protonates and forms neutral Asp residue in stress conditions. While in D169G, the negatively charged Asp amino acid gets replaced by a neutral amino acid (Glu). These events do not affect the positive charge density of the protein. Hence, no changes in the coacervation propensity of the mutant were observed (Figure 4.6A).

On the contrary, increased coacervation propensity in another mutant, P112H, was observed (Figure 4.6B). The proline replacement by histidine introduces a positive charge at pH 3.8. We speculated that the increased positive charge density on the P112H triggers its coacervation even at low DNA concentrations.

4.5 Conclusions

We showed complex coacervation of TDP-43^{tRRM}, which prevents its amyloid-like aggregation. The coacervates were less dynamic. Our study has provided evidence representing important differences from the previous literature, which states that CTD is indispensable for phase separation. In addition, the phase separation described in this study has a protective role in contrast to the detrimental role of the globules described previously. These differences can be attributed to the presence of folded domain in TDP-43^{tRRM}, which prevents aggregation in the presence of DNA. Finally, the multiparametric studies explain the dynamics and tuning of the phase separation equilibrium by environmental factors.

4.6 References

(1) de Nadal, E.; Ammerer, G.; Posas, F. Controlling Gene Expression in Response to Stress. *Nat. Rev. Genet.* **2011**, *12* (12), 833–845. https://doi.org/10.1038/nrg3055.

(2) Anderson, P.; Kedersha, N. RNA Granules. *J. Cell Biol.* **2006**, *172* (6), 803–808. https://doi.org/10.1083/jcb.200512082.

(3) Buchan, J. R.; Parker, R. Eukaryotic Stress Granules: The Ins and Out of Translation. *Mol. Cell* **2009**, *36* (6), 932. https://doi.org/10.1016/j.molcel.2009.11.020.

(4) Cherkasov, V.; Hofmann, S.; Druffel-Augustin, S.; Mogk, A.; Tyedmers, J.; Stoecklin, G.; Bukau, B. Coordination of Translational Control and Protein Homeostasis During Severe

Heat Stress. *Curr. Biol. CB* **2013**, *23* (24), 2452–2462. https://doi.org/10.1016/j.cub.2013.09.058.

(5) Farny, N. G.; Kedersha, N. L.; Silver, P. A. Metazoan Stress Granule Assembly is Mediated by P-EIF2α-Dependent and -Independent Mechanisms. *RNA* **2009**, *15* (10), 1814–1821. https://doi.org/10.1261/rna.1684009.

(6) Anderson, P.; Kedersha, N. Stress Granules. *Curr. Biol. CB* **2009**, *19* (10), R397-398. https://doi.org/10.1016/j.cub.2009.03.013.

(7) Protter, D. S. W.; Parker, R. Principles and Properties of Stress Granules. *Trends Cell Biol.* **2016**, *26* (9), 668–679. https://doi.org/10.1016/j.tcb.2016.05.004.

(8) Souquere, S.; Mollet, S.; Kress, M.; Dautry, F.; Pierron, G.; Weil, D. Unravelling the Ultrastructure of Stress Granules and Associated P-Bodies in Human Cells. *J. Cell Sci.* **2009**, *122* (20), 3619–3626. https://doi.org/10.1242/jcs.054437.

(9) Kedersha, N.; Stoecklin, G.; Ayodele, M.; Yacono, P.; Lykke-Andersen, J.; Fritzler, M. J.; Scheuner, D.; Kaufman, R. J.; Golan, D. E.; Anderson, P. Stress Granules and Processing Bodies are Dynamically Linked Sites of mRNP Remodeling. *J. Cell Biol.* **2005**, *169* (6), 871–884. https://doi.org/10.1083/jcb.200502088.

(10) Alberti, S. Phase Separation in Biology. *Curr. Biol.* **2017**, *27* (20), R1097–R1102. https://doi.org/10.1016/j.cub.2017.08.069.

(11) Nover, L.; Scharf, K. D.; Neumann, D. Formation of Cytoplasmic Heat Shock Granules in Tomato Cell Cultures and Leaves. *Mol. Cell. Biol.* **1983**, *3* (9), 1648–1655. https://doi.org/10.1128/mcb.3.9.1648-1655.1983.

(12) Thomas, M.G.; Loschi, M.; Desbats, M.A.; Boccaccio, G.L. RNA granules: the good, the bad and the ugly. *Cell Signal.* **2011** 23 (2), 324-34. doi: 10.1016/j.cellsig.2010.08.011.

(13) Gutierrez-Beltran, E.; Moschou, P. N.; Smertenko, A. P.; Bozhkov, P. V. Tudor Staphylococcal Nuclease Links Formation of Stress Granules and Processing Bodies with mRNA Catabolism in Arabidopsis. *Plant Cell* **2015**, *27* (3), 926–943. https://doi.org/10.1105/tpc.114.134494.

(14) Hyman, A. A.; Weber, C. A.; Jülicher, F. Liquid-Liquid Phase Separation in Biology. *Annu. Rev. Cell Dev. Biol.* **2014**, *30*, 39–58. https://doi.org/10.1146/annurev-cellbio-100913-013325.

(15) Kedersha, N. L.; Gupta, M.; Li, W.; Miller, I.; Anderson, P. RNA-Binding Proteins Tia-1 and Tiar Link the Phosphorylation of Eif-2α to the Assembly of Mammalian Stress Granules. *J. Cell Biol.* **1999**, *147* (7), 1431–1442. https://doi.org/10.1083/jcb.147.7.1431.

(16) Tourrière, H.; Chebli, K.; Zekri, L.; Courselaud, B.; Blanchard, J. M.; Bertrand, E.; Tazi, J. The RasGAP-Associated Endoribonuclease G3BP Assembles Stress Granules. *J. Cell Biol.* **2003**, *160* (6), 823–831. https://doi.org/10.1083/jcb.200212128.

(17) Kedersha, N.; Chen, S.; Gilks, N.; Li, W.; Miller, I. J.; Stahl, J.; Anderson, P. Evidence that Ternary Complex (EIF2-GTP-TRNAi Met)–Deficient Preinitiation Complexes are Core Constituents of Mammalian Stress Granules. *Mol. Biol. Cell* **2002**, *13* (1), 195–210. https://doi.org/10.1091/mbc.01-05-0221.

(18) Mahboubi, H.; Seganathy, E.; Kong, D.; Stochaj, U. Identification of Novel Stress Granule Components that are Involved in Nuclear Transport. *PLOS ONE* **2013**, *8* (6), e68356. https://doi.org/10.1371/journal.pone.0068356.

(19) Adeli, K. Translational Control Mechanisms in Metabolic Regulation: Critical Role of RNA Binding Proteins, MicroRNAs, and Cytoplasmic RNA Granules. *Am. J. Physiol.-Endocrinol. Metab.* **2011**, *301* (6), E1051–E1064. https://doi.org/10.1152/ajpendo.00399.2011.

(20) Kedersha, N.; Ivanov, P.; Anderson, P. Stress Granules and Cell Signaling: More than Just a Passing Phase? *Trends Biochem. Sci.* **2013**, *38* (10), 494–506. https://doi.org/10.1016/j.tibs.2013.07.004.

(21) Anderson, P.; Kedersha, N. Stress Granules: The Tao of RNA Triage. *Trends Biochem. Sci.* **2008**, *33* (3), 141–150. https://doi.org/10.1016/j.tibs.2007.12.003.

(22) Guil, S.; Long, J. C.; Cáceres, J. F. HnRNP A1 Relocalization to the Stress Granules Reflects a Role in the Stress Response. *Mol. Cell. Biol.* **2006**, *26* (15), 5744–5758. https://doi.org/10.1128/MCB.00224-06.

(23) Neumann, M.; Sampathu, D. M.; Kwong, L. K.; Truax, A. C.; Micsenyi, M. C.; Chou, T. T.; Bruce, J.; Schuck, T.; Grossman, M.; Clark, C. M.; McCluskey, L. F.; Miller, B. L.; Masliah, E.; Mackenzie, I. R.; Feldman, H.; Feiden, W.; Kretzschmar, H. A.; Trojanowski, J. Q.; Lee, V. M.-Y. Ubiquitinated TDP-43 in Frontotemporal Lobar Degeneration and Amyotrophic Lateral Sclerosis. *Science* **2006**, *314* (5796), 130–133. https://doi.org/10.1126/science.1134108.

(24) Arai, T.; Hasegawa, M.; Akiyama, H.; Ikeda, K.; Nonaka, T.; Mori, H.; Mann, D.; Tsuchiya, K.; Yoshida, M.; Hashizume, Y.; Oda, T. TDP-43 is a Component of Ubiquitin-Positive Tau-Negative Inclusions in Frontotemporal Lobar Degeneration and Amyotrophic Lateral Sclerosis. *Biochem. Biophys. Res. Commun.* **2006**, *351* (3), 602–611. https://doi.org/10.1016/j.bbrc.2006.10.093.

(25) Colombrita, C.; Zennaro, E.; Fallini, C.; Weber, M.; Sommacal, A.; Buratti, E.; Silani, V.; Ratti, A. TDP-43 is Recruited to Stress Granules in Conditions of Oxidative Insult. *J. Neurochem.* **2009**, *111* (4), 1051–1061. https://doi.org/10.1111/j.1471-4159.2009.06383.x.

(26) Liu-Yesucevitz, L.; Bilgutay, A.; Zhang, Y.-J.; Vanderwyde, T.; Citro, A.; Mehta, T.; Zaarur, N.; McKee, A.; Bowser, R.; Sherman, M.; Petrucelli, L.; Wolozin, B. Tar DNA Binding Protein-43 (TDP-43) Associates with Stress Granules: Analysis of Cultured Cells and Pathological Brain Tissue. *PLOS ONE* **2010**, *5* (10), e13250. https://doi.org/10.1371/journal.pone.0013250.

(27) McDonald, K. K.; Aulas, A.; Destroismaisons, L.; Pickles, S.; Beleac, E.; Camu, W.; Rouleau, G. A.; Vande Velde, C. TAR DNA-Binding Protein 43 (TDP-43) Regulates Stress Granule Dynamics via Differential Regulation of G3BP and TIA-1. *Hum. Mol. Genet.* **2011**, *20* (7), 1400–1410. https://doi.org/10.1093/hmg/ddr021.

(28) Dewey, C. M.; Cenik, B.; Sephton, C. F.; Dries, D. R.; Mayer, P.; Good, S. K.; Johnson, B. A.; Herz, J.; Yu, G. TDP-43 is Directed to Stress Granules by Sorbitol, a Novel Physiological Osmotic and Oxidative Stressor. *Mol. Cell. Biol.* **2011**, *31* (5), 1098–1108. https://doi.org/10.1128/MCB.01279-10.

(29) Mompeán, M.; Romano, V.; Pantoja-Uceda, D.; Stuani, C.; Baralle, F. E.; Buratti, E.; Laurents, D. V. The TDP-43 N-Terminal Domain Structure at High Resolution. *FEBS J.* **2016**, *283* (7), 1242–1260. https://doi.org/10.1111/febs.13651.

(30) Dd, S.; L, F.-M.; Vk, K.; M, K. 1H, 15N and 13C Backbone Assignment of Apo TDP-43 RNA Recognition Motifs. *Biomol. NMR Assign.* **2019**, *13* (1). https://doi.org/10.1007/s12104-018-09870-x.

(31) Conicella, A. E.; Zerze, G. H.; Mittal, J.; Fawzi, N. L. ALS Mutations Disrupt Phase Separation Mediated by α-Helical Structure in the TDP-43 Low-Complexity C-Terminal Domain. *Structure* **2016**, *24* (9), 1537–1549. https://doi.org/10.1016/j.str.2016.07.007.

(32) Buratti, E.; Baralle, F. E. TDP-43: Gumming up Neurons through Protein-Protein and Protein-RNA Interactions. *Trends Biochem. Sci.* **2012**, *37* (6), 237–247. https://doi.org/10.1016/j.tibs.2012.03.003.

(33) Lee, E. B.; Lee, V. M.-Y.; Trojanowski, J. Q. Gains or Losses: Molecular Mechanisms of TDP43-Mediated Neurodegeneration. *Nat. Rev. Neurosci.* **2012**, *13* (1), 38–50.

(34) Buratti, E.; Baralle, F. E. Characterization and Functional Implications of the RNA Binding Properties of Nuclear Factor TDP-43, a Novel Splicing Regulator of CFTR Exon 9. *J. Biol. Chem.* **2001**, *276* (39), 36337–36343. https://doi.org/10.1074/jbc.M104236200.

(35) Tollervey, J. R.; Curk, T.; Rogelj, B.; Briese, M.; Cereda, M.; Kayikci, M.; König, J.; Hortobágyi, T.; Nishimura, A. L.; Zupunski, V.; Patani, R.; Chandran, S.; Rot, G.; Zupan, B.; Shaw, C. E.; Ule, J. Characterizing the RNA Targets and Position-Dependent Splicing Regulation by TDP-43. *Nat. Neurosci.* **2011**, *14* (4), 452–458. https://doi.org/10.1038/nn.2778.

(36) Polymenidou, M.; Lagier-Tourenne, C.; Hutt, K. R.; Huelga, S. C.; Moran, J.; Liang, T. Y.; Ling, S.-C.; Sun, E.; Wancewicz, E.; Mazur, C.; Kordasiewicz, H.; Sedaghat, Y.; Donohue, J. P.; Shiue, L.; Bennett, C. F.; Yeo, G. W.; Cleveland, D. W. Long Pre-mRNA Depletion and RNA Missplicing Contribute to Neuronal Vulnerability from Loss of TDP-43. *Nat. Neurosci.* **2011**, *14* (4), 459–468. https://doi.org/10.1038/nn.2779.

(37) Coyne, A. N.; Siddegowda, B. B.; Estes, P. S.; Johannesmeyer, J.; Kovalik, T.; Daniel, S. G.; Pearson, A.; Bowser, R.; Zarnescu, D. C. Futsch/MAP1B mRNA is a Translational

Target of TDP-43 and is Neuroprotective in a Drosophila Model of Amyotrophic Lateral Sclerosis. *J. Neurosci. Off. J. Soc. Neurosci.* **2014**, *34* (48), 15962–15974. https://doi.org/10.1523/JNEUROSCI.2526-14.2014.

(38) Russo, A.; Scardigli, R.; La Regina, F.; Murray, M. E.; Romano, N.; Dickson, D. W.; Wolozin, B.; Cattaneo, A.; Ceci, M. Increased Cytoplasmic TDP-43 Reduces Global Protein Synthesis by Interacting with RACK1 on Polyribosomes. *Hum. Mol. Genet.* **2017**, *26* (8), 1407–1418. https://doi.org/10.1093/hmg/ddx035.

(39) Kawahara, Y.; Mieda-Sato, A. TDP-43 Promotes microRNA Biogenesis as a Component of the Drosha and Dicer Complexes. *Proc. Natl. Acad. Sci.* **2012**, *109* (9), 3347–3352. https://doi.org/10.1073/pnas.1112427109.

(40) Sephton, C. F.; Good, S. K.; Atkin, S.; Dewey, C. M.; Mayer, P.; Herz, J.; Yu, G. TDP-43 is a Developmentally Regulated Protein Essential for Early Embryonic Development. *J. Biol. Chem.* **2010**, *285* (9), 6826–6834. https://doi.org/10.1074/jbc.M109.061846.

(41) Sephton, C. F.; Cenik, B.; Cenik, B. K.; Herz, J.; Yu, G. TDP-43 in Central Nervous System Development and Function: Clues to TDP-43-Associated Neurodegeneration. *Biol. Chem.* **2012**, *393* (7), 589–594. https://doi.org/10.1515/hsz-2012-0115.

(42) Strong, M. J.; Volkening, K.; Hammond, R.; Yang, W.; Strong, W.; Leystra-Lantz, C.; Shoesmith, C. TDP43 is a Human Low Molecular Weight Neurofilament (HNFL) mRNA-Binding Protein. *Mol. Cell. Neurosci.* **2007**, *35* (2), 320–327. https://doi.org/10.1016/j.mcn.2007.03.007.

(43) Volkening, K.; Leystra-Lantz, C.; Yang, W.; Jaffee, H.; Strong, M. J. Tar DNA Binding Protein of 43 KDa (TDP-43), 14-3-3 Proteins and Copper/Zinc Superoxide Dismutase (SOD1) Interact to Modulate NFL mRNA Stability. Implications for Altered RNA Processing in Amyotrophic Lateral Sclerosis (ALS). *Brain Res.* **2009**, *1305*, 168–182. https://doi.org/10.1016/j.brainres.2009.09.105.

(44) Colombrita, C.; Onesto, E.; Megiorni, F.; Pizzuti, A.; Baralle, F. E.; Buratti, E.; Silani, V.; Ratti, A. TDP-43 and FUS RNA-Binding Proteins Bind Distinct Sets of Cytoplasmic Messenger RNAs and Differently Regulate their Post-Transcriptional Fate in Motoneuron-Like Cells. *J. Biol. Chem.* **2012**, *287* (19), 15635–15647. https://doi.org/10.1074/jbc.M111.333450.

(45) Costessi, L.; Porro, F.; Iaconcig, A.; Muro, A. F. TDP-43 Regulates β-Adducin (Add2) Transcript Stability. *RNA Biol.* **2014**, *11* (10), 1280–1290. https://doi.org/10.1080/15476286.2014.996081.

(46) Alami, N. H.; Smith, R. B.; Carrasco, M. A.; Williams, L. A.; Winborn, C. S.; Han, S. S. W.; Kiskinis, E.; Winborn, B.; Freibaum, B. D.; Kanagaraj, A.; Clare, A. J.; Badders, N. M.; Bilican, B.; Chaum, E.; Chandran, S.; Shaw, C. E.; Eggan, K. C.; Maniatis, T.; Taylor, J. P. Axonal Transport of TDP-43 mRNA Granules is Impaired by ALS-Causing Mutations. *Neuron* **2014**, *81* (3), 536–543. https://doi.org/10.1016/j.neuron.2013.12.018.

(47) Kato, M.; Han, T. W.; Xie, S.; Shi, K.; Du, X.; Wu, L. C.; Mirzaei, H.; Goldsmith, E. J.; Longgood, J.; Pei, J.; Grishin, N. V.; Frantz, D. E.; Schneider, J. W.; Chen, S.; Li, L.; Sawaya, M. R.; Eisenberg, D.; Tycko, R.; McKnight, S. L. Cell-Free Formation of RNA Granules: Low Complexity Sequence Domains Form Dynamic Fibers within Hydrogels. *Cell* **2012**, *149* (4), 753–767. https://doi.org/10.1016/j.cell.2012.04.017.

(48) Lin, Y.; Protter, D. S. W.; Rosen, M. K.; Parker, R. Formation and Maturation of Phase-Separated Liquid Droplets by RNA-Binding Proteins. *Mol. Cell* **2015**, *60* (2), 208–219. https://doi.org/10.1016/j.molcel.2015.08.018.

(49) Molliex, A.; Temirov, J.; Lee, J.; Coughlin, M.; Kanagaraj, A.; Kim, H. J.; Mittag, T.; Taylor, J. P. Phase Separation by Low Complexity Domains Promotes Stress Granule Assembly and Drives Pathological Fibrillization. *Cell* **2015**, *163*, 123–133. https://doi.org/10.1016/j.cell.2015.09.015.

(50) Patel, A.; Lee, H. O.; Jawerth, L. M.; Maharana, S.; Jahnel, M.; Hein, M. Y.; Stoynov, S. S.; Mahamid, J.; Saha, S.; Franzmann, T. M.; Pozniakovski, A.; Poser, I.; Maghelli, N.; Royer, L. A.; Weigert, M.; Myers, E. W.; Grill, S. W.; Drechsel, D. N.; Hyman, A. A.; Alberti, S. A Liquid-to-Solid Phase Transition of the ALS Protein FUS Accelerated by Disease Mutation. *Cell* **2015**. https://doi.org/10.1016/j.cell.2015.07.047.

(51) Ray, S.; Singh, N.; Kumar, R.; Patel, K.; Pandey, S.; Datta, D.; Mahato, J.; Panigrahi, R.; Navalkar, A.; Mehra, S.; Gadhe, L.; Chatterjee, D.; Sawner, A. S.; Maiti, S.; Bhatia, S.; Gerez, J. A.; Chowdhury, A.; Kumar, A.; Padinhateeri, R.; Riek, R.; Krishnamoorthy, G.; Maji, S. K. α-Synuclein Aggregation Nucleates through Liquid-Liquid Phase Separation. *Nat. Chem.* **2020**, *12* (8), 705–716. https://doi.org/10.1038/s41557-020-0465-9.

(52) Zhang, L.; Wang, S.; Wang, W.; Shi, J.; Stovall, D. B.; Li, D.; Sui, G. Phase-Separated Subcellular Compartmentation and Related Human Diseases. *Int. J. Mol. Sci.* **2022**, *23* (10), 5491. https://doi.org/10.3390/ijms23105491.

(53) Ambadipudi, S.; Biernat, J.; Riedel, D.; Mandelkow, E.; Zweckstetter, M. Liquid–Liquid Phase Separation of the Microtubule-Binding Repeats of the Alzheimer-Related Protein Tau. *Nat. Commun.* **2017**, *8* (1), 275. https://doi.org/10.1038/s41467-017-00480-0.

(54) Murakami, T.; Qamar, S.; Lin, J. Q.; Schierle, G. S. K.; Rees, E.; Miyashita, A.; Costa, A. R.; Dodd, R. B.; Chan, F. T. S.; Michel, C. H.; Kronenberg-Versteeg, D.; Li, Y.; Yang, S.-P.; Wakutani, Y.; Meadows, W.; Ferry, R. R.; Dong, L.; Tartaglia, G. G.; Favrin, G.; Lin, W.-L.; Dickson, D. W.; Zhen, M.; Ron, D.; Schmitt-Ulms, G.; Fraser, P. E.; Shneider, N. A.; Holt, C.; Vendruscolo, M.; Kaminski, C. F.; St George-Hyslop, P. ALS/FTD Mutation-Induced Phase Transition of FUS Liquid Droplets and Reversible Hydrogels into Irreversible Hydrogels Impairs RNP Granule Function. *Neuron* **2015**, *88* (4), 678–690. https://doi.org/10.1016/j.neuron.2015.10.030.

(55) Riback, J. A.; Katanski, C. D.; Kear-Scott, J. L.; Pilipenko, E. V.; Rojek, A. E.; Sosnick, T. R.; Drummond, D. A. Stress-Triggered Phase Separation is an Adaptive, Evolutionarily

Tuned Response. *Cell* **2017**, *168* (6), 1028-1040.e19. https://doi.org/10.1016/j.cell.2017.02.027.

(56) Kroschwald, S.; Munder, M. C.; Maharana, S.; Franzmann, T. M.; Richter, D.; Ruer, M.; Hyman, A. A.; Alberti, S. Different Material States of Pub1 Condensates Define Distinct Modes of Stress Adaptation and Recovery. *Cell Rep.* **2018**, *23* (11), 3327–3339. https://doi.org/10.1016/j.celrep.2018.05.041.

(57) Iserman, C.; Desroches Altamirano, C.; Jegers, C.; Friedrich, U.; Zarin, T.; Fritsch, A. W.; Mittasch, M.; Domingues, A.; Hersemann, L.; Jahnel, M.; Richter, D.; Guenther, U.-P.; Hentze, M. W.; Moses, A. M.; Hyman, A. A.; Kramer, G.; Kreysing, M.; Franzmann, T. M.; Alberti, S. Condensation of Ded1p Promotes a Translational Switch from Housekeeping to Stress Protein Production. *Cell* **2020**, *181* (4), 818-831.e19. https://doi.org/10.1016/j.cell.2020.04.009.

(58) Franzmann, T. M.; Jahnel, M.; Pozniakovsky, A.; Mahamid, J.; Holehouse, A. S.; Nüske, E.; Richter, D.; Baumeister, W.; Grill, S. W.; Pappu, R. V.; Hyman, A. A.; Alberti, S. Phase Separation of a Yeast Prion Protein Promotes Cellular Fitness. *Science* **2018**, *359* (6371). https://doi.org/10.1126/science.aao5654.

(59) Staderini, T.; Bigi, A.; Mongiello, D.; Cecchi, C.; Chiti, F. Biophysical Characterization of Full-Length TAR DNA-Binding Protein (TDP-43) Phase Separation. *Protein Sci. Publ. Protein Soc.* **2022**, *31* (12), e4509. https://doi.org/10.1002/pro.4509.

(60) Li, H.-R.; Chiang, W.-C.; Chou, P.-C.; Wang, W.-J.; Huang, J. TAR DNA-Binding Protein 43 (TDP-43) Liquid–Liquid Phase Separation is Mediated by Just a Few Aromatic Residues. *J. Biol. Chem.* **2018**, *293* (16), 6090. https://doi.org/10.1074/jbc.AC117.001037.

(61) Babinchak, W. M.; Haider, R.; Dumm, B. K.; Sarkar, P.; Surewicz, K.; Choi, J.-K.; Surewicz, W. K. The Role of Liquid–Liquid Phase Separation in Aggregation of the TDP-43 Low-Complexity Domain. *J. Biol. Chem.* **2019**, *294* (16), 6306–6317. https://doi.org/10.1074/jbc.RA118.007222.

(62) McGurk, L.; Gomes, E.; Guo, L.; Mojsilovic-Petrovic, J.; Tran, V.; Kalb, R. G.; Shorter, J.; Bonini, N. M. Poly(ADP-Ribose) Prevents Pathological Phase Separation of TDP-43 by Promoting Liquid Demixing and Stress Granule Localization. *Mol. Cell* **2018**, *71* (5), 703-717.e9. https://doi.org/10.1016/j.molcel.2018.07.002.

(63) Grese, Z. R.; Bastos, A. C.; Mamede, L. D.; French, R. L.; Miller, T. M.; Ayala, Y. M. Specific RNA Interactions Promote TDP-43 Multivalent Phase Separation and Maintain Liquid Properties. *EMBO Rep.* **2021**, *22* (12), e53632. https://doi.org/10.15252/embr.202153632.

(64) Hallegger, M.; Chakrabarti, A. M.; Lee, F. C. Y.; Lee, B. L.; Amalietti, A. G.; Odeh, H. M.; Copley, K. E.; Rubien, J. D.; Portz, B.; Kuret, K.; Huppertz, I.; Rau, F.; Patani, R.; Fawzi, N. L.; Shorter, J.; Luscombe, N. M.; Ule, J. TDP-43 Condensation Properties Specify Its

RNA-Binding and Regulatory Repertoire. *Cell* **2021**, *184* (18), 4680-4696.e22. https://doi.org/10.1016/j.cell.2021.07.018.

(65) Pakravan, D.; Michiels, E.; Bratek-Skicki, A.; De Decker, M.; Van Lindt, J.; Alsteens, D.; Derclaye, S.; Van Damme, P.; Schymkowitz, J.; Rousseau, F.; Tompa, P.; Van Den Bosch, L. Liquid–Liquid Phase Separation Enhances TDP-43 LCD Aggregation but Delays Seeded Aggregation. *Biomolecules* **2021**, *11* (4), 548. https://doi.org/10.3390/biom11040548.

(66) Koehler, L. C.; Grese, Z. R.; Bastos, A. C. S.; Mamede, L. D.; Heyduk, T.; Ayala, Y. M. TDP-43 Oligomerization and Phase Separation Properties are Necessary for Autoregulation. *Front. Neurosci.* **2022**, *16*, 818655. https://doi.org/10.3389/fnins.2022.818655.

(67) Wang, A.; Conicella, A.E.; Schmidt, H.B.; Martin, E.W.; Rhoads, S.N.; Reeb, A.N.; Nourse, A.; Ramirez Montero, D.; Ryan, V.H.; Rohatgi, R.; Shewmaker, F.; Naik, M.T.; Mittag, T.; Ayala, Y.M.; Fawzi, N.L. A Single N-Terminal Phosphomimic Disrupts TDP-43 Polymerization, Phase Separation, And RNA Splicing. *EMBO J.* **2018,** 37 (5), e97452. https://doi.org/10.15252/embj.201797452.

(68) Carter, G. C.; Hsiung, C.-H.; Simpson, L.; Yang, H.; Zhang, X. N-Terminal Domain of TDP43 Enhances Liquid-Liquid Phase Separation of Globular Proteins. *J. Mol. Biol.* **2021**, *433* (10), 166948. https://doi.org/10.1016/j.jmb.2021.166948.

(69) Xiao, S.; Sanelli, T.; Chiang, H.; Sun, Y.; Chakrabartty, A.; Keith, J.; Rogaeva, E.; Zinman, L.; Robertson, J. Low Molecular Weight Species of TDP-43 Generated by Abnormal Splicing Form Inclusions in Amyotrophic Lateral Sclerosis and Result in Motor Neuron Death. *Acta Neuropathol. (Berl.)* **2015**, *130* (1), 49–61. https://doi.org/10.1007/s00401-015-1412-5.

(70) Zhang, Y.-J.; Xu, Y.; Dickey, C. A.; Buratti, E.; Baralle, F.; Bailey, R.; Pickering-Brown, S.; Dickson, D.; Petrucelli, L. Progranulin Mediates Caspase-Dependent Cleavage of TAR DNA Binding Protein-43. *J. Neurosci.* **2007**, *27* (39), 10530–10534. https://doi.org/10.1523/JNEUROSCI.3421-07.2007.

(71) Patni, D.; Jha, S. K. Protonation–Deprotonation Switch Controls the Amyloid-like Misfolding of Nucleic-Acid-Binding Domains of TDP-43. *J. Phys. Chem. B* **2021**, *125* (30), 8383–8394. https://doi.org/10.1021/acs.jpcb.1c03262.

(72) Pillai, M.; Jha, S. K. The Folding and Aggregation Energy Landscapes of Tethered RRM Domains of Human TDP-43 are Coupled Via a Metastable Molten Globule-Like Oligomer. *Biochemistry* **2019**, *58* (6), 608–620. https://doi.org/10.1021/acs.biochem.8b01013.

(73) Pillai, M.; Jha, S. K. Early Metastable Assembly During the Stress-Induced Formation of Worm-Like Amyloid Fibrils of Nucleic Acid Binding Domains of TDP-43. *Biochemistry* **2020**, *59* (3), 315–328. https://doi.org/10.1021/acs.biochem.9b00780.

(74) Pillai, M.; Jha, S. K. Multistep Molecular Mechanism of Amyloid-like Aggregation of Nucleic Acid-Binding Domain of TDP-43. *Proteins* **2022**. https://doi.org/10.1002/prot.26455.

(75) Chang, C.; Chiang, M.; Toh, E. K.-W.; Chang, C.-F.; Huang, T. Molecular Mechanism of Oxidation-Induced TDP-43 RRM1 Aggregation and Loss of Function. *FEBS Lett.* **2013**, *587* (6), 575–582. https://doi.org/10.1016/j.febslet.2013.01.038.

(76) Agrawal, S.; Kuo, P.-H.; Chu, L.-Y.; Golzarroshan, B.; Jain, M.; Yuan, H. S. RNA Recognition Motifs of Disease-Linked RNA-Binding Proteins Contribute to Amyloid Formation. *Sci. Rep.* **2019**, *9*, 6171. https://doi.org/10.1038/s41598-019-42367-8.

(77) Zacco, E.; Martin, S. R.; Thorogate, R.; Pastore, A. The RNA-Recognition Motifs of TAR DNA-Binding Protein 43 May Play a Role in the Aberrant Self-Assembly of the Protein. *Front. Mol. Neurosci.* **2018**, *11*, 372. https://doi.org/10.3389/fnmol.2018.00372.

(78) Patni, D.; Jha, S.K. Thermodynamic Modulation of Folding and Aggregation Energy Landscape by DNA Binding of Functional Domains of TDP-43. Biochim. Biophys. Acta BBA-Proteins Proteom. 1871 (4), 140916. https://doi.org/10.1016/j.bbapap.2023.140916.

(79) Mishra, P.; Jha, S. K. An Alternatively Packed Dry Molten Globule-like Intermediate in the Native State Ensemble of a Multidomain Protein. *J. Phys. Chem. B* **2017**, *121* (40), 9336–9347. https://doi.org/10.1021/acs.jpcb.7b07032.

(80) Singh, J.; Udgaonkar, J. B. Unraveling the Molecular Mechanism of pH-Induced Misfolding and Oligomerization of the Prion Protein. *J. Mol. Biol.* **2016**, *428* (6), 1345–1355. https://doi.org/10.1016/j.jmb.2016.01.030.

(81) Kuo, P.-H.; Doudeva, L. G.; Wang, Y.-T.; Shen, C.-K. J.; Yuan, H. S. Structural Insights into TDP-43 in Nucleic-Acid Binding and Domain Interactions. *Nucleic Acids Res.* **2009**, *37* (6), 1799–1808. https://doi.org/10.1093/nar/gkp013.

(82) Mackness, B. C.; Tran, M. T.; McClain, S. P.; Matthews, C. R.; Zitzewitz, J. A. Folding of the RNA Recognition Motif (RRM) Domains of the Amyotrophic Lateral Sclerosis (ALS)-Linked Protein TDP-43 Reveals an Intermediate State. *J. Biol. Chem.* **2014**, *289* (12), 8264–8276. https://doi.org/10.1074/jbc.M113.542779.

(83) Priftis, D.; Tirrell, M. Phase Behaviour and Complex Coacervation of Aqueous Polypeptide Solutions. *Soft Matter* **2012**, *8* (36), 9396–9405. https://doi.org/10.1039/C2SM25604E.

(84) Frankel, E. A.; Bevilacqua, P. C.; Keating, C. D. Polyamine/Nucleotide Coacervates Provide Strong Compartmentalization of Mg^{2+}, Nucleotides, and RNA. *Langmuir* **2016**, *32* (8), 2041–2049. https://doi.org/10.1021/acs.langmuir.5b04462.

(85) Aumiller, W. M.; Pir Cakmak, F.; Davis, B. W.; Keating, C. D. RNA-Based Coacervates as a Model for Membraneless Organelles: Formation, Properties, and Interfacial Liposome Assembly. *Langmuir* **2016**, *32* (39), 10042–10053. https://doi.org/10.1021/acs.langmuir.6b02499.

(86) Aumiller, W. M.; Keating, C. D. Phosphorylation-Mediated RNA/Peptide Complex Coacervation as a Model for Intracellular Liquid Organelles. *Nat. Chem.* **2016**, *8* (2), 129–137. https://doi.org/10.1038/nchem.2414.

(87) Koga, S.; Williams, D. S.; Perriman, A. W.; Mann, S. Peptide–Nucleotide Microdroplets as a Step towards a Membrane-Free Protocell Model. *Nat. Chem.* **2011**, *3* (9), 720–724. https://doi.org/10.1038/nchem.1110.

(88) Dora Tang, T.-Y.; Rohaida Che Hak, C.; Thompson, A. J.; Kuimova, M. K.; Williams, D. S.; Perriman, A. W.; Mann, S. Fatty Acid Membrane Assembly on Coacervate Microdroplets as a Step towards a Hybrid Protocell Model. *Nat. Chem.* **2014**, *6* (6), 527–533. https://doi.org/10.1038/nchem.1921.

(89) Krainer, G.; Welsh, T. J.; Joseph, J. A.; Espinosa, J. R.; Wittmann, S.; de Csilléry, E.; Sridhar, A.; Toprakcioglu, Z.; Gudiškytė, G.; Czekalska, M. A.; Arter, W. E.; Guillén-Boixet, J.; Franzmann, T. M.; Qamar, S.; George-Hyslop, P. S.; Hyman, A. A.; Collepardo-Guevara, R.; Alberti, S.; Knowles, T. P. J. Reentrant Liquid Condensate Phase of Proteins is Stabilized by Hydrophobic and Non-Ionic Interactions. *Nat. Commun.* **2021**, *12* (1), 1085. https://doi.org/10.1038/s41467-021-21181-9.

(90) Sama, R. R. K.; Ward, C. L.; Kaushansky, L. J.; Lemay, N.; Ishigaki, S.; Urano, F.; Bosco, D. A. FUS/TLS Assembles into Stress Granules and is a Prosurvival Factor during Hyperosmolar Stress. *J. Cell. Physiol.* **2013**, *228* (11), 2222–2231. https://doi.org/10.1002/jcp.24395.

(91) Ash, P. E. A.; Lei, S.; Shattuck, J.; Boudeau, S.; Carlomagno, Y.; Medalla, M.; Mashimo, B. L.; Socorro, G.; Al-Mohanna, L. F. A.; Jiang, L.; Öztürk, M. M.; Knobel, M.; Ivanov, P.; Petrucelli, L.; Wegmann, S.; Kanaan, N. M.; Wolozin, B. TIA1 Potentiates Tau Phase Separation and Promotes Generation of Toxic Oligomeric Tau. *Proc. Natl. Acad. Sci. U. S. A.* **2021**, *118* (9). https://doi.org/10.1073/pnas.2014188118.

(92) Gilks, N.; Kedersha, N.; Ayodele, M.; Shen, L.; Stoecklin, G.; Dember, L. M.; Anderson, P. Stress Granule Assembly is Mediated by Prion-Like Aggregation of TIA-1. *Mol. Biol. Cell* **2004**, *15* (12), 5383–5398. https://doi.org/10.1091/mbc.e04-08-0715.

(93) Rai, S. K.; Savastano, A.; Singh, P.; Mukhopadhyay, S.; Zweckstetter, M. Liquid–Liquid Phase Separation of Tau: From Molecular Biophysics to Physiology and Disease. *Protein Sci. Publ. Protein Soc.* **2021**, *30* (7), 1294–1314. https://doi.org/10.1002/pro.4093.

(94) Li, H.-R.; Chen, T.-C.; Hsiao, C.-L.; Shi, L.; Chou, C.-Y.; Huang, J. The Physical Forces Mediating Self-Association and Phase-Separation in the C-Terminal Domain of TDP-43. *Biochim. Biophys. Acta BBA - Proteins Proteomics* **2018**, *1866* (2), 214–223. https://doi.org/10.1016/j.bbapap.2017.10.001.

(95) Conicella, A. E.; Dignon, G. L.; Zerze, G. H.; Schmidt, H. B.; D'Ordine, A. M.; Kim, Y. C.; Rohatgi, R.; Ayala, Y. M.; Mittal, J.; Fawzi, N. L. TDP-43 α-Helical Structure Tunes

Liquid–Liquid Phase Separation and Function. *Proc. Natl. Acad. Sci.* **2020**, *117* (11), 5883–5894. https://doi.org/10.1073/pnas.1912055117.

(96) Bhopatkar, A. A.; Dhakal, S.; Rangachari, V. Cytoplasmic Colocalization of Granulins and TDP-43 Prion-like Domain Involves Electrostatically Driven Complex Coacervation Tuned by the Redox State of Cysteines. bioRxiv July 14, 2021, p 2021.06.25.449959. https://doi.org/10.1101/2021.06.25.449959.

(97) Alemasova, E.E.; Lavrik, O.I. A SePARate Phase? Poly(ADP-Ribose) versus RNA in the Organization of Biomolecular Condensates. *Nucleic Acids Res.* **2022**, 50 (19), 10817-10838. https://doi.org/10.1093/nar/gkac866.

(98) Bounedjah, O.; Desforges, B.; Wu, T.-D.; Pioche-Durieu, C.; Marco, S.; Hamon, L.; Curmi, P. A.; Guerquin-Kern, J.-L.; Piétrement, O.; Pastré, D. Free mRNA in Excess upon Polysome Dissociation is a Scaffold for Protein Multimerization to Form Stress Granules. *Nucleic Acids Res.* **2014**, 42 (13), 8678-8691. https://doi.org/10.1093/nar/gku582.

(99) Roden, C.; Gladfelter, A. S. RNA Contributions to the Form and Function of Biomolecular Condensates. *Nat. Rev. Mol. Cell Biol.* **2021**, 22 (3), 183–195. https://doi.org/10.1038/s41580-020-0264-6.

(100) Boeynaems, S.; Holehouse, A. S.; Weinhardt, V.; Kovacs, D.; Van Lindt, J.; Larabell, C.; Van Den Bosch, L.; Das, R.; Tompa, P. S.; Pappu, R. V.; Gitler, A. D. Spontaneous Driving Forces Give Rise to Protein−RNA Condensates with Coexisting Phases and Complex Material Properties. *Proc. Natl. Acad. Sci. U. S. A.* **2019**, 116 (16), 7889–7898. https://doi.org/10.1073/pnas.1821038116.

(101) Khong, A.; Matheny, T.; Jain, S.; Mitchell, S. F.; Wheeler, J. R.; Parker, R. The Stress Granule Transcriptome Reveals Principles of mRNA Accumulation in Stress Granules. *Mol. Cell* **2017**, 68 (4), 808-820.e5. https://doi.org/10.1016/j.molcel.2017.10.015.

(102) Burke, K. A.; Janke, A. M.; Rhine, C. L.; Fawzi, N. L. Residue-by-Residue View of in Vitro FUS Granules That Bind the C-Terminal Domain of RNA Polymerase II. *Mol. Cell* **2015**, 60 (2), 231–241. https://doi.org/10.1016/j.molcel.2015.09.006.

(103) Maharana, S.; Wang, J.; Papadopoulos, D. K.; Richter, D.; Pozniakovsky, A.; Poser, I.; Bickle, M.; Rizk, S.; Guillén-Boixet, J.; Franzmann, T. M.; Jahnel, M.; Marrone, L.; Chang, Y.-T.; Sterneckert, J.; Tomancak, P.; Hyman, A. A.; Alberti, S. RNA Buffers the Phase Separation Behavior of Prion-Like RNA Binding Proteins. *Science* **2018**, 360 (6391), 918–921. https://doi.org/10.1126/science.aar7366.

(104) Mann, J. R.; Gleixner, A. M.; Mauna, J. C.; Gomes, E.; DeChellis-Marks, M. R.; Needham, P. G.; Copley, K. E.; Hurtle, B.; Portz, B.; Pyles, N. J.; Guo, L.; Calder, C. B.; Wills, Z. P.; Pandey, U. B.; Kofler, J. K.; Brodsky, J. L.; Thathiah, A.; Shorter, J.; Donnelly, C. J. RNA Binding Antagonizes Neurotoxic Phase Transitions of TDP-43. *Neuron* **2019**, 102 (2), 321-338.e8. https://doi.org/10.1016/j.neuron.2019.01.048.

(105) Shin, Y.; Brangwynne, C. P. Liquid Phase Condensation in Cell Physiology and Disease. *Science* **2017**, *357* (6357), eaaf4382. https://doi.org/10.1126/science.aaf4382.

(106) Yewdall, N. A.; André, A. A. M.; Lu, T.; Spruijt, E. Coacervates as Models of Membraneless Organelles. *Curr. Opin. Colloid Interface Sci.* **2021**, *52*, 101416. https://doi.org/10.1016/j.cocis.2020.101416.

(107) *Protein Calculator*. https://protcalc.sourceforge.net/ (accessed 2023-04-10).

(108) Dong, S.; Heyda, J.; Yuan, J.; A. Schalley, C. Lower Critical Solution Temperature (LCST) Phase Behaviour of an Ionic Liquid and its Control by Supramolecular Host–Guest Interactions. *Chem. Commun.* **2016**, *52* (51), 7970–7973. https://doi.org/10.1039/C6CC02838A.

(109) Najafi, S.; Lin, Y.; Longhini, A. P.; Zhang, X.; Delaney, K. T.; Kosik, K. S.; Fredrickson, G. H.; Shea, J.; Han, S. Liquid–Liquid Phase Separation of Tau by Self and Complex Coacervation. *Protein Sci. Publ. Protein Soc.* **2021**, *30* (7), 1393–1407. https://doi.org/10.1002/pro.4101.

4.7 Supporting figures

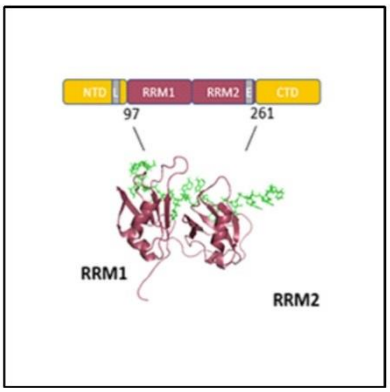

Figure 4.S1 Schematic representation of different domains of TDP-43. The arrows show the diagrammatic representation of TDP-43^{tRRM} created using PDB file 4BS2 with the help of PyMOL. TDP-43 is a multidomain protein consisting of N-terminal (residues 1-102): involved in dimerization; RRM 1 and 2: involved in nucleic acid binding and is the primary functional domain of the protein; C-terminal: prion-like domain involved in protein-protein interactions.

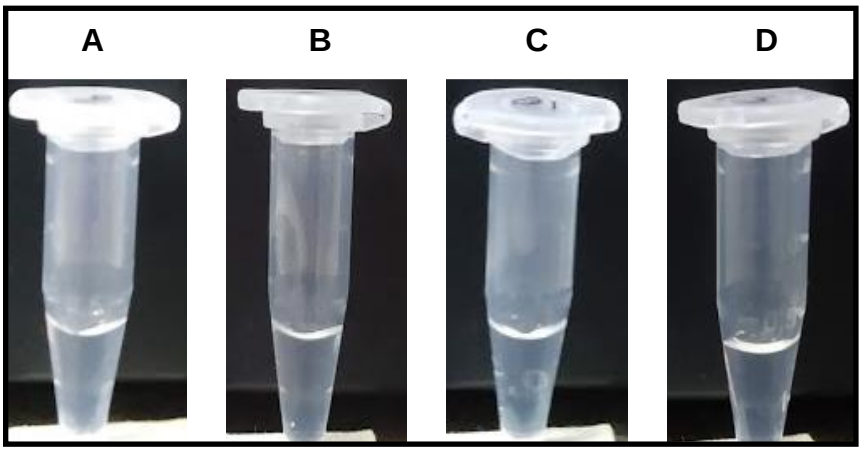

Figure 4.S2 Microcentrifuge tubes showing the solution containing 10 μM TDP-43^{tRRM} in the presence of following concentrations of DNA (A) 4 μM, (B) 11 μM, (C) 15 μM, (D) 30 μM.

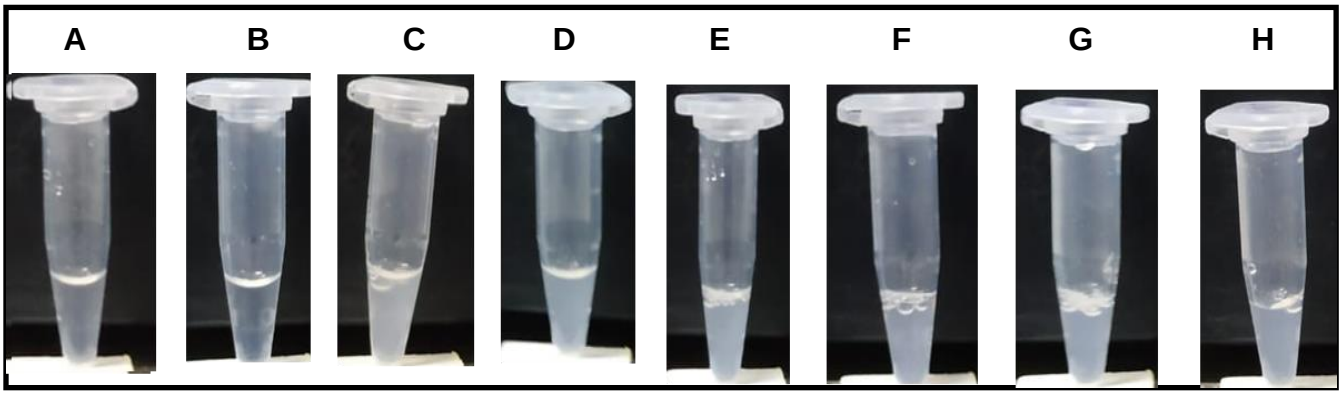

Figure 4.S3 Microcentrifuge tubes showing the solution containing the 11 μM DNA in the presence of following concentrations of TDP-43^{tRRM} (A) 7 μM, (B) 8 μM, (C) 15 μM, (D) 20 μM, (E) 25 μM, (F) 30 μM, (G) 40 μM, (H) 45 μM.

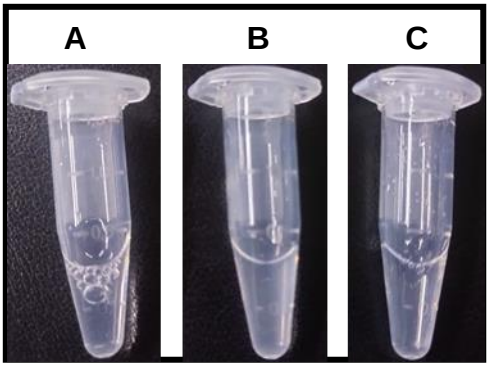

Figure 4.S4 Microcentrifuge tubes showing the solution containing 10 μM D169G in the presence of following concentrations of DNA. (A) 0 μM, (B) 4 μM, (C) 20 μM.

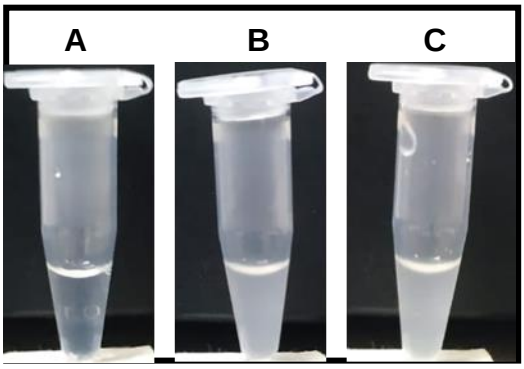

Figure 4.S5 Microcentrifuge tubes showing the solution containing 10 μM P112H in the presence of following concentrations of DNA. (A) 0 μM, (B) 2 μM, (C) 20 μM.

Chapter 5

Conclusions and future directions

This chapter reviews the most important findings of the thesis and discusses some future directions of the current work. Some limitations of the work are also discussed.

5.1 Summary

Certain proteins are very sensitive to environmental conditions and can assess different conformations due to the modulation of the energy landscape with the solvation environment. Several environments promote misfolding and aggregation of proteins leading to fatal diseases. A comprehensive understanding of the coupling of their folding and aggregation energy landscape in different solvation environments remains an evolving area of research. The prime focus of research in this study has been to decode the thermodynamic and molecular basis of the conformational changes to the protein molecules as it detects changes in the solvation environment and utilizing the knowledge to prevent detrimental conformational change. We briefly discuss the specific aims and conclusions of the study:

a) ***Chapter 2*****:** In the first working chapter, we explored the changes at the molecular level as the TDP-43^{tRRM} detects the low pH stress (mimic of starvation stress). It has been proposed that the proteins sense the starvation stress by protonating the ionizable side chain residues, further triggering intermolecular assembly. This coupling of protonation-deprotonation with the assembly-disassembly of proteins mitigates the starvation stress, but persistent stress can lead to the formation of higher-order aggregates. We observed that the native TDP-43^{tRRM} misfolds to an oligomeric β-sheet rich structure (β form) with exposed hydrophobic patches in the pH range (pH 1.5 – 4.5). The transition midpoint lies around pH 4.0. The observation implies that the protonation of a buried critical amino acid residue with a pKa value near 4.0 acts as a gatekeeper and triggers further misfolding to amyloid-like β form. To examine the critical amino acid responsible for the behavior mentioned above, we systematically mutated three amino acids (D105, H166, and H256) to neutral amino acids and studied their conformational change as the solvation environment changed. We observed that the mutation of the H166 to glutamine inhibits the conformational changes. Moreover, the mutant acquires a molten-globule-like structure. Therefore, our results emphasized that the protonation-deprotonation of a critical residue is coupled to the assembly-disassembly of protein. The molten globule formed resists misfolding.

b) ***Chapter 3:*** We understand that the TDP-43^{tRRM} experiences pH-dependent conformational changes to the misfolded β form. To further explore the thermodynamic basis of the misfolding, we employed various biophysical tools to study the thermodynamic parameters in different pH environments. We report that the TDP-43^{tRRM} experiences pH-dependent thermodynamic stability and remain maximally stable at pH 7.5. It achieves minimum thermodynamic stability at pH 5.0. The point of minimum thermodynamic stability coincides with the point of misfolding initiation. We argue that the destabilization makes TDP-43^{tRRM} prone to misfolding to an amyloid-like β form. Since TDP-43^{tRRM} is a nucleic

acid binding protein, we examined the effect of natural DNA binding ligand on the thermodynamic stability of TDP-43^{tRRM} in native and stress conditions. DNA binding increases the thermodynamic stability of TDP-43^{tRRM}, and as a result, the amyloid-like misfolding is inhibited. DNA binding maintains the monomeric native-like structure of TDP-43^{tRRM}. Our results conveyed that the events destabilizing the TDP-43^{tRRM} are the crucial events that lead to misfolding, which could be inhibited by the DNA binding partner. The DNA bound native-like TDP-43^{tRRM} is more stable than free TDP-43^{tRRM} in all the pH conditions studied and is resistant to misfolding

c) ***Chapter 4*****:** In the previous chapter, we demonstrated that the DNA binding stabilizes the TDP-43^{tRRM} and maintains its monomeric native-like structure. In the final chapter, we explored an alternative conformer of TDP-43^{tRRM} in the presence of a binding partner and pH stress. The increase in the positive charge on TDP-43^{tRRM} in low pH triggers its complex coacervation in the presence of anionic DNA. The coacervates remain in equilibrium with the soluble monomeric TDP-43^{tRRM}. The phenomenon inhibits the amyloid-like misfolding of TDP-43^{tRRM}. Multiparametric analysis dictates that the electrostatic interactions and the hydrophobic interactions are the important forces behind the coacervation. Disease-associated electrostatic mutations, which increase the positive charge on TDP-43^{tRRM}, increases the coacervation tendency of TDP-43^{tRRM}. Our results conveyed that the TDP-43^{tRRM} detects stress and undergoes complex coacervation as a stress response. The coacervation prevents the amyloid-like misfolding of TDP-43^{tRRM}.

5.2 Contributions to the field

Our study has made the following significant contributions to the field:

a) Our study showed that the protonation of a critical amino acid residue drives the further assembly of TDP-43^{tRRM} in a stress environment. In this way, our study supports the hypothesis that the protonation-deprotonation equilibrium is linked to the assembly-disassembly equilibrium.
b) We have quantitatively established that TDP-43^{tRRM} destabilizes in a pH-dependent manner before undergoing misfolding, making it an important event in the amyloid-like aggregation.
c) We further studied the events which disfavor the transition of TDP-43^{tRRM} to the aggregation energy landscape. We noticed that mutation of H166 and natural binding ligand inhibits the amyloid-like aggregation of TDP-43^{tRRM} by maintaining its alternate conformers, like native-like molten globule form and monomeric form, respectively.
d) We also studied the protective role of the TDP-43^{tRRM} in stress conditions. The formation of complex coacervates in the presence of the DNA acts as a survival strategy in stressed conditions. This result supports the theory that coacervates protects the protein from amyloid-like aggregation.

e) Our study contradicts the general notion of drivers and the fate of phase separation. We conveyed that TDP-43^{tRRM}, in conjunction with nucleic acid can phase separate to less dynamic globules, thereby preventing aggregation.
f) Our results suggest that understanding the effect of different factors on the folding energy landscape should be considered in designing therapeutics for protein misfolding diseases.

5.3 Future directions

The discussed thesis work paves for the following scopes, which can be explored in the future.

a) It would be interesting to explore the changes in the protein at the molecular level in different solvation conditions. High-resolution studies on the protein structure in native, misfolded, stabilized, and phase-separated forms will provide information on the salient events administering the changes. Improved information will reflect on the discovery of novel therapeutics.
b) All these studies were performed in in-vitro conditions for simplicity and more control of the experimental conditions for a better understanding of the basic events. However, in-vivo conditions in the cellular system may vary widely, and it would be interesting to compare the results of an in-vivo system with the in-vitro system.
c) It would be exciting to explore the effect of protein stabilization (both kinetic and thermodynamic) from a therapeutic point of view.
d) Phase separation of proteins is one of the most sought-after phenomena in protein chemistry. Understanding its molecular grammar will improve our understanding of how proteins remain functional after experiencing a surfeit of environmental conditions

ABSTRACT

Name of the Student: Divya Patni **Registration No. : 10BB16A26040**
Faculty of Study: Biochemical Science **Year of Submission: 2023**
CSIR Lab: NCL, Pune **Name of the Supervisor: Dr. Santosh K. Jha**

Title of the thesis: Thermodynamic regulation of the amyloid-like aggregation of the functional domains of TDP-43

Environmental stress plays an important role in the aggregation of TDP-43, which has been the underlying cause of many neurodegenerative diseases like ALS and FTLD. Multiple studies have shown the effect of stresses on different domains of TDP-43, but what remains to be understood is how the energy landscape of the TDP-43 is modulated upon stress detection leading to the subsequent molecular level changes that form the misfolded aggregated form. In this thesis, we have probed the changes in the folding energy landscape that occur due to various factors on the functional RRM domain of TDP-43 (TDP-43^{tRRM}). We observed that low pH stress destabilizes TDP-43^{tRRM}, thereby populating the partially unfolded forms and leading to amyloid-like aggregation. We further dissected that protonation of a previously buried ionizable residue triggers the assembly of the aggregation-prone species to an amyloid-like β-sheet-rich structure. Interestingly, we identified the critical amino acid residue, H166, whose protonation was responsible for the aggregation. Inhibition of protonation by introducing a neutral amino acid, glutamine, at position 166 impedes the amyloid-like aggregation. The mutant (H166Q) forms a molten globule that remains resistant to misfolding. Additionally, we report that the DNA binding inhibits the amyloid-like aggregation of TDP-43^{tRRM} by forming a more stable soluble monomeric native-like DNA-protein complex even in low-pH stress conditions which resists aggregation. Furthermore, we report that under a certain specific set of conditions, TDP-43^{tRRM} undergoes complex coacervation in the presence of DNA to soluble native-like light phase and an insoluble protein-DNA rich dense phase (coacervates). The phenomenon prevents the aggregation of TDP-43^{tRRM}. The coacervates were spherical with rigid dynamics. Multiparametric studies suggest that the coacervates are formed as a result of favorable electrostatic and hydrophobic interactions. The interplay of these interactions determines the extent of coacervation. Therefore, competition exists between the β form, native-like light phase, and coacervates controlled by the surrounding environment. We further dissected the role of disease-relevant electrostatic mutations, P112H, and D169G, on the coacervation propensity. P112H mutation showed a substantial increase in the coacervation, while the mutant D169G behaved similarly to TDP-43^{tRRM}. Finally, we report that the coacervation is driven by multivalent interactions, which are hampered even in the presence of a minute amount of denaturant. Weakened interactions do not promote coacervation, and TDP-43^{tRRM} misfolds to an amyloid-like β form. Our study provides strong evidence to support the hypothesis that proteins can act as biosensors and undergo multiple structural changes to form metastable assemblies that can act as a precursor for amyloid-like aggregates.

List of publications

1. Prajna Mishra, **Divya Patni**, Santosh Kumar Jha, 2021. A pH-dependent protein stability switch coupled to the perturbed pKa of a single ionizable residue. Biophys Chem. 274,106591. https://doi.org/10.1016/j.bpc.2021.106591
2. **Divya Patni**, Santosh Kumar Jha, 2021. Protonation-deprotonation switch controls the amyloid-like misfolding of nucleic acid binding domains of TDP-43. J. Phys. Chem. B. 125 (30), 8383-8394. https://doi.org/10.1021/acs.jpcb.1c03262.
3. **Divya Patni**, Santosh Kumar Jha, 2023. Thermodynamic modulation of folding and aggregation landscape by DNA binding of functional of TDP-43. Biochim. Biophys. Acta-BBA Proteins Proteom. 1871 (4), 140916. https://doi.org/10.1016/j.bbapap.2023.140916.

List of posters at national/international conferences/seminars

1. Presented poster at "Biophysics Paschim" at ACTREC, Navi Mumbai. Dec 2018

Interplay of folding, unfolding and misfolding of TDP-43^{tRRM}

Aggregation of TDP-43 has been been implicated in ALS and multiple neurodegenerative diseases. Evidences gathered till now focusses on role of mutations, truncations, modifications as the major cause of disease prone behavior of TDP-43. However, not much is known about the correlation between nucleic acid binding and aggregation. We have used the tethered RNA Recognition Motifs (tRRM) to study this correlation. Using ss(TG)$_6$ as the binding partner, we have analysed the effect on aggregation upon pH change. Our results suggest that upon pH stress, tRRM domain undergo conformational changes to β sheet rich amyloid like fibril which is abolished upon DNA binding. Interestingly, in the presence of DNA, TDP-43^{tRRM} rather phase separate to tiny globules depending on protein and DNA concentration. We speculate that the driving force behind this phase transition is electrostatics and hydrophobic forces. We have also established that stability and aggregation of TDP-43^{tRRM} are related and aggregation propensity can be decreased by increasing stability. We here, have shown that ionisation of H166 is the important factor in destabilizing the protein under acidic conditions. These results shed light on

the role of tRRM domain on the aggregation of TDP-43 and here we suggest that RNA Recognition Motif also play a crucial role in aggregation and loss of nucleic acid binding ability might be a contributing factor in aggregation.

2. Presented poster at "Biophysics Paschim" at IIT, Bombay, India. August 2019

DNA binding triggers phase separation of TDP-43^{tRRM}

Aggregation of TDP-43 has been been implicated in ALS and multiple neurodegenerative diseases. Evidences gathered till now focusses on role of mutations, truncations, modifications as the major cause of disease prone behavior of TDP-43. However, not much is known about the correlation between nucleic acid binding and aggregation. We have used the tethered RNA Recognition Motifs (tRRM) to study this correlation. Using ss(TG)$_6$ as the binding partner, we have analysed the effect on aggregation upon pH change. Our results suggest that upon pH stress, tRRM domain undergo conformational changes to β sheet rich amyloid like fibril which is abolished upon DNA binding. Interestingly, in the presence of DNA, TDP-43^{tRRM} rather phase separate to tiny globules depending on protein and DNA concentration. We speculate that the driving force behind this phase transition is electrostatics and hydrophobic forces. We have also established that stability and aggregation of TDP-43^{tRRM} are related and aggregation propensity can be decreased by increasing stability. We here, speculate the protonation deprotonation of H166 might be the important factor destabilizing the protein under acidic conditions. These results shed light on the role of tRRM domain on the aggregation of TDP-43 and here we suggest that RNA Recognition Motif might also be playing a crucial role in aggregation and loss of nucleic acid binding ability might be a contributing factor in aggregation.

3. Presented poster at "FCS 2019" at TIFR-Hyderabad, India. December 2019

DNA induced phase separation of TDP-43^{tRRM}

Sequestration of protein molecules and nucleic acids to stress granules is one of the most promising strategies cells employ to protect themselves from stress. In vitro studies suggest that TDP-43^{tRRM} undergoes aggregation to misfolded β form under low pH stress-like conditions. In contrast, we observed that the ss(TG)$_6$-TDP-43^{tRRM} undergoes phase separation under pH stress to a biomolecule-rich dense phase and a large and dilute native-like light phase, separated by a

phase boundary. Generally, the IDRs have been considered the drivers of phase separation. We report that the cross interactions between the RRM domains and DNA are capable to trigger coacervation. We suggest that the coacervation is driven by cross interactions between positively charged proteins and negatively charged ss(TG)$_6$. The phase boundary decides the extent of phase separation, and it can be modulated by multiple factors like biomolecular concentration, salt, temperature, and pH. We present that phase separation is a function of the concentration of participating biomolecules and is driven by multivalent interactions, including electrostatics and hydrophobic interactions. The interplay of these forces determines the extent of phase separation. Together our results illuminate an alternate function of the RNA binding domain of TDP-43 in response to pH stress in the presence of the ss(TG)$_6$, where it could act as a stress sensor and undergo stress-triggered coacervation to save the protein from irreversible aggregation.

4. Presented poster on "National Science Day" at CSIR-NCL, India. February 2020

pH-dependent amyloid-like aggregation of nucleic acids binding domains of TDP-43, is linked to the ionization of a buried amino acid residue

Nutrient starvation stress acidifies the cytosol and leads to the formation of large protein assemblies and misfolded aggregates. However, how starvation stress is sensed at the molecular level and leads to protein misfolding is poorly understood. TDP-43 is a vital protein which, under stress-like conditions, associates with stress granule proteins via its functional nucleic acid binding domains (TDP-43^{tRRM}) and misfolds to form aberrant aggregates. Here, we show that the monomeric N form of TDP-43^{tRRM} forms a misfolded amyloid-like protein assembly, β form, in a pH-dependent manner and identified the critical protein side-chain residue whose protonation triggers its misfolding. We systematically mutated the three buried ionizable residues, D105, H166 and H256, to neutral amino acids to block the pH-dependent protonation-deprotonation titration of their side-chain and studied their effect on the N to β transition. We observed that D105A and H256Q resembled TDP-43^{tRRM} in their pH-dependent misfolding behavior. However, H166Q retains the N-like secondary structure under low pH conditions and does not show pH-dependent misfolding to the □ form. These results indicate that H166 is the critical side-chain residue whose protonation triggers the misfolding of TDP-43^{tRRM} and shed light on how stress-induced misfolding of proteins during neurodegeneration could begin from site-specific triggers.

Publications

Biophysical Chemistry 274 (2021) 106591

Contents lists available at ScienceDirect

Biophysical Chemistry

journal homepage: www.elsevier.com/locate/biophyschem

A pH-dependent protein stability switch coupled to the perturbed pKa of a single ionizable residue

Prajna Mishra [a,b,1], Divya Patni [a,b,1], Santosh Kumar Jha [a,b,*]

[a] Physical and Materials Chemistry Division, CSIR-National Chemical Laboratory, Dr. Homi Bhabha Road, Pune 411008, Maharashtra, India
[b] Academy of Scientific and Innovative Research (AcSIR), Ghaziabad 201002, India

ARTICLE INFO

Keywords:
Thermodynamic stability
Electrostatic interactions
Unfolded proteins
Fluorescence spectroscopy

ABSTRACT

The contribution of electrostatic interactions in protein stability has not been fully understood. Burial of an ionizable amino acid inside the hydrophobic protein core can affect its ionization equilibrium and shift its pKa differentially in the native (N) and unfolded (U) states of a protein and this coupling between the folding/unfolding cycle and the ionization equilibria of the ionizable residue can substantially influence the protein stability. Here, we studied the coupling of the folding/unfolding cycle with the ionization of a buried ionizable residue in a multi-domain protein, Human Serum Albumin (HSA) using fluorescence spectroscopy. A pH-dependent change in the stability of HSA was observed in the near native pH range (pH 6.0–9.0). The protonation-deprotonation equilibrium of a single thiol residue that is buried in the protein structure was identified to give rise to the pH-dependent protein stability. We quantified the pKa of the thiol residue in the N and the U states. The mean pKa of the thiol in the N state was upshifted by 0.5 units to 8.7 due to the burial of the thiol in the protein structure. Surprisingly, the mean pKa of the thiol in the U state was observed to be down-shifted by 1.3 units to 6.9. These results indicate that some charged residues are spatially proximal to the thiol group in the U state. Our results suggest that, in addition to the N state, electrostatic interactions in the U state are important determinants of protein stability.

1. Introduction

The role of electrostatics in protein function, solubility and stability has long been recognized [1–7]. The major contributors of electrostatic forces in proteins are the charged states of individual ionizable residues. More often, ionizable amino acid residues are excluded from the interior of the folded proteins because of their intrinsic incompatibility with the hydrophobic environment of the core [8–12]. However, they occasionally get buried inside the protein core to perform certain crucial biological functions [13–15]. This energetically unfavorable process of burial, where ionizable amino acids get sequestered into the less polar protein core from bulk water, allows them to experience different microenvironments, bringing a shift in their pKa. The value of pKa, which gives the information about the equilibrium between the charged and neutral state of an ionizable amino acid, can be modulated by multiple factors. Apart from the dielectric constant of the environment of the ionizable residue, coulombic interactions and hydrogen bonding with nearby polar/ionic residues can affect the pKa of the residue [16]. However, the structural adaptations to facilitate the burial of an ionizable residue inside the core and its effect on protein stability are not fully understood [17–20].

The stability of a protein is determined by the difference in the free energies of its native (N) and the unfolded (U) states. Therefore, the knowledge of the parameters that influence the stabilities of the N and the U states becomes crucial. pH, being a well-known modulator of electrostatic interaction, can affect the thermodynamic stabilities of the N and the U states in different ways. A buried ionizable amino acid can titrate differently as a function of pH in the folded and the unfolded conformations of the protein [17,19,21]. In addition, contrary to the initial notion, recent reports on the U states have emphasized on the presence of nonrandom conformers with local and long range interactions similar or different to their respective native structures [22–24]. These interactions shift the pKa of unfolded protein from its standard value. This disparity in the pKa values of the residue in the N and the U states, therefore, gives rise to a pH dependent protein stability. The site-specific measurement of the pKa values of the buried ionizable

* Corresponding author.
E-mail address: sk.jha@ncl.res.in (S.K. Jha).
[1] These authors contributed equally to this work.

https://doi.org/10.1016/j.bpc.2021.106591
Received 4 February 2021; Received in revised form 15 March 2021; Accepted 7 April 2021
Available online 20 April 2021

residue becomes essential for the detailed understanding of the thermodynamic stability of the protein.

Limited methods have been able to measure the pKa of an ionizable residue in the N and the U states of a protein reliably. Although theoretical studies have succeeded in calculating the pKa of the ionizable residues of a protein, the calculations are yet to attain the experimental accuracy [25,26]. The major complications arise in determining the molecular force field factors due to the heterogeneous environment experienced by the buried residues and generating the precise conformational unfolded state ensemble of the protein [25–27].

Experimentally pKa can be determined by studying the coupling of thermodynamics of folding and unfolding of a protein to the ionization equilibria of a buried ionizable residue (Fig. 1). For the illustration, the model protein in its N state is assumed to have an acidic amino acid (A–H) buried inside its hydrophobic core and there exists an equilibrium between the protonated / neutral and deprotonated / charged states of the acidic residue in the folded and unfolded conformations of the protein (Fig. 1). The four species in equilibrium are represented as N^P, N^D, U^P and U^D in which N and U are native and unfolded conformations, respectively, and the superscripts P and D, respectively, denote the protonated and deprotonated states of the ionizable residue. K^P_{NU} and K^D_{NU} are the equilibrium constants of the equilibrium between the folded and unfolded conformations, respectively, in their protonated and deprotonated states. K^N_a is the acid dissociation constant of $N^P \rightleftharpoons N^D$, while K^U_a are the acid dissociation constant of the equilibrium between U^P and U^D. At any pH, the standard free energy of unfolding, which is a measure of the thermodynamic stability of the protein, $\Delta G^{H_2O}_{NU}$ is given by [17]:

$$\Delta G^{H_2O}_{NU} = \Delta G^{H_2O,NE}_{NU} + \Delta G^{H_2O,pH}_{NU} \quad (1)$$

where $\Delta G^{H_2O,\ NE}_{NU}$ and $\Delta G^{H_2O,\ pH}_{NU}$ are the non-electrostatic contribution (involving folding / unfolding equilibria) and electrostatic contribution (involving protonation / deprotonation equilibria) to $\Delta G^{H_2O}_{NU}$. The

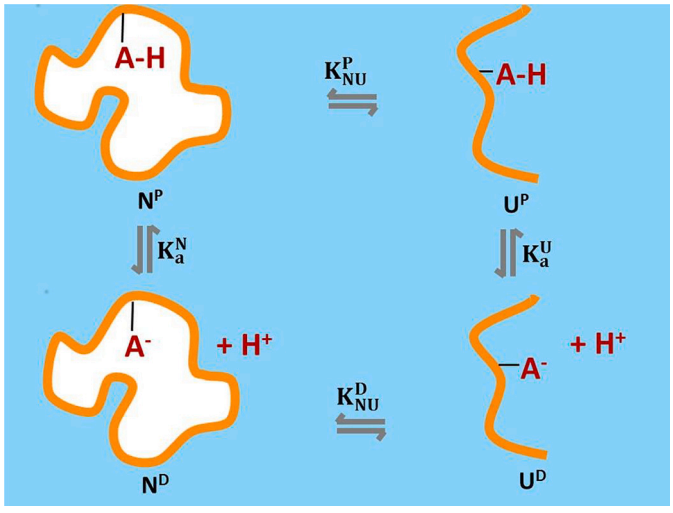

Fig. 1. The coupling of the folding / unfolding cycle of proteins with the ionization of an ionizable amino acid residue buried in the protein core. The orange lines in the figure represent the protein backbone. A-H is the protonated acidic ionizable residue in its neutral form buried inside the core (white patch) of the fully folded protein and exposed in its unfolded counterpart. A^- refers to the deprotonated / charged state of the acidic residue. N^P and U^P, respectively, refer to the folded and unfolded state of protein when the ionizable amino acid is protonated and K^P_{NU} is the equilibrium constant between them. N^D and U^D are, respectively, the folded and unfolded conformations of the protein when the ionizable amino acid is deprotonated / charged and K^D_{NU} refers to their equilibrium constant. K^N_a is the equilibrium acid dissociation constant between the charged and neutral states of the native protein. Similarly, the acid dissociation constant for the equilibrium between the charged and the neutral states of the unfolded protein is represented by K^U_a.

electrostatic contribution to the standard free energy can be calculated from the following [17]:

$$\Delta G^{H_2O,pH}_{NU} = -2.303RT\ log\left(\frac{[H^+] + K^U_a}{[H^+] + K^N_a}\right) \quad (2)$$

This thermodynamic cycle that links the equilibria between the charged and uncharged states of a protein to its folding / unfolding cycle has been implemented in various cases to determine the pKa of an ionizable residue in the N and the U states of a protein. NMR has been the method of choice for most of these studies [17,19,24,28]. Although an elegant approach, NMR can only be applied to small and soluble proteins and has limited applications for large, multi-domain and aggregation-prone proteins.

In this work, we have tried to understand the pH-dependence of stability of a multi-domain protein, human serum albumin (HSA). HSA is an all helical protein found abundantly in blood plasma and plays a distinct role in the transportation of metabolites, drugs and ions in the bloodstream and the maintenance of the pH of the plasma and extravascular fluids [29,30]. HSA maintains its native structure in the pH range of 5.0–9.0 [29,31,32]. However, it is also known to undergo several pH dependent conformational transitions. The N form of HSA converts to a fast migrating form (F) in the pH range of 5.0–3.5 followed by a transition into the acid expanded or the extended (E) form below pH 3.5 [29,31,33,34]. Above pH 9.0, the N form transforms to a basic (B) form [29,31,35]. We explored the pH dependence of the thermodynamic stability of HSA in the N state ensemble, *i.e.*, in the near neutral pH range of 6.0–9.0. This is an important pH range because the functional pH of HSA in plasma is ~7.4. The crystal structure of HSA reveals that it consists of three domains and each domain is divided into two subdomains. A cluster of hydrophobic residues holds together the three domains of HSA in its N state [32]. The sole tryptophan residue (W214) is located in the interdomain cluster (Fig. 2A). We used the fluorescence method to understand the coupling of the folding / unfolding cycle of HSA with the ionization of the ionizable residues. We show that the pH dependent changes in the stability of HSA in the pH range of 6.0–9.0 are due to perturbed ionization of a single thiol group (C34). C34 is known to impart antioxidant properties to HSA as its reduced form is highly abundant in blood plasma [36–38]. This makes C34 an important target for reactive oxidizing species [37] and the determination of its pKa in the N and the U states of the protein becomes crucial considering its redox potential. We calculated the pKa of C34 in the N and the U states. Our results show that the pKa of the thiol is also perturbed in the U state in addition to the N state indicating that the charged interactions in the U state are also important for the thermodynamic stability of the proteins.

2. Materials and methods

2.1. Spectroscopic methods and instruments

Fluorescence experiments were performed on Fluoromax-4 spectrofluorometer from HORIBA Scientific, while absorption studies were done using UV 3200 spectrophotometer procured from LABINDIA Analytical. Quartz cuvettes of path length of 1 cm were used for signal acquisition for both fluorescence and absorption studies. Circular Dichroism (CD) studies were performed on Jasco J-815 CD spectrometer. For far-UV CD experiments, cuvettes of path lengths 1 mm were used. An Abbe refractometer from Rajdhani Scientific Instruments Co. (model: RSR-2) was used to calculate the denaturant concentration by measuring the refractive index [39].

2.2. Chemicals and buffers

HSA (99% pure, fatty acid and globulin free) and urea (ultrapure grade) were sourced from Alfa Aesar. 5-((((2-Iodoacetyl)amino)ethyl)

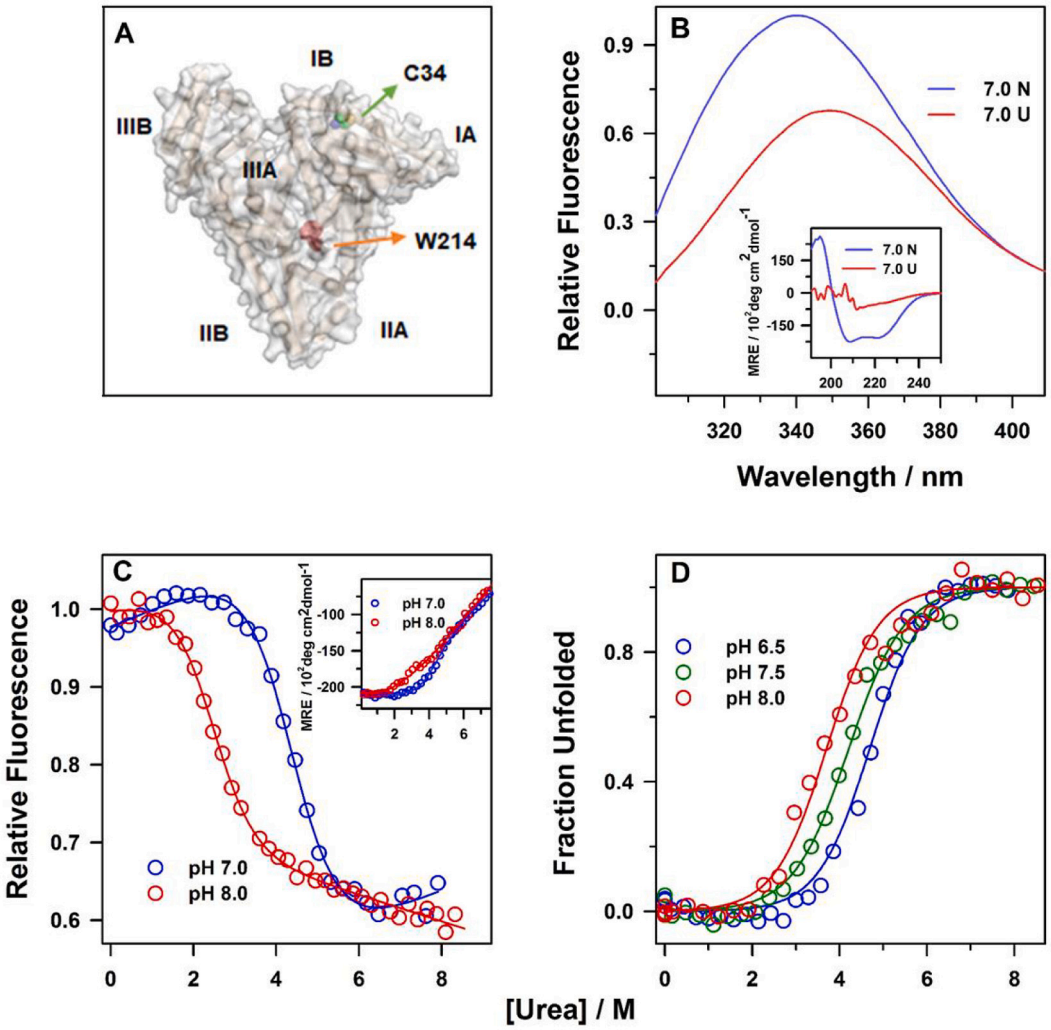

Fig. 2. The thermodynamic stability of HSA is pH dependent. (A) Structure of HSA, depicting its six sub-domains and the locations of free cysteine residue (C34) and single tryptophan residue (W214). This image was drawn from the pdb file 1AO6 using the PyMol Molecular Graphics System, Version 2.0 Schrodinger, LLC. (B) Fluorescence emission spectra of W214 in the native (N) and unfolded (U) states of HSA at pH 7.0. The inset of panel B shows the change in the mean residue ellipticity (MRE) of HSA in the N and U states at pH 7.0 in the far-UV region. (C) Urea induced equilibrium unfolding transitions of HSA at pH 7.0 and pH 8.0 as monitored by the changes in the fluorescence signal of W214 at 340 nm and change in the MRE at 222 nm (inset). (D) The fractions of the unfolded protein at pH 6.5, pH 7.5 and pH 8.5 are plotted as a function of the [urea]. The solid lines through the data in panel C, inset of panel C and panel D are fits to a two-state, N⇌U model (Eqs. (3) and (5), Section 2.5). The plots in Fig. 2C, C inset and 2D are representative plots of one set of experiments.

amino)naphthalene-1-sulfonic acid (1,5-IAEDANS) was purchased from Life Technologies. All other chemicals of the highest purity grade were purchased from HiMedia and used directly without further purification. HSA concentration was measured using an extinction coefficient of 36,500 M^{-1} cm^{-1} by measuring absorbance at 280 nm [40]. For all the pH titration studies, native buffers consisted of 20 mM MES, 20 mM phosphate and 20 mM Tris-HCl for pH 6.0, pH 6.5 - pH 7.5 and pH 8.0 – pH 9.0, respectively. The unfolding buffers constituted of 9 M urea in their respective native buffer.

2.3. 1,5-IAEDANS labeled HSA preparation

We followed the previously reported protocol for the site-specific covalent labeling of HSA [32]. In brief, 20 fold molar excess of 1,5-IAEDANS was added to HSA, which was previously unfolded in 6 M Guanidine Hydrochloride (GdmCl) and 20 mM Tris-HCl at pH 8.0. The reaction mixture was stirred for 4 h in the dark followed by refolding in 15 fold volume excess of 20 mM phosphate buffer at pH 7.0 with an overnight incubation at 4 °C. Refolded protein was then concentrated by centrifugal concentrator (GE healthcare, molecular weight cutoff-30 kDa) to 2.5 mL. To remove the remaining unbound dye and GdmCl, the concentrated reaction mixture was passed through a PD-10 desalting column (GE healthcare). The percentage of labeling in the labeled protein (HSA-IAEDANS) was estimated as discussed previously [32] and was observed to be >95%.

2.4. Fluorescence and CD experiments

For fluorescence experiments, the protein concentration used was 4–6 μM. In HSA and HSA-IAEDANS, W214 was excited at 295 nm and the emission spectra were collected from 310 nm – 550 nm. 1,5-IAEDANS attached to the C34 (C34-IAEDANS) was excited at 337 nm. The excitation slit widths for all the fluorescence experiments were kept between 1.0 nm to 1.5 nm, while the emission slit widths used were in the range of 8–12 nm.

For far-UV CD measurements, 3–4 μM of protein concentrations were used. Scans were collected from 190 nm - 250 nm. The data pitch, data integration time, scan speed and bandwidth were kept at 1 nm, 1 s, 50

nm/min and 2 nm, respectively, for all the experiments. Background signal corrections have been done for all the CD and fluorescence experiments by subtracting the buffer signal.

2.5. Urea induced equilibrium unfolding experiments

For urea induced equilibrium unfolding experiments, protein samples (HSA and HSA-IAEDANS) were subjected to a gradient of urea concentration and incubated for 3 h at room temperature in the pH range of 6.0–9.0. For fluorescence measured experiments, W214 and C34-IAEDANS were excited at 295 nm and 337 nm, respectively, and equilibrium unfolding was measured by the change in respective fluorescence signal at 340 nm and 469 nm, respectively. For far-UV CD measured equilibrium unfolding experiments, the signals were measured at 222 nm. The data were fitted to the following equation based on a two state, N⇌U model [32,41].

$$y_{obs} = \frac{y_N + y_U\, e^{\frac{-\Delta G_{NU}}{RT}}}{1 + e^{\frac{-\Delta G_{NU}}{RT}}} \quad (3)$$

In the above equation, y_{obs} is the observed fluorescence / CD signal; y_N and y_U are the signals of the N and the U states, respectively; ΔG_{NU} is the free energy of unfolding of N⇌U, which has a linear dependency on denaturant concentration and is given by:

$$\Delta G_{NU} = \Delta G_{NU}^{H_2O} + m_{NU}[D] \quad (4)$$

where $\Delta G_{NU}^{H_2O}$ is the standard free energy of unfolding in 0 M urea and m_{NU} is the slope of the N⇌U transition.

The fractions of unfolded states, f_U, at any particular denaturant concentration were determined as per the equation mentioned below:

$$f_U = \frac{e^{\frac{-\Delta G_{NU}}{RT}}}{1 + e^{\frac{-\Delta G_{NU}}{RT}}} \quad (5)$$

All the urea induced denaturation experiments shown in Figs. 2C, D, 3C and D were repeated two or more times. The error in thermodynamic parameters shown in Figs. 4 and 5 were determined from the spread of two or more independent measurements.

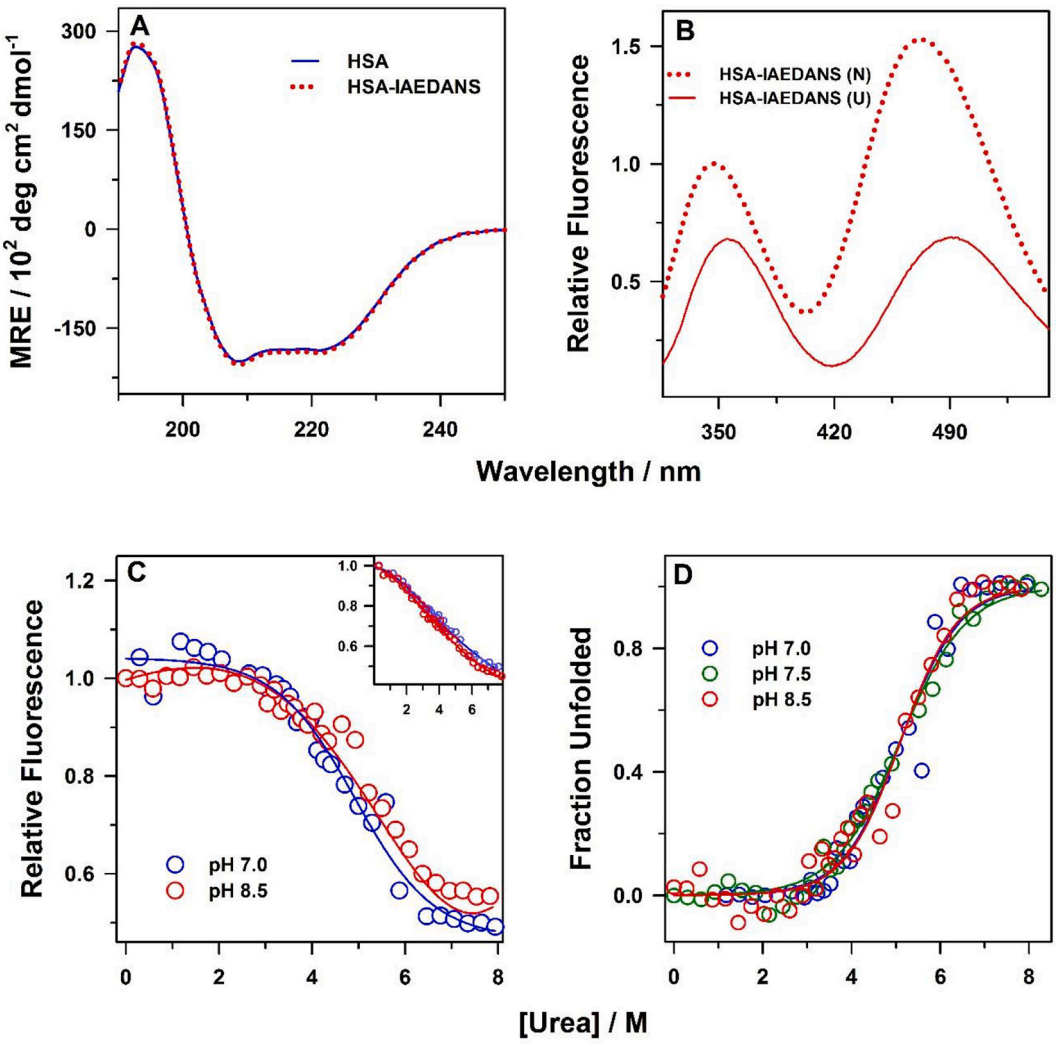

Fig. 3. The thermodynamic stability of HSA-IAEDANS is independent of pH. (A) far-UV CD spectra of HSA and HSA-IAEDANS at pH 7.0 as a measure of their global secondary structure content are shown in panel A. (B) Fluorescence emission spectra of W214 and C34-IAEDANS, when excited at 295 nm, in the N and the U states of HSA-IAEDANS at pH 7.0 are shown. (C) Urea induced equilibrium unfolding transitions of HSA-IAEDANS as monitored by the change in W214 fluorescence at 340 nm at pH 7.0 and pH 8.5. The inset shows the pH dependence of the urea induced equilibrium unfolding transitions as monitored by the change in fluorescence signal of C34-IAEDANS at 469 nm at pH 7.0 and pH 8.5. (D) The fractions of unfolded protein were plotted as a function of [urea] at pH 7.0, pH 7.5 and pH 8.5. The solid lines through the data in panel C, inset of panel C and panel D are fit to a two-state, N⇌U model. In the Fig. 3C, C inset and 3D, representative plots of one set of experiments are shown.

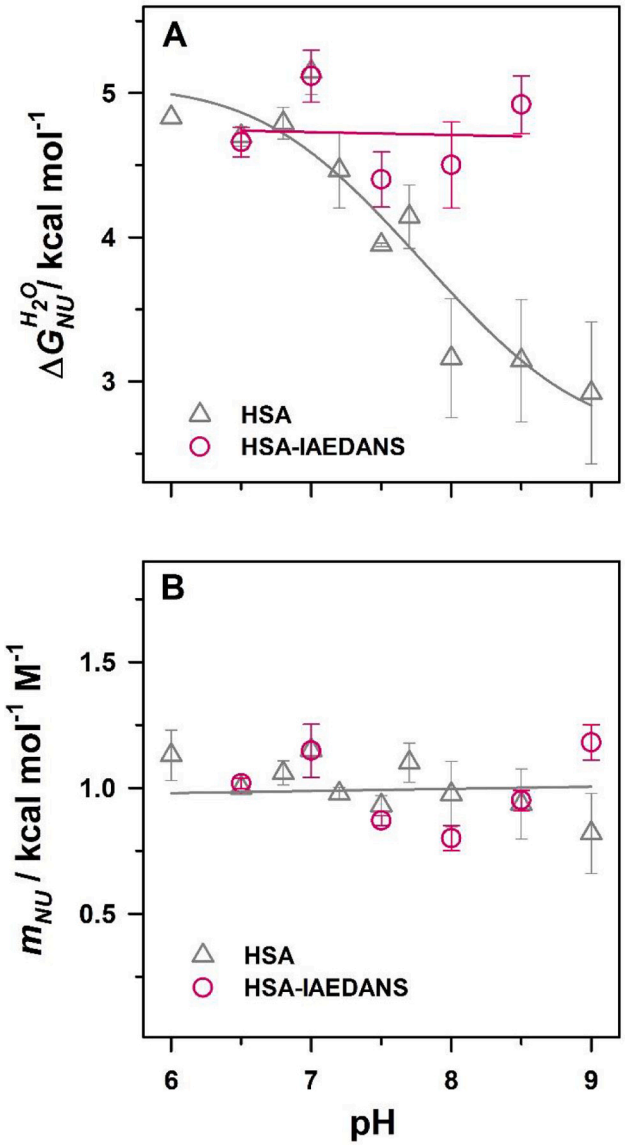

Fig. 4. pH dependence of the thermodynamic parameters. (A) Changes in the standard free energy of unfolding ($\Delta G_{NU}^{H_2O}$) of HSA and HSA-IAEDANS as a function of pH. The solid line through the data of HSA is a least-square fit to Eq. (6), while that of HSA-IAEDANS was drawn to guide the eye. (B) Dependence of change in solvent exposed surface area (m_{NU}) during N⇌U transition of HSA and HSA-IAEDANS with respect to pH. Error bars shown in panel A and panel B represent the spread for at least 2 or more independent sets of experiments.

2.6. Analysis of titration of thermodynamic parameters as a function of pH

Assuming that the single titratable group (C34) in HSA has different pKa values in the native (pK_a^N) and the unfolded states (pK_a^U), the dependency of the free energy of unfolding, $\Delta G_{NU}^{H_2O}$ on pH was analyzed using the following equation [17,20]:

$$\Delta G_{NU}^{H_2O} = \Delta G_{NU}^{H_2O,NE} - 2.303RT\ log\left(\frac{1+10^{pK_a^U-pH}}{1+10^{pK_a^N-pH}}\right) \quad (6)$$

The above equation is a combined and modified form of Eqs. (1) and (2) (see Section 1).

3. Results and discussion

3.1. The N and U states of HSA have distinct spectroscopic properties

We first compared the fluorescence signal of W214 in the N and the U states of HSA at pH 7.0 and we observed that the signal from the U state was highly quenched and the wavelength of the maximum fluorescence emission (λ_{max}^{em}) in the U state (349 nm) was red shifted as compared to the N state (340 nm), pertaining to the hydration of W214, which lead to the quenching of its fluorescence (Fig. 2B). Similarly, the global secondary structure content of HSA in the N and U states were distinctly different, as revealed by the far-UV CD spectra with the global secondary structure being entirely lost in the U state (Fig. 2B, inset). The mean residual ellipticity (MRE) at 222 nm for the N and the U states of HSA were −18,690 and −4868 deg. cm^2 dmol^{-1}, respectively. All these results conveyed that the N and the U states of HSA have distinct spectroscopic properties.

3.2. The thermodynamic stability of HSA is pH dependent

We utilized the difference in spectroscopic properties of the N and the U states of HSA to monitor their equilibrium population distribution as a function of urea concentration and the thermodynamic stability of HSA over a range of pH (pH 6.0 – pH 9.0). We first used W214 fluorescence as a measure of structure loss upon unfolding during the N⇌U transition. Urea induced single sigmoidal equilibrium unfolding curves for HSA were obtained in the pH range of 6.0 – 9.0. Two representative plots at pH 7.0 and pH 8.0 are shown in Fig. 2C. We observed that the midpoint of the N⇌U transition (C_m) changed as a function of pH in the pH range of 7.0 – 8.0. We further compared the thermodynamic stability of the secondary structure of HSA as measured by far-UV CD at pH 7.0 and pH 8.0 (Fig. 2C, inset). The slopy nature of the unfolded baseline in the equilibrium unfolding experiments monitored by far-UV CD limited the correct estimation of the thermodynamic parameters. Nevertheless, we observed that, at pH 7.0, the loss of the protein secondary structure was initiated ~3 M [urea] and C_m was ~4.5 M [urea]. However, at pH 8.0, the unfolding of HSA started ~1.5 M [urea] and the observed C_m was ~3 M [urea]. These results were in very well correspondence with the W214 fluorescence measured unfolding transitions (Fig. 2C). W214 fluorescence is also a measure of the change in the tertiary structure. These results suggested that the global secondary and tertiary structure of the protein dissolved similarly during urea induced unfolding studies. The unfolding curves as measured by W214 fluorescence were converted into fractions of unfolded protein and were analyzed using a two-state N⇌U model (Fig. 2D, Section 2.5). The mean value of standard free energy of unfolding of the N⇌U transition,$\Delta G_{NU}^{H_2O}$, at pH 6.5 was 4.8 kcal mol^{-1}, at pH 7.5 was 4.0 kcal mol^{-1} and at pH 8.0 was 3.1 kcal mol^{-1}. The mean value of the change in the solvent accessible surface area (m_{NU}), as measured by the slope of the N⇌U transition, was 1.00 kcal mol^{-1} M^{-1} at pH 6.5, 0.94 kcal mol^{-1} M^{-1} at pH 7.5 and 0.98 kcal mol^{-1} M^{-1} at pH 8.0. These results show that the thermodynamic stability of HSA is dependent on pH and decreases upon increasing the pH above 6.5. However, the value of m_{NU} remains unperturbed.

3.3. C34-IAEDANS is buried in the protein core

Since pH is a well-known modulator of the structure of proteins and, by extension, their thermodynamic stabilities [33,35,42], it can be argued that the observed dependence of thermodynamic stability of HSA on pH was due to the change in its structural properties. However, it has been previously reported that HSA conserves its N-like structure in the pH range of 4.8 to 8.5 [29,31–33]. The similar values of m_{NU} at all the pH (Fig. 2D), which measures the change in solvent exposed surface area, also indicated that the pH dependence of the stability was not due to a structural change. The other possibility for the destabilization of protein in the pH range of 7.0 to 8.0 could be due to the titration of a

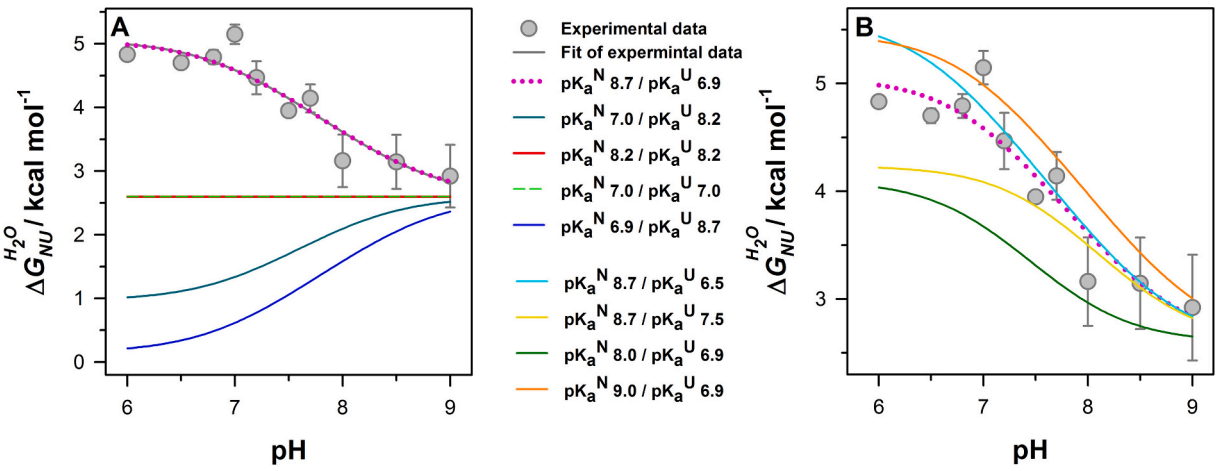

Fig. 5. The pKa of C34 in the N state is upshifted, while in the U state, it is downshifted with respect to a free thiol group. (A) The simulated $\Delta G_{NU}^{H_2O}$*versus* pH curves when i) $pK_a^U = 6.9$ and $pK_a^N = 8.7$ (pink dotted line) and hence are equal to the experimental value (gray filled circles); ii) $pK_a^U = pK_a^N$ (red line and green dashed line); and iii) $pK_a^U > pK_a^N$(blue line and dark cyan dashed line). (B) Comparison of simulated $\Delta G_{NU}^{H_2O}$*versus* pH curves by keeping pK_a^Nconstant while varying pK_a^U and *vice versa.* All the curves were simulated using Eq. (6). (For interpretation of the references to colour in this figure legend, the reader is referred to the web version of this article.)

buried ionizable amino acid residue inside the core of the protein. Since free cysteine has a pKa ~8.2 and upon burial inside a hydrophobic core, its pKa is likely to get modulated, we hypothesized that the titration of a buried cysteine might be leading to the protein destabilization in this pH range. HSA has 35 cysteines, out of which 34 forms disulfide linkages in the protein. The sole free cysteine, C34, has its side chain buried in the hydrophobic core of protein (Fig. 2A) [43]. The titration of the protonation-deprotonation equilibrium of cysteine could be blocked in two ways: i) by site-directed mutation of C34 to a non-ionizable residue and ii) test-tube engineering in which C34 is covalently labeled with a molecule that prohibits its ionization. As we had successfully labeled the C34 and performed multiple experiments with labeled HSA, previously [32,33,35,43], we opted for the second alternative. To block its titration with pH, we labeled C34 with a fluorophore 1,5-IAEDANS (C34-IAEDANS) (Section 2.3). It is important to confirm that labeling does not alter the conformational properties of the protein. We compared the global secondary structural difference between the unlabeled HSA and the labeled HSA (HSA-IAEDANS) by far-UV CD (Fig. 3A). The MRE for HSA and HSA-IAEDANS at 222 nm were −18,690 deg. cm^2 dmol^{-1} and −18,282 deg. cm^2 dmol^{-1}, respectively, which implied that the labeling of HSA did not perturb its secondary structural content. We further compared the tertiary structural difference of HSA and HSA-IAEDANS as measured by W214 fluorescence and we observed that λ_{max}^{em} in the N and the U states of HSA did not change upon labeling (Fig. 2B, Fig. 3B). In previous global tertiary structural studies, low values of MRE at 261 nm in the N state (−121 ± 3 deg. cm^2 dmol^{-1}) was observed which was marginally higher than the MRE value of the U state (−72 ± 10 deg. cm^2 dmol^{-1}) [43]. This result conveyed that the global tertiary structure of HSA is flexible and loosely packed. So it is not surprising that the loose packing of the N state of HSA is being able to accommodate 1,5-IAEDANS without disrupting its conformation. In our earlier studies, we have shown that W214 and C34-IAEDANS form a FRET pair [32,33,35]. Upon excitation of W214 (Donor) at 295 nm, the fluorescence of C34-IAEDANS (Acceptor) increased significantly in the N state with a λ_{max}^{em} of 469 nm due to FRET as compared to the U state (λ_{max}^{em} of 483 nm) (Fig. 3B). The differences in the fluorescence intensity and λ_{max}^{em} in the N and U states of HSA-IAEDANS implied that the N and the U states have characteristic spectroscopic properties and C34-IAEDANS is buried in the core of the protein in the N state.

3.4. Thermodynamic stability of HSA-IAEDANS does not change with pH

In order to investigate the dependence of the thermodynamic stability of HSA-IAEDANS on pH, we performed the urea induced equilibrium unfolding experiments on HSA-IAEDANS in the pH range of 6.0 – 9.0. We first monitored the W214 fluorescence as a function of [urea] at different pH and observed that the sigmoidal curves at 340 nm for the N⇌U transition perfectly overlapped on each other (Fig. 3C). We also checked C34-IAEDANS fluorescence to compare the thermodynamic stability of HSA-IAEDANS (Fig. 3C, inset). The equilibrium values at 469 nm showed a gradual and non-cooperative dependence on [urea] which limited the correct estimation of the thermodynamic parameters. This observation could be due to the high fluorescence sensitivity of C34-IAEDANS. Nevertheless, the C_m values obtained from W214 and C34-IAEDANS fluorescence measurement studies in the pH range of 6.0 – 9.0 were analogous. We converted the unfolding curves of HSA-IAEDANS acquired from W214 fluorescence measurements to fractions of unfolded protein (Fig. 3D) and analyzed them using a two-state N⇌U model. The obtained thermodynamic parameters, both $\Delta G_{NU}^{H_2O}$ and m_{NU} were strikingly similar in the pH range of 6.0–9.0. All these results suggested that the thermodynamic stability of HSA-IAEDANS was pH independent.

3.5. Titration of C34 was responsible for the destabilization of HSA in the pH range of 6.0–9.0

We compared the change in thermodynamic parameters, $\Delta G_{NU}^{H_2O}$ and m_{NU}, governing the denaturation of HSA and HSA-IAEDANS as a function of pH (Fig. 4A and B). Fig. 4A shows that the dependency of $\Delta G_{NU}^{H_2O}$ on pH in HSA was sigmoidal, while in HSA-IAEDANS, this dependency was abolished. Above pH 6.0, the thermodynamic stability of HSA decreased in a sigmoidal manner and plateaued near pH 8.5 to pH 9.0. The m_{NU} values for HSA and HSA-IAEDANS did not change with pH (Fig. 4B). All the above results clearly conveyed that the titration of buried C34 was responsible for the pH dependency of $\Delta G_{NU}^{H_2O}$ of HSA. We fitted the pH dependency of $\Delta G_{NU}^{H_2O}$ of HSA (Fig. 4A) to Eq. (6) to obtain the pKa values of C34 in the N and the U states (Section 2.6). For a cysteine residue buried in the protein core, an increase in its pKa value is expected. For the U state, the anticipated pKa was similar to that of free cysteine in water (8.2). The pKa value obtained for the buried C34 in the N state was 8.7 ± 0.5. Interestingly, in the open U state, the pKa value of C34 was 6.9 ± 0.3.

The observed decrease in the mean pKa of the C34 in the U state by 1.3 units was quite significant which could be due to the presence of electrostatic interactions near C34 in the U state. However, it is important to confirm that the observed pKa of the thiol group in the N and the U states were not an artifact of the fitting errors. In order to gauge the reliability of the values of pK_a^N and pK_a^U obtained from the fit, we simulated and compared the graphs of $\Delta G_{NU}^{H_2O}$ as a function of pH for different values of pK_a^N and pK_a^U, using Eq. (6) (Fig. 5). Fig. 5A shows that when $pK_a^N = pK_a^U$, no pH-dependent change in the values of $\Delta G_{NU}^{H_2O}$ will be observed. Fig. 5A also shows that when $pK_a^N < pK_a^U$, the value of values of $\Delta G_{NU}^{H_2O}$ will increase with pH and not decrease, as observed experimentally. Hence, for the experimentally observed dependence of $\Delta G_{NU}^{H_2O}$ on pH, pK_a^N must be greater than pK_a^U. Fig. 5A shows that for the values of $pK_a^N = 8.7$ and $pK_a^U = 6.9$, the simulated curve fits the experimental data very well.

We further checked the robustness of the observed values of pK_a^U and pK_a^N by simulating $\Delta G_{NU}^{H_2O}$*versus* pH plots, keeping one parameter constant and varying the other by about ±0.5 pH units (Fig. 5B). The generated $\Delta G_{NU}^{H_2O}$*versus* pH curves markedly deviated from the experimental data (Fig. 5B). Collectively these results confirmed that the experimentally obtained values of pK_a^U and pK_a^N of C34 were quite reliable.

3.6. The electrostatic interactions in both the N and the U states are important for the thermodynamic stability of proteins

Our results show that the protonation-deprotonation equilibrium of a single ionizable residue, C34, modulates the thermodynamic stability of HSA in the near neutral pH range of 6.0 – 9.0 (Fig. 4). This result is significant considering the vital role HSA plays in maintaining the pH of the blood plasma, extravascular fluids and ascitic fluid [30]. In the crystal structure of HSA, ~99% of the total surface area of C34 is buried inside the core of domain I of HSA in the N state and is solvated by the side-chains of 12 amino acid residues out of which 2 basic residues (H39 and R144), 1 acidic residue (D38) and 3 polar residues (Q33, Y84 and Y140) directly affect the pKa of C34 [43]. The interactions of C34 with H39 and R144 will be stabilizing and will lead to a decrease in its pKa; whereas, D38 will destabilize and increase the pKa of C34. The observed pKa of C34 in the N state of HSA could be a combination of its burial as well as its interactions with adjacent acidic/basic amino acid residues. Such observations have been previously reported for other proteins [18–20,44]. For HSA, the pKa of C34 in the N state of the protein have been reported to range from 8.0–9.0 depending upon the methodologies and experimental conditions used (buffer, ionic strength, temperature *etc.*) [45–47]. The estimated pKa of C34 in the N state of HSA from our study, in its error range (8.7 ± 0.5), is in good agreement with the previously reported pKa values.

Another significant result from the present study is that the mean pKa of the C34 in the U state is ~1.3 unit less than the expected pKa of thiol in water (~8.2). We conjectured this could be due to the presence of some polar residues in the primary sequence of HSA near C34, thereby reducing its pKa. Assuming the U state to be completely unfolded and random coil-like structure, we checked for the adjacent amino acid residues of C34 in the sequence. The pentapeptide segment of HSA containing C34 in the middle has other residues as Q32, Q33, P35 and F36. These residues, being neutral in nature, are unlikely to affect the pKa of C34. The only other possibility is that there exists some residual structure in the U state in which some charged residues are interacting with C34, thereby, lowering its pKa. It is important to note that the m_{NU} value of a large protein like HSA is only ~1 kcal mol^{-1} M^{-1} (Fig. 4B). This result indicates that only a small amount of the buried surface area is exposed to solvent upon unfolding and there exist substantial residual structure in the U state. It appears that the residual structure brings one or more charged residue in the spatial proximity of C34 and hence decreasing its pKa. Multiple reports have demonstrated the presence of both favorable and unfavorable electrostatic interactions in the U states of proteins largely affecting their energetics [22–24,48–51].

The thermodynamic stability of proteins is a difference in the free energy of their N and the U states. Therefore, understanding the thermodynamic and structural properties of the U state is also essential in addition to that of the N state for decoding the factors that govern the stability of proteins. Generally, the free energy of the U state is considered zero and the difference between the free energies of the N and the U states is taken as the thermodynamic stability of the N state. However, our observations that the pH-dependent thermodynamic stability of HSA is controlled by the perturbed pKa of a single ionizable group in the N state and the U state and that in the U state, the ionizable residue participates in electrostatic interactions indicate that the electrostatics of the U state is also an important determinant of protein stability.

The findings of this study also point towards the significant contribution of interdomain coupling to the thermodynamic stability of HSA. In this study, the far-UV CD monitored unfolding experiments at pH 7 and pH 8 suggested that the global secondary structure of HSA changed differently as a function of urea concentration at two different pH conditions. The C_m of the far-UV monitored transition was observed to be in very well correspondence with that of the W214 fluorescence monitored transitions. It is important to note that W214 is placed at the interdomain region of the protein and reports about the site-specific structural change of that region. Excitingly, the observation that the abolition of the titration of C34 (which is placed in the core of domain I) is eliminating the pH dependence of the stability of HSA as monitored by W214 fluorescence (at the interdomain region) shows that the protein stability is coupled to the interdomain coupling. In one of our previous studies, we have observed that in the E form of HSA at low pH, domain III was fully unfolded while domain I and II were expanded but retained N-like secondary structures [33]. Interestingly, the thermodynamic stabilities of the protein in its E form as estimated from the changes in W214 fluorescence and far-UV CD were in very well agreement. Both these studies highlight the importance of interdomain coupling in protein stability.

4. Conclusion

In this study, we have explored the pH dependence of the thermodynamic stability of the human serum protein, HSA. We used fluorescence spectroscopy to understand the coupling of folding/unfolding of the protein with the ionization of the ionizable residues. We observed that the thermodynamic stability of HSA was pH dependent and changed in a sigmoidal fashion in the near neutral pH range (pH 6.0 – 9.0). In order to understand the cause of this dependency, we labeled a buried ionizable residue C34 with a dye, 1,5-IAEDANS and blocked its titration due to pH. The thermodynamic stability of the labeled protein became pH independent. These results conveyed that the pH dependent changes in the stability of HSA were due to the aberrant titration of the single thiol group. We calculated the pKa of the thiol in the N and U states. In the N state, the mean value of the calculated pKa was ~0.5 unit higher than that of the free cysteine in water, whereas, in the U state, there was a significant decrease in the pKa of C34 (by ~1.3 unit). The pKa in the N state could be attributed to the burial of the ionizable thiol group inside the hydrophobic core and its interactions with multiple nearby polar/ionizable residues. However, the perturbation of the pKa of the thiol in the U state indicated some local electrostatic interactions near C34 in the U state. These results together suggest that the electrostatic interactions regulate the ionization equilibrium of the ionizable residues and therefore affect their pKa values. The knowledge of pKa of these residues in both the N and the U states is essential in understanding the pH dependence of the thermodynamic stability of proteins.

Declaration of Competing Interest

The authors declare that they have no known competing financial interests or personal relationships that could have appeared to influence

the work reported in this paper.

Acknowledgments

We thank Minnu M. Lal for helping in some of the equilibrium unfolding experiments. This work was funded by SERB-DST core research grant (project CRG/2019/002922) to S.K.J. P.M. is a recipient of the Senior Research Fellowship by University Grants Commission, India. D.P. is a recipient of the Senior Research Fellowship by the Council of Scientific and Industrial Research, India.

References

[1] C. Tanford, Protein denaturation. C. Theoretical models for the mechanism of denaturation, Adv. Protein Chem. 24 (1970) 1–95.
[2] J.B. Matthew, Electrostatic effects in proteins, Annu. Rev. Biophys. Biophys. Chem. 14 (1985) 387–417.
[3] N.M. Allewell, H. Oberoi, Electrostatic effects in protein folding, stability, and function, Methods Enzymol. 202 (1991) 3–19.
[4] C.N. Pace, Polar group burial contributes more to protein stability than nonpolar group burial, Biochemistry 40 (2001) 310–313.
[5] S. Kumar, R. Nussinov, Close-range electrostatic interactions in proteins, Chembiochem 3 (2002) 604–617.
[6] K. Takano, J.M. Scholtz, J.C. Sacchettini, C.N. Pace, The contribution of polar group burial to protein stability is strongly context-dependent, J. Biol. Chem. 278 (2003) 31790–31795.
[7] G.I. Makhatadze, V.V. Loladze, D.N. Ermolenko, X. Chen, S.T. Thomas, Contribution of surface salt bridges to protein stability: guidelines for protein engineering, J. Mol. Biol. 327 (2003) 1135–1148.
[8] G.D. Rose, A.R. Geselowitz, G.J. Lesser, R.H. Lee, M.H. Zehfus, Hydrophobicity of amino acid residues in globular proteins, Science 229 (1985) 834–838.
[9] S. Miller, J. Janin, A.M. Lesk, C. Chothia, Interior and surface of monomeric proteins, J. Mol. Biol. 196 (1987) 641–656.
[10] K.A. Dill, Dominant forces in protein folding, Biochemistry 29 (1990) 7133–7155.
[11] G.J. Lesser, G.D. Rose, Hydrophobicity of amino acid subgroups in proteins, Proteins 8 (1990) 6–13.
[12] L. Lins, A. Thomas, R. Brasseur, Analysis of accessible surface of residues in proteins, Protein Sci. 12 (2003) 1406–1417.
[13] S. Iwata, C. Ostermeier, B. Ludwig, H. Michel, Structure at 2.8 a resolution of cytochrome c oxidase from Paracoccus denitrificans, Nature 376 (1995) 660–669.
[14] H. Luecke, H.T. Richter, J.K. Lanyi, Proton transfer pathways in bacteriorhodopsin at 2.3 angstrom resolution, Science 280 (1998) 1934–1937.
[15] Y. Jiang, A. Lee, J. Chen, V. Ruta, M. Cadene, B.T. Chait, R. MacKinnon, X-ray structure of a voltage-dependent K+ channel, Nature 423 (2003) 33–41.
[16] C.N. Pace, G.R. Grimsley, J.M. Scholtz, Protein ionizable groups: pK values and their contribution to protein stability and solubility, J. Biol. Chem. 284 (2009) 13285–13289.
[17] M. Tollinger, K.A. Crowhurst, L.E. Kay, J.D. Forman-Kay, Site-specific contributions to the pH dependence of protein stability, Proc. Natl. Acad. Sci. U. S. A. 100 (2003) 4545–4550.
[18] D.G. Isom, C.A. Castaneda, B.R. Cannon, P.D. Velu, E.B. Garcia-Moreno, Charges in the hydrophobic interior of proteins, Proc. Natl. Acad. Sci. U. S. A. 107 (2010) 16096–16100.
[19] D.G. Isom, C.A. Castaneda, B.R. Cannon, B. Garcia-Moreno, Large shifts in pKa values of lysine residues buried inside a protein, Proc. Natl. Acad. Sci. U. S. A. 108 (2011) 5260–5265.
[20] N. Aghera, I. Dasgupta, J.B. Udgaonkar, A buried ionizable residue destabilizes the native state and the transition state in the folding of monellin, Biochemistry 51 (2012) 9058–9066.
[21] C.A. Fitch, S.T. Whitten, V.J. Hilser, E.B. Garcia-Moreno, Molecular mechanisms of pH-driven conformational transitions of proteins: insights from continuum electrostatics calculations of acid unfolding, Proteins 63 (2006) 113–126.
[22] S.T. Whitten, E.B. Garcia-Moreno, pH dependence of stability of staphylococcal nuclease: evidence of substantial electrostatic interactions in the denatured state, Biochemistry 39 (2000) 14292–14304.
[23] C.N. Pace, R.W. Alston, K.L. Shaw, Charge-charge interactions influence the denatured state ensemble and contribute to protein stability, Protein Sci. 9 (2000) 1395–1398.
[24] S. Lindman, M.C. Bauer, M. Lund, C. Diehl, F.A. Mulder, M. Akke, S. Linse, pK(a) values for the unfolded state under native conditions explain the pH-dependent stability of PGB1, Biophys. J. 99 (2010) 3365–3373.
[25] A.S. Yang, B. Honig, On the pH dependence of protein stability, J. Mol. Biol. 231 (1993) 459–474.
[26] J. Makowska, K. Baginska, A. Liwo, L. Chmurzynski, H.A. Scheraga, Acidic-basic properties of three alanine-based peptides containing acidic and basic side chains: comparison between theory and experiment, Biopolymers 90 (2008) 724–732.
[27] C.N. Schutz, A. Warshel, What are the dielectric "constants" of proteins and how to validate electrostatic models? Proteins 44 (2001) 400–417.
[28] D.L. Luisi, C.D. Snow, J.J. Lin, Z.S. Hendsch, B. Tidor, D.P. Raleigh, Surface salt bridges, double-mutant cycles, and protein stability: an experimental and computational analysis of the interaction of the Asp 23 side chain with the N-terminus of the N-terminal domain of the ribosomal protein l9, Biochemistry 42 (2003) 7050–7060.
[29] D.C. Carter, J.X. Ho, Structure of serum albumin, Adv. Protein Chem. 45 (1994) 153–203.
[30] T.U. Peters, All About Albumin: Biochemistry, Genetics, and Medical Applications, Academic Press, 1996.
[31] M. Dockal, D.C. Carter, F. Ruker, Conformational transitions of the three recombinant domains of human serum albumin depending on pH, J. Biol. Chem. 275 (2000) 3042–3050.
[32] P. Mishra, S.K. Jha, An alternatively packed dry molten globule-like intermediate in the native state ensemble of a multidomain protein, J. Phys. Chem. B 121 (2017) 9336–9347.
[33] N. Acharya, P. Mishra, S.K. Jha, Evidence for dry molten globule-like domains in the pH-induced equilibrium folding intermediate of a multidomain protein, J. Phys. Chem. Lett. 7 (2016) 173–179.
[34] J.R. Olivieri, A.F. Craievich, The subdomain structure of human serum albumin in solution under different pH conditions studied by small angle X-ray scattering, Eur. Biophys. J. 24 (1995) 77–84.
[35] N. Acharya, P. Mishra, S.K. Jha, A dry molten globule-like intermediate during the base-induced unfolding of a multidomain protein, Phys. Chem. Chem. Phys. 19 (2017) 30207–30216.
[36] M. Steglich, R. Lombide, I. López, Expression, Purification and Initial Characterization of Human Serum Albumin Domain I and Its Cysteine 34 15, 2020 (e0240580).
[37] L. Turell, R. Radi, B. Alvarez, The thiol pool in human plasma: the central contribution of albumin to redox processes, Free Radic. Biol. Med. 65 (2013) 244–253.
[38] L. Turell, S. Carballal, H. Botti, R. Radi, B. Alvarez, Oxidation of the albumin thiol to sulfenic acid and its implications in the intravascular compartment, Brazil. J. Med. Biol. Res. 42 (2009) 305–311.
[39] C.N. Pace, Determination and analysis of urea and guanidine hydrochloride denaturation curves, Methods Enzymol. 131 (1986) 266–280.
[40] L. Painter, M.M. Harding, P.J. Beeby, Synthesis and interaction with human serum albumin of the first 3,18-disubstituted derivative of bilirubin, J. Chem. Soc. Perk. T 1 (1998) 3041–3044.
[41] T.O. Street, N. Courtemanche, D. Barrick, Protein folding and stability using denaturants, Methods Cell Biol. 84 (2008) 295–325.
[42] R. Khurana, A.T. Hate, U. Nath, J.B. Udgaonkar, pH dependence of the stability of barstar to chemical and thermal denaturation, Protein Sci. 4 (1995) 1133–1144.
[43] P. Mishra, S.K. Jha, Slow motion protein dance visualized using red-edge excitation shift of a buried fluorophore, J. Phys. Chem. B 123 (2019) 1256–1264.
[44] A. Giletto, C.N. Pace, Buried, charged, non-ion-paired aspartic acid 76 contributes favorably to the conformational stability of ribonuclease T1, Biochemistry 38 (1999) 13379–13384.
[45] A. Bocedi, G. Cattani, L. Stella, R. Massoud, G. Ricci, Thiol disulfide exchange reactions in human serum albumin: the apparent paradox of the redox transitions of Cys(34), FEBS J. 285 (2018) 3225–3237.
[46] J. Bonanata, L. Turell, L. Antmann, G. Ferrer-Sueta, S. Botasini, E. Méndez, B. Alvarez, E.L. Coitiño, The thiol of human serum albumin: acidity, microenvironment and mechanistic insights on its oxidation to sulfenic acid, Free Radic. Biol. Med. 108 (2017) 952–962.
[47] O. Spiga, D. Summa, S. Cirri, A. Bernini, V. Venditti, M. De Chiara, R. Priora, S. Frosali, A. Margaritis, D. Di Giuseppe, P. Di Simplicio, N. Niccolai, A structurally driven analysis of thiol reactivity in mammalian albumins, Biopolymers 95 (2011) 278–285.
[48] M. Guzman-Casado, A. Parody-Morreale, S. Robic, S. Marqusee, J.M. Sanchez-Ruiz, Energetic evidence for formation of a pH-dependent hydrophobic cluster in the denatured state of Thermus thermophilus ribonuclease H, J. Mol. Biol. 329 (2003) 731–743.
[49] J.H. Cho, S. Sato, D.P. Raleigh, Thermodynamics and kinetics of non-native interactions in protein folding: a single point mutant significantly stabilizes the N-terminal domain of L9 by modulating non-native interactions in the denatured state, J. Mol. Biol. 338 (2004) 827–837.
[50] B.E. Bowler, Thermodynamics of protein denatured states, Mol. BioSyst. 3 (2007) 88–99.
[51] E. Arbely, T.J. Rutherford, H. Neuweiler, T.D. Sharpe, N. Ferguson, A.R. Fersht, Carboxyl pK(a) values and acid denaturation of BBL, J. Mol. Biol. 403 (2010) 313–327.

THE JOURNAL OF PHYSICAL CHEMISTRY B
A JOURNAL OF THE AMERICAN CHEMICAL SOCIETY

pubs.acs.org/JPCB

Article

Protonation−Deprotonation Switch Controls the Amyloid-like Misfolding of Nucleic-Acid-Binding Domains of TDP-43

Divya Patni and Santosh Kumar Jha*

Cite This: *J. Phys. Chem. B* 2021, 125, 8383−8394

Read Online

ACCESS | Metrics & More | Article Recommendations | Supporting Information

ABSTRACT: Nutrient starvation stress acidifies the cytosol and leads to the formation of large protein assemblies and misfolded aggregates. However, how starvation stress is sensed at the molecular level and leads to protein misfolding is poorly understood. TDP-43 is a vital protein, which, under stress-like conditions, associates with stress granule proteins via its functional nucleic-acid-binding domains (TDP-43^{tRRM}) and misfolds to form aberrant aggregates. Here, we show that the monomeric N form of TDP-43^{tRRM} forms a misfolded amyloid-like protein assembly, β form, in a pH-dependent manner and identified the critical protein side-chain residue whose protonation triggers its misfolding. We systematically mutated the three buried ionizable residues, D105, H166, and H256, to neutral amino acids to block the pH-dependent protonation−deprotonation titration of their side chain and studied their effect on the N-to-β transition. We observed that D105A and H256Q resembled TDP-43^{tRRM} in their pH-dependent misfolding behavior. However, H166Q retains the N-like secondary structure under low-pH conditions and does not show pH-dependent misfolding to the β form. These results indicate that H166 is the critical side-chain residue whose protonation triggers the misfolding of TDP-43^{tRRM} and shed light on how stress-induced misfolding of proteins during neurodegeneration could begin from site-specific triggers.

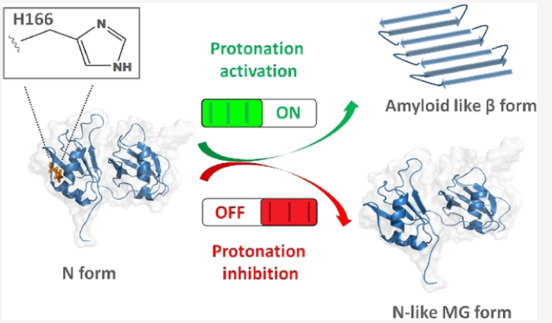

INTRODUCTION

The misfolding of TDP-43 (transactive response DNA-binding protein 43 kDa) into pathogenic aggregates has been linked to two fatal neurodegenerative diseases, amyotrophic lateral sclerosis (ALS) and frontotemporal lobar degeneration (FTLD).[1,2] ALS is a progressive neurodegenerative disease causing damage to neurons in the brain and spinal cord,[3,4] and FTLD is marked by a progressive decrease in language and behavior.[5−8] In addition to the above two diseases, aberrant aggregates of TDP-43 have also been reported in various other neurodegenerative diseases, together referred to as TDP-43 proteinopathies.[9−12] The hallmark of these proteinopathies is the depletion of TDP-43 from the nucleus and its subsequent aggregation into the cytosol of neurons and glia cells.[9] In particular in ALS, around 97% of the patients examined to date have been reported to contain inclusions of TDP-43 in the affected areas.[13,14] It has been shown that under stress-like conditions, TDP-43 forms protein assemblies referred to as stress granules.[15−18] These assemblies can form disease-associated aggregates in persistent chronic stress.[19] Not surprisingly, almost 90% of the cases of ALS occur due to sporadic factors and chronic environmental stress is believed to play a major role in the aggregation of TDP-43.[4,12,20] However, the molecular mechanism of how different types of stress are detected by protein molecules and how they trigger protein misfolding remains very poorly understood.

TDP-43 belongs to a family of highly conserved nuclear RNA binding proteins known as heterogeneous nuclear ribonucleoprotein (hnRNP).[21−23] It is a 43 kDa protein composed of 414 amino acids and is divided into four domains (Figure 1): N-terminal, two RNA binding domains RRM1 and RRM2 connected with a 15 amino acid long linker (called TDP-43^{tRRM} hereafter), and a glycine-rich, prion-like C-terminal domain[24−26] (UniProtKB/Swiss-Prot entry Q13148). The N-terminal contains a nuclear localization sequence (NLS), and TDP-43^{tRRM} contains a nuclear export sequence (NES). N-terminal is required for dimerization.[27] Low-complexity C-terminal is required for the protein−protein interaction.[28] NLS and NES are responsible for the shuttling of TDP-43 into and out of the nucleus.[29] TDP-43^{tRRM} is the principal functional domain and is responsible for binding to pyrimidine-rich nucleic acids.[12,25,30,31] It performs various crucial functions in the cells like mRNA stability, mRNA splicing, etc.[32−40] under physiological conditions but has been

Received: April 12, 2021
Revised: June 24, 2021
Published: July 28, 2021

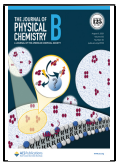

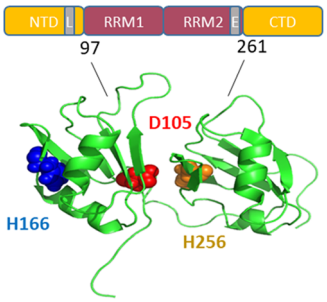

Figure 1. Schematic depiction of the four domains of the TDP-43. NTD: N-terminal domain; RRM1, RRM2: two RNA recognition motifs (collectively called TDP-43^{tRRM} in this paper); CTD: C-terminal domain. The letters L and E correspond to the nuclear localization and nuclear export sequence, respectively. Structural representation of TDP-43^{tRRM} (amino acid residues 97−261) is shown below. The locations of the side chains of the amino acid residues D105, H166, and H256 are highlighted. The side chains of D105, H166, and H256 are buried to the extents of 97, 93, and 91.5%, respectively. The image is produced using PyMOL with the PDB file 4BS2.

recently reported to form disease-associated aggregates in stress-like destabilizing conditions.[41−43]

Cells experience a variety of stress-like conditions, and each stress changes the physiochemical and solvation environment inside the cells in a different manner.[44−47] In particular, nutrient starvation stress acidifies the cytosol and increases the cytosolic proton ion concentration due to the reduced efficiency of ATP proton pump.[48−50] Some proteins or protein domains inside the cells can function as biosensors.[46,47,49,51] It has been proposed that cells sense starvation stress at the molecular level by protonating the side chains of biosensor protein molecules that triggers their intermolecular assembly.[47,49] Cells are believed to mitigate the starvation stress by coupling the protonation−deprotonation of proteins with their assembly−disassembly reaction, but under persistent stress, these large protein assemblies lead to the formation of disease-associated amyloid-like aggregates.[15,44−47,49,51] In line with this hypothesis, we observed in a previous study that TDP-43^{tRRM} could function as a biosensor and sense pH stress but undergoes misfolding to form β-sheet-rich amyloid-like fibrils on prolonged stress[41,44] in the presence of salt. However, the identity of protein side chains whose protonation is coupled to misfolding and aggregation of TDP-43^{tRRM} remains unknown. The side chains of the ionizable amino acid residues buried inside the protein structure have differential pK_a in the folded and unfolded states[52] and can protonate or deprotonate only upon partial or complete unfolding. They are promising candidates to function as gatekeeper residues for protein aggregation as it often begins with partial unfolding of the protein. It has been also shown recently that pathogenicity in the case of multiple disease-related proteins is more frequently associated with the buried amino acid residues.[53] In this study, we have systematically mutated the three buried ionizable amino acids to neutral amino acids whose side chains cannot undergo protonation−deprotonation reaction (D105A, H166Q, and H256Q). We compared the aggregation behavior of the mutant proteins to that of the TDP-43^{tRRM}. We observed that while the mutant protein variants D105A and H256Q show the misfolding behavior similar to the TDP-43^{tRRM}, H166Q retains the native-like (N-like) secondary structure under low-pH conditions and does not misfold to the β-sheet-rich, β form. Instead, H166Q predominantly forms a molten globule that binds to ANS. Our results shed important light on how site-specific modification of proteins under stress-like conditions could trigger the misfolding into amyloid-like forms in neurodegenerative diseases.

MATERIALS AND METHODS

Buffers and Chemicals. All of the chemicals used are of highest-purity grade and were obtained from Sigma and Sisco Research Laboratories (SRL). For the pH-dependent experimental studies, the following buffers for different pH range are used: 20 mM glycine−HCl (pH 1.5−3.5), 20 mM sodium acetate (pH 3.8−5.0), 20 mM 2-(N-Morpholino) ethanesulfonic acid (MES) (pH 5.5−6.0), 20 mM 3-(N-Morpholino) propanesulfonic acid (MOPS) (pH 7.0, 7.5), and 20 mM Tris (pH 8.0). All of the buffers contained 150 mM KCl and 1 mM dithiothreitol (DTT). The buffers were filtered with 0.2 μm filter before use.

Expression and Purification of TDP-43^{tRRM}. TDP-43^{tRRM} was purified as described previously[41] and stored in the storage buffer (10 mM potassium phosphate, 150 mM KCl, 1 mM DTT, and 5% glycerol at pH 7.2). The protein was highly pure as checked by sodium dodecyl sulfate−polyacrylamide gel electrophoresis (SDS−PAGE). The concentration of the protein was determined by measuring the absorbance at 280 nm using the extinction coefficient of 15 470 M^{-1} cm^{-1}.[54]

Site-Directed Mutagenesis. Primers containing the desired mutations were constructed with the help of QuikChange primer design program (https://www.agilent.com/store/primerDesignProgram.jsp). The designed primers were procured from IDT Technologies. QuikChange Lightning kit from Agilent was used to generate the single-site mutants of TDP-43^{tRRM} using the protocol provided with it. The mutations were confirmed by DNA sequencing. The three mutant variants studied are D105A, H166Q, and H256Q. The mutant proteins D105A and H256Q were purified using the same protocol as that of TDP-43^{tRRM}. Both of the proteins were highly pure as checked by SDS−PAGE.

Purification of H166Q. H166Q showed a different expression profile and was found in inclusion bodies and hence was extracted from the cell pellet. The BL21 cells were transformed with the mutation containing plasmid and grown in Luria Bertani (LB) agar containing 100 μg/mL of ampicillin. Single-cell colony was used to grow primary culture in LB media containing 100 μg/mL of ampicillin. The primary culture was then used to inoculate secondary culture, where the cells were allowed to grow till the OD_{600} reached 0.7 in LB media. To overexpress the protein, the cells were induced by 1 mM isopropyl β-D-1-thiogalactopyranoside (IPTG) and spun at 20 °C for 24 h. The cells were pelleted at 4500 rpm for 30 min at 4 °C and then lysed by sonication in lysis buffer (20 mM sodium phosphate, 300 mM NaCl, 30 mM imidazole, DNaseI at pH 7.4). The lysed cells were centrifuged to separate them from the supernatant at 14 000 rpm for 45 min. The cell pellets were dissolved in urea containing lysis buffer (7.2 M urea, 20 mM sodium phosphate, 300 mM NaCl, 30 mM imidazole, and DNaseI at pH 7.4) for 30 min. The cell debris was separated from the supernatant by centrifugation at 14 000 rpm for 45 min. The supernatant was filtered through a 0.2 μm filter. Filtered supernatant was passed through Ni Sepharose 6-Fast Flow beads (GE Healthcare) preequilibrated with the urea containing lysis buffer. The bound mutant

https://doi.org/10.1021/acs.jpcb.1c03262
J. Phys. Chem. B 2021, 125, 8383−8394

protein was eluted in the elution buffer (7.2 M urea, 20 mM sodium phosphate, 300 mM NaCl, and 300 mM imidazole at pH 7.4). The eluted protein was further desalted using a HiPrep 26/10 desalting column (GE Healthcare) into 7.2 M urea and 20 mM sodium phosphate buffer followed by anion exchange chromatography on a HiPrep Q FF 16/10 column (GE Healthcare). Finally, the protein was buffer-exchanged in the storage buffer (10 mM potassium phosphate, 7.2 M urea, and 1 mM DTT at pH 7.2) by passing the protein through a PD10 desalting column. Glycerol (5%) was further added to the protein solution. The purity of the purified protein was checked by SDS−PAGE and found to be highly pure. The protein was refolded in the desired buffer just before performing the experiments. The concentration of the protein was determined by measuring the absorbance at 280 nm, using an extinction coefficient of 15 470 M^{-1} cm^{-1}.

pH-Induced Formation of the β form. The buffers used at different pH values are described above. For the pH-induced formation of the β form, the proteins were incubated in the desired buffer for at least 4 h at room temperature before any measurement.

Circular Dichroism (CD). All of the circular dichroism (CD) measurements were performed on a Jasco J-815 spectropolarimeter. The instrument setting used for collecting spectra is as follows: data integration time of 4 s, bandwidth of 2 nm, data pitch of 1 nm, and scan speed of 20 nm/min. Each CD spectrum collected was an average of two accumulations. For far-UV CD spectra, the data were collected in the wavelength range of 205−250 nm and a cuvette of path length 0.1 cm was used. For all of the equilibrium and kinetics measurements, the concentration of the protein used was in the range of 8−20 μM. The buffer spectra were recorded under similar settings and were subtracted from the acquired CD spectra. The signals obtained from CD were used to calculate fraction misfolded for all of the mutant variants using the equation

$$\text{fraction misfolded} = \frac{S_N - S_O}{S_N - S_M} \quad (1)$$

where S_N is the signal of native protein, S_O is the observed signal, and S_M refers to the signal of misfolded protein.

8-Anilino-1-Naphthalenesulfonic Acid (ANS) Fluorescence Assay. A stock solution of 10 mM ANS was prepared in dimethyl sulfoxide (DMSO). The concentration of ANS was measured by monitoring the absorbance at 350 nm and using an extinction coefficient of 5000 M^{-1} cm^{-1}.[55] TDP-43^{tRRM} (2 μM) was incubated with ANS (60 μM) for 15 min. The experiments were carried out on a FluoroMax-4 spectrofluorometer (Horiba Scientific). The fluorescence spectrum for each sample was measured by exciting ANS at 380 nm and acquiring emission from 400 to 600 nm. The slits used were 1 and 8 nm for excitation and emission, respectively. Some of the ANS experiments were also performed on a PerkinElmer Fluorescence spectrometer LS55. For those experiments, the slits used were 8 nm for excitation and 9 nm for emission.

Analysis of the pH Dependence of the N⇌β Transition. Kinetic experiments in the previous studies[44] have shown that the pH-dependent N⇌β transition occurs in multiple steps. However, at equilibrium, the N⇌β transition monitored by CD signal at 216 nm and ANS fluorescence signal at 469 nm for TDP-43^{tRRM}, D105A, and H256Q showed an apparently two-state sigmoidal change as a function of pH. This result suggests that only the N form or the β are stable enough to be populated at equilibrium under the experimental conditions used in this study (in the presence of 150 mM KCl). In view of this result, we fitted the pH-dependent equilibrium data to a simplified apparently two-state model, in which the formation of the misfolded β form was coupled to the protonation of a single critical residue of the N form, with a dissociation constant of K_a, as shown in the following scheme

$$N + H^+ \rightleftharpoons NH^+ \rightleftharpoons \beta \text{ (Scheme 1)}$$

It is assumed in the model that only NH^+ is competent to transform into the β form. In that case, the pH dependence is that of the protonation of N and is given by a transformation of the Henderson−Hasselbalch equation

$$Y_{obs} = \frac{Y_{NH^+} + Y_N 10^{(pH - pK_a)}}{1 + 10^{(pH - pK_a)}} \quad (2)$$

where Y_{obs} corresponds to the observed spectroscopic signal at a particular pH value, and Y_N and Y_{NH^+} correspond to the signals of the N form and the protonated NH^+ form. It is assumed that under the experimental conditions and the protein concentrations used in this study, NH^+⇌β equilibrium completely favors the β form, and hence, the amount of NH^+ is equal to the amount of the β form.

The fraction of the protonated NH^+ form, i.e., the fraction of protein protonated at the critical titrating residue, as a function pH will be given by

$$\text{fraction of } NH^+ = \frac{1}{1 + 10^{(pH - pK_a)}} \quad (3)$$

Estimation of Solvent Accessibility of Acidic Amino Acid Residues. The absolute solvent-accessible surface area (ASA) of each amino acid residue was calculated using DSSP program.[56] The relative solvent-accessible surface area (RSA) was calculated by dividing absolute solvent-accessible surface area by the total surface area of the amino acid residue.[57,58]

Size Exclusion Chromatography (SEC). Size exclusion chromatography (SEC) was performed on a Superdex 75 10/300 GL column having fractionation range from 3 to 70 kDa with a void volume of 7.2 mL and a bed volume of 23.5 mL. For the SEC experiments, an AKTA Pure M FPLC system (GE Healthcare) was used. SEC experiment on the N form was performed at pH 7.5. The concentration of the protein used was 20 μM. SEC experiment on the misfolded β form was performed at pH 3.0. The concentration of the protein used was 15 μM. The flow rate used was 0.8 mL/min. All of the experiments were performed at 4 °C.

To determine the apparent molecular weight (M_W^{app}) of the N form, we first created a calibration curve (Figure S1) between the partition coefficient (K_{av}) of the five standard biomolecules (bovine serum albumin (BSA), ovalbumin, ribonuclease A, aprotonin, and vitamin B12) and their respective molecular weights, as described in the GE Healthcare manual. The value of K_{av} was calculated using the below-mentioned equation

$$K_{av} = \frac{V_e - V_o}{V_t - V_o} \quad (4)$$

where V_e refers to the elution volume of the protein molecule, V_o refers to the void volume of the column, and V_t refers to the total bed volume of the column. The values of V_o and V_t were taken from the column specifications provided in the manual

https://doi.org/10.1021/acs.jpcb.1c03262
J. Phys. Chem. B 2021, 125, 8383−8394

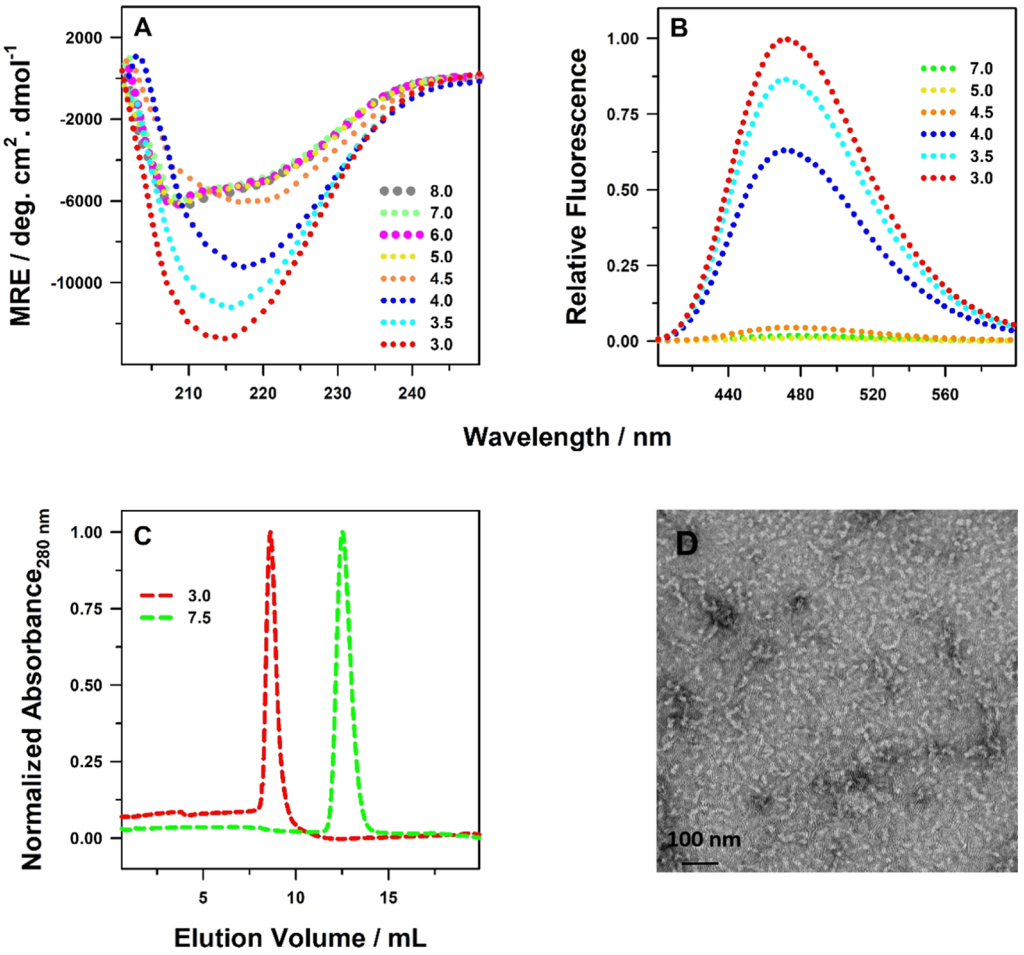

Figure 2. TDP-43^{tRRM} undergoes pH-dependent misfolding and aggregation. (A) Far-UV CD spectra of TDP-43^{tRRM} as a function of pH. (B) Changes in the fluorescence spectrum of ANS in the presence of TDP-43^{tRRM} as a function of pH. (C) Elution profile of TDP-43^{tRRM} in SEC, in the N form (pH 7.5) and in the β form (pH 3.0). (D) TEM image of the β form.

for Superdex 75 10/300 GL column. V_e and molecular weight of different standards were also taken from the instruction manual provided along with the column. We used the experimentally measured elution volume of the N form to calculate the partition coefficient and in turn determined its M_W^{app} from the calibration curve.

Transmission Electron Microscopy (TEM). TEM was used to visualize the morphology of the β form. The β form (10 μL of 1 μM concentration) was loaded onto the 300-mesh carbon-coated grid (Electron Microscopy Science) and allowed to get absorbed for 5 min. Excess sample was removed. Uranyl acetate (2%) was used for 1.5 min to negatively stain the samples. Excess stain was removed. This was followed by a wash by Milli-Q water for 1 min to wash off any extra stain stuck on the grid. The sample was then covered and allowed to dry overnight and imaged under a transmission electron microscope (Technai-T20) at an accelerating voltage of 200 kV.

Guanidinium Chloride (GdmCl)-Induced Equilibrium Unfolding Experiments. All of the equilibrium unfolding experiments were performed at pH 7.5. Proteins (4 μM) were equilibrated in the presence of different concentrations of GdmCl. The samples were excited at 280 nm, and the emission was collected from 295 to 400 nm. The slit width of 1 nm was used for excitation and 8−12 nm for emission. Buffer spectra were acquired under similar settings and were subtracted from the protein spectra. The data were converted to fraction unfolded as a function of [GdmCl] and analyzed using an N⇌U two-state model, as described previously.[59]

Thioflavin T (ThT) Fluorescence Assay. The ThT assay was performed on the N form and the β form of all of the proteins. The N form or the β form was added to the ThT buffer (50 mM Tris, pH 8.0) so that the final concentration of the protein and ThT were 2 and 40 μM, respectively. The ThT fluorescence was acquired within 1 min of mixing. The experiments were performed on a PerkinElmer fluorescence spectrometer LS55. The slit widths used for excitation and emission were 8 and 11 nm, respectively. Excitation was carried out at 440 nm, and emission spectra were monitored from 460 to 600 nm. Buffer spectra were acquired under similar settings and were subtracted from the protein spectra.

RESULTS

TDP-43^{tRRM} Undergoes pH-Dependent Misfolding. We monitored the changes in the secondary structure content of TDP-43^{tRRM} as a function of pH using far-UV CD (Figure 2A). At pH 8.0, the far-UV CD spectrum displayed minima at 208 and 222 nm. The mean value of mean residue ellipticity (MRE) at 222 nm was −4700 deg cm^2 dmol^{-1}. The secondary structure of TDP-43^{tRRM} contains α-helices, β-sheets, and disordered loops (Figure 1) and the far-UV CD spectrum at pH 8.0 is characteristic of TDP-43^{tRRM} in its native state.[41] We

https://doi.org/10.1021/acs.jpcb.1c03262
J. Phys. Chem. B 2021, 125, 8383−8394

observed that the far-UV CD spectra of TDP-43^{tRRM} remain highly identical to the spectrum of the native protein in the pH range of 8.0−5.0 (Figure 2A). As the pH is decreased below 5.0, the far-UV CD spectra gradually shift to a spectrum of a β-sheet with a minima at 216 nm. This result indicates that at low pH and physiological concentration of salt (150 mM KCl), TDP-43^{tRRM} transitions into an alternative misfolded conformation that is rich in β-sheet (β form). Interestingly, both native and urea-unfolded TDP-43^{tRRM} form almost identical β form when transferred to a low pH (Figure S2), indicating that the β form is thermodynamically the most stable form at a low pH. At pH 3.0, the value of MRE at 216 nm is −12 645 deg cm^2 dmol^{-1}. Such an increase in the value of MRE at the low pH is indicative of a disorder-to-order transition in the protein molecules.[41]

The N⇌β transition is also accompanied by a large change in the tertiary structure of the protein molecules, in addition to the secondary structure. Figure 2B shows the changes in the tertiary structure of TDP-43^{tRRM} as a function of pH as probed by the ANS binding assay. ANS is a dye that binds to the exposed hydrophobic patches of the protein resulting in its increased fluorescence signal. We observed that in the pH range of 8.0−5.0, ANS does not bind to TDP-43^{tRRM} as indicated by a near-zero fluorescence signal (Figure 2B). In contrast, the fluorescence of ANS increases dramatically as the pH is decreased in the range of 5.0−3.0. These results indicate that the misfolded β form has exposed hydrophobic patches.

β Form is an Amyloid-like Protein Assembly. To understand, if the misfolding is accompanied by intermolecular self-assembly, we performed SEC of TDP-43^{tRRM} at different pH on a Superdex 75 10/300 GL column (Figure 2C). TDP-43^{tRRM} under native conditions at pH 7.5 elutes at 12.5 mL, corresponding to a molecular weight of 19952 Da (see the Materials and Methods section), which suggests it to be a monomer. However, at pH 3.0, the elution of the TDP-43^{tRRM} occurs at 8.6 mL, which is near to void volume (7.2 mL) of the column. These results indicate that the misfolded β form is a large-size protein assembly.

We examined the external morphology of the β form using TEM (Figure 2D). In the TEM micrograph, the β form appears to be curly amyloid-like protein assembly, which are around 100 nm long, as observed in a previous study.[44] These results indicate that the β form has amyloid-like ordered morphology.

pH Dependence of the N⇌β Transition. The above results show that when the monomeric N form of TDP-43^{tRRM} is subjected to a low pH in the presence of 150 mM KCl, it transforms into an amyloid-like protein assembly, β form, which is rich in β sheet and has exposed hydrophobic patches. Figure 3A shows the pH dependence of the change in CD signal at 216 nm during the N⇌β transition. Figure 3B does likewise for the change in the signal of ANS fluorescence at 469 nm. We observed that in both the cases, the signal changes in an apparently sigmoidal manner as a function of pH. These results suggest that the structural changes in the protein molecules during the N⇌β transition is coupled to the ionization of at least one ionizable residue. The results of the ANS experiments (Figures 2B and 3B) show that the disruption of side-chain packing in the hydrophobic core is required for ionization. This result suggests that the ionizing side-chain residue is buried in the protein core. We fitted the data on pH dependence of misfolding (Figure 3) to a model in which the formation of the misfolded β form was coupled to

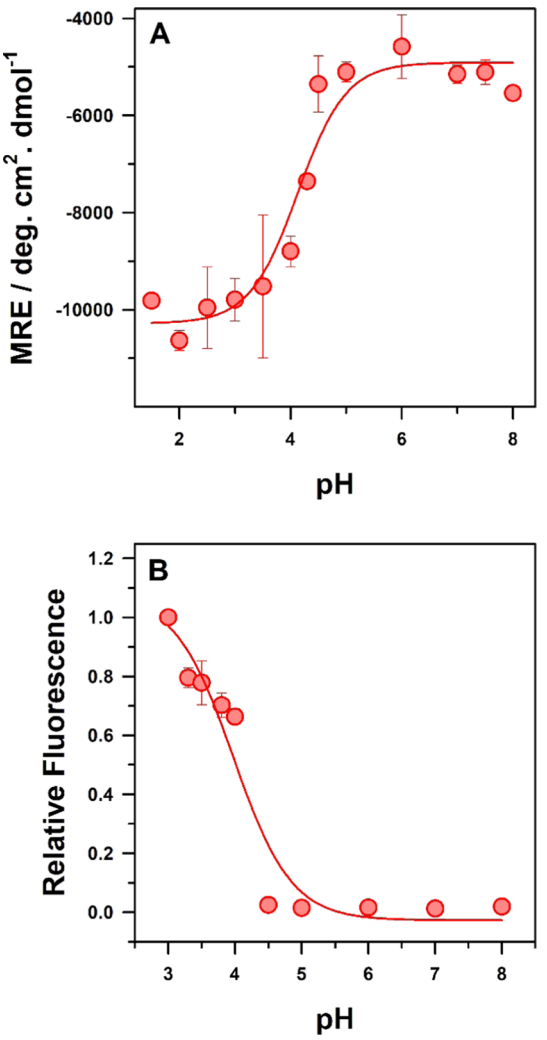

Figure 3. pH dependence of the misfolding transition. Changes in the values of (A) MRE at 216 nm obtained by far-UV CD and (B) ANS fluorescence emission at 469 nm as a function of pH. In both the panels, the solid line through the data is a least-square fit to eq 2. The error bars in both the panels are standard deviation in values of the data points from three independent experiments.

the protonation of at least one critical residue of the N form (see the Materials and Methods section). A fit of the data in Figure 3 to eq 2 yielded the pK_a of the critical titrating residue to be ∼4.0. This result suggests that the titration of a buried aspartate, glutamate, or a histidine residue with a perturbed pK_a might be coupled to the formation of the β form. There are 12 glutamate, 13 aspartate, and 3 histidine residues in the primary sequence of TDP-43^{tRRM}. Out of these, only one aspartate (D105) and two histidine (H166 and H256) residues are almost completely buried in the protein structure (Figure 1 and Table S1). We targeted these three residues to check whether the ionization of any one of them is coupled to the formation of the β form. We mutated them to a neutral amino acid, one at a time, by site-directed mutagenesis to abolish the protonation−deprotonation equilibrium of their side chains in the acidic pH. Aspartate was mutated to alanine, and both the histidine residues were mutated to the glutamine because of their similar size. The three mutant protein variants are named D105A, H256Q, and H166Q.

https://doi.org/10.1021/acs.jpcb.1c03262
J. Phys. Chem. B 2021, 125, 8383−8394

Single-Site Mutant Variants Have Similar Structure and Thermodynamic Stability. It was important to first check whether the single-site mutations affect the structure and stability of the N form. Figure 4A compares the far-UV CD spectra of D105A, H256Q, and H166Q to those of the TDP-43^{tRRM} in the N form and the GdmCl unfolded U form. The far-UV CD spectra of all of the mutant variants are very similar to the TDP-43^{tRRM}, both in the N form and the U form. These results indicate that the mutant variants have a very similar secondary structure to that of the TDP-43^{tRRM} and that they are completely and similarly unfolded in 6.2 M GdmCl.

Figure 4B compares the maximum wavelength of fluorescence emission (λ_{max}) of D105A, H256Q, and H166Q to that of the TDP-43^{tRRM} protein in the N form and the U form. There are two tryptophan residues, W113 and W172, in the three-dimensional structure of TDP-43^{tRRM}. Solvent accessibility calculations (Materials and Methods section) suggest that W113 is 52% exposed and W172 is 41% exposed to the solvent. We observed that all of the proteins in the N form showed similar λ_{max} of ∼347 nm (Figure 4B), indicating that the side chains of tryptophan residues are buried to a similar extent in the mutant variants and in the TDP-43^{tRRM}.[44] Similarly, in the U form, all of the proteins show similar λ_{max} of ∼357 nm (Figure 4B), indicating that in the U form of all of the proteins, tryptophan residues are completely exposed to solvent.

We measured the thermodynamic stabilities of the proteins using GdmCl-induced equilibrium unfolding experiments. Figure 4C shows that all of the three mutant variants display an apparent two-state unfolding behavior. The free energies of unfolding of TDP-43^{tRRM}, D105A, H256Q, and H166Q are 4.6, 5.2, 4.4, and 5.2 kcal mol^{-1}, respectively (Table S2). These results suggest that the effect of mutations on protein stability is very minimal. These results conclude that all of the mutant variants have similar secondary and tertiary structures (Figure 4A,B) and thermodynamic stability (Figure 4C) to that of the TDP-43^{tRRM}. Hence, the mutations do not alter the overall structure and stability of TDP-43^{tRRM} and all of the variants can be directly compared to each other.

D105A and H256Q Shows pH-Dependent Misfolding Similar to TDP-43^{tRRM}. Figure 5A,B displays the changes in the far-UV CD spectra of D105A and H256Q, respectively, as a function of pH. The pH-dependent changes in secondary structure are strikingly similar to that of TDP-43^{tRRM} (Figure 2A) for both the mutant variants. The far-UV CD spectra of the N form gradually shifts to the spectrum of a β sheet, with a minima at 216 nm, as the pH is decreased from 7.5 to 3.0. Both the mutant variants display an apparently sigmoidal change in CD signal at 216 nm with midpoint of transition at pH 4.0 (Figure 5A,B, insets), similar to TDP-43^{tRRM} (Figure 3A). These results indicate that D105A and H256Q undergo N⇌β transition, akin to TDP-43^{tRRM}. Hence, the ionization of D105 and H256 is not coupled to the misfolding of TDP-43^{tRRM}.

H166Q Does Not Show pH-Dependent Misfolding. Interestingly, we observed that in contrast to D105A, H256Q, and TDP-43^{tRRM}, the mutant variant H166Q does not undergo pH-dependent misfolding. Figure 5C shows the changes in the far-UV CD spectra of H166Q, as a function of pH. The far-UV CD spectrum of H166Q in the N form does not change to a spectrum of β sheet as the pH is decreased from 7.5 to 3.0. Instead, the far-UV CD spectrum remains N-like throughout the range of pH, indicating that H166Q maintains N-like

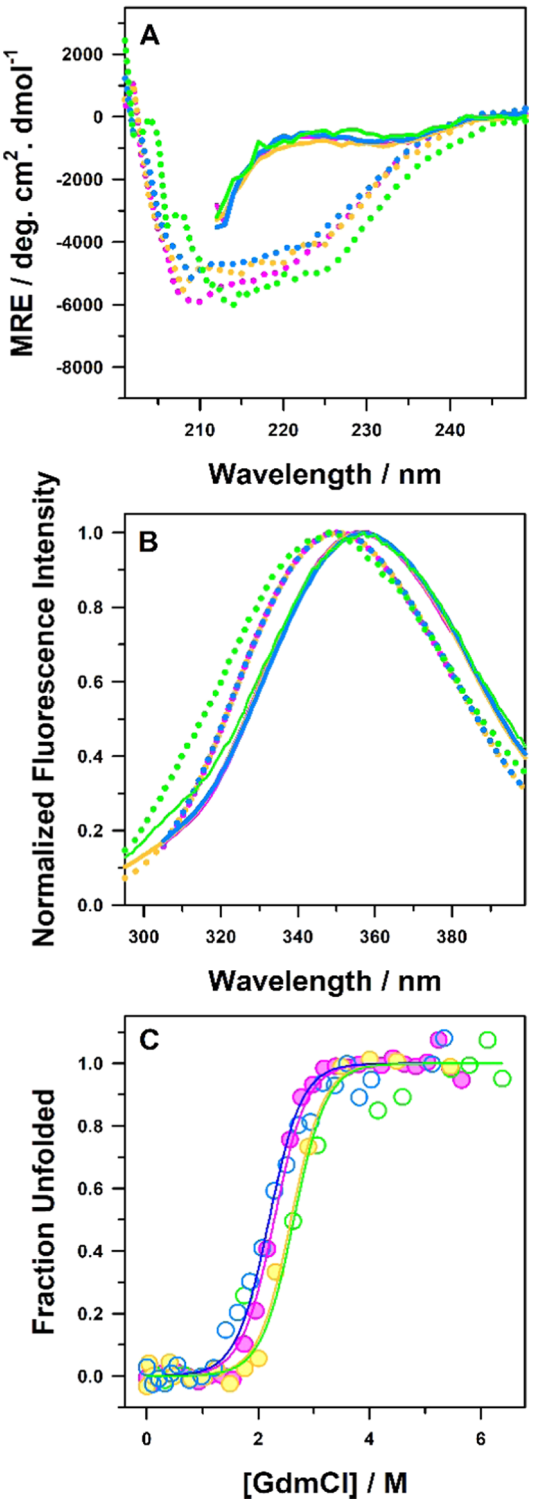

Figure 4. Mutant protein variants and TDP-43^{tRRM} have similar structure and thermodynamic stability. (A) Far-UV CD spectra and (B) fluorescence spectra of TDP-43^{tRRM} (pink lines), D105A (yellow lines), H166Q (green lines), and H256Q (blue lines), in the N form (dotted lines) and the GdmCl unfolded U form (6.2 M GdmCl) (solid lines) at pH 7.5. (C) Fraction unfolded as a function of [GdmCl] obtained from GdmCl-induced equilibrium unfolding at pH 7.5 is plotted for TDP-43^{tRRM} (filled pink circles), D105A (filled yellow circles), H166Q (empty green circles), and H256Q (empty blue circles). The solid lines through the data are fits to a two-state N⇌U model.[59,60]

https://doi.org/10.1021/acs.jpcb.1c03262
J. Phys. Chem. B 2021, 125, 8383−8394

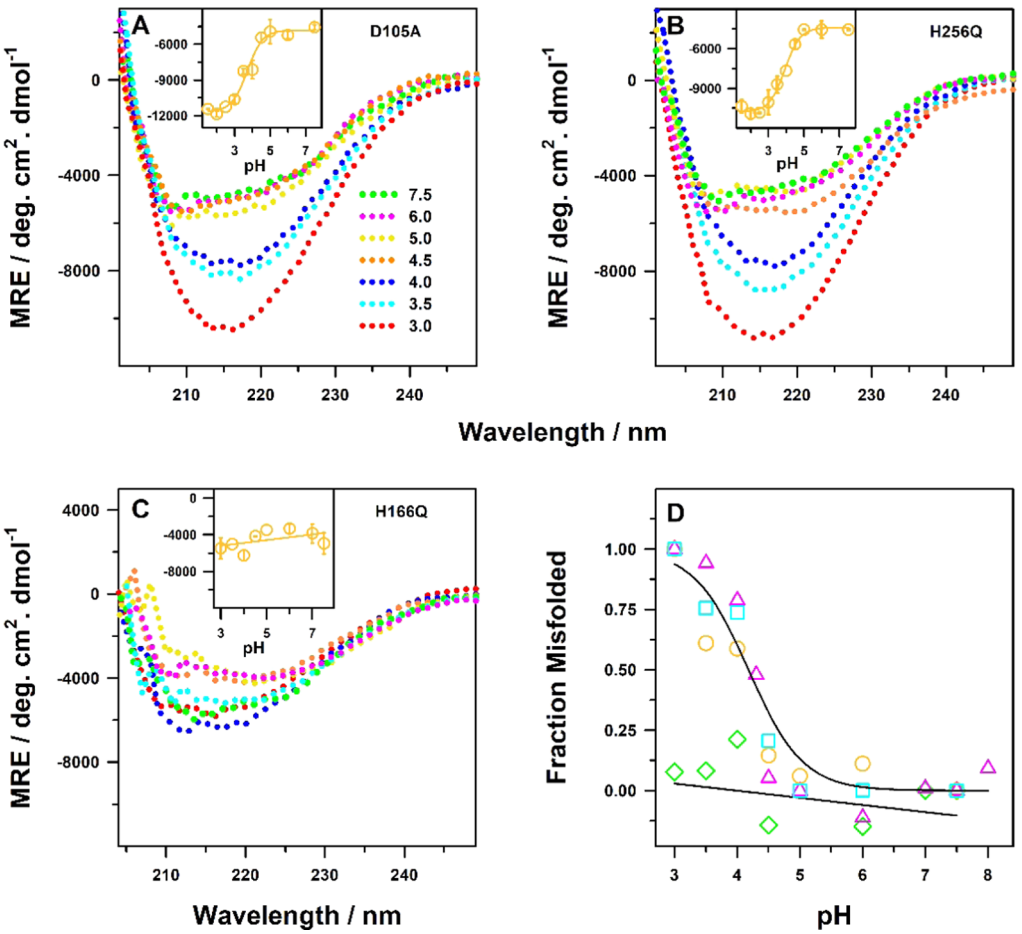

Figure 5. Effect of site-specific mutations on the N⇌β transition. Changes in the far-UV CD spectra of (A) D105A, (B) H256Q, and (C) H166Q, as a function of pH. In (A–C), the different colors of the dotted lines denote different pH values, as indicated in (A). The insets in (A–C) show the changes in the values of MRE at 216 nm as a function of pH, for the corresponding protein. The solid yellow line through the data in the insets of (A) and (B) is a fit to eq 2. The solid yellow line through the data in the inset of (C) is drawn to guide the eye. The error bars are the spread in values of the data points from two independent experiments. (D) Fraction of the misfolded protein as a function of pH is compared for TDP-43^{tRRM} (pink triangles), D105A (yellow circles), H256Q (blue squares), and H166Q (green diamonds). The solid black line through the data for TDP-43^{tRRM}, D105A, and H256Q is a global fit to eq 3. The solid black line through the data for H166Q is drawn to guide the eye.

secondary structure in the pH range 7.5–3.0. The mean value of MRE at 216 nm does not show a sigmoidal behavior as a function of pH (Figure 5C, inset) and remains roughly the same across the pH range (7.5–3.0). The average of the mean value of MRE across the pH range is −4571 deg cm^2 dmol^{-1}, and the standard deviation is −1028 deg cm^2 dmol^{-1}. These results indicate that H166Q does not undergo N⇌β transition. Hence, the pH-dependent ionization of H166Q is coupled to the misfolding of TDP-43^{tRRM} and is a key trigger for the formation of amyloid-like β form.

We calculated the fraction of misfolded β form, formed by each protein, as a function of pH from the changes in value of MRE at 216 nm (see the Materials and Methods section). Figure 5D compares the fraction misfolded as a function of pH, for all of the four proteins. Remarkably, the change in the fraction of the misfolded β form during the N⇌β transition of D105A and H256Q is highly comparable to that of TDP-43^{tRRM} with midpoint of transition near ∼4.0. In contrast, the fraction of misfolded β form for H166Q is almost near zero in the pH range 7.5–3.0.

D105A and H256Q Show Similar Kinetics of Misfolding to TDP-43^{tRRM}. Figure 6A shows the kinetics of misfolding of TDP-43^{tRRM} to the β form at pH 7.5 and pH 3.0 as measured by the change in the far-UV CD signal at 216 nm. At pH 7.5, the far-UV CD signal remains constant at the value of MRE of the N form as a function of time, indicating that the N-like structure is maintained and that the rate of misfolding is negligible under N-like conditions. Upon transferring the protein under aggregation condition at pH 3.0, there appears to be a fast change in the MRE signal during the dead time of mixing (ca. 20–30 s), in which ca. 10–15% of the total expected amplitude of the MRE signal is lost. This is followed by a double-exponential change in the MRE signal with time. Both the observable phases have roughly equal amplitudes. These results indicate that TDP-43^{tRRM} misfolds in at least three steps during the formation of the β form. The time constants of the two observable steps were estimated to be ∼6.3 and ∼65 min at pH 3.0.

The mutant variants D105A (Figure 6B) and H256Q (Figure 6C) show strikingly similar pH-dependent kinetics of misfolding at pH 3.0 as TDP-43^{tRRM} (Figure 6A). For both the proteins, there is a fast change in the MRE signal at 216 nm within the dead time of mixing in which ca. 15–25% of the total expected change in MRE signal is lost. This is followed by a double-exponential change in the MRE signal with time with roughly equal amplitudes. The time constant of the two

https://doi.org/10.1021/acs.jpcb.1c03262
J. Phys. Chem. B 2021, 125, 8383–8394

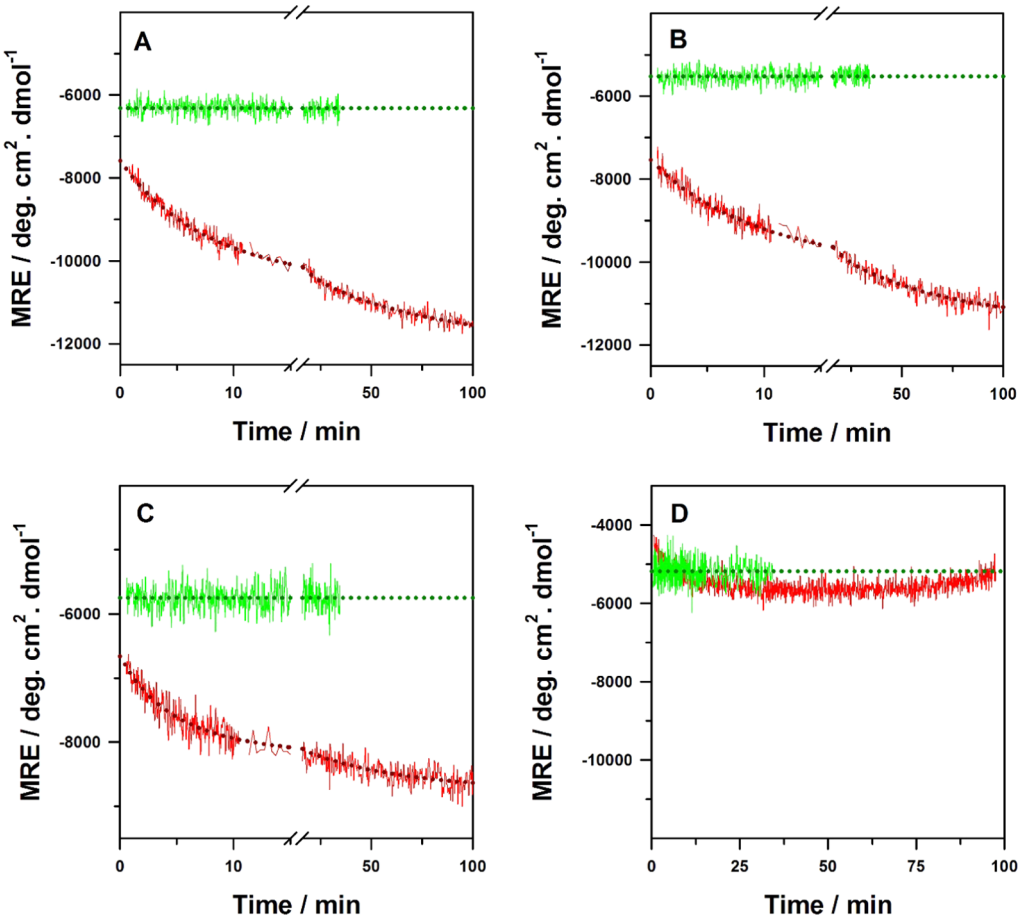

Figure 6. Comparison of the pH-dependent kinetics of misfolding of TDP-43^{tRRM} and the three mutant protein variants. The change in far-UV CD MRE signal at 216 nm with time is shown for (A) TDP-43^{tRRM}, (B) D105A, (C) H256Q, and (D) H166Q when each of the protein variants is transferred to pH 7.5 (green line) and pH 3.0 (red line). In (A−C), the dotted red lines through the data for pH 3.0 are fits to a double-exponential equation. In all of the panels, the dotted green line through the data for pH 7.5 is shown to guide the eye.

observable phases at pH 3.0 was estimated to be ∼7.1 and 60 min for D105A and ∼4.5 and ∼50 min for H256Q. At pH 7.5, for both the proteins, the far-UV CD signal remains constant at the value of MRE of the N form, indicating that both the proteins maintain their native structure for a long time under N-like conditions. These results indicate that D105A and H256Q display similar pH-dependent kinetics of misfolding to TDP-43^{tRRM}.

H166Q Does Not Show pH-Dependent Kinetics of Misfolding. In contrast to those of TDP-43^{tRRM}, D105A, and H256Q, the N form of H166Q does not transition to the misfolded β form when transferred to pH 3.0 (Figure 6D). The far-UV CD signal of H166Q remains constant at the value of MRE of the N form at both pH 7.5 and pH 3.0. These results indicate that H166Q does not undergo a change in its secondary structure and retains its N-like secondary structure even at a low pH, for a long time. Hence, the process of pH-dependent misfolding is highly arrested for H166Q mutant protein.

Low-pH Form of H166Q Shows Very Little Binding to Amyloid Staining Dye ThT but Has Disrupted Side-Chain Packing. H166Q maintains its N-like secondary structure under pH stress and does not misfold to form amyloid-like misfolded β form as shown by far-UV CD experiments (Figures 5C,D and 6D). We further probed the nature of the structure formed by H166Q at the physiological and low pH values by measuring its ability to bind ThT and ANS dyes. ThT dye binds strongly to amyloid-like cross-β structure[61] and, upon binding, gives an increased fluorescence at 482 nm. ThT dye has also been shown to bind weakly to nonamyloid N-like oligomers of some variants of TDP-43[62] and amorphous aggregates of other proteins.[63] Figure 7A and its inset compare the ThT binding efficiency of the species populated at pH 3.0 and pH 7.5 for H166Q with those of TDP-43^{tRRM}, D105A, and H256Q. For all of the four proteins, no ThT fluorescence was observed for the N form at pH 7.5, indicating that no amyloidogenic structures are present under N-like conditions. For the misfolded β forms formed by TDP-43^{tRRM}, D105A, and H256Q at pH 3.0, a huge and similar increase in ThT fluorescence was observed, indicating the presence of amyloid-like β-sheet-rich structure. In contrast, the N-like species formed by H166Q at pH 3.0 showed very minimal binding to the ThT dye (∼20%). As the low pH form of H166Q does not contain amyloid-like β-sheet-rich structure as indicated by far-UV CD experiments (Figures 5C,D and 6D), the small binding to the ThT dye might be due to the association of a small fraction of TDP-43^{tRRM} in N-like oligomers as shown previously[44,62] or amorphous aggregates[63] via its strand regions.

ANS assay was performed to compare the tertiary structure and packing of hydrophobic core[64] of H166Q in the N form and the low-pH form to that of TDP-43^{tRRM}, D105A, and

https://doi.org/10.1021/acs.jpcb.1c03262
J. Phys. Chem. B 2021, 125, 8383−8394

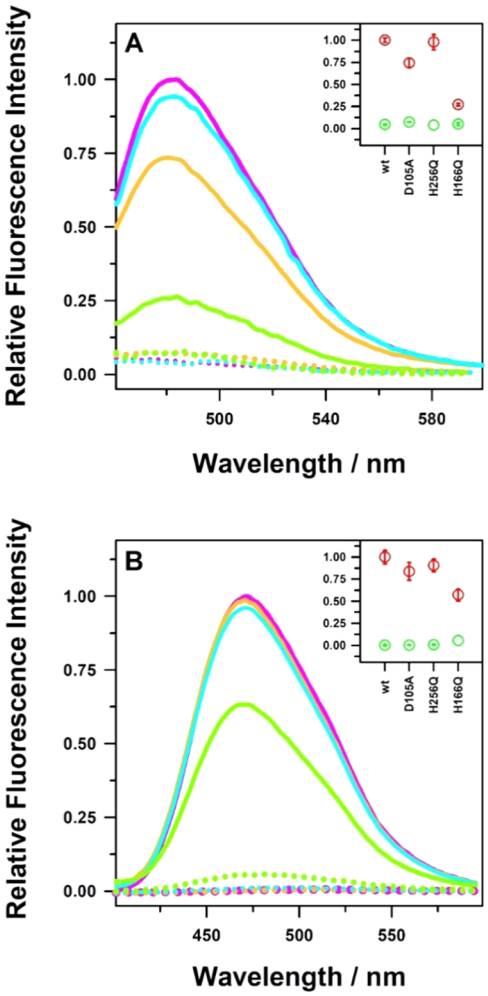

Figure 7. Comparison of the binding of ThT and ANS dyes to TDP-43^{tRRM} and the three mutant protein variants. TDP-43^{tRRM} (pink), D105A (yellow), H166Q (green), and H256Q (blue) were transferred to pH 7.5 (dotted lines) and pH 3.0 (solid lines) and (A) ThT fluorescence and (B) ANS fluorescence spectra were obtained for the species populated at both the pHs. The inset in (A) compares the ThT fluorescence emission at 482 nm for all of the proteins for the species populated at pH 7.5 (green circles) and pH 3.0 (red circles). The inset in (B) compares the ANS fluorescence emission at 469 nm for all of the proteins for the species populated at pH 7.5 (green circles) and pH 3.0 (red circles). The error bars in the insets are the spread in the values of the data points from two independent experiments.

H256Q. Figure 7B and its inset compare the binding efficiency of the ANS dye to the species populated at pH 3.0 and pH 7.5 for H166Q with those of TDP-43^{tRRM}, D105A, and H256Q. For all of the four proteins, near-zero fluorescence was observed for the N form at pH 7.5, indicating that the hydrophobic core is tightly packed in the N form of all of the proteins. For the misfolded β forms formed by TDP-43^{tRRM}, D105A, and H256Q at pH 3.0, a huge and similar increase in ANS fluorescence was observed, indicating that the β forms of all of the proteins have a similar but large amount of exposed hydrophobic patches. The N-like species formed by H166Q at pH 3.0 also binds to the ANS dye, but the ANS fluorescence in this case is only about 50−60% to that of the β form of the other three proteins. This result indicates that the N-like species formed by H166Q at pH 3.0 have disrupted side-chain packing and exposed hydrophobic patches. The intact secondary structure and disrupted tertiary structure suggest that H166Q forms a molten globular structure at a low pH.

The ANS binding signal of the molten globular structure formed by H166Q at a low pH is around 50−60% of the amyloid-like β forms formed for other three proteins. This is because the amyloid-like β forms have a sheeted structure and likely to have more exposed hydrophobic surface and ANS binding sites compared to a molten globule.

DISCUSSION AND CONCLUSIONS

For the proper functioning of the cells, neutral pH is required. For maintaining the neutral cytosolic pH, the cells employ hydrolysis of ATP and proton pumps to export protons into the extracellular space.[47] However, during nutrient starvation stress, the ATP level decreases, thereby affecting the proton pump, which fails to export protons out of the cell.[65] These events lead to an increase in the concentration of protons and acidification of the cytosol.[45,47,49,50] It has been suggested that one of the energy-efficient ways cells employed to negate the effect of starvation stress and increased concentration of protons is the formation of large reversible protein assemblies like stress granules.[46,47,49,51] According to this hypothesis, certain biosensor proteins in the cell (for example, Pab1,[46] Pub1,[45] Sup 35,[51] etc.) sense and mitigate starvation stress at the molecular level by coupling the protonation−deprotonation equilibrium of their side chains with their assembly−disassembly reaction.[47,49,51] These assemblies are metastable and aggregation-prone and could misfold to form amyloid-like aggregates under persistent stress. However, the experimental evidence for this hypothesis remains limited.[44−47,51] In particular, it is critical to identify the side-chain residues whose protonation is important for the formation of large assemblies and triggers misfolding.

TDP-43 is known to associate with stress granule proteins and nucleic acids via its TDP-43^{tRRM} and C-terminal regions under stress-like conditions[16,66,67] and misfold to form aberrant aggregates.[15] In this paper, we showed that the monomeric N form of TDP-43^{tRRM} forms a misfolded amyloid-like protein assembly, β form, in a pH-dependent manner (Figures 2 and 3). The change in the secondary structure to β sheet during N-to-β transition occurs concomitantly with the disruption of the side-chain packing in the hydrophobic core (Figure 3). Both the events follow the same pH dependence with pK_a around 4.0. These results suggest that ionization of a protein side-chain buried in the protein structure might be coupled to the formation of the misfolded β form. An examination of the protein structure revealed that out of all of the amino acid residues whose side chain could titrate in the acidic pH range, only D105, H166, and H256 are almost completely buried in the protein structure (Figure 1). We systematically mutated these residues, one at a time, to neutral amino acids to block the pH-dependent protonation−deprotonation titration of their side chain and studied their effect on the N-to-β transition. All of the four proteins have similar structure and thermodynamic stability under native conditions (Figure 4). We observed that D105A and H256Q resembled TDP-43^{tRRM} (Figures 2A and 3A) in their pH-dependent misfolding behavior, both in the equilibrium (Figure 5A,B,D) and the kinetic experiments (Figure 6A−C). However, in the case of H166Q, the pH-dependent misfolding of the N form to the β form is highly arrested (Figures 5C,D and 6D). These results indicate that H166 is

https://doi.org/10.1021/acs.jpcb.1c03262
J. Phys. Chem. B 2021, 125, 8383−8394

the critical side-chain residue whose protonation triggers the misfolding of TDP-43^{tRRM} to the β form.

The observation that the protonation of a histidine residue triggers the misfolding of TDP-43^{tRRM} at a low pH is surprising. Histidine residues usually have a pK_a near 6.5, and their protonation−deprotonation is known to play important roles in protein function.[68−70] However, the pK_a of the H166 in TDP-43^{tRRM} is near ∼4.0 (Figure 3). H166 is around 93% buried in the protein structure (Figure 1). A positively charged arginine residue, R165, is just next to H166 in the primary sequence and it has spatial proximity with the side chains of Q164, C173, and C175. It appears that these residues create a complex microenvironment around H166 that results in the decrease of its pK_a. It is important to note that out of the other two histidine residues of TDP-43^{tRRM}, H143 participates in DNA binding[25] at the near-neutral physiological pH, whereas H256 does not participate in either the function or the misfolding. Hence, decreasing the pK_a of the sole histidine residue, H166, whose protonation triggers the misfolding, might be the natural way of protecting the protein from aggregation under mild starvation stress. The protonation of a single-histidine residue near pH 4.0 has also been shown recently to partially control the misfolding of the mouse prion protein at a low pH.[71]

We observed that H166Q forms a molten globule at a low pH and a small fraction of the protein forms N-like oligomers (Figures 5C and 7). We have shown earlier that TDP-43^{tRRM} can sense pH stress and form reversible metastable assemblies[41,44] that form amyloid-like aggregates upon persistent stress. We observed that at a low pH in the presence of a small amount of salt (∼5 mM KCl), TDP-43^{tRRM} partially unfolds to form a molten globule that slowly transforms into metastable N-like oligomers.[44] Upon increasing the concentration of salt to more than 20 mM, the N-like oligomers transform to the misfolded β form.[44] At 150 mM KCl, β form is the predominantly populated form of the protein.[44] In the case of H166Q, under these conditions, only the molten globule form is predominantly populated with a small amount of N-like oligomers (Figures 5C, 6D, and 7), but not the β form. These results indicate that the protonation of H166 functions as a critical trigger switch that controls the amyloid-like misfolding of TDP-43^{tRRM} upon pH stress sensing. It appears that the protonation of H166 results in proximal or distal conformational changes that initiate the misfolding of the protein. The result of this study that protonation−deprotonation of a single side-chain residue controls the misfolding is an important step for understanding how the stress-induced misfolding of proteins can begin from site-specific triggers[44,45,47] and the design of site-specific therapeutics. The results of this study also hold significance for misfolding of prion proteins and prion diseases where the misfolding of protein begins under low-pH conditions encountered in the endocytic pathways.[72−74]

■ ASSOCIATED CONTENT

Supporting Information

The Supporting Information is available free of charge at https://pubs.acs.org/doi/10.1021/acs.jpcb.1c03262.

Calibration curve for molecular weight determination using size exclusion chromatography (Figure S1); formation of similar β form from both the N and U states of TDP-43^{tRRM} (Figure S2); relative solvent accessibilities of acidic residues of TDP-43^{tRRM} (Table S1); and thermodynamic parameters of free energy of unfolding (Table S2) (PDF)

Accession Codes

TAR DNA-binding protein 43 (TDP-43): UniProtKB/Swiss-Prot entry Q13148 (TADBP_HUMAN).

■ AUTHOR INFORMATION

Corresponding Author

Santosh Kumar Jha − *Physical and Materials Chemistry Division, CSIR-National Chemical Laboratory, Pune 411008, India; Academy of Scientific and Innovative Research (AcSIR), Ghaziabad 201002, India;* orcid.org/0000-0003-1339-7409; Phone: 91-20-25902588; Email: sk.jha@ncl.res.in; Fax: 91-20-25902615

Author

Divya Patni − *Physical and Materials Chemistry Division, CSIR-National Chemical Laboratory, Pune 411008, India; Academy of Scientific and Innovative Research (AcSIR), Ghaziabad 201002, India*

Complete contact information is available at: https://pubs.acs.org/10.1021/acs.jpcb.1c03262

Notes

The authors declare no competing financial interest.

■ ACKNOWLEDGMENTS

The authors thank Meenakshi Pillai for discussions and her comments on the manuscript. This work was funded by a SERB-DST core research grant (Project: CRG/2019/002922) to S.K.J. D.P. is a recipient of a Senior Research Fellowship awarded by Council of Scientific and Industrial Research, India.

■ REFERENCES

(1) Neumann, M.; Sampathu, D. M.; Kwong, L. K.; Truax, A. C.; Micsenyi, M. C.; Chou, T. T.; Bruce, J.; Schuck, T.; Grossman, M.; Clark, C. M.; et al. Ubiquitinated TDP-43 in Frontotemporal Lobar Degeneration and Amyotrophic Lateral Sclerosis. *Science* **2006**, *314*, 130−133.

(2) Arai, T.; Hasegawa, M.; Akiyama, H.; Ikeda, K.; Nonaka, T.; Mori, H.; Mann, D.; Tsuchiya, K.; Yoshida, M.; Hashizume, Y.; et al. TDP-43 is a Component of Ubiquitin-Positive Tau-Negative Inclusions in Frontotemporal Lobar Degeneration and Amyotrophic Lateral Sclerosis. *Biochem. Biophys. Res. Commun.* **2006**, *351*, 602−611.

(3) Strong, M. J.; Kesavapany, S.; Pant, H. C. The Pathobiology of Amyotrophic Lateral Sclerosis: A Proteinopathy? *J. Neuropathol. Exp. Neurol.* **2005**, *64*, 649−664.

(4) Rowland, L. P.; Shneider, N. A. Amyotrophic Lateral Sclerosis. *N. Engl. J. Med.* **2001**, *344*, 1688−1700.

(5) Rabinovici, G. D.; Miller, B. L. Frontotemporal Lobar Degeneration. *CNS Drugs* **2010**, *24*, 375−398.

(6) Cairns, N. J.; Neumann, M.; Bigio, E. H.; Holm, I. E.; Troost, D.; Hatanpaa, K. J.; Foong, C.; White, C. L.; Schneider, J. A.; Kretzschmar, H. A.; et al. TDP-43 in Familial and Sporadic Frontotemporal Lobar Degeneration with Ubiquitin Inclusions. *Am. J. Pathol.* **2007**, *171*, 227−240.

(7) Neary, D.; Snowden, J. S.; Mann, D. M. Classification and Description of Frontotemporal Dementias. *Ann. N. Y. Acad. Sci.* **2000**, *920*, 46−51.

(8) Neary, D.; Snowden, J. S.; Mann, D. M.; Northen, B.; Goulding, P. J.; Macdermott, N. Frontal Lobe Dementia and Motor Neuron Disease. *J. Neurol. Neurosurg. Psychiatry* **1990**, *53*, 23−32.

(9) Lee, E. B.; Lee, V. M.-Y.; Trojanowski, J. Q. Gains or Losses: Molecular Mechanisms of TDP43-Mediated Neurodegeneration. *Nat. Rev. Neurosci.* **2012**, *13*, 38−50.
(10) Dugger, B. N.; Dickson, D. W. Pathology of Neurodegenerative Diseases. *Cold Spring Harbor Perspect. Biol.* **2017**, *9*, No. a028035.
(11) Davidson, Y. S.; Raby, S.; Foulds, P. G.; Robinson, A.; Thompson, J. C.; Sikkink, S.; Yusuf, I.; Amin, H.; DuPlessis, D.; Troakes, C.; et al. TDP-43 Pathological Changes in Early Onset Familial and Sporadic Alzheimer's Disease, Late Onset Alzheimer's Disease and Down's Syndrome: Association with Age, Hippocampal Sclerosis and Clinical Phenotype. *Acta Neuropathol.* **2011**, *122*, 703−713.
(12) Sun, Y.; Chakrabartty, A. Phase to Phase with TDP-43. *Biochemistry* **2017**, *56*, 809−823.
(13) Ling, S.-C.; Polymenidou, M.; Cleveland, D. W. Converging Mechanisms in ALS and FTD: Disrupted RNA and Protein Homeostasis. *Neuron* **2013**, *79*, 416−438.
(14) Tan, R. H.; Ke, Y. D.; Ittner, L. M.; Halliday, G. M. ALS/FTLD: Experimental Models and Reality. *Acta Neuropathol.* **2017**, *133*, 177−196.
(15) Dewey, C. M.; Cenik, B.; Sephton, C. F.; Johnson, B. A.; Herz, J.; Yu, G. TDP-43 Aggregation in Neurodegeneration: Are Stress Granules The Key? *Brain Res.* **2012**, *1462*, 16−25.
(16) Colombrita, C.; Zennaro, E.; Fallini, C.; Weber, M.; Sommacal, A.; Buratti, E.; Silani, V.; Ratti, A. TDP-43 is Recruited to Stress Granules in Conditions of Oxidative Insult. *J. Neurochem.* **2009**, *111*, 1051−1061.
(17) Aulas, A.; Vande Velde, C. Alterations in Stress Granule Dynamics Driven by TDP-43 and FUS: A Link to Pathological Inclusions in ALS? *Front. Cell. Neurosci.* **2015**, *9*, No. 423.
(18) Liu-Yesucevitz, L.; Bilgutay, A.; Zhang, Y.-J.; Vanderwyde, T.; Citro, A.; Mehta, T.; Zaarur, N.; McKee, A.; Bowser, R.; Sherman, M.; et al. Tar DNA Binding Protein-43 (TDP-43) Associates with Stress Granules: Analysis of Cultured Cells and Pathological Brain Tissue. *PLoS One* **2010**, *5*, No. e13250.
(19) Parker, S. J.; Meyerowitz, J.; James, J. L.; Liddell, J. R.; Crouch, P. J.; Kanninen, K. M.; White, A. R. Endogenous TDP-43 Localized to Stress Granules Can Subsequently Form Protein Aggregates. *Neurochem. Int.* **2012**, *60*, 415−424.
(20) Hergesheimer, R. C.; Chami, A. A.; de Assis, D. R.; Vourc'h, P.; Andres, C. R.; Corcia, P.; Lanznaster, D.; Blasco, H. The Debated Toxic Role of Aggregated TDP-43 in Amyotrophic Lateral Sclerosis: A Resolution in Sight? *Brain* **2019**, *142*, 1176−1194.
(21) Dreyfuss, G.; Matunis, M. J.; Piñol-Roma, S.; Burd, C. G. hnRNP Proteins and the Biogenesis of mRNA. *Annu. Rev. Biochem.* **1993**, *62*, 289−321.
(22) Geuens, T.; Bouhy, D.; Timmerman, V. The hnRNP Family: Insights into Their Role in Health and Disease. *Hum. Genet.* **2016**, *135*, 851−867.
(23) Wang, H.-Y.; Wang, I.-F.; Bose, J.; Shen, C.-K. J. Structural Diversity and Functional Implications of the Eukaryotic TDP Gene Family. *Genomics* **2004**, *83*, 130−139.
(24) Kuo, P.-H.; Chiang, C.-H.; Wang, Y.-T.; Doudeva, L. G.; Yuan, H. S. The Crystal Structure of TDP-43 RRM1-DNA Complex Reveals the Specific Recognition for UG- and TG-Rich Nucleic Acids. *Nucleic Acids Res.* **2014**, *42*, 4712−4722.
(25) Lukavsky, P. J.; Daujotyte, D.; Tollervey, J. R.; Ule, J.; Stuani, C.; Buratti, E.; Baralle, F. E.; Damberger, F. F.; Allain, F. H. T. Molecular Basis of UG-Rich RNA Recognition by the Human Splicing Factor TDP-43. *Nat. Struct. Mol. Biol.* **2013**, *20*, 1443−1449.
(26) Qin, H.; Lim, L.-Z.; Wei, Y.; Song, J. TDP-43 N Terminus Encodes a Novel Ubiquitin-Like Fold and its Unfolded Form in Equilibrium That Can Be Shifted by Binding to ssDNA. *Proc. Natl. Acad. Sci. U.S.A.* **2014**, *111*, 18619−18624.
(27) Jiang, L.-L.; Xue, W.; Hong, J.-Y.; Zhang, J.-T.; Li, M.-J.; Yu, S.-N.; He, J.-H.; Hu, H.-Y. The N-Terminal Dimerization is Required for TDP-43 Splicing Activity. *Sci. Rep.* **2017**, *7*, No. 6196.
(28) Conicella, A. E.; Zerze, G. H.; Mittal, J.; Fawzi, N. L. ALS Mutations Disrupt Phase Separation Mediated by Helical Structure in the TDP-43 Low Complexity C-Terminal Domain. *Structure* **2016**, *24*, 1537−1549.
(29) Winton, M. J.; Igaz, L. M.; Wong, M. M.; Kwong, L. K.; Trojanowski, J. Q.; Lee, V. M.-Y. Disturbance of Nuclear and Cytoplasmic TAR DNA-Binding Protein (TDP-43) Induces Disease-Like Redistribution, Sequestration, and Aggregate Formation. *J. Biol. Chem.* **2008**, *283*, 13302−13309.
(30) Ou, S. H.; Wu, F.; Harrich, D.; García-Martínez, L. F.; Gaynor, R. B. Cloning and Characterization of a Novel Cellular Protein, TDP-43, That Binds to Human Immunodeficiency Virus Type 1 Tar DNA Sequence Motifs. *J. Virol.* **1995**, *69*, 3584−3596.
(31) François-Moutal, L.; Perez-Miller, S.; Scott, D. D.; Miranda, V. G.; Mollasalehi, N.; Khanna, M. Structural Insights into TDP-43 and Effects of Post-Translational Modifications. *Front. Mol. Neurosci.* **2019**, *12*, No. 301.
(32) Ratti, A.; Buratti, E. Physiological Functions and Pathobiology of TDP-43 and FUS/TLS Proteins. *J. Neurochem.* **2016**, *138*, 95−111.
(33) Ayala, Y. M.; Pantano, S.; D'Ambrogio, A.; Buratti, E.; Brindisi, A.; Marchetti, C.; Romano, M.; Baralle, F. E. Human, Drosophila, and C.Elegans TDP43: Nucleic Acid Binding Properties and Splicing Regulatory Function. *J. Mol. Biol.* **2005**, *348*, 575−588.
(34) Lagier-Tourenne, C.; Polymenidou, M.; Cleveland, D. W. TDP-43 and FUS/TLS: Emerging Roles in RNA Processing and Neurodegeneration. *Hum. Mol. Genet.* **2010**, *19*, R46−R64.
(35) Buratti, E.; Dörk, T.; Zuccato, E.; Pagani, F.; Romano, M.; Baralle, F. E. Nuclear Factor TDP-43 and SR Proteins Promote in Vitro and in Vivo CFTR Exon 9 Skipping. *EMBO J.* **2001**, *20*, 1774−1784.
(36) Deshaies, J.-E.; Shkreta, L.; Moszczynski, A. J.; Sidibé, H.; Semmler, S.; Fouillen, A.; Bennett, E. R.; Bekenstein, U.; Destroismaisons, L.; Toutant, J.; et al. TDP-43 Regulates the Alternative Splicing of hnRNP A1 to Yield an Aggregation-Prone Variant in Amyotrophic Lateral Sclerosis. *Brain* **2018**, *141*, 1320−1333.
(37) Ayala, Y. M.; De Conti, L.; Avendaño-Vázquez, S. E.; Dhir, A.; Romano, M.; D'Ambrogio, A.; Tollervey, J.; Ule, J.; Baralle, M.; Buratti, E.; et al. TDP-43 Regulates its mRNA Levels Through a Negative Feedback Loop. *EMBO J.* **2011**, *30*, 277−288.
(38) Buratti, E.; Baralle, F. E. Characterization and Functional Implications of the RNA Binding Properties of Nuclear Factor TDP-43, A Novel Splicing Regulator of CFTR Exon 9. *J. Biol. Chem.* **2001**, *276*, 36337−36343.
(39) Sephton, C. F.; Cenik, B.; Cenik, B. K.; Herz, J.; Yu, G. TDP-43 in Central Nervous System Development and Function: Clues to TDP-43-Associated Neurodegeneration. *Biol. Chem.* **2012**, *393*, 589−594.
(40) Sephton, C. F.; Good, S. K.; Atkin, S.; Dewey, C. M.; Mayer, P.; Herz, J.; Yu, G. TDP-43 is a Developmentally Regulated Protein Essential for Early Embryonic Development. *J. Biol. Chem.* **2010**, *285*, 6826−6834.
(41) Pillai, M.; Jha, S. K. The Folding and Aggregation Energy Landscapes of Tethered RRM Domains of Human TDP-43 are Coupled Via a Metastable Molten Globule-Like Oligomer. *Biochemistry* **2019**, *58*, 608−620.
(42) Zacco, E.; Graña-Montes, R.; Martin, S. R.; de Groot, N. S.; Alfano, C.; Tartaglia, G. G.; Pastore, A. RNA as a Key Factor in Driving or Preventing Self-Assembly of the TAR DNA-Binding Protein 43. *J. Mol. Biol.* **2019**, *431*, 1671−1688.
(43) Garnier, C.; Devred, F.; Byrne, D.; Puppo, R.; Roman, A. Y.; Malesinski, S.; Golovin, A. V.; Lebrun, R.; Ninkina, N. N.; Tsvetkov, P. O. Zinc Binding to RNA Recognition Motif of TDP-43 Induces the Formation of Amyloid-Like Aggregates. *Sci. Rep.* **2017**, *7*, No. 6812.
(44) Pillai, M.; Jha, S. K. Early Metastable Assembly During the Stress-Induced Formation of Worm-Like Amyloid Fibrils of Nucleic Acid Binding Domains of TDP-43. *Biochemistry* **2020**, *59*, 315−328.
(45) Kroschwald, S.; Munder, M. C.; Maharana, S.; Franzmann, T. M.; Richter, D.; Ruer, M.; Hyman, A. A.; Alberti, S. Different Material States of Pub1 Condensates Define Distinct Modes of Stress Adaptation and Recovery. *Cell Rep.* **2018**, *23*, 3327−3339.

https://doi.org/10.1021/acs.jpcb.1c03262
J. Phys. Chem. B 2021, 125, 8383−8394

(46) Riback, J. A.; Katanski, C. D.; Kear-Scott, J. L.; Pilipenko, E. V.; Rojek, A. E.; Sosnick, T. R.; Drummond, D. A. Stress-Triggered Phase Separation is an Adaptive, Evolutionarily Tuned Response. *Cell* **2017**, *168*, 1028−1040.
(47) Rabouille, C.; et al. Cell Adaptation Upon Stress: The Emerging Role of Membrane-Less Compartments. *Curr. Opin. Cell Biol.* **2017**, *47*, 34−42.
(48) Petrovska, I.; Nüske, E.; Munder, M. C.; Kulasegaran, G.; Malinovska, L.; Kroschwald, S.; Richter, D.; Fahmy, K.; Gibson, K.; Verbavatz, J.-M.; et al. Filament Formation by Metabolic Enzymes is a Specific Adaptation to an Advanced State of Cellular Starvation. *eLife* **2014**, *3*, No. e02409.
(49) Kroschwald, S.; Alberti, S. Gel or Die: Phase Separation as a Survival Strategy. *Cell* **2017**, *168*, 947−948.
(50) Munder, M. C.; Midtvedt, D.; Franzmann, T.; Nüske, E.; Otto, O.; Herbig, M.; Ulbricht, E.; Müller, P.; Taubenberger, A.; Maharana, S.; et al. A pH-Driven Transition of the Cytoplasm from a Fluid- to a Solid-Like State Promotes Entry into Dormancy. *eLife* **2016**, *5*, No. e09347.
(51) Franzmann, T. M.; Jahnel, M.; Pozniakovsky, A.; Mahamid, J.; Holehouse, A. S.; Nüske, E.; Richter, D.; Baumeister, W.; Grill, S. W.; Pappu, R. V.; et al. Phase Separation of a Yeast Prion Protein Promotes Cellular Fitness. *Science* **2018**, *359*, No. eaao5654.
(52) Mishra, P.; Patni, D.; Jha, S. K. A pH-Dependent Protein Stability Switch Coupled to the Perturbed pK_a of a Single Ionizable Residue. *Biophys. Chem.* **2021**, *274*, No. 106591.
(53) Savojardo, C.; et al. Mapping OMIM Disease-Related Variations on Protein Domains Reveals an Association Among Variation Type, Pfam Models, and Disease Classes. *Front. Mol. Biosci.* **2021**, *8*, No. 617016.
(54) Gill, S. C.; von Hippel, P. H. Calculation of Protein Extinction Coefficients from Amino Acid Sequence Data. *Anal. Biochem.* **1989**, *182*, 319−326.
(55) Stryer, L. The Interaction of a Naphthalene Dye with Apomyoglobin and Apohemoglobin. A Fluorescent Probe of Non-Polar Binding Sites. *J. Mol. Biol.* **1965**, *13*, 482−495.
(56) Kabsch, W.; Sander, C. Dictionary of Protein Secondary Structure: Pattern Recognition of Hydrogen-Bonded and Geometrical Features. *Biopolymers* **1983**, *22*, 2577−2637.
(57) Gong, H.; Zhang, H.; Zhu, J.; Wang, C.; Sun, S.; Zheng, W.-M.; Bu, D. Improving Prediction of Burial State of Residues by Exploiting Correlation Among Residues. *BMC Bioinform.* **2017**, *18*, No. 70.
(58) Tien, M. Z.; Meyer, A. G.; Sydykova, D. K.; Spielman, S. J.; Wilke, C. O. Maximum Allowed Solvent Accessibilites of Residues in Proteins. *PLoS One* **2013**, *8*, No. e80635.
(59) Mishra, P.; Jha, S. K. An Alternatively Packed Dry Molten Globule-Like Intermediate in the Native State Ensemble of a Multidomain Protein. *J. Phys. Chem. B* **2017**, *121*, 9336−9347.
(60) Bolen, D. W.; Santoro, M. M. Unfolding Free Energy Changes Determined by the Linear Extrapolation Method. 2. Incorporation of $\Delta G_{N\text{-}U}^{\circ}$ Values in a Thermodynamic Cycle. *Biochemistry* **1988**, *27*, 8069−8074.
(61) Naiki, H.; Gejyo, F. Kinetic Analysis of Amyloid Fibril Formation. *Methods Enzymol.* **1999**, *309*, 305−318.
(62) Sun, Y.; Medina Cruz, A.; Hadley, K. C.; Galant, N. J.; Law, R.; Vernon, R. M.; Morris, V. K.; Robertson, J.; Chakrabartty, A. Physiologically Important Electrolytes as Regulators of TDP-43 Aggregation and Droplet-Phase Behavior. *Biochemistry* **2019**, *58*, 590−607.
(63) Adachi, M.; Noji, M.; So, M.; Sasahara, K.; Kardos, J.; Naiki, H.; Goto, Y. Aggregation-Phase Diagrams of β 2-Microglobulin Reveal Temperature and Salt Effects on Competitive Formation of Amyloids Versus Amorphous Aggregates. *J. Biol. Chem.* **2018**, *293*, 14775−14785.
(64) Khurana, R.; Udgaonkar, J. B. Equilibrium Unfolding Studies of Barstar: Evidence for an Alternative Conformation Which Resembles a Molten Globule. *Biochemistry* **1994**, *33*, 106−115.
(65) Orij, R.; Brul, S.; Smits, G. J. Intracellular pH is a Tightly Controlled Signal in Yeast. *Biochim. Biophys. Acta* **2011**, *1810*, 933−944.
(66) Bentmann, E.; Neumann, M.; Tahirovic, S.; Rodde, R.; Dormann, D.; Haass, C. Requirements for Stress Granule Recruitment of Fused in Sarcoma (FUS) and Tar DNA-Binding Protein of 43 kDa (TDP-43). *J. Biol. Chem.* **2012**, *287*, 23079−23094.
(67) Mann, J. R.; Gleixner, A. M.; Mauna, J. C.; Gomes, E.; DeChellis-Marks, M. R.; Needham, P. G.; Copley, K. E.; Hurtle, B.; Portz, B.; Pyles, N. J.; et al. RNA Binding Antagonizes Neurotoxic Phase Transitions of TDP-43. *Neuron* **2019**, *102*, 321−338.
(68) Medina, E.; Villalobos, P.; Coñuecar, R.; Ramírez-Sarmiento, C. A.; Babul, J. The Protonation State of an Evolutionarily Conserved Histidine Modulates Domainswapping Stability of FoxP1. *Sci. Rep.* **2019**, *9*, No. 5441.
(69) Hu, J.; Fu, R.; Nishimura, K.; Zhang, L.; Zhou, H.-X.; Busath, D. D.; Vijayvergiya, V.; Cross, T. A. Histidines, Heart of the Hydrogen Ion Channel from Influenza A Virus: Toward an Understanding of Conductance and Proton Selectivity. *Proc. Natl. Acad. Sci. U.S.A.* **2006**, *103*, 6865−6870.
(70) Rötzschke, O.; Lau, J. M.; Hofstätter, M.; Falk, K.; Strominger, J. L. A pH-Sensitive Histidine Residue as Control Element for Ligand Release from HLA-DR Molecules. *Proc. Natl. Acad. Sci. U.S.A.* **2002**, *99*, 16946−16950.
(71) Singh, J.; Udgaonkar, J. B. Unraveling the Molecular Mechanism of pH-Induced Misfolding and Oligomerization of the Prion Protein. *J. Mol. Biol.* **2016**, *428*, 1345−1355.
(72) Borchelt, D. R.; Taraboulos, A.; Prusiner, S. B. Evidence for Synthesis of Scrapie Prion Proteins in the Endocytic Pathway. *J. Biol. Chem.* **1992**, *267*, 16188−16199.
(73) Arnold, J. E.; Tipler, C.; Laszlo, L.; Hope, J.; Landon, M.; Mayer, R. J. The Abnormal Isoform of the Prion Protein Accumulates in Late-Endosome-Like Organelles in Scrapie-Infected Mouse Brain. *J. Pathol.* **1995**, *176*, 403−411.
(74) Sunyach, C.; Jen, A.; Deng, J.; Fitzgerald, K. T.; Frobert, Y.; Grassi, J.; McCaffrey, M. W.; Morris, R. The Mechanism of Internalization of Glycosylphosphatidylinositol-Anchored Prion Protein. *EMBO J.* **2003**, *22*, 3591−3601.

https://doi.org/10.1021/acs.jpcb.1c03262
J. Phys. Chem. B 2021, 125, 8383−8394

BBA - Proteins and Proteomics 1871 (2023) 140916

Contents lists available at ScienceDirect

BBA - Proteins and Proteomics

journal homepage: www.elsevier.com/locate/bbapap

Research Paper

Thermodynamic modulation of folding and aggregation energy landscape by DNA binding of functional domains of TDP-43

Divya Patni [a,b], Santosh Kumar Jha [a,b,*]

[a] Physical and Materials Chemistry Division, CSIR-National Chemical Laboratory, Dr. Homi Bhabha Road, Pune 411008, Maharashtra, India
[b] Academy of Scientific and Innovative Research (AcSIR), Ghaziabad 201002, India

ARTICLE INFO

Keywords:
TDP-43
Amyloid-like aggregation
Thermodynamic stability
RNA recognition motifs (RRMs)
Nucleic acid binding

ABSTRACT

TDP-43 is a vital nucleic acid binding protein which forms stress-induced aberrant aggregates in around 97% cases of ALS, a fatal neurodegenerative disease. The functional tandem RRM domain of the protein (TDP-43^{tRRM}) has been shown to undergo amyloid-like aggregation under stress in a pH-dependent fashion. However, the underlying thermodynamic and molecular basis of aggregation and how the energy landscape of folding, stability, and aggregation are coupled and modulated by nucleic acid binding is poorly understood. Here, we show that the pH stress thermodynamically destabilizes the native protein and systematically populates the unfolded-like aggregation-prone molecules which leads to amyloid-like aggregation. We observed that specific DNA binding inhibits aggregation and populates native-like compact monomeric state even under low-pH stress as measured by circular dichroism, ANS binding, size exclusion chromatography, and transmission electron microscopy. We show that DNA-binding thermodynamically stabilizes and populates the native state even under stress and reduces the population of unfolded-like aggregation-prone molecules which leads to systematic aggregation inhibition. Our results suggest that thermodynamic modulation of the folding and aggregation energy landscape by nucleic-acid-like molecules could be a promising approach for effective therapeutic intervention in TDP-43-associated proteinopathies.

1. Introduction

TAR DNA binding protein (TDP-43) is a ubiquitously expressed member of the heterogeneous nuclear ribonucleoprotein family (hnRNP) [1,2]. It is a 414 amino acid-long multidomain protein (Fig. 1). It consists of an N-terminal domain (NTD), two tandem RNA recognition motifs (RRM 1 and RRM 2, referred to as TDP-43^{tRRM}), and a C-terminal domain (CTD) [3]. TDP-43^{tRRM} is the primary functional domain of the protein, which associates explicitly with the UG and TG-rich nucleic acid sequences [4]. These motifs were highly conserved throughout evolution [5,6]. Under normal physiological conditions, TDP-43 predominately resides in the nucleus but often shuttles to the cytoplasm to perform some of its functions [7,8]. In its native state, TDP-43, with the help of TDP-43^{tRRM}, performs crucial functions like mRNA splicing [9–11], mRNA transcription [12,13], non-coding RNA processing [14], embryonic development [15], and CNS development [16]. TDP-43 is also involved in mRNA stability [17–20], and mRNA transport [21], along with self-regulating its level in the cells [22]. However, it has been observed that TDP-43 loses its natively folded conformation under stress conditions [23,24]. Cytoplasmic aggregates of the TDP-43 have been predominately found in amyotrophic lateral sclerosis (ALS), the adult-onset motor neuron disease [25], and frontotemporal lobar degeneration (FTLD), the second most common form of pre-senile dementia [23,26,27]. In addition to these diseases, aggregates of TDP-43 have also been associated with Huntington's disease [28], Alzheimer's disease [29,30], and Parkinson's disease [31]. These diseases are collectively

Abbreviations: TDP-43, TAR-DNA binding protein-43; NTD, N-terminal domain; RRM, RNA Recognition Motifs; CTD, C-terminal domain; TDP-43^{tRRM}, RRM1 and RRM2; ALS, amyotrophic lateral sclerosis; FTLD, frontotemporal lobar degeneration; ss, single stranded; ss(TG)$_6$-TDP-43^{tRRM}, ss(TG)$_6$ bound TDP-43^{tRRM}; CD, circular dichroism; ANS, 8-anilino-1-naphthalenesulfonic acid; ThT, thioflavin T; SEC, size exclusion chromatography; TEM, transmission electron microscope; λ_{max}^{em}, the maximum fluorescence emission; f_U, fraction unfolded; C_m, midpoint of unfolding; T_m, midpoint of thermal unfolding; N, native; $\triangle G_{NU}^{H_2O}$, free energy of unfolding at 0 M denaturant..

* Corresponding author at: Physical and Materials Chemistry Division, CSIR-National Chemical Laboratory, Dr. Homi Bhabha Road, Pune 411008, Maharashtra, India.
E-mail address: sk.jha@ncl.res.in (S.K. Jha).

https://doi.org/10.1016/j.bbapap.2023.140916
Received 4 January 2023; Received in revised form 31 March 2023; Accepted 11 April 2023
Available online 13 April 2023

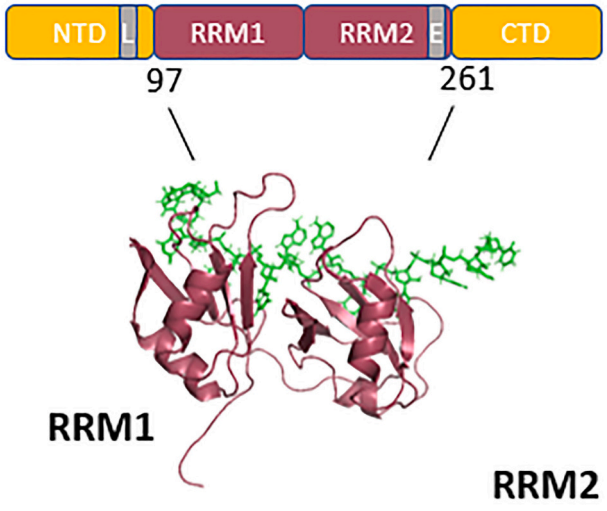

Fig. 1. TDP-43 binds to nucleic acid. Schematic depiction of the full-length TDP-43 constituting NTD: N-terminal domain-involved in dimerization; RRM1, RRM2: two tethered RNA recognition motifs (tRRM)-binds specifically to UG-rich RNA and TG-rich DNA [6] and therefore are the major functional domains of TDP-43; CTD: C-terminal domain-involved in the protein-protein interactions; L and E: nuclear localization and nuclear export sequence, respectively, which shuttles TDP-43 in and out of the nucleus. A structural representation of the nucleic acid binding domain of TDP-43 with its binding partner RNA (PDB ID: 4BS2) is shown below. The green colour depicts RNA. The image is created from the PDB file 4BS2 using PyMOL Molecular Graphics System. (For interpretation of the references to colour in this figure legend, the reader is referred to the web version of this article.)

termed TDP-43 proteinopathies [32–35]. It is noteworthy that due to the lack of understanding of the mechanism of TDP-43 aggregation and aggregation inhibition under stress conditions, these neurodegenerative disorders remain incurable till date.

The majority of the research has focused on deciphering the role of both N and C-terminal domains on the aggregation of TDP-43 [36–42]. A few studies on the C-terminal fragments suggest that the glycine-rich region and the Q/N (glutamine/aspargine) rich region of CTD play an important role in the aggregation [37–41]. Interestingly, small peptides in the CTD have also been shown to undergo fibrilization in vitro [40,43]. Moreover, C-terminal fragments of various lengths have been implicated in TDP-43-associated pathogenesis [44–50]. Furthermore, CTD has also been shown to undergo liquid-liquid phase separation [51,52]. On the other hand, NTD facilitates dimer and higher-order oligomer formation [53–56]. NTD oligomerization is also involved in droplet formation by full-length TDP-43 [57]. Removal of the first few residues of NTD annihilates the aggregation propensity of the TDP-43 [58]. N-terminal fragments were found lethal as they trigger motor dysfunction in mice [42]. However, the role of TDP-43^{tRRM} in aggregation is poorly understood. With the increased association of TDP-43 with different neurodegenerative diseases, it becomes crucial to study the role of different domains in disease onset. Recent accumulating evidence suggests the role of RRMs in the formation of aberrant aggregates [40,59–63]. As TDP-43^{tRRM} associates with the nucleic acids to perform its functions, dissecting their impact on the aggregation behavior of TDP-43 could help establish the role of TDP-43^{tRRM} and their interaction with nucleic acids in aggregation control.

The binding with nucleic acids has been shown to modulate the self-assembly energy landscape of TDP-43 and its multiple fragments and variants [64–66]. It has been observed that binding to single-stranded (ss) DNA enhances the solubility of TDP-43 purified from a rabbit reticulocyte cell-free system [66]. The binding to ss$(TG)_{12}$ also enhances the solubility of a yellow fluorescent protein (YFP)-tagged TDP-43 [65]. RNA binding has also been shown to promote liquid-liquid phase separation of SUMO-tagged TDP-43 and low complexity domain of TDP-43 [64]. Interestingly, in a separate study, it has been observed using an optogenetic approach that RNA binding antagonizes the phase transition of various variants of TDP-43 containing the RRM domains [67]. Recently, it has been observed that nucleic acid binding inhibits the thermal aggregation of a variant consisting of N-terminal along with TDP-43^{tRRM} (N-RRM1-2) [68]. However, the underlying thermodynamic and molecular basis of aggregation and how the energy landscape of folding, stability, and aggregation are coupled and modulated by nucleic acid binding is not well understood. This knowledge could help in the identification of the natural binding partners, which could prove beneficial in designing the therapeutic strategy against the detrimental aggregation of proteins.

TDP-43^{tRRM} has been shown to undergo pH-dependent amyloid-like aggregation in the presence of physiological salt concentration [62,69,70]. In the current study, we show that the specific binding of a single-stranded DNA oligo (ss$(TG)_6$) inhibits the pH-dependent amyloid-like aggregation of TDP-43^{tRRM}. We also observed that DNA-binding keeps the protein in the native-like monomeric state even at low pH as measured by circular dichroism (CD), ANS assay, and size exclusion chromatography (SEC). TEM studies show that in the DNA-bound protein does not show the ordered morphology of amyloid-like fibrils under aggregation conditions. We observed that pH decreases the thermodynamic stability of TDP-43^{tRRM} and reduces the mid-point of unfolding (C_m) from 2.2 to 1.3 M [GdmCl] as we go down from pH 7.5 to 5.0. This destabilization initiates the amyloid-like aggregation below pH 5.0. The ss$(TG)_6$ binding increases the thermodynamic stability of TDP-43^{tRRM}, making it more stable even at low pH and hence, ss$(TG)_6$ bound TDP-43^{tRRM} (ss$(TG)_6$-TDP-43^{tRRM}) does not undergo amyloid-like aggregation. Our study suggests that modulation of the self assembly energy landscape by natural binding ligands could be exploited for therapeutic strategies against aggregation-prone proteins.

2. Materials and methods

2.1. Chemicals and buffers

All the chemicals and buffers were procured from HiMedia, Sigma, and Sisco Research Laboratories (SRL) and were used directly without further purification. The buffers that were used for pH-dependent studies are as follows: 20 mM glycine-HCl (pH 3.0–3.5), 20 mM sodium acetate (pH 3.8–5.0), 20 mM 2-(N-Morpholino) ethanesulfonic acid (MES) (pH 5.5–6.0), 20 mM 3-(N-Morpholino) propanesufonic acid (MOPS) (pH 6.5–7.5) and 20 mM Tris (pH 8.0). All the buffers contained 150 mM KCl. 1 mM DTT (dithiothreitol) was added to the buffers before the experiments. All the buffers were filtered with a 0.2 μm filter before use.

2.2. Expression and purification of TDP-43^{tRRM}

We followed the previously reported protocol to express and purify TDP-43^{tRRM} (UniProtKB/Swiss-Prot entry Q13148) [62]. In brief, the induced BL21(DE3) *Escherichia coli* cells were sonicated, and the supernatant was passed through Ni Sepharose 6-Fast Flow beads (GE Healthcare) to separate His_6-tagged TDP-43^{tRRM}. The eluted protein was buffer exchanged in protease cleavage buffer followed by overnight cleavage of the His_6-tag by PreScission protease at 15 °C. The purified His_6-tag cleaved TDP-43^{tRRM} was stored in a storage buffer (10 mM KPi, 150 mM KCl, 5% glycerol, and 1 mM DTT). The purity of the protein was confirmed by SDS-PAGE (sodium dodecyl sulfate-polyacrylamide gel electrophoresis). The protein concentration was measured by UV-VIS spectroscopy using an extinction coefficient of 15,470 M^{-1} cm^{-1} at 280 nm. The molecular weight of the purified and His_6 tagged-cleaved TDP-43^{tRRM} protein as determined by Synapt G2 HD mass spectrometer (Waters) was 19,429 Da.

2.3. Preparation of DNA bound sample

Single-stranded (ss) ss$(TG)_6$, ss$(CA)_6$, and ss$(TG)_{12}$ DNA oligos were procured from Integrated DNA Technologies (IDT). The 1 M DNA oligos stock was prepared in HyPure™ Molecular Biology Grade Water (nuclease-free, deionized, distilled-GE Lifesciences). Further dilutions were made as per the requirement and their concentrations were checked using an extinction coefficient of 113,000 M^{-1} cm^{-1} for ss$(TG)_6$, 119,200 M^{-1} cm^{-1} for ss$(CA)_6$ and 225,800 M^{-1} cm^{-1} for ss$(TG)_{12}$ at 260 nm. The values of the extinction coefficients were taken from the manual provided along with DNA oligos. For the preparation of the DNA-bound TDP-43^{tRRM} samples (ss(DNA)-TDP-43^{tRRM}), the required ratios of the ss(DNA) and TDP-43^{tRRM} were mixed and allowed to incubate at pH 7.2 for 2 h, followed which all the experiments were performed.

2.4. Steady-state fluorescence anisotropy measurements

Steady-state fluorescence anisotropy was measured on a Fluoromax-4 spectrofluorometer from HORIBA Scientific, coupled to the FM4-Pol polarization accessory in the L-format configuration. The ss$(TG)_6$ conjugated with 6-carboxyfluorescein at its 5′ end (labeled ss$(TG)_6$) was purchased from IDT. The oligo was dissolved in HyPure™ Molecular Biology Grade Water. The concentration of the labeled ss$(TG)_6$ was confirmed by taking the absorbance at 260 nm and using an extinction coefficient of 133,960 M^{-1} cm^{-1}. To estimate the anisotropy, an increasing concentration of TDP-43^{tRRM} (0–2 μM) was incubated with 30 nM of labeled ss$(TG)_6$. The incubation was conducted in pH 7.5 buffer for 2.5 h at room temperature. The anisotropy data was acquired by exciting the labeled ss$(TG)_6$ at 482 nm and collecting the emission at 515 nm.. All the measurements were carried out in a quartz cuvette with a path length of 1 cm. The fluorescence anisotropy (r) and emission intensity (I) are related to each other by

$$r = \frac{I_{VV} - I_{VH}G}{I_{VV} + 2I_{VH}G} \quad (1)$$

where subscript V (vertical) and H (horizontal) refer to the position of the polarizer in the excitation beam (first subscript) and emission beam (second subscript) for every measurement performed. G refers to the instrumental correction factor and is given by I_{HV}:I_{HH}.

The binding affinity of the 6-carboxyfluorescein labeled ss$(TG)_6$ for TDP-43^{tRRM} was calculated by fitting the obtained binding curve to the equation:

$$\Delta r = n\,\frac{[TDP - 43^{tRRM}]}{[TDP - 43^{tRRM}] + K_d} \quad (2)$$

where Δr is the buffer subtracted anisotropy signal, [TDP-43^{tRRM}] is the protein concentration, n is the valency of the interaction of DNA and protein, and K_d refers to the dissociation constant.

2.5. Size exclusion chromatography

The size exclusion chromatography (SEC) of the free and the ss$(TG)_6$-TDP-43^{tRRM} was performed on the AKTA Pure M FPLC system (GE Healthcare). A Superdex™ 75 10/300 GL size exclusion column having a fractionation range of 3 kDa–70 kDa was used. The bed and void volume of the column is 23.5 mL and 7.2 mL, respectively.

Free TDP-43^{tRRM} (8 μM - 10 μM) was incubated with pH 3.0 and pH 7.5 buffer. For the SEC study of the bound sample, ss$(TG)_6$-TDP-43^{tRRM} complex was prepared at pH 7.5 and later incubated with pH 3.0 and pH 7.5 buffer for 30 min. The final concentration of the TDP-43^{tRRM} and ss$(TG)_6$ was 8 μM and 10 μM, respectively. All the buffers used in the SEC contained 150 mM KCl. The column was pre-equilibrated with required buffers of respective pH. The flow rate used was 0.8 mL/min. All the experiments were performed at 4 °C.

To determine the apparent molecular weight (M_W^{app}) of the TDP-43^{tRRM} under different conditions, we created the calibration curve between the partition coefficient (K_{av}) of the five standard biomolecules (bovine serum albumin (BSA), ovalbumin, ribonuclease A, aprotinin and vitamin B12) and their respective molecular weights [70]. The calibration curve was further used to deduce M_W^{app} based on the elution volume of the sample.

2.6. Circular dichroism (CD)

The far-UV CD measurements were performed on a Jasco J-815 spectropolarimeter using a data integration time of 4 s, bandwidth of 2 nm, data pitch of 1 nm, and a scan speed of 20 nm/min at a constant temperature of 20 °C. Each CD spectrum collected was an average of at least two accumulations and was acquired with the help of a quartz cuvette with a path length of 1 mm. The spectra were collected in the wavelength range from 205 to 250 nm. The concentration of free TDP-43^{tRRM} used was 8 μM. For acquiring the far-UV CD of ss(DNA)-TDP-43^{tRRM}, their preformed complex was diluted with respective buffers to make a final concentration of 10–11 μM of ssDNA and 8–10 μM of TDP-43^{tRRM}. Buffer spectra were acquired under similar conditions for all the buffer conditions and were subtracted from the CD spectra of each sample.

2.7. Analysis of the pH dependence of the N⇌ β transition

We have fitted the pH-dependent spectroscopic data by assuming the protonation of a single critical residue in the transition of the native-state (N) to β form, as discussed previously [70] using the scheme:

$$N + H^+ \rightleftharpoons NH^+ \rightleftharpoons \beta \quad \text{(Scheme 1)}$$

In the above scheme, it is assumed that only NH^+ is capable of transitioning to β [71]. In that case, the pH dependence is that of the protonation of N and is given by a transformation of the Henderson-Hasselbalch equation:

$$Y_{obs} = \frac{Y_{NH^+} + Y_N 10^{(pH - pK_a)}}{1 + 10^{(pH - pK_a)}} \quad (3)$$

where Y_{obs} corresponds to the observed spectroscopic signal at a particular pH value; Y_N and Y_{NH^+} correspond to the N form and the protonated NH^+ form signals, respectively. It is assumed that under the experimental conditions and the protein concentrations used in this study, $NH^+ \rightleftharpoons \beta$ equilibrium ultimately favors the β form. Hence, the amount of NH^+ is equal to the amount of the β form.

2.8. Dissociation kinetics of the β⇌N transition

We monitored the dissociation kinetics of β⇌N transition using ThT assay. The β form (80 μM) was prepared from the N-state by performing pH jump from pH 7.5 to pH 3.8. The sample was allowed to incubate for 2 h. The incubation was followed by a 10-fold jump to pH 7.5 (β to N) and to pH 3.8 (β to β). For the native control, the N-state (80 μM) was prepared from the N-state by performing pH jump from pH 7.5 to pH 7.5. The final sample was prepared by performing 10-fold jump to the pH 7.5 buffer. The final concentration of the protein was 8 μM.

At different times of the reaction, the required amount of the protein was taken from the above samples and assayed for the amount of the β form using ThT assay. The ThT fluorescence assay was performed in 50 mM pH 8.0 Tris buffer. The concentration of the protein was 1 μM while that of ThT was 40 μM. The ThT fluorescence was measured within 1 min of protein addition. The samples were excited at 440 nm, and emission was collected from 460 nm to 600 nm. The excitation and emission slit widths used were 4 nm. Fluorescence of the free ThT dye was also acquired under similar settings before every ThT acquisition. All the data have been buffer subtracted.

Far-UV CD spectra of the samples were also acquired at the end of the reaction using similar settings as mentioned above at 25 °C, and all the spectra were buffer subtracted.

2.9. Reversibility of N⇌β transition

The reversibility of the N⇌β transition was monitored using circular dichroism. The β form (62.6 μM) was prepared from the N-state by performing pH jump from pH 7.5 to pH 3.0. The sample was allowed to incubate for 2 h. The incubation was followed by a 10-fold jump to different pH (7.5–3.0). For control, the N-state was also prepared using a similar sequence of dilution in the native buffer. The final concentration of the protein was 6.26 μM.

Equilibrium far-UV CD signals were acquired at 216 nm using a data integration time of 2 s, bandwidth of 2 nm, and data pitch of 1 s. The values plotted are an average of data acquired for 30 s. All the signals were buffer subtracted.

2.10. Transmission electron microscopy

The free TDP-43^{tRRM} (1 μM) and ss(TG)$_6$-TDP-43^{tRRM} (1.5 μM ss(TG)$_6$ and 1 μM TDP-43^{tRRM}) were incubated at pH 3.8 buffer for 45 min. 10 μL of these samples were placed on the copper-coated 300 mesh grid (Electron Microscopy Science) for 5 min. The excess sample was removed, followed by a milliQ wash for 30 s. 2% uranyl acetate was used for 1.5 min to stain the samples negatively. The excess stain was removed with MilliQ water. The samples were then covered and allowed to dry overnight and imaged under Technai-T20 at an accelerating voltage of 200 kV.

2.11. 8-Anilino-1-naphthalenesulfonic acid (ANS) fluorescence assay

A stock solution of 10 mM ANS was prepared in Dimethyl Sulfoxide (DMSO). The concentration of the ANS solution was confirmed using absorbance measurement at 350 nm with an extinction coefficient of 5000 M^{-1} cm^{-1} [72]. Pre-equilibrated free TDP-43^{tRRM} (2 μM), and ss(TG)$_6$ -TDP-43^{tRRM} (2 μM TDP-43^{tRRM} and 5 μM ss(TG)$_6$) were incubated in 60 μM ANS for 15 min. The fluorescence spectrum for each sample was measured by exciting ANS at 380 nm and obtaining emissions from 400 to 600 nm.

2.12. GdmCl-mediated equilibrium unfolding experiments

The GdmCl-mediated equilibrium unfolding experiments were performed under different pH conditions (3.0–8.0). TDP-43^{tRRM} (4 μM) was incubated with a gradient of GdmCl concentration for 3 h at room temperature. Tryptophan present in TDP-43^{tRRM} was excited at 280 nm, and the emission spectrum was acquired from 295 nm to 380 nm. The fluorescence spectra of buffers were collected under similar settings and were subtracted from each fluorescence spectrum. Fluoromax-4 spectrofluorometer from HORIBA Scientific was used for the measurements.

The transitions were analyzed using a two-step N⇌U model. The fraction of unfolded states (f_U) at any particular denaturant concentration were calculated using the following equation:

$$f_U = \frac{Y_o - (Y_N + m_N{*}[D])}{(Y_U + m_U{*}[D]) - (Y_N + m_N{*}[D])} \quad (4)$$

where Y_O is the observed MRE signal being measured at different denaturant concentrations [D]. Y_N and Y_U refer to the intercepts, whereas m_N and m_U are the slopes of native and unfolded baseline, respectively [73,74].

f_U is related to the equilibrium constant (K_{eq}) by the relationship: $K_{eq} = f_U/(1\text{-}f_U)$. K_{eq} is further related to free energy ΔG_{NU} by the relationship: $\Delta G_{NU} = -RTlnK_{eq}$. f_U and ΔG_{NU} are related by a modification of Gibbs Helmholtz equation:

$$f_U = \frac{e^{\frac{-\triangle G_{NU}}{RT}}}{1 + e^{\frac{-\triangle G_{NU}}{RT}}} \quad (5)$$

where R refers to the gas constant and ΔG_{NU} is the free energy of N⇋U transition. It is related to denaturant concentration [D] by the equation

$$\triangle G_{NU} = \triangle G_{NU}^{H_2O} + m_{NU}\,[D] \quad (6)$$

where $\triangle G_{NU}^{H_2O}$ and m_{NU} are the standard free energy at 0 M denaturant and slope of the N⇋U transition [73–75].

2.13. Reversibility of N⇌U transition

The U-state (40 μM) was prepared from the N-state by performing a jump to 5 M GdmCl (U buffer; pH 7.5). For the native control, the N-state (40 μM) was prepared from the N-state by performing a jump to pH 7.5 (no GdmCl). The samples were allowed to incubate for 3 h. The N and the U-state were further incubated in a gradient of GdmCl concentrations for 3 h by performing a 10-fold jump by manual mixing. Following incubation, the changes in the fluorescence signals were monitored by exciting TDP-43^{tRRM} at 280 nm and obtaining emission from 300 to 400 nm. The excitation and emission slit widths used were 1 nm and 8 nm, respectively. The final TDP-43^{tRRM} concentration was 4 μM. All the signals were acquired at pH 7.5 in the presence of 150 mM KCl and were buffer subtracted accordingly.

2.14. Calculation of N and U populations

K_{eq} and population of the N and the U-state ([N] and [U]) are related by equation:

$$K_{eq} = \frac{[N]}{[U]} \quad (7)$$

The population of different ensembles can be calculated by:

$$\triangle G_{NU}^{H_2O} = -RT\ ln\ K_{eq} \text{ or } \triangle G_{NU}^{H_2O} = -RT\ ln\ \frac{[N]}{[U]} \quad (8)$$

where R is the universal gas constant and T refers to the temperature of measurement in Kelvin.

2.15. Characterization of the thermal stability

The heat-induced unfolding of TDP-43^{tRRM} was used to measure the thermal stability of the free and ss(TG)$_6$-TDP-43^{tRRM} from pH 5.0–7.5. A PTC-424S/15 Peltier system was attached to the CD instrument for temperature ramping. The temperature was ramped up by 1 °C/min. Far-UV CD signals were acquired at 222 nm from 25 °C to 70 °C in a cuvette with a path length of 1 mm. The concentration of the free TDP-43^{tRRM} used was 8 μM. ss(TG)$_6$-TDP-43^{tRRM} were incubated in pH 7.2 to make a final concentration of 10 μM of ss(TG)$_6$ and 8 μM of TDP-43^{tRRM}. Samples were incubated in their respective buffers for at least 30 min. Respective buffer spectra were acquired at similar settings, and the buffer subtraction was carried out for all the CD spectra.

The mean residue ellipticity (MRE) values obtained were converted to fraction unfolded (f_U) using the following equation:

$$f_U = \frac{Y_o - (Y_N + m_N{*}T)}{(Y_U + m_U{*}T) - (Y_N + m_N{*}T)} \quad (9)$$

where Y_O is the observed MRE signal being measured at different temperatures (T). Y_N and Y_U refers to the intercepts, whereas m_N and m_U are the slopes of native and unfolded baseline, respectively.

The f_U versus temperature plots were fitted to the equation:

$$f_U = \frac{exp\left[\frac{\Delta H\left(\frac{T}{Tm}-1\right)+\Delta C\left[Tm-T+Tln\left(\frac{T}{Tm}\right)\right]}{RT}\right]}{1+exp\left[\left(\Delta H\left(\frac{T}{Tm}-1\right)+\Delta C\left[\,Tm-T+T\,ln\left(\frac{T}{Tm}\right)\,\right]\right)/RT\right]} \quad (10)$$

where ΔH is enthalpy and ΔC refers to specific heat capacity (ΔC_P). T refers to different temperatures and T_m is the midpoint of unfolding transition [73–75].

2.16. Reversibility of β⇌U transition

The β form and the U state were incubated in the gradient of GdmCl at pH 3.8 for 3 h. The fluorescence signal of the samples was acquired using similar settings as mentioned in subsection 2.13.

3. Results

3.1. TDP-43^{tRRM} binds strongly to TG-rich DNA

Fig. 2A shows the emission spectrum of fluorescently labeled ss$(TG)_6$ upon excitation at 482 nm. The wavelength of the maximum fluorescence emission (λ_{max}^{em}) was observed at 515 nm. Fig. 2A, inset, compares the mean value of steady-state anisotropy at 515 nm of labeled ss$(TG)_6$ in free and bound form at pH 7.5. The mean steady-state anisotropy of free and bound forms are 0.026 ± 0.001 and 0.049 ± 0.003, respectively.

Fig. 2B shows the relative change in the anisotropy values of labeled ss$(TG)_6$ as a function of increasing TDP-43^{tRRM} concentration at 515 nm. The curve shows a hyperbolic increase in the signal. We observed that the relative value of steady-state anisotropy of the labeled ss$(TG)_6$ has increased from 0.0 to 0.023 upon increasing TDP-43^{tRRM} concentration from 0 μM to 2 μM. The low value of the anisotropy of the free labeled ss $(TG)_6$ indicates free tumbling of the fluorophore owing to the smaller size of the attached ssDNA. The gradual increase in the value of anisotropy with an increase in TDP-43^{tRRM} concentration could be attributed to the slowed movement of the fluorophore upon binding of ssDNA to TDP-43^{tRRM}. Upon fitting the data to eq. 2, we obtained a K_d value of 0.3 ± 0.05 μM, indicating a strong binding affinity of TDP-43^{tRRM} towards ss$(TG)_6$. Our results are in accordance (0.28 ± 0.09 μM) to the K_d values of the TDP-43^{tRRM} and unlabeled $(TG)_6$ measured using change in fluorescence lifetime of tryptophan residues present in the protein [76]. These results suggest that the 6-carboxyfluorescein does not interfere with the measurement of the binding constant.

3.2. The molecular size of TDP-43^{tRRM} increases upon binding to ss$(TG)_6$

We employed size exclusion chromatography to estimate the molecular mass of TDP-43^{tRRM} in its free and ss$(TG)_6$ bound form at pH 7.5. Fig. 2C shows their normalized elution profile monitored at 280 nm. We observed that the free TDP-43^{tRRM} elutes at 12.51 mL, corresponding to a molecular weight of 19.4 ± 0.5 kDa. The obtained molecular weight is similar to that obtained with the mass spectrometer of monomeric TDP-43^{tRRM}. This data suggests that TDP-43^{tRRM} exists as a monomer under

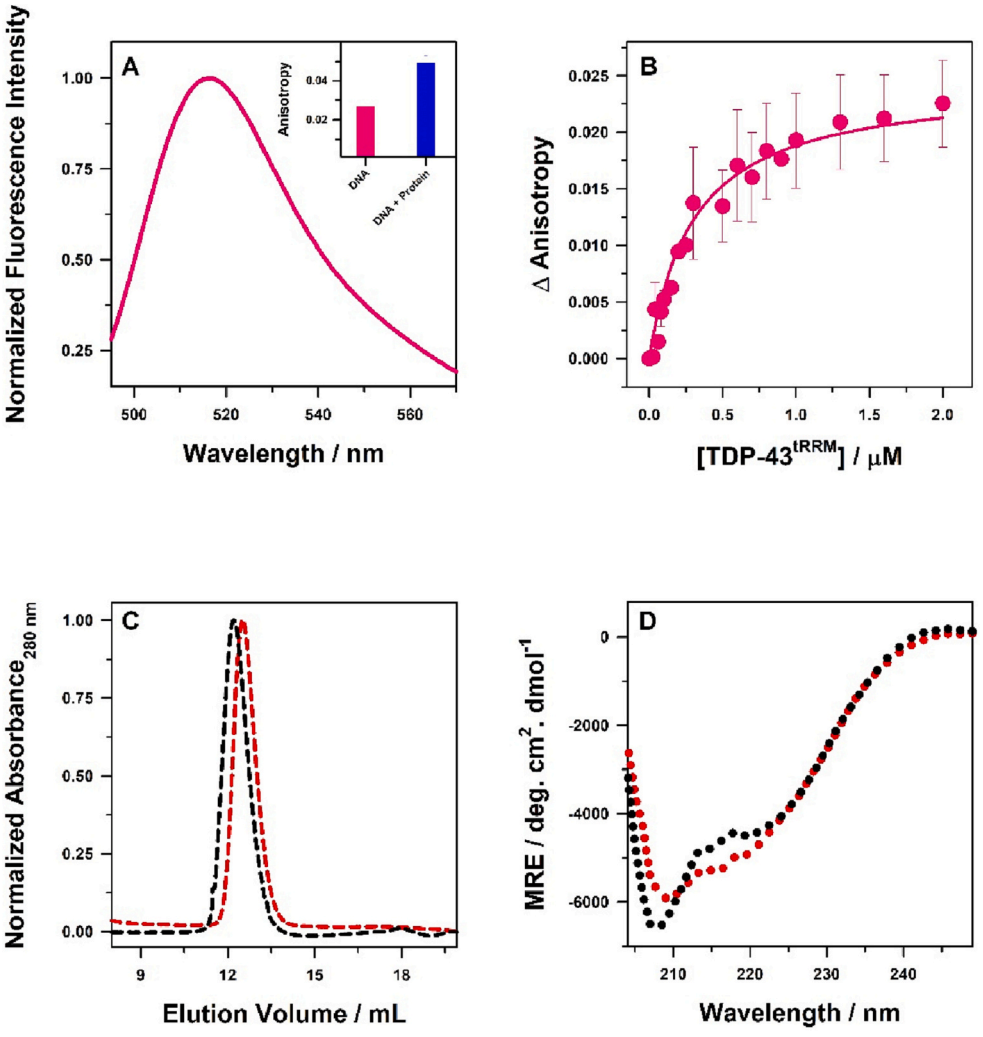

Fig. 2. ss$(TG)_6$ binds to TDP-43^{tRRM} (A) Fluorescence emission spectra of labeled ss $(TG)_6$ upon excitation at 482 nm. Mean anisotropy values of free and bound labeled ss$(TG)_6$ (Fig. 2A, inset). (B) Binding curve of TDP-43^{tRRM} with labeled ss$(TG)_6$ as a function of TDP-43^{tRRM} concentration as monitored by fluorescence anisotropy assay. The error bars represent the spread in values of the data points from three independent sets of experiments. (C) Normalized chromatograms obtained from SEC plotted at 280 nm for the free TDP-43^{tRRM} (red) and ss$(TG)_6$-TDP-43^{tRRM} (black) at pH 7.5. (D) Far-UV CD spectra of the free TDP-43^{tRRM} (red) and ss $(TG)_6$-TDP-43^{tRRM} (black) at pH 7.5.

physiological conditions.

ss(TG)$_6$-TDP-43^{tRRM}, on the other hand, eluted at 12.13 ± 0.07 mL, which corresponds to a molecular weight of 23.3 ± 0.6 kDa. The early elution and higher molecular weight of ss(TG)$_6$-TDP-43^{tRRM} indicate that DNA is bound to the protein.

3.3. The secondary structure of TDP-43^{tRRM} remains native-like upon DNA binding

Fig. 2D compares the far-UV CD spectra for both free and ss(TG)$_6$-TDP-43^{tRRM} at pH 7.5. The secondary structure of free TDP-43^{tRRM} is rich in α-helix, β-sheet, and the disordered region. The signal minima at 208 nm and 222 nm with MRE values of -5764 and -4550 deg. cm^2. dmol^{-1} suggests the presence of both α-helix and β-sheet rich structures (referred to hereafter as the native state). Interestingly, we also observed similar far-UV CD spectra for ss(TG)$_6$-TDP-43^{tRRM} with a MRE value of -6584 deg. cm^2. dmol^{-1} at 208 nm and -4340 deg. cm^2. dmol^{-1} at 222 nm. The similar MRE values imply that upon binding to ss(TG)$_6$, the secondary structure of TDP-43^{tRRM} remains similar to the native state. Thus, DNA binding induces no significant secondary structural changes under physiological conditions. Therefore, both free and bound TDP-43^{tRRM} can be compared directly.

3.4. pH-dependent misfolding of TDP-43^{tRRM} is abolished upon ss(TG)$_6$ binding

Previously, we have shown that free TDP-43^{tRRM} undergoes a transition to soluble amyloid-like conformation at low pH stress conditions (aggregation conditions), which is predominately rich in β sheeted structure [62,69,70]. The far-UV CD spectrum of free TDP-43^{tRRM} at pH 3.8 (Fig. 3A) shows a shift in the signal minima to 216 nm, which signifies the dominance of β sheets (β form) in the protein sample. The shift is accompanied by an increase in the signal with an MRE value of -9536 deg. cm^2. dmol^{-1}. We observed that the β form binds to the amyloid-staining dye ThT (Fig. S1A) [77]. Together, these results indicate that the aggregates observed in this study are amyloid-like.

To study the effect of the ssDNA on the secondary structure of TDP-43^{tRRM} under aggregation conditions, we have used ss(TG)$_6$ and ss(TG)$_{12}$, which are specific binding partners of TDP-43^{tRRM} [6]. We measured the far-UV signal of the free ss(TG)$_6$ and did not observe any appreciable absorbance, suggesting the lack of structure (Fig. 3A, inset). We observed a far-UV CD spectrum similar to the native TDP-43^{tRRM} with minima at 208 and 222 nm for the ss(TG)$_n$-TDP-43^{tRRM} (Fig. 3A). The observed values of the MRE at 216 nm for ss(TG)$_6$ and ss(TG)$_{12}$ bound TDP-43^{tRRM} were -4401 deg. cm^2. dmol^{-1} and -3031 deg. cm^2. dmol^{-1}, respectively. These results imply that the transition to β form is abolished in the presence of ss(TG)$_6$ and ss(TG)$_{12}$, and TDP-43^{tRRM} maintains its native-like form under aggregation conditions.

We also used ss(CA)$_6$ to look for the effect of non-specific nucleic acid sequences [6]. We observed signal minima at 216 nm in the far-UV CD spectrum with an MRE value of -9052 deg. cm^2 dmol^{-1}. The appearance of the far-UV CD spectrum and the signal strength resembles that of free TDP-43^{tRRM} under aggregation conditions. These results provide an important observation that suggests that the specific binding of ss(TG)$_6$ and ss(TG)$_{12}$ plays a vital role in abolishing the misfolding behavior of the TDP-43^{tRRM} under the studied conditions.

We measured the pH-induced structural transition under equilibrium conditions of the native state to β form at 216 nm using far-UV CD spectroscopy (Fig. 3B). We observed that the secondary structure of the TDP-43^{tRRM} remains native-like from pH 7.5 to pH 5.0. The average MRE value at 216 nm was -5096 ± 340 deg. cm^2 dmol^{-1}. However, with a further decrease in the pH, we observed an increase in the MRE, which saturated at pH 3.0. This increase in the signal at 216 nm signifies the transition to β form. The transition from native-state to β form as a function of pH has a steep slope, and the midpoint of the transition is pH 4.0. The plot was fitted using eq. 3. It is crucial to point out that the N⇌β transition is reversible (Fig. 3B, inset). The β form dissociates and acquires a native-like secondary structure upon stress removal (Fig. S1).

However, ss(TG)$_6$-TDP-43^{tRRM} did not show any such transition under low pH conditions and retained an average MRE value of -4591 ± 271 deg. cm^2 dmol^{-1} at 216 nm throughout the studied pH range. The results suggest that the ss(TG)$_6$ binding to the TDP-43^{tRRM} inhibits the conformation conversion of TDP-43^{tRRM} to β form while retaining its native structure.

3.5. DNA binding inhibits oligomerization of TDP-43^{tRRM}

To characterize the size of ss(TG)$_6$-TDP-43^{tRRM}, we compared the elution profile of the free and ss(TG)$_6$ -TDP-43^{tRRM} at low pH (Fig. 3C). Free TDP-43^{tRRM} eluted at 8.69 mL. The void volume of the SEC column employed is comparable to the elution volume, due to which the exact molecular weight of free TDP-43^{tRRM} cannot be deduced. However, this suggests that the β form is much larger than the monomeric TDP-43^{tRRM}. Interestingly, the ss(TG)$_6$-TDP-43^{tRRM} eluted at 12.7 mL corresponding to a molecular mass of 18.6 kDa, which is similar to the molecular mass of the monomeric TDP-43^{tRRM} at pH 7.5. The delayed elution of ss(TG)$_6$-TDP-43^{tRRM} at pH 3.0 suggests the formation of a compact structure at pH 3.0. The results in Fig. 3 confirm that DNA binding inhibits structural change and prevents oligomerization of TDP-43^{tRRM} under aggregation conditions. An intact secondary structure with a compact size suggests that ss(TG)$_n$ could induce the formation of compact native-like states under aggregation conditions.

3.6. ss(TG)$_6$ abolishes the formation of worm-like β form

We examined the effect of DNA binding on the morphology of the amyloid-like aggregates at low pH. Fig. 4 compares the TEM image of the free and ss(TG)$_6$-TDP-43^{tRRM}. In the case of free TDP-43^{tRRM}, we observed small worm-like assemblies of approximately 50–70 nm. The observed small fibrils are similar to the fibrils of mouse prion protein observed previously in a separate study [78]. The result suggests that the oligomeric β form appears to be worm-like fibrils. In contrast, no visible assemblies were observed in the presence of ss(TG)$_6$ (Fig. 4B). The absence of visible assemblies proves that the formation of the worm-like β form is abolished in the presence of ss(TG)$_6$.

3.7. ss(TG)$_6$ binding preserves the tertiary structure of TDP-43^{tRRM} under stress-like conditions

We performed pH-dependent ANS binding assay on the free and ss(TG)$_6$-TDP-43^{tRRM} to study the effect of DNA binding on the tertiary structure of TDP-43^{tRRM} under aggregation conditions. ANS is a dye that binds to the solvent-exposed hydrophobic amino acids and fluoresces. Fig. 5A shows the relative ANS fluorescence signal of the free TDP-43^{tRRM}. We did not observe ANS fluorescence under native conditions (pH 5.0-pH 7.5). The result indicates that the native state of TDP-43^{tRRM} is appropriately folded, and no exposed hydrophobic patches are present. However, we observed a gradual increase in the ANS fluorescence below pH 5.0. The λ^{em}_{max} of the fluorescence emission was observed at 472 nm. An increase in the fluorescence signal indicates an increase in the exposed hydrophobic patches, a characteristic of the misfolded state of proteins. The gradual increase with a decrease in the pH indicates a higher amount of misfolded species under low pH conditions.

In contrast, we observed a negligible ANS fluorescence signal for the ss(TG)$_6$-TDP-43^{tRRM} across the studied pH range (Fig. 5B). The inability of ANS dye to bind and fluoresce suggests that the native structure of TDP-43^{tRRM} is intact under various pH stress in the presence of ss(TG)$_6$. However, ss(TG)$_6$-TDP-43^{tRRM} at pH 3.3 showed 20% ANS fluorescence than its free counterpart (Fig. 5B). As the secondary structure of ss(TG)$_6$-TDP-43^{tRRM} is similar to the native state at pH 3.3, the results indicate that some molten globular structure is forming at very low pH conditions.

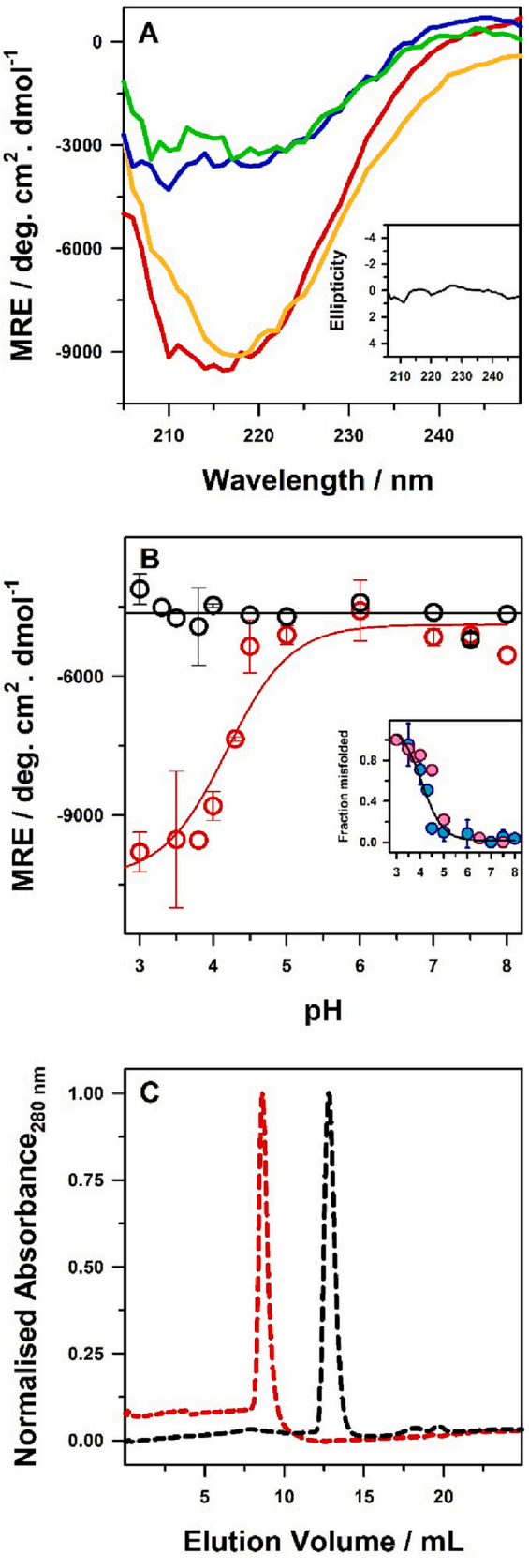

(caption on next column)

Fig. 3. ss(TG)$_6$ binding inhibits the pH-induced misfolding of TDP-43^{tRRM}. (A) Far-UV CD spectra of free (red), ss(TG)$_6$ (blue), ss(TG)$_{12}$ (green) and ss(CA)$_6$ (yellow) bound TDP-43^{tRRM} at pH 3.8. Inset shows the ellipticity of ss(TG)$_6$ at pH 3.8. (B) Changes in the mean residue ellipticity at 216 nm as a function of pH for the free TDP-43^{tRRM} (red) and ss(TG)$_6$-TDP-43^{tRRM} (black). The error bars represent the spread in values of the data points from at least two independent sets of experiments. The solid line through the free TDP-43^{tRRM} data is a fit to eq. 3, while that of ss(TG)$_6$-TDP-43^{tRRM} is drawn to guide the eye. Inset demonstrates that the N⇌β transition is reversible. Fraction misfolded calculated upon jumping β form to different pH (pink, circle) are compared with the fraction misfolded calculated from jumping N-state to different pH (blue, circle). The fraction misfolded is calculated as discussed previously [70]. The solid line is a fit to eq. 3. (C) Normalized size-exclusion chromatograms for the free TDP-43^{tRRM} (red) and ss(TG)$_6$-TDP-43^{tRRM} (black).

Fig. 5C compares the ANS fluorescence during pH-induced equilibrium transition of free and ssDNA bound TDP-43^{tRRM}. The increase in the ANS fluorescence with a decrease in the pH indicates the exposure of the hydrophobic patches of free TDP-43^{tRRM}. However, ss(TG)$_6$-TDP-43^{tRRM} shows no increase in the ANS fluorescence until pH 3.5. The results indicate that ss(TG)$_6$ binding keeps the native tertiary structure TDP-43^{tRRM} intact. The figure also shows the relative signal of the buffer containing ANS in different pH conditions. We virtually observed no change in the ANS fluorescence as a function of pH.

These results together conclude that the presence of ss(TG)$_6$ prevents side-chain breaking and keeps the tertiary structure of TDP-43^{tRRM} intact.

3.8. *TDP-43^{tRRM} exhibits pH-dependent thermodynamic stability*

In order to understand the effect of pH on the thermodynamic stability of TDP-43^{tRRM}, we employed fluorescence spectroscopy. Two tryptophan residues are located at positions 113 and 172 in the RRM1 domain of TDP-43^{tRRM}. We observed that these tryptophans fluoresce differently in the native and chemically unfolded states. Their fluorescence was found to decrease upon protein unfolding due to increased quenching as a result of the solvation environment. Also, the λ_{max}^{em} of emission was observed at 347 nm and 357 nm for the native and unfolded states, respectively. These two results signify the solvation of the tryptophans. We utilized this difference in the spectroscopic properties of the native and unfolded states of the protein to calculate the population distribution and hence the thermodynamic stability of the TDP-43^{tRRM}. The unfolding curves obtained as a function of GdmCl concentration were converted to the fraction of unfolded protein (f_U) using eq. 4. Fig. 6A shows the representative plots of the f_U as a function of GdmCl concentration for pH 5.0, 6.0, and 7.5. The plots were fitted to eq. 5 to calculate the associated thermodynamic parameters.

Fig. 6A demonstrates that the midpoint of the unfolding transition (C_m) changes as a function of pH in the pH range of 5.0–7.5. C_m is a measure of protein stability [79]. For pH 7.5, we noticed that the native baseline (N-baseline) extends till ~1.5 M, and C_m is reached at 2.2 ± 0.15 M.

In contrast, the N-baseline decreases to 1.1 M for pH 6.0, and C_m was achieved at ~1.9 M. With a further decrease in the pH to 5.0, the transition zone begins early at 0.65 M, and C_m is achieved at 1.3 M. These results confirm that TDP-43^{tRRM} exhibits pH-dependent thermodynamic stability, which starts decreasing upon decreasing the pH below 7.5. It is important to note that the m_{NU} value remains constant (2.1 ± 0.2 kcal mol^{-1} M^{-1}) throughout the pH range studied (Fig. 6B, inset). The observation suggests that the pH-dependent changes in the stability are not due to the structural changes.

It is also important to point out that the N⇌U transition is reversible (Fig. 6A, inset). We observed the expected change in the fraction of the unfolded protein population upon dilution of the U-state in a gradient of GdmCl, demonstrating the reversibility of the N⇌U transition.

Fig. 6B shows the variations in the value of C_m value as a function of

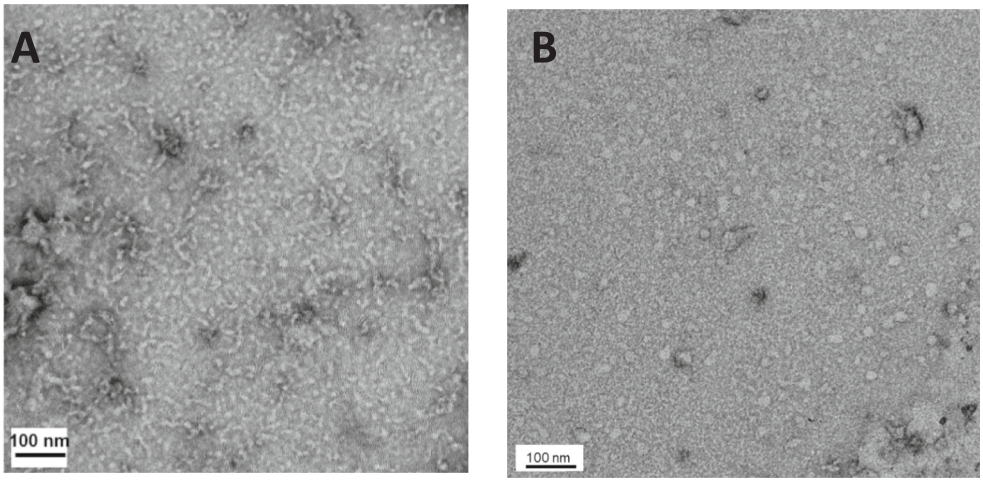

Fig. 4. DNA binding inhibits the worm-like fibril formation of TDP-43^{tRRM}. TEM image of (A) free TDP-43^{tRRM} (B) ss(TG)$_6$-TDP-43^{tRRM}.

pH under equilibrium conditions. The mean value of C_m remains 2.16 ± 0.03 M [GdmCl] for the pH range 6.8–8.0. Below pH 6.8, the C_m value starts decreasing. It achieves a minimum at pH 5.0 with a value of 1.26 ± 0.14 M. We observed that C_m increases below pH 5.0. Fig. 6B, inset shows the value of ΔG_{NU}^{H2O} as a function of pH. We noticed a decrease in the ΔG_{NU}^{H2O} (4.8 to 2.8 kcal mol^{-1}) with decrease in the pH from pH 7.5 to 5.0. The previous results from Figs. 3B and 5C show that the TDP-43^{tRRM} begins to form an amyloid-like assembly below pH 5.0. Hence, the increase in the C_m values below pH 5.0 represents the structural unfolding of the heterogeneous mixture of the native and aggregated state.

The data presented in Fig. 3B were utilized to calculate the fraction of misfolded protein as a function of pH (Fig. 6B), as discussed previously [70]. Interestingly, we observed that misfolding of TDP-43^{tRRM} starts below pH 5.0, the point of minimum thermodynamic stability of TDP-43^{tRRM}. These results together convey that misfolding of TDP-43^{tRRM} happens as a result of its destabilization.

We also converted the MRE values obtained for ss(TG)$_6$-TDP-43^{tRRM} from Fig. 3B to obtain the fraction misfolded as a function of pH (Fig. 6B). We observed that the conformational conversion of the TDP-43^{tRRM} in the presence of ss(TG)$_6$ is inhibited throughout the studied pH range.

3.9. ss(TG)$_6$ binding increases the thermal stability of TDP-43^{tRRM}

The above results indicate that the extent of misfolding of TDP-43^{tRRM} is directly linked to its destabilization. In order to understand the effect of ss(TG)$_6$ on the thermodynamic stability, denaturant-induced unfolding could not be used as ss(TG)$_6$ does not bind to TDP-43^{tRRM} in the presence of even small amount of denaturant. Therefore, we employed temperature-mediated unfolding experiments in the pH range of 5.0–7.5 to estimate the midpoint of thermal unfolding (T_m) as a measure of stability. We used the difference in the far-UV CD spectrum of native and unfolded states to monitor the unfolding of the TDP-43^{tRRM}. Fig. 7A shows the representative thermal unfolding plots of free and ss(TG)$_6$-TDP-43^{tRRM} at pH 5.0 and 7.5. We observed that the transition from native to unfolded form is a two-step process, and the midpoint of unfolding changes with the pH.

In the case of free TDP-43^{tRRM}, the native baseline extends till 318 K at pH 5.0, beyond which the transition zone begins. The unfolding transition follows a sigmoidal pattern with a midpoint of unfolding at 321 K. Complete unfolding is achieved at 328 K. Interestingly, free TDP-43^{tRRM} under pH 7.5 showed higher stability than pH 5.0 as evident with a more extended native baseline till 324 K. The midpoint of transition shifted to 328.5 K. In contrast, the complete unfolding of TDP-43^{tRRM} occurred at 333 K.

On the contrary, ss(TG)$_6$-TDP-43^{tRRM} showed a difference in the midpoint of the unfolding transition. We observed extended native baselines both at pH 5.0 and 7.5. The more extended native baseline suggests an increase in the resistance to thermal unfolding. The unfolding transition was observed to begin near 324 K, and the midpoint of transition was achieved at 327 K at pH 5.0. The transition midpoint at pH 7.5 was observed to shift to 332 K. This data suggests that ss(TG)$_6$ binding increases the thermal stability of TDP-43^{tRRM} under both pH conditions.

Fig. 7B compares the mean value of T_m as a function of pH for free and ss(TG)$_6$-TDP-43^{tRRM}. In the case of free TDP-43^{tRRM}, the mean value of T_m at pH 5.0 is 321 K. The T_m value increased with the increase in the pH, making the T_m value equivalent to 324.8 K at pH 5.5, 328.8 K at pH 6.5, and 330.4 K at pH 7.5. The presence of ss(TG)$_6$ increased the T_m to ~332K, suggesting increased stability of the ss(TG)$_6$-TDP-43^{tRRM}.

4. Discussion

TDP-43 is a nucleic acid-binding protein whose aggregation has been implicated in TDP-43-associated proteinopathies [23,26,28,30]. Nucleic acids have been shown to modulate the aggregation behavior of TDP-43 [66,67,80,81]. For instance, Huang et al. have shown that DNA binding increases the solubility of TDP-43 generated from a cell-free system by centrifugation and western blotting. They have also shown a decrease in the turbidity of purified TDP-43 expressed from *E.coli* in the presence of ssDNA, suggesting increased solubility [66]. Another paper by Qin et al. explores the effect of DNA binding on the N-terminal domain. However, the N-terminal domain is not the primary nucleic acid binding domain of TDP-43 [81]. In addition, nucleic acids have also been shown to modulate the other self-assembly reactions of TDP-43, like phase separation. It has been shown that RNA molecules can buffer the phase separation of TDP-43 [80]. In a separate study, RNA binding has been shown to antagonize the phase separation and aggregation of TDP-43 variants containing RRM domain [67]. These elegant studies have provided important observations regarding the role of nucleic acids. However, a quantitative thermodynamic basis for these observations was missing. In addition, none of these studies have studied the relationship between nucleic acid binding and amyloid-like aggregation of the protein. One major way in which amyloid-like aggregation differs from other insoluble aggregates is that there is a large structural change in the protein from the native structure to a predominately β-sheet rich structure. It is not known how DNA binding affects this structural transition of the functional domain of TDP-43.

In this study, we have explored the role of DNA on the primary functional domain of TDP-43, TDP-43^{tRRM}. Because TDP-43^{tRRM} forms an essential part of the 35 kDa fragments (TDP-35), which is implicated in ALS and FTLD [82,83], it becomes important to understand the TDP-

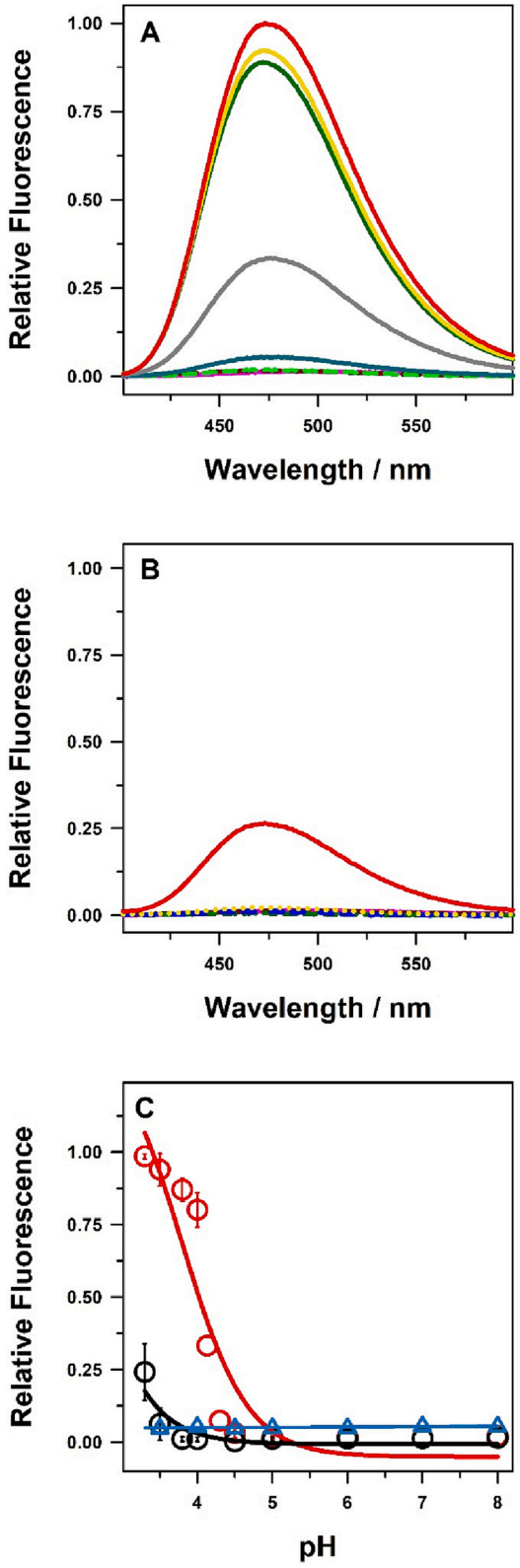

Fig. 5. ss(TG)$_6$-TDP-43^{tRRM} averts changes in the tertiary structure by forming a molten globule. (A) Normalized ANS fluorescence spectra for free TDP-43^{tRRM}. pH 3.3 (red), pH 3.5 (yellow), 4.0 (dark green), 4.1 (grey) 4.3 (dark cyan), 4.5 (light green) 5.0 (maroon), 7.5 (pink). (B) Normalized ANS fluorescence spectra for ss(TG)$_6$-TDP-43^{tRRM}. (C) Relative comparison of the fluorescence points at 480 nm for free (red), ss(TG)$_6$-TDP-43^{tRRM} (black), and buffer (teal blue) as a function of pH. Error bars represent the spread of at least two independent data sets.

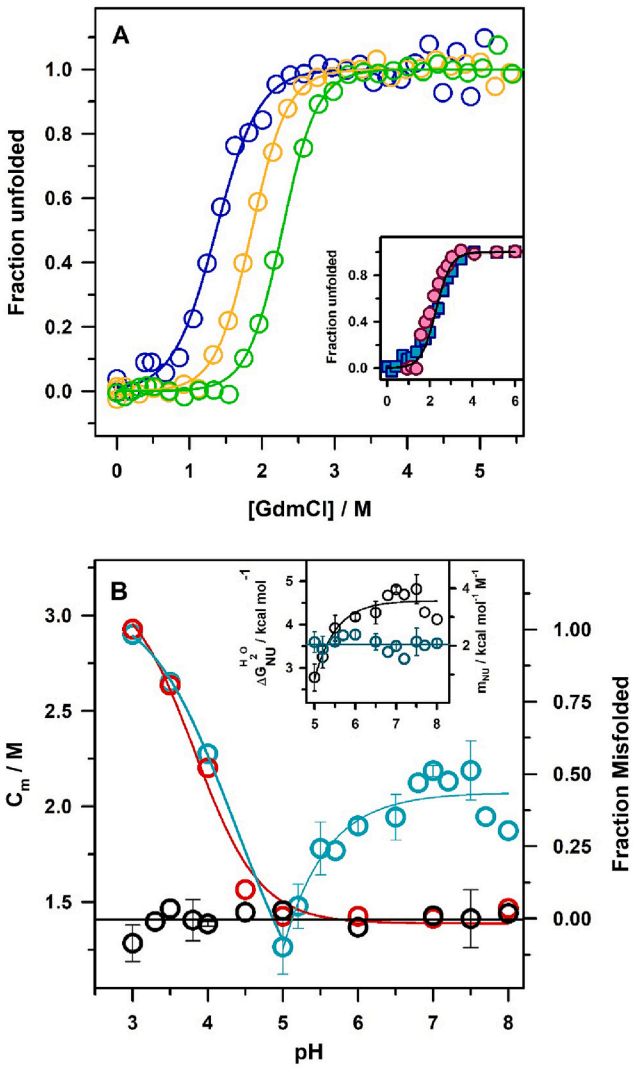

Fig. 6. pH-induced misfolding is coupled to pH-induced destabilization. (A) Representative plots show fraction unfolded as the function of GdmCl concentration at pH 5.0 (blue), 6.0 (yellow), 7.5 (green). The inset shows the N⇌U transition is reversible. Fraction unfolded calculated from the unfolding transition of the N-state (blue, square) as a function of GdmCl concentration are compared with fraction unfolded calculated from the refolding transition of the U-state (pink, circle) at 340 nm at pH 7.5. The fraction unfolded is calculated using eq. 4. The solid line is a simulated fit to eq. 5. (B) C_m of free TDP-43^{tRRM} (dark cyan) is compared with the fraction misfolded of free TDP-43^{tRRM} (red) and ss(TG)$_6$-TDP-43^{tRRM} (black) as a function of pH. ΔG_{NU}^{H2O} (black) and m_{NU} (dark cyan) dependence on pH (Fig. 6B, inset). The error bars represent the spread in values of the data points from at least two independent sets of experiments.

43^{tRRM}-mediated aggregation and aggregation inhibition. Till now, very limited studies exist which has specifically studied the thermodynamic basis of aggregation and aggregation inhibition of the TDP-43^{tRRM}. We have used a thermodynamic approach in a systematic manner and quantitatively show how stress destabilizes the TDP-43^{tRRM} leading to large structural change to form amyloid-like aggregates, and how DNA binding inhibits the amyloid-like aggregation of the TDP-43^{tRRM} by stabilizing the native state.

We have employed fluorescence spectroscopy, circular dichroism, size exclusion chromatography, and TEM to study the structure and thermodynamics of TDP-43^{tRRM} in free and ss(TG)$_6$ bound states. The secondary and tertiary structure analysis suggests that the transition from the native state to oligomeric β form (Fig. 3C) begins below pH 5.0,

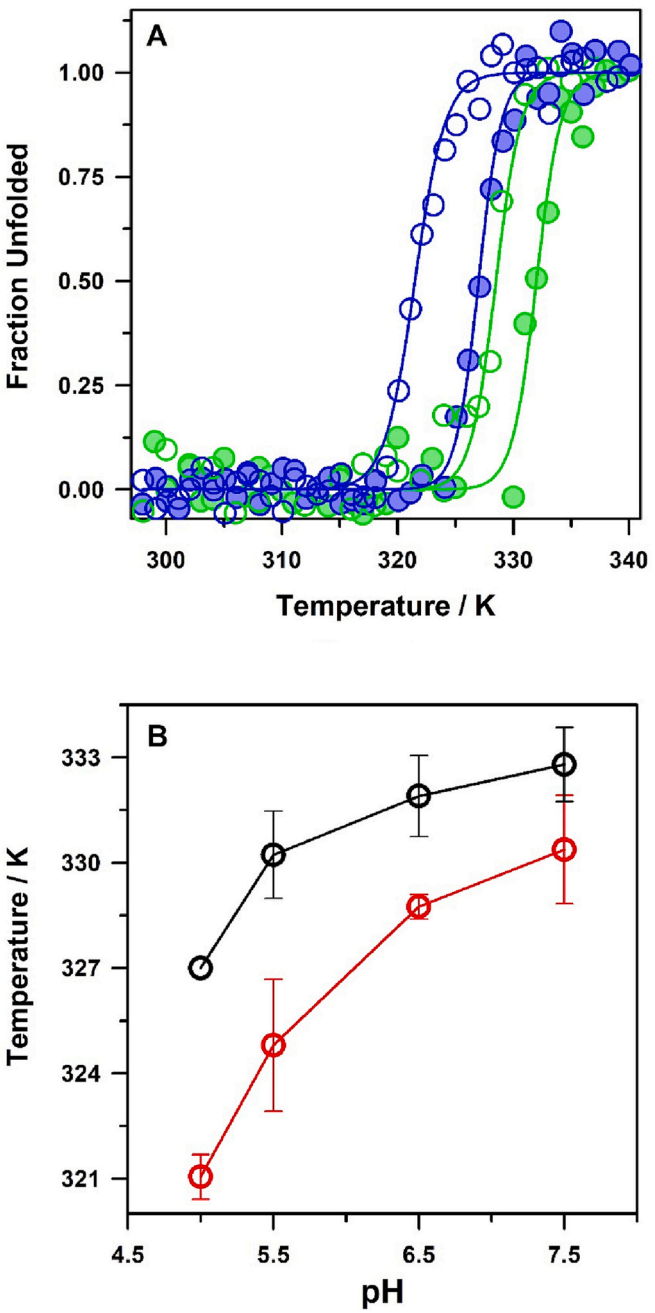

Fig. 7. DNA binding increases the thermal stability of TDP-43^{tRRM}. (A) Fraction unfolded of TDP-43^{tRRM} at 222 nm as a function of temperature. The fraction unfolded is compared for free TDP-43^{tRRM} at pH 5.0 (blue, open), pH 7.5 (green, open) with ss(TG)$_6$-TDP-43^{tRRM} at pH 5.0 (blue, filled) and pH 7.5 (green, filled). The plots are fitted through eq. 10. (B) T_m of free (red) and ss(TG)$_6$-TDP-43^{tRRM} (black) plotted as a function of pH. Error bars represent the spread of at least two data sets. The lines drawn are to guide the eye. (For interpretation of the references to colour in this figure legend, the reader is referred to the web version of this article.)

with a midpoint of the transition ~pH 4.0 (Figs. 3B and 5C). We employed GdmCl and heat-mediated denaturation under different pH conditions to probe the cause of misfolding under low pH conditions (Figs. 6 and 7). The denaturation experiments suggest that the free TDP-43^{tRRM} exhibits pH-dependent stability (Figs. 6 and 7). The thermodynamic parameters calculated from GdmCl mediated denaturation experiments suggest that free TDP-43^{tRRM} remains most stable in the pH range of 6.8 to 7.5 with a mean C_m value of 2.16 M [GdmCl] (Mean $\Delta G_{NU}^{H2O} = 4.74$ kcal mol^{-1}). Below pH 6.8, C_m decreases as a function of pH and becomes 1.26 M [GdmCl] at pH 5.0 ($\Delta G_{NU}^{H2O} = 2.78$ kcal mol^{-1}) (Fig. 6B and inset). The thermal denaturation experiments also confirmed the pH-dependent stability of TDP-43^{tRRM} being higher at pH 7.5 (T_m = 330.38 K) compared to pH 5.0 (T_m = 321 K) (Fig. 7A). The observed destabilization of TDP-43^{tRRM} at low pH stress conditions makes it aggregation prone as evident from the increased misfolding accompanied with destabilization (Fig. 6B). We also observed that the specific ss(TG)$_6$ binding abolishes the pH-dependent secondary and tertiary structural changes (Figs. 3B and 5C). The ss(TG)$_6$-TDP-43^{tRRM} remains in the monomeric state even at low pH (Fig. 3C) and does not form amyloid-like pre-fibrils (Fig. 4, Fig. 6B). The binding of ss(TG)$_6$ increases the stability of TDP-43^{tRRM} under native and stress-like conditions. The mean value of T_m observed for ss(TG)$_6$-TDP-43^{tRRM} in native and stress conditions was 332.8 K and 327 K, respectively (Fig. 7B).

Our results can be explained from the model energy diagram as shown in Fig. 8. An energy diagram postulates various species that can be populated under a specific set of conditions. Fig. 8 shows the structural transition between the N-state, U-state, PUFs, and β form. In this study, we show that the N⇌U transition is reversible (Fig. 6A, inset). Previous studies from our lab and the present study have established the reversibility of the β⇌U transition (Fig. S2) [62,70]. In this study, we also point out that the N⇌β transition is reversible in nature (Fig. 3B, inset, and S1). Therefore, the different species accessed by the protein are reversible as their population depends on the solution environment. Under native conditions (Fig. 8A), the N-state of TDP-43^{tRRM} is the most stable conformation. Therefore, this energy minima is favored by a majority of the TDP-43^{tRRM} molecules. The calculated value of ΔG_{NU}^{H2O} at pH 7.5 is 4.74 kcal mol^{-1}. This translates into 3 unfolded molecules per 10,000 molecules of TDP-43^{tRRM}. This suggests that only 3 molecules are able to traverse the energy landscape to non-native minima at equilibrium, while remaining molecules populate the N-state. These molecules are not enough to trigger self-assembly to amyloid-like aggregates and therefore, aggregated conformation is not favored under native conditions. In contrast, the low-pH stress destabilizes the native-state of TDP-43^{tRRM} (Fig. 8B). The calculated value of ΔG_{NU}^{H2O} at pH 5.0 is 2.78 kcal mol^{-1}, which translates to 91 unfolded molecules per 10,000 molecules of TDP-43^{tRRM}. Therefore, compared to native conditions, a higher number of TDP-43^{tRRM} molecules (30 times higher) could traverse the energy landscape. Some of these conformers could be aggregation prone (partially unfolded forms), hence can interact with each other with their exposed hydrophobic patches to undergo amyloid-like aggregation (amyloid fibrils). Therefore, destabilization of TDP-43^{tRRM} allows it to access the aggregation energy landscape. The pH-dependent destabilization is observed by thermal denaturation experiments as well (Fig. 7). Interestingly, we observed that ss(TG)$_6$ binding stabilizes N-state of TDP-43^{tRRM} in both the native and the stress-like conditions (Fig. 7). The T_m of DNA-bound protein at pH 5.0 is 327 K which is similar to the T_m of the unbound protein at pH 6.5 (328.75 K) (Fig. 7B). Hence, for the DNA-bound protein the N-state of TDP-43^{tRRM} is thermodynamically favored even at low pH conditions. It is also interesting to note that the change in T_m as a function of pH is much shallower for the DNA bound protein compared to the unbound protein. For the free protein, the value of T_m changes by ~9 K as we move from pH 7.5 to 5.0, but it changes only by ~5 K for the DNA-bound protein (Fig. 7B). These results indicate that the DNA-bound protein is much better able to tolerate low-pH stress. Overall, our results indicate that specific ss(DNA) binding modulates the energy landscape of TDP-43^{tRRM} such that the N-state of TDP-43^{tRRM} gets populated and very few partially or fully unfolded-like molecules are available for interactions, and hence amyloid-like aggregation is inhibited even in stress conditions (Fig. 8C).

The inhibition of amyloid-like aggregation and the stabilization of TDP-43^{tRRM} in the presence of DNA indicates that the protein regions involved in the DNA binding are also involved in the amyloid-like aggregation of the protein. It appears that the DNA binding interferes with the non-native interactions between the two protein molecules that

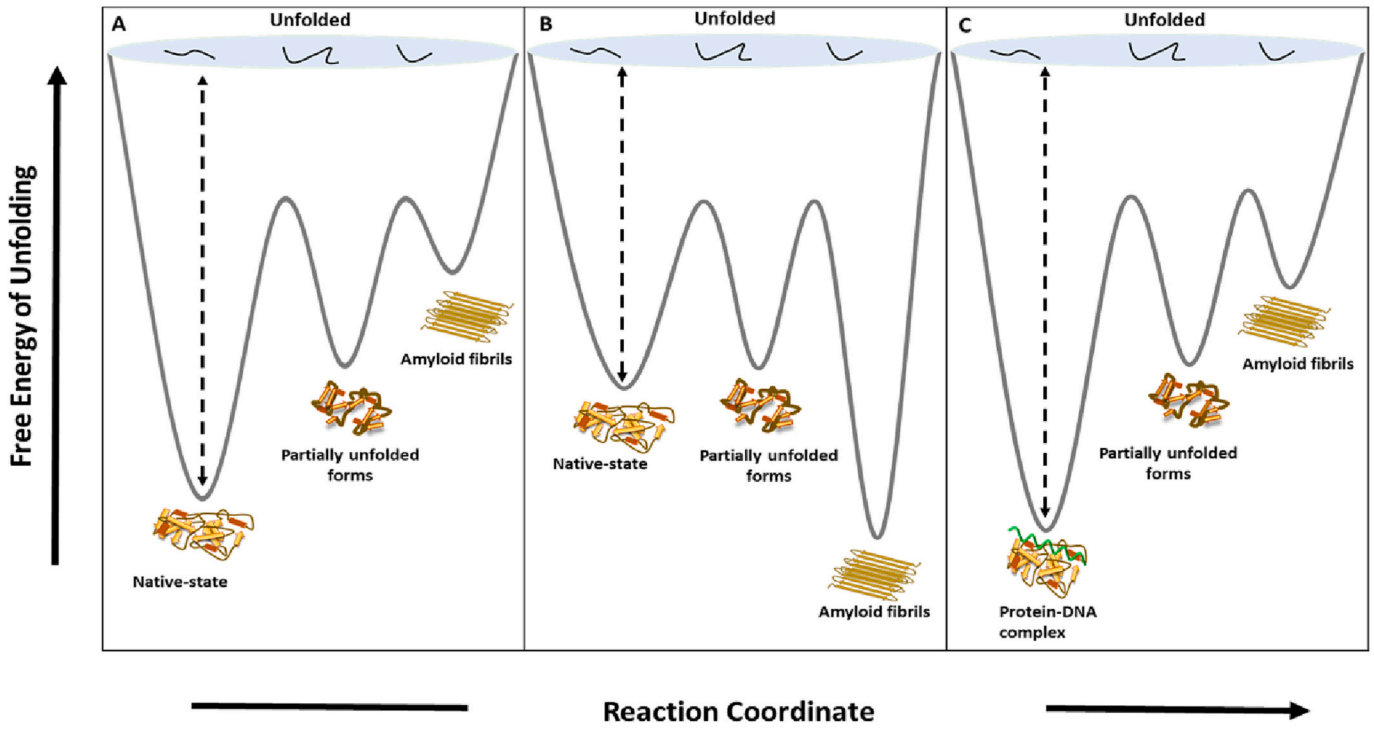

Fig. 8. Free energy landscape model of TDP-43^{tRRM} in (A) native conditions (pH 7.5), (B) low pH stress-like conditions, and (C) ss(TG)$_6$ bound in native and stress conditions.

trigger aggregation. The hydrogen-deuterium studies coupled to mass spectrometry are ongoing in the laboratory to identify the amino acid residues responsible for amyloid-like aggregation and inhibition. Nevertheless, our observations are in line with a few recent studies that show that the functionally important regions of the proteins are the same region that promotes aggregation [84].

The stabilization of aggregation prone proteins by ligands hold therapeutic importance. A conceptual advantage of the protein stabilization strategy is that stabilizing the native protein conformation prevents the formation of all the non-native conformations (non-native monomers, oligomers, fibrils), thereby having a mass effect on disease control. It is interesting to know that a FDA approved drug, Tafamidis [85] which is used to treat transthyretin (TTR)-related hereditary amyloidosis stabilizes the tetramer of the native TTR, thereby preventing its dissociation into monomers and hence aggregation. The natural DNA aptamer reported in this study targets the monomeric TDP-43^{tRRM}, stabilizes it and inhibits amyloid-like aggregation. Therefore, we propose that nucleic acid like molecules which can modulate the thermodynamic energy landscape and hence aggregation behavior of TDP-43^{tRRM} could be prime candidates for therapeutic intervention in TDP-43-associated proteinopathies.

Accession codes

TAR DNA-binding protein 43 (TDP-43): UniProtKB/Swiss-Prot entry Q13148 (TADBP_HUMAN).

CRediT authorship contribution statement

Divya Patni: Conceptualization, Methodology, Validation, Formal analysis, Investigation, Writing – original draft. **Santosh Kumar Jha:** Conceptualization, Methodology, Resources, Writing – review & editing, Supervision, Project administration, Funding acquisition.

Declaration of Competing Interest

There are no conflicts of interest to declare.

Data availability

Data will be made available on request.

Acknowledgement

This work was funded by a SERB-DST core research grant (Project: CRG/2019/002922) to S.K.J. D.P. is a recipient of a Senior Research Fellowship awarded by Council of Scientific and Industrial Research, India.

Appendix A. Supplementary data

Supplementary data to this article can be found online at https://doi.org/10.1016/j.bbapap.2023.140916.

References

[1] D. Arseni, M. Hasegawa, A.G. Murzin, F. Kametani, M. Arai, M. Yoshida, B. Ryskeldi-Falcon, Structure of pathological TDP-43 filaments from ALS with FTLD, Nature. 601 (2022) 139–143, https://doi.org/10.1038/s41586-021-04199-3.
[2] B.D. Freibaum, R.K. Chitta, A.A. High, J.P. Taylor, Global analysis of TDP-43 interacting proteins reveals Strong association with RNA splicing and translation machinery, J. Proteome Res. 9 (2010) 1104–1120, https://doi.org/10.1021/pr901076y.
[3] I.-F. Wang, L.-S. Wu, C.-K.J. Shen, TDP-43: an emerging new player in neurodegenerative diseases, Trends Mol. Med. 14 (2008) 479–485, https://doi.org/10.1016/j.molmed.2008.09.001.
[4] P.-H. Kuo, C.-H. Chiang, Y.-T. Wang, L.G. Doudeva, H.S. Yuan, The crystal structure of TDP-43 RRM1-DNA complex reveals the specific recognition for UG- and TG-rich nucleic acids, Nucleic Acids Res. 42 (2014) 4712–4722, https://doi.org/10.1093/nar/gkt1407.
[5] L. François-Moutal, S. Perez-Miller, D.D. Scott, V.G. Miranda, N. Mollasalehi, M. Khanna, Structural insights into TDP-43 and effects of post-translational

modifications, Front. Mol. Neurosci. 12 (2019), https://doi.org/10.3389/fnmol.2019.00301.
[6] P.-H. Kuo, L.G. Doudeva, Y.-T. Wang, C.-K.J. Shen, H.S. Yuan, Structural insights into TDP-43 in nucleic-acid binding and domain interactions, Nucleic Acids Res. 37 (2009) 1799–1808, https://doi.org/10.1093/nar/gkp013.
[7] Y.M. Ayala, P. Zago, A. D'Ambrogio, Y.-F. Xu, L. Petrucelli, E. Buratti, F.E. Baralle, Structural determinants of the cellular localization and shuttling of TDP-43, J. Cell Sci. 121 (2008) 3778–3785, https://doi.org/10.1242/jcs.038950.
[8] H. Ederle, D. Dormann, TDP-43 and FUS en route from the nucleus to the cytoplasm, FEBS Lett. 591 (2017) 1489–1507, https://doi.org/10.1002/1873-3468.12646.
[9] E. Buratti, F.E. Baralle, Characterization and functional implications of the RNA binding properties of nuclear factor TDP-43, a novel splicing regulator of CFTR exon 9, J. Biol. Chem. 276 (2001) 36337–36343, https://doi.org/10.1074/jbc.M104236200.
[10] J.R. Tollervey, T. Curk, B. Rogelj, M. Briese, M. Cereda, M. Kayikci, J. König, T. Hortobágyi, A.L. Nishimura, V. Zupunski, R. Patani, S. Chandran, G. Rot, B. Zupan, C.E. Shaw, J. Ule, Characterizing the RNA targets and position-dependent splicing regulation by TDP-43, Nat. Neurosci. 14 (2011) 452–458, https://doi.org/10.1038/nn.2778.
[11] M. Polymenidou, C. Lagier-Tourenne, K.R. Hutt, S.C. Huelga, J. Moran, T.Y. Liang, S.-C. Ling, E. Sun, E. Wancewicz, C. Mazur, H. Kordasiewicz, Y. Sedaghat, J. P. Donohue, L. Shiue, C.F. Bennett, G.W. Yeo, D.W. Cleveland, Long pre-mRNA depletion and RNA missplicing contribute to neuronal vulnerability from loss of TDP-43, Nat. Neurosci. 14 (2011) 459–468, https://doi.org/10.1038/nn.2779.
[12] A.N. Coyne, B.B. Siddegowda, P.S. Estes, J. Johannesmeyer, T. Kovalik, S. G. Daniel, A. Pearson, R. Bowser, D.C. Zarnescu, Futsch/MAP1B mRNA is a translational target of TDP-43 and is neuroprotective in a Drosophila model of amyotrophic lateral sclerosis, J. Neurosci. 34 (2014) 15962–15974, https://doi.org/10.1523/JNEUROSCI.2526-14.2014.
[13] A. Russo, R. Scardigli, F. La Regina, M.E. Murray, N. Romano, D.W. Dickson, B. Wolozin, A. Cattaneo, M. Ceci, Increased cytoplasmic TDP-43 reduces global protein synthesis by interacting with RACK1 on polyribosomes, Hum. Mol. Genet. 26 (2017) 1407–1418, https://doi.org/10.1093/hmg/ddx035.
[14] Y. Kawahara, A. Mieda-Sato, TDP-43 promotes microRNA biogenesis as a component of the Drosha and dicer complexes, Proc. Natl. Acad. Sci. U. S. A. 109 (2012) 3347–3352, https://doi.org/10.1073/pnas.1112427109.
[15] C.F. Sephton, S.K. Good, S. Atkin, C.M. Dewey, P. Mayer, J. Herz, G. Yu, TDP-43 is a developmentally regulated protein essential for early embryonic development, J. Biol. Chem. 285 (2010) 6826–6834, https://doi.org/10.1074/jbc.M109.061846.
[16] C.F. Sephton, B. Cenik, B.K. Cenik, J. Herz, G. Yu, TDP-43 in central nervous system development and function: clues to TDP-43-associated neurodegeneration, Biol. Chem. 393 (2012) 589–594, https://doi.org/10.1515/hsz-2012-0115.
[17] M.J. Strong, K. Volkening, R. Hammond, W. Yang, W. Strong, C. Leystra-Lantz, C. Shoesmith, TDP43 is a human low molecular weight Neurofilament (hNFL) mRNA-binding protein, Mol. Cell. Neurosci. 35 (2007) 320–327, https://doi.org/10.1016/j.mcn.2007.03.007.
[18] K. Volkening, C. Leystra-Lantz, W. Yang, H. Jaffee, M.J. Strong, TAR DNA Binding Protein of 43 kDa (TDP-43), 14–3-3 Proteins and Copper/Zinc Superoxide Dismutase (SOD1) Interact to Modulate NFL mRNA Stability. Implications for Altered RNA Processing in Amyotrophic Lateral Sclerosis (ALS), Brain Res. 1305 (2009) 168–182, https://doi.org/10.1016/j.brainres.2009.09.105.
[19] C. Colombrita, E. Onesto, F. Megiorni, A. Pizzuti, F.E. Baralle, E. Buratti, V. Silani, A. Ratti, TDP-43 and FUS RNA-binding proteins bind distinct sets of cytoplasmic messenger RNAs and differently regulate their post-transcriptional fate in Motoneuron-like cells, J. Biol. Chem. 287 (2012) 15635–15647, https://doi.org/10.1074/jbc.M111.333450.
[20] L. Costessi, F. Porro, A. Iaconcig, A.F. Muro, TDP-43 regulates β-adducin (Add2) transcript stability, RNA Biol. 11 (2014) 1280–1290, https://doi.org/10.1080/15476286.2014.996081.
[21] N.H. Alami, R.B. Smith, M.A. Carrasco, L.A. Williams, C.S. Winborn, S.S.W. Han, E. Kiskinis, B. Winborn, B.D. Freibaum, A. Kanagaraj, A.J. Clare, N.M. Badders, B. Bilican, E. Chaum, S. Chandran, C.E. Shaw, K.C. Eggan, T. Maniatis, J.P. Taylor, Axonal transport of TDP-43 mRNA granules is impaired by ALS-causing mutations, Neuron. 81 (2014) 536–543, https://doi.org/10.1016/j.neuron.2013.12.018.
[22] Y.M. Ayala, L. De Conti, S.E. Avendaño-Vázquez, A. Dhir, M. Romano, A. D'Ambrogio, J. Tollervey, J. Ule, M. Baralle, E. Buratti, F.E. Baralle, TDP-43 regulates its mRNA levels through a negative feedback loop, EMBO J. 30 (2011) 277–288, https://doi.org/10.1038/emboj.2010.310.
[23] M. Neumann, D.M. Sampathu, L.K. Kwong, A.C. Truax, M.C. Micsenyi, T.T. Chou, J. Bruce, T. Schuck, M. Grossman, C.M. Clark, L.F. McCluskey, B.L. Miller, E. Masliah, I.R. Mackenzie, H. Feldman, W. Feiden, H.A. Kretzschmar, J. Q. Trojanowski, V.M.-Y. Lee, Ubiquitinated TDP-43 in frontotemporal lobar degeneration and amyotrophic lateral sclerosis, Science. 314 (2006) 130–133, https://doi.org/10.1126/science.1134108.
[24] T. Nonaka, F. Kametani, T. Arai, H. Akiyama, M. Hasegawa, Truncation and pathogenic mutations facilitate the formation of intracellular aggregates of TDP-43, Hum. Mol. Genet. 18 (2009) 3353–3364, https://doi.org/10.1093/hmg/ddp275.
[25] M.C. Kiernan, S. Vucic, B.C. Cheah, M.R. Turner, A. Eisen, O. Hardiman, J. R. Burrell, M.C. Zoing, Amyotrophic lateral sclerosis, Lancet. 377 (2011) 942–955, https://doi.org/10.1016/S0140-6736(10)61156-7.
[26] T. Arai, M. Hasegawa, H. Akiyama, K. Ikeda, T. Nonaka, H. Mori, D. Mann, K. Tsuchiya, M. Yoshida, Y. Hashizume, T. Oda, TDP-43 is a component of ubiquitin-positive tau-negative inclusions in frontotemporal lobar degeneration and amyotrophic lateral sclerosis, Biochem. Biophys. Res. Commun. 351 (2006) 602–611, https://doi.org/10.1016/j.bbrc.2006.10.093.
[27] G.D. Rabinovici, B.L. Miller, Frontotemporal Lobar Degeneration, CNS Drugs. 24 (2010) 375–398, https://doi.org/10.2165/11533100-000000000-00000.
[28] C. Schwab, T. Arai, M. Hasegawa, S. Yu, P.L. McGeer, Colocalization of transactivation-responsive DNA-binding protein 43 and huntingtin in inclusions of Huntington disease, J. Neuropathol. Exp. Neurol. 67 (2008) 1159–1165, https://doi.org/10.1097/NEN.0b013e31818e8951.
[29] X.-L. Chang, M.-S. Tan, L. Tan, J.-T. Yu, The role of TDP-43 in Alzheimer's disease, Mol. Neurobiol. 53 (2016) 3349–3359, https://doi.org/10.1007/s12035-015-9264-5.
[30] A. Meneses, S. Koga, J. O'Leary, D.W. Dickson, G. Bu, N. Zhao, TDP-43 pathology in Alzheimer's disease, Mol. Neurodegener. 16 (2021) 84, https://doi.org/10.1186/s13024-021-00503-x.
[31] K. Markopoulou, D.W. Dickson, R.D. McComb, Z.K. Wszolek, L. Katechalidou, L. Avery, M.S. Stansbury, B.A. Chase, Clinical, neuropathological and genotypic variability in SNCA A53T familial Parkinson's disease. Variability in familial Parkinson's disease, Acta Neuropathol. 116 (2008) 25–35, https://doi.org/10.1007/s00401-008-0372-4.
[32] A.S. Chen-Plotkin, V.M.-Y. Lee, J.Q. Trojanowski, TAR DNA-binding protein 43 in neurodegenerative disease, Nat. Rev. Neurol. 6 (2010) 211–220, https://doi.org/10.1038/nrneurol.2010.18.
[33] E.B. Lee, V.M.-Y. Lee, J.Q. Trojanowski, Gains or losses: molecular mechanisms of TDP43-mediated neurodegeneration, Nat. Rev. Neurosci. 13 (2012) 38–50, https://doi.org/10.1038/nrn3121.
[34] F. Geser, V.M.-Y. Lee, J.Q. Trojanowski, Amyotrophic lateral sclerosis and frontotemporal lobar degeneration: a spectrum of TDP-43 proteinopathies, Neuropathol. 30 (2010) 103–112, https://doi.org/10.1111/j.1440-1789.2009.01091.x.
[35] E.M.J. de Boer, V.K. Orie, T. Williams, M.R. Baker, H.M. De Oliveira, T. Polvikoski, M. Silsby, P. Menon, M. van den Bos, G.M. Halliday, L.H. van den Berg, L. Van Den Bosch, P. van Damme, M.C. Kiernan, M.A. van Es, S. Vucic, TDP-43 proteinopathies: a new wave of neurodegenerative diseases, J. Neurol. Neurosurg. Psychiatry 92 (2020) 86–95, https://doi.org/10.1136/jnnp-2020-322983.
[36] L.-L. Jiang, M.-X. Che, J. Zhao, C.-J. Zhou, M.-Y. Xie, H.-Y. Li, J.-H. He, H.-Y. Hu, Structural transformation of the Amyloidogenic Core region of TDP-43 protein initiates its aggregation and cytoplasmic inclusion, J. Biol. Chem. 288 (2013) 19614–19624, https://doi.org/10.1074/jbc.M113.463828.
[37] A.K.-H. Chen, R.Y.-Y. Lin, E.Z.-J. Hsieh, P.-H. Tu, R.P.-Y. Chen, T.-Y. Liao, W. Chen, C.-H. Wang, J.J.-T. Huang, Induction of amyloid fibrils by the C-terminal fragments of TDP-43 in amyotrophic lateral sclerosis, J. Am. Chem. Soc. 132 (2010) 1186–1187, https://doi.org/10.1021/ja9066207.
[38] M. Udan, R.H. Baloh, Implications of the prion-related Q/N domains in TDP-43 and FUS, Prion. 5 (2011) 1–5, https://doi.org/10.4161/pri.5.1.14265.
[39] R.A. Fuentealba, M. Udan, S. Bell, I. Wegorzewska, J. Shao, M.I. Diamond, C. C. Weihl, R.H. Baloh, Interaction with Polyglutamine aggregates reveals a Q/N-rich domain in TDP-43, J. Biol. Chem. 285 (2010) 26304–26314, https://doi.org/10.1074/jbc.M110.125039.
[40] A. Saini, V.S. Chauhan, Delineation of the Core aggregation sequences of TDP-43 C-terminal fragment, Chembiochem. 12 (2011) 2495–2501, https://doi.org/10.1002/cbic.201100427.
[41] M. Budini, E. Buratti, C. Stuani, C. Guarnaccia, V. Romano, L. De Conti, F. E. Baralle, Cellular model of TAR DNA-binding protein 43 (TDP-43) aggregation based on its C-terminal Gln/Asn-rich region, J. Biol. Chem. 287 (2012) 7512–7525, https://doi.org/10.1074/jbc.M111.288720.
[42] K. Nishino, S. Watanabe, J. Shijie, Y. Murata, K. Oiwa, O. Komine, F. Endo, H. Tsuiji, M. Abe, K. Sakimura, A. Mishra, K. Yamanaka, Mice deficient in the C-terminal domain of TAR DNA-binding protein 43 develop age-dependent motor dysfunction associated with impaired Notch1−Akt signaling pathway, Acta Neuropathol. Commun. 7 (2019) 118, https://doi.org/10.1186/s40478-019-0776-5.
[43] W. Guo, Y. Chen, X. Zhou, A. Kar, P. Ray, X. Chen, E.J. Rao, M. Yang, H. Ye, L. Zhu, J. Liu, M. Xu, Y. Yang, C. Wang, D. Zhang, E.H. Bigio, M. Mesulam, Y. Shen, Q. Xu, K. Fushimi, J.Y. Wu, An ALS-associated mutation affecting TDP-43 enhances protein aggregation, fibril formation and neurotoxicity, Nat. Struct. Mol. Biol. 18 (2011) 822–830, https://doi.org/10.1038/nsmb.2053.
[44] L.M. Igaz, L.K. Kwong, A. Chen-Plotkin, M.J. Winton, T.L. Unger, Y. Xu, M. Neumann, J.Q. Trojanowski, V.M.-Y. Lee, Expression of TDP-43 C-terminal fragments in vitro recapitulates pathological features of TDP-43 Proteinopathies, J. Biol. Chem. 284 (2009) 8516–8524, https://doi.org/10.1074/jbc.M809462200.
[45] Y.-J. Zhang, Y.-F. Xu, C. Cook, T.F. Gendron, P. Roettges, C.D. Link, W.-L. Lin, J. Tong, M. Castanedes-Casey, P. Ash, J. Gass, V. Rangachari, E. Buratti, F. Baralle, T.E. Golde, D.W. Dickson, L. Petrucelli, Aberrant cleavage of TDP-43 enhances aggregation and cellular toxicity, Proc. Natl. Acad. Sci. U. S. A. 106 (2009) 7607–7612, https://doi.org/10.1073/pnas.0900688106.
[46] M. Hasegawa, T. Arai, T. Nonaka, F. Kametani, M. Yoshida, Y. Hashizume, T. G. Beach, E. Buratti, F. Baralle, M. Morita, I. Nakano, T. Oda, K. Tsuchiya, H. Akiyama, Phosphorylated TDP-43 in frontotemporal lobar degeneration and amyotrophic lateral sclerosis, Ann. Neurol. 64 (2008) 60–70, https://doi.org/10.1002/ana.21425.
[47] M.-X. Che, Y.-J. Jiang, Y.-Y. Xie, L.-L. Jiang, H.-Y. Hu, Aggregation of the 35-kDa fragment of TDP-43 causes formation of cytoplasmic inclusions and alteration of RNA processing, FASEB J. 25 (2011) 2344–2353, https://doi.org/10.1096/fj.10-174482.
[48] Y. Liu, W. Duan, Y. Guo, Z. Li, H. Han, S. Zhang, P. Yuan, C. Li, A new cellular model of pathological TDP-43: the neurotoxicity of stably expressed CTF25 of TDP-

43 depends on the proteasome, Neuroscience. 281 (2014) 88–98, https://doi.org/10.1016/j.neuroscience.2014.09.043.
[49] D.X. Medina, M.E. Orr, S. Oddo, Accumulation of C-terminal fragments of Transactive response DNA-binding protein 43 leads to synaptic loss and cognitive deficits in human TDP-43 transgenic mice, Neurobiol. Aging 35 (2014) 79–87, https://doi.org/10.1016/j.neurobiolaging.2013.07.006.
[50] A. Prasad, V. Sivalingam, V. Bharathi, A. Girdhar, B.K. Patel, The Amyloidogenicity of a C-terminal region of TDP-43 implicated in amyotrophic lateral sclerosis can be affected by anions, acetylation and Homodimerization, Biochimie. 150 (2018) 76–87, https://doi.org/10.1016/j.biochi.2018.05.003.
[51] A.E. Conicella, G.H. Zerze, J. Mittal, N.L. Fawzi, ALS mutations disrupt phase separation mediated by α-helical structure in the TDP-43 low complexity C-terminal domain, Structure 1993 (24) (2016) 1537–1549, https://doi.org/10.1016/j.str.2016.07.007.
[52] H.-R. Li, T.-C. Chen, C.-L. Hsiao, L. Shi, C.-Y. Chou, J. Huang, The physical forces mediating self-association and phase-separation in the C-terminal domain of TDP-43, Biochim. Biophys. Acta, Proteins Proteomics 2018 (1866) 214–223, https://doi.org/10.1016/j.bbapap.2017.10.001.
[53] Y. Shiina, K. Arima, H. Tabunoki, J. Satoh, TDP-43 dimerizes in human cells in culture, Cell. Mol. Neurobiol. 30 (2010) 641–652, https://doi.org/10.1007/s10571-009-9489-9.
[54] M. Vivoli-Vega, P. Guri, F. Chiti, F. Bemporad, Insight into the folding and dimerization mechanisms of the N-terminal domain from human TDP-43, Int. J. Mol. Sci. 21 (2020) 6259, https://doi.org/10.3390/ijms21176259.
[55] C. Ke Chang, T.H. Wu, C.Y. Wu, M. Hui Chiang, E.K.W. Toh, Y.C. Hsu, K.F. Lin, Y. Heng Liao, T. Huang Huang, J.J.T. Huang, The N-terminus of TDP-43 promotes its oligomerization and enhances DNA binding affinity, Biochem. Biophys. Res. Commun. 425 (2012) 219–224, https://doi.org/10.1016/j.bbrc.2012.07.071.
[56] L.-L. Jiang, W. Xue, J.-Y. Hong, J.-T. Zhang, M.-J. Li, S.-N. Yu, J.-H. He, H.-Y. Hu, The N-terminal dimerization is required for TDP-43 splicing activity, Sci. Rep. 7 (2017) 6196, https://doi.org/10.1038/s41598-017-06263-3.
[57] A. Wang, A.E. Conicella, H.B. Schmidt, E.W. Martin, S.N. Rhoads, A.N. Reeb, A. Nourse, D. Ramirez Montero, V.H. Ryan, R. Rohatgi, F. Shewmaker, M.T. Naik, T. Mittag, Y.M. Ayala, N.L. Fawzi, A single N-terminal Phosphomimic disrupts TDP-43 polymerization, phase separation, and RNA splicing, EMBO J. 37 (2018), e97452, https://doi.org/10.15252/embj.201797452.
[58] Y.-J. Zhang, T. Caulfield, Y.-F. Xu, T.F. Gendron, J. Hubbard, C. Stetler, H. Sasaguri, E.C. Whitelaw, S. Cai, W.C. Lee, L. Petrucelli, The dual functions of the extreme N-terminus of TDP-43 in regulating its biological activity and inclusion formation, Hum. Mol. Genet. 22 (2013) 3112–3122, https://doi.org/10.1093/hmg/ddt166.
[59] A. Shodai, A. Ido, N. Fujiwara, T. Ayaki, T. Morimura, M. Oono, Conserved acidic amino acid residues in a second RNA recognition motif regulate assembly and function of TDP-43, PLoS One 7 (2012), e52776, https://doi.org/10.1371/journal.pone.0052776.
[60] A. Shodai, T. Morimura, A. Ido, T. Uchida, T. Ayaki, R. Takahashi, S. Kitazawa, S. Suzuki, M. Shirouzu, T. Kigawa, Y. Muto, S. Yokoyama, R. Takahashi, R. Kitahara, H. Ito, N. Fujiwara, M. Urushitani, Aberrant assembly of RNA recognition motif 1 links to pathogenic conversion of TAR DNA-binding protein of 43 kDa (TDP-43), J. Biol. Chem. 288 (2013) 14886–14905, https://doi.org/10.1074/jbc.M113.451849.
[61] S. Agrawal, P.-H. Kuo, L.-Y. Chu, B. Golzarroshan, M. Jain, H.S. Yuan, RNA recognition motifs of disease-linked RNA-binding proteins contribute to amyloid formation, Sci. Rep. 9 (2019) 6171, https://doi.org/10.1038/s41598-019-42367-8.
[62] M. Pillai, S.K. Jha, The folding and aggregation energy landscapes of tethered RRM domains of human TDP-43 are coupled via a metastable molten globule-like oligomer, Biochemistry. 58 (2019) 608–620, https://doi.org/10.1021/acs.biochem.8b01013.
[63] C. Yang, W. Tan, C. Whittle, L. Qiu, L. Cao, S. Akbarian, Z. Xu, The C-terminal TDP-43 fragments have a High aggregation propensity and harm neurons by a dominant-negative mechanism, PLoS One 5 (2010), e15878, https://doi.org/10.1371/journal.pone.0015878.
[64] Z.R. Grese, A.C. Bastos, L.D. Mamede, R.L. French, T.M. Miller, Y.M. Ayala, Specific RNA interactions promote TDP-43 multivalent phase separation and maintain liquid properties, EMBO Rep. 22 (2021), e53632, https://doi.org/10.15252/embr.202153632.
[65] Y. Sun, P.E. Arslan, A. Won, C.M. Yip, A. Chakrabartty, Binding of TDP-43 to the 3'UTR of its cognate mRNA enhances its solubility, Biochemistry. 53 (2014) 5885–5894, https://doi.org/10.1021/bi500617x.
[66] Y.C. Huang, K.F. Lin, R.Y. He, P.H. Tu, J. Koubek, Y.C. Hsu, J.J.T. Huang, Inhibition of TDP-43 aggregation by nucleic acid binding, PLoS One 8 (2013), e64002, https://doi.org/10.1371/journal.pone.0064002.
[67] J.R. Mann, A.M. Gleixner, J.C. Mauna, E. Gomes, M.R. DeChellis-Marks, P. G. Needham, K.E. Copley, B. Hurtle, B. Portz, N.J. Pyles, L. Guo, C.B. Calder, Z. P. Wills, U.B. Pandey, J.K. Kofler, J.L. Brodsky, A. Thathiah, J. Shorter, C. J. Donnelly, RNA binding antagonizes neurotoxic phase transitions of TDP-43, Neuron. 102 (2019) 321–338.e8, https://doi.org/10.1016/j.neuron.2019.01.048.
[68] E. Zacco, R. Graña-Montes, S.R. Martin, N.S. de Groot, C. Alfano, G.G. Tartaglia, A. Pastore, RNA as a key factor in driving or preventing self-assembly of the TAR DNA-binding protein 43, J. Mol. Biol. 431 (2019) 1671–1688, https://doi.org/10.1016/j.jmb.2019.01.028.
[69] M. Pillai, S.K. Jha, Early metastable assembly during the stress-induced formation of worm-like amyloid fibrils of nucleic acid binding domains of TDP-43, Biochemistry. 59 (2020) 315–328, https://doi.org/10.1021/acs.biochem.9b00780.
[70] D. Patni, S.K. Jha, Protonation–deprotonation switch controls the amyloid-like misfolding of nucleic-acid-binding domains of TDP-43, J. Phys. Chem. B 125 (2021) 8383–8394, https://doi.org/10.1021/acs.jpcb.1c03262.
[71] J. Singh, J.B. Udgaonkar, Unraveling the molecular mechanism of pH-induced misfolding and oligomerization of the prion protein, J. Mol. Biol. 428 (2016) 1345–1355, https://doi.org/10.1016/j.jmb.2016.01.030.
[72] L. Stryer, The interaction of a naphthalene dye with Apomyoglobin and Apohemoglobin. A fluorescent probe of non-polar binding sites, J. Mol. Biol. 13 (1965) 482–495, https://doi.org/10.1016/s0022-2836(65)80111-5.
[73] V.R. Agashe, J.B. Udgaonkar, Thermodynamics of denaturation of Barstar: evidence for cold denaturation and evaluation of the interaction with guanidine hydrochloride, Biochemistry. 34 (1995) 3286–3299, https://doi.org/10.1021/bi00010a019.
[74] R. Moulick, J.B. Udgaonkar, Thermodynamic characterization of the unfolding of the prion protein, Biophys. J. 106 (2014) 410–420, https://doi.org/10.1016/j.bpj.2013.11.4491.
[75] J.A. Schellman, The thermodynamic stability of proteins, Annu. Rev. Biophys. Biophys. Chem. 16 (1987) 115–137, https://doi.org/10.1146/annurev.bb.16.060187.000555.
[76] B.C. Mackness, M.T. Tran, S.P. McClain, C.R. Matthews, J.A. Zitzewitz, Folding of the RNA recognition motif (RRM) domains of the amyotrophic lateral sclerosis (ALS)-linked protein TDP-43 reveals an intermediate state, J. Biol. Chem. 289 (2014) 8264–8276, https://doi.org/10.1074/jbc.M113.542779.
[77] H. Naiki, F. Gejyo, Kinetic analysis of amyloid fibril formation, Methods Enzymol. 309 (1999) 305–318, https://doi.org/10.1016/s0076-6879(99)09022-9.
[78] S. Jain, J.B. Udgaonkar, Evidence for stepwise formation of amyloid fibrils by the mouse prion protein, J. Mol. Biol. 382 (2008) 1228–1241, https://doi.org/10.1016/j.jmb.2008.07.052.
[79] K. Nasreen, Z.A. Parray, S. Ahamad, F. Ahmad, A. Ahmed, S. Freeh Alamery, T. Hussain, M.I. Hassan, A. Islam, Interactions under crowding milieu: chemical-induced denaturation of myoglobin is determined by the extent of Heme dissociation on interaction with Crowders, Biomolecules. 10 (2020) 490, https://doi.org/10.3390/biom10030490.
[80] S. Maharana, J. Wang, D.K. Papadopoulos, D. Richter, A. Pozniakovsky, I. Poser, M. Bickle, S. Rizk, J. Guillén-Boixet, T.M. Franzmann, M. Jahnel, L. Marrone, Y.-T. Chang, J. Sterneckert, P. Tomancak, A.A. Hyman, S. Alberti, RNA buffers the phase separation behavior of prion-like RNA binding proteins, Science. 360 (2018) 918–921, https://doi.org/10.1126/science.aar7366.
[81] H. Qin, L.-Z. Lim, Y. Wei, J. Song, TDP-43 N terminus encodes a novel ubiquitin-like fold and its unfolded form in equilibrium that can be shifted by binding to ssDNA, Proc. Natl. Acad. Sci. 111 (2014) 18619–18624, https://doi.org/10.1073/pnas.1413994112.
[82] S. Xiao, T. Sanelli, H. Chiang, Y. Sun, A. Chakrabartty, J. Keith, E. Rogaeva, L. Zinman, J. Robertson, Low molecular weight species of TDP-43 generated by abnormal splicing form inclusions in amyotrophic lateral sclerosis and result in motor neuron death, Acta Neuropathol. (Berl.). 130 (2015) 49–61, https://doi.org/10.1007/s00401-015-1412-5.
[83] Y.-J. Zhang, Y. Xu, C.A. Dickey, E. Buratti, F. Baralle, R. Bailey, S. Pickering-Brown, D. Dickson, L. Petrucelli, Progranulin mediates caspase-dependent cleavage of TAR DNA binding Protein-43, J. Neurosci. 27 (2007) 10530–10534, https://doi.org/10.1523/JNEUROSCI.3421-07.2007.
[84] M. Laura, N. Giuseppe, C. Lesley, V. Michele, P. Annalisa, Functional interactions as a survival strategy against abnormal aggregation, FASEB J. 25 (2011) 45–54, https://doi.org/10.1096/fj.10-161208.
[85] C.E. Bulawa, S. Connelly, M. Devit, L. Wang, C. Weigel, J.A. Fleming, J. Packman, E.T. Powers, R.L. Wiseman, T.R. Foss, I.A. Wilson, J.W. Kelly, R. Labaudinière, Tafamidis, a potent and selective transthyretin kinetic stabilizer that inhibits the amyloid Cascade, Proc. Natl. Acad. Sci. U. S. A. 109 (2012) 9629–9634, https://doi.org/10.1073/pnas.1121005109.